Doctoral Dissertation

博士論文

Optical and thermal study of molecular thin layers on cryogenic mirrors in next-generation gravitational wave telescopes

(次世代重力波望遠鏡における低温鏡への分子吸着薄膜層形成による光学的および熱的影響)

A Dissertation Submitted for the Degree of Doctor of Philosophy

December 2019

令和元年 12 月博士 (理学) 申請

Department of Physics, Graduate School of Science,
The University of Tokyo

東京大学大学院理学系研究科物理学専攻

Kunihiko Hasegawa

長谷川 邦彦

Acknowledgements

Firstly, I would like to thank my supervisor Shinji Miyoki for his continuous huge supports. He has supervised me for five years since I entered his laboratory. His deep understanding of the interferometer experiments has excited me. During the meeting, he always concerns the progress of my experiment, and a lot of experimental equipment was purchased by him. Thanks to his great support, I could do what I wanted to do and managed to finish this dissertation. I'm proud of these five years passes as a student of him.

Next, I am grateful to Takayuki Tomaru. He was pleased to enter the KAGRA cryogenic subgroup and come to KEK when I start my doctoral course. He always introduced me to his interesting ideas, and the discussions of these ideas trained me to think everything. Large experimental setups were purchased by him, and I could concentrate on my experiment and analysis.

Toshikazu Suzuki answered my stupid questions whenever he was in KEK. His deep understanding of physics solved my questions and it made great progress in the study. Nobuhiro Kimura gave me understandings of the cryogenic system of KAGRA.Thanks to his support and suggestions, I could manage to finish my experiment in KAGRA. Kazuhiro Yamamoto gave me fruitful comments on the Brownian noise analysis in the thesis. His deep understandings of the thermal noise surprised me every time. Takafumi Ushiba gave me accurate advice for my research. Whenever I had a problem, I asked him to get his knowledge.

Ettore Majorana gave me a chance to work on the suspension system for Virgo test mass when I visited Virgo observatory. His good personality relaxed me and I could spend great days in Italy without any trouble. He also interested in my research and asked me about the progress of the study every time we met. Flavio Travasso always makes me smile.Thanks to his smile, I could enjoy life in Italy. His passion for the gravitational wave physics motivates me to work hard.

Yoshikazu Namai made my experimental staffs with his sophisticated skills.His workpieces are very beautiful and there is no mistake. He always accepted my selfishness, and made may things "as soon as possible". I would like to beat him in golf shortly. Ayako Ueda always supported my experiment in KEK.All handmade experimental setups were designed by her. She is very

friendly and chatting with her increases the motivation to the research. During writing the dissertation, she worried about my malnutrition and made tasty dishes. Ayako Hagiwara helps me to check the detailed design of the KAGRA cryogenic payload.Without her continuous efforts on the cryogenic payload, it was not completed. She is always simile, give snacks for hungry students.

Rie Kikuchi and Nomi Kudo are secretaries of the gravitational wave group of ICRR. Thanks to their help, I was able to concentrate my research.

Thanks to funny moments with group members I could enjoy my life at the University of Tokyo. Koji Nagano, Yutaro Enomoto, Tomofumi Shimoda, Yoshinori Fujii, Koseki Miyo, and Naoki Aritomi are my colleagues of experimental GWs group. They have been always helped me and kept me smiling. Without them, I think I could not finish the thesis within a time. I would also thank students in the KEK laboratory, Tomohiro Yamada, Tadaharu Shishido, and Rishabh Bajpai.The combination of our originalities and personalities make uncountable funny moments. I cannot forget the days in KEK spent with them.

Masaki Ando, Masahiro Takada, Masato Takita, Osamu Yamamuro, and Kimihiro Okumura were the reviews of this doctoral dissertation. They gave fruitful discussions and comments following their specialties.

This work was supported by MEXT, JSPS Leading-edge Research Infrastructure Program, JSPS Grant-in-Aid for Specially Promoted Research 26000005, MEXT Grant-in-Aid for Scientific Research on Innovative Areas 24103005, JSPS Core-to-Core Program, A. Advanced Research Networks, the joint research program of the Institute for Cosmic Ray Research, University of Tokyo, National Research Foundation (NRF) and Computing Infrastructure Project of KISTI-GSDC in Korea, the LIGO project, and the Virgo project. I also received financial support from ALPS (Advanced Leading Graduate Course for Photon Science) program at the University of Tokyo.

Finally, I appreciate all the support of my parents, sister, aunts, uncles, cousins, grandmothers. I also thank grandfathers in heaven.

Abstract

Detections of the gravitational waves (GWs) opened the new window for us, and they have been bringing physically and astronomically important information. From now on, precise measurement of the signal and accurate sky localization are important for the multi-messenger astronomy with the electromagnetic waves and the neutrino.

KAGRA is the Japanese GW telescope which is aiming the precise measurement by adapting the cryogenic mirrors for the first time in the world to reduce the thermal noise that limits the most sensitive frequencies. For the more precise measurement, the next generation GW telescopes such as Einstein Telescope in Europe and Cosmic Explorer in the U.S also plan to adapt cryogenic mirrors with its 10 km scale baseline. The development of the cryogenic system adaptable in the GW telescope is important not only to complete KAGRA but also to improve the sensitivity of the future detectors. The material properties at the cryogenic temperature and the low vibration refrigerator have been measured and developed for this purpose. However, the interaction between the cryogenic mirrors and the vacuum residual gasses has never studied except for a few experimental evaluations, though it is a well known phenomenon.

The molecules that are transported from the long beam duct hit the surface of the cryogenic mirrors, decrease their kinetic energy and caught up by the surface potential. The frequency of the molecular injection to the cryogenic mirror was evaluated by adopting the KAGRA cryogenic and vacuum system into the vacuum engineering theory. The KAGRA vacuum system is not finalized and the vacuum pressure is worse than the designed value by a factor of 10. Utilizing the situation, the molecular incident frequency was experimentally and numerically evaluated, and we confirmed that these two evaluation are well consistent.

A number of molecules form the layer on the mirror, and it works as the optical coating. The impacts of the molecular layer were simulated and we pointed out that it decreases the sensitivity by 84% at worst within the thickness of 2.5 μm.

To solve the problem, the thermal desorption system using the CO_2 laser was suggested and tested in the laboratory. As a result, we confirmed that

it can heat the cryogenic mirror enough to remove the molecular layer, and it shortens the thermal cycle to remove the molecular layer from about 1.5 months to 60 hours.

CONTENTS

LIST OF FIGURES

LIST OF TABLES

PREFACE

Detections of the gravitational waves (GWs) opened the new window for us, and they have been bringing physically and astronomically important information. From now on, precise measurement of the signal and accurate sky localization are important for the multi-messenger astronomy with the electromagnetic waves and the neutrino.

KAGRA is the Japanese GW telescope which is aiming the precise measurement by adapting the cryogenic mirrors for the first time in the world to reduce the thermal noise that limits the most sensitive frequencies. For the more precise measurement, the next generation GW telescopes such as Einstein Telescope (ET) in Europe and Voyager in the U.S also plan to adapt cryogenic mirrors with its 10km scale baseline. The size of the mirror also improve the thermal noise, but it is not so easy to provide a high quality large optics, and the combination with the cryogenics is necessary for them.

The development of the cryogenic system adaptable in the GW telescope is important not only to achieve the KAGRA sensitivity but also to improve the sensitivity of the future detectors. The material properties at the cryogenic temperature and the low vibration refrigerator have been measured and developed for this purpose. However, the interaction between the cryogenic mirrors and the vacuum residual gasses has never studied except for a few experimental evaluations, though it is a well known phenomenon.

Even if that is inside the vacuum chamber, there are many molecules inside. When these molecules hit the cryogenic surface, they reduce their kinetic energy and caught up by the surface potential. This phenomenon is applied as a cryopump, the technique to get the ultra-high vacuum. The cryogenic system, including the cryogenic mirrors, inside the cryogenic GWD, works as the cryopump and it helps to improve the vacuum pressure inside the vacuum duct by adsorbing the molecules on their surfaces.

The adsorbed molecules form a molecular layer, and it is considered to

work as the lossy optical coating. If it changes the optical property of the cryogenic mirrors that are carefully chosen to maximize the detector sensitivity, the detector cannot realize its original performance.

The formalization of the molecular layer growth on the cryogenic mirror is necessary to design the future cryogenic GWDs. Further, the evaluation of the impacts of the molecular layer on the cryogenic GWD shows the potential risk of the cryogenics.

Though the molecular layer formation is very troublesome, the cryogenics is necessary for the next generation GWDs. The understanding of the process of the molecular layer and the impacts on the detector is the first step of the study. We hope that this dissertation is sure one step towards the perfect cryogenic GWD.

Outline of the dissertation

The outline of the dissertation is as follows. Chapter 1 derives the GWs from the general relativity and introduces the detection of GWs with the current configuration of the interferometric GWDs. The fundamental noises that limit detector sensitivity are also explained. Chapter 2 summarizes KAGRA and the significance of the study is also mentioned. The main part of this dissertation starts from Chapter 3. Chapter 3 deal with the vacuum engineering theory, simulate the conductance of the KAGRA cryogenic and vacuum system, and the frequency of the molecular injection to the cryogenic mirror is calculated. Chapter 4 describes the principle of the experiment, and details the experiment to measure the frequency of the molecular layer formation on the cryogenic mirror in the KAGRA cryostat. Chapter 5 evaluates the optical and thermal impacts of the molecular layer on the GWD and simulates how it worsen the detector sensitivity. Chapter 6 introduces the thermal desorption system using the CO_2 laser and its evaluation. The performance of the scaled desorption system to the KAGRA cryogenic system is also discussed. Chapter 7 mainly discusses the application of the study. Chapter 8 provides the future prospects and the conclusion.

Chapter 1
GRAVITATIONAL WAVES AND INTERFEROMETRIC DETECTION

Gravitational wave (GW) is the phenomenon that causes expansion and constraction of spacetime, propagating as the speed of light. A. Einstein introduced them by linearizing the fundamental equation of general relativity, Einstein equation [1, 2]. To detect GWs, interferometric gravitational wave detectors (GWDs) have been constructed on earth, such as LIGO, Virgo and KAGRA [3–5]. Finally, advanced LIGO and Virgo detected the GWs from the binary black hole merger in 2015 [6]. In this section, starting from the general relativity, GWs and their characteristics are derived. The basic principle of the grand-based GWDs and the fundamental noise of the detector are also introduced.

1.1 General relativity and gravitational waves

1.1.1 General relativity

A. Einstein predicted the existence of GWs using general relativity. General relativity is a theory to determine the construction of spacetime and gravity is understood as a curvature of spacetime in this theory. In general relativity, the construction of spacetime is described by the metric tensor $g_{\mu\nu}$[‡1] and the interval ds between the two points, x^μ and $x^\mu + dx^\mu$, as

$$ds^2 = g_{\mu\nu} dx^\mu dx^\nu \tag{1.1}$$

[‡1] Greek index (α, μ, ν etc.) means the coordinate number from 0 to 3

Relation between the metric tensor and the distribution of the energy and the mass in spacetime follows the Einstein equation as

$$R_{\mu\nu} - \frac{1}{2}g_{\mu\nu}R = \frac{8\pi G}{c^4}T_{\mu\nu} \tag{1.2}$$

where $G = 6.67259 \times 10^{-11}\mathrm{Nm}^2/\mathrm{kg}^2$, $c = 2.99792458 \times 10^8\mathrm{m/s}$ and $T_{\mu\nu}$ are the gravity constant, the speed of light and the energy-momentum tensor which denotes the distribution of the energy and the mass in spacetime, respectively. $R_{\mu\nu}$ and R are Ricchi tensor and Ricchi scalar. Especially, the left side of Eq.(1.2) is called as Einstein tensor $G_{\mu\nu} = R_{\mu\nu} - \frac{1}{2}g_{\mu\nu}R$. The features of gravitational field can be investigated by considering the perturbation from the flat spacetime. Metric tensor for the flat spacetime is called Minkowski metric $\eta_{\mu\nu}$. For weak gravitational field, the metric can written as $g_{\mu\nu} = \eta_{\mu\nu} + h_{\mu\nu}$, where $h_{\mu\nu}$ describes the perturbation around Minkowski spacetime and satisfies $|h_{\mu\nu}| \ll 1$. By taking first order of $h_{\mu\nu}$ and the Lorentz gauge condition $\bar{h}^{\mu\sigma}{}_{,\sigma} = 0$ where $\bar{h}_{\mu\nu} \equiv h_{\mu\nu} - \frac{1}{2}\nu_{\mu\nu}h$ and $h = h^{\alpha}_{\alpha}$, Eq.(1.2) is rewritten as

$$\Box\overline{h}_{\mu\nu} = -\frac{16\pi G}{c^4}T_{\mu\nu}. \tag{1.3}$$

The equation implies that the perturbation $h_{\mu\nu}$ follows the wave equation, and the answer of the equation is so called gravitational waves.

To study the propagation of GWs and the interaction with the test masses in spacetime, we consider the spacetime outside the source of GWs where the energy-momentum tensor is zero, $T_{\mu\nu} = 0$. The linearized Einstein equation in vacuum is written as $\Box\overline{h}_{\mu\nu} = 0$, and the simplest solution to the wave equation Eq.(1.3) is a plane wave solution of the form

$$\overline{h}_{\mu\nu} = A_{\mu\nu}e^{ik_\sigma x^\sigma}, \tag{1.4}$$

where $A_{\mu\nu}$ is the polarization tensor which contains the information about the amplitude and the polarization of the waves, and k_σ is the wave number vector which determines the direction of the propagation and the frequency of the wave.

To reduce the residual gauge freedom in the Lorentz gauge, here we define and set the transverse-traceless (TT) gauge as $A^{\mu 0} = 0$, $A^{\mathrm{i}}{}_{\mathrm{i}} = 0$ and $\partial^{\mathrm{j}}A_{\mathrm{ij}} = 0$. Assuming GWs propagating along the z axis, Eq.(1.4) is rewritten as

$$\overline{h}_{\mu\nu} = A_{\mu\nu}e^{ik(ct-z)}, \tag{1.5}$$

with

$$A_{\mu\nu} = \begin{bmatrix} 0 & 0 & 0 & 0 \\ 0 & h_+ & h_\times & 0 \\ 0 & h_\times & -h_+ & 0 \\ 0 & 0 & 0 & 0 \end{bmatrix}, \tag{1.6}$$

where $h_+ = A_{11}$ and $h_\times = A_{12}$. In general relativity, GWs have two independent polarization called the plus mode and the cross mode. Next subsection explains how these polarization affect to the test masses in spacetime.

1.1.2 Tidal effect and polarization of gravitational waves

We define the distance δl between $\mathrm{P}_1 = (0, 0, 0, 0)$ and $\mathrm{P}_2 = (0, \varepsilon, 0, 0)$, where $|\varepsilon| \ll 1$. For example, in the Minkowski spacetime, δl is calculated as

$$\delta l = \int |\eta_{\mu\nu} dx^\mu dx^\nu|^{1/2} = \int_0^\varepsilon dx^1 = \varepsilon. \tag{1.7}$$

When GWs described in Eq.(1.5) come up vertically against the points $\mathrm{P}_1\mathrm{P}_2$, the metric tensor changes as

$$g_{\mu\nu} = \eta_{\mu\nu} + \overline{h}_{\mu\nu} = \begin{bmatrix} -1 & 0 & 0 & 0 \\ 0 & 1 + h_+ e^{ik(ct-z)} & h_\times e^{ik(ct-z)} & 0 \\ 0 & h_\times e^{ik(ct-z)} & 1 - h_+ e^{ik(ct-z)} & 0 \\ 0 & 0 & 0 & 1 \end{bmatrix}. \tag{1.8}$$

Hence, the distance δl between P_1 and P_2 becomes as

$$\delta l = \int |g_{\mu\nu} dx^\mu dx^\nu|^{1/2} = \int_0^\varepsilon |g_{11}|^{1/2} \, dx^1 \sim \left[1 + \frac{1}{2} h_+ e^{ik(ct-z)}\right] \varepsilon. \tag{1.9}$$

Hence, GWs change the distance between the two points periodically.

Next, we consider the test masses that are put on a circle as shown in Fig.(1.1). The radius of the circle is ε, and the coordinates of each test mass are $(\varepsilon \cos\theta_\mathrm{i}, \varepsilon \sin\theta_\mathrm{i}, 0)$, where θ_i is the angle between the x axis and the i-th test mass. By taking the distance change for x and y axes due to the plus mode of GWs independently into account, the amount of the distance change between the origin and the i-th test mass is

$$\delta l = \left[1 + \frac{1}{2} h_+ e^{ik(ct-z)} \cos 2\theta_\mathrm{i}\right] \varepsilon. \tag{1.10}$$

Figure (1.1) shows the motion of the test masses in spacetime due to the injection of GWs with the plus and the cross mode. As a result of the GWs injection, the relative distance of the test masses oscillates. Generally, the polarization of GWs is described by the superposition of the plus mode and the cross mode.

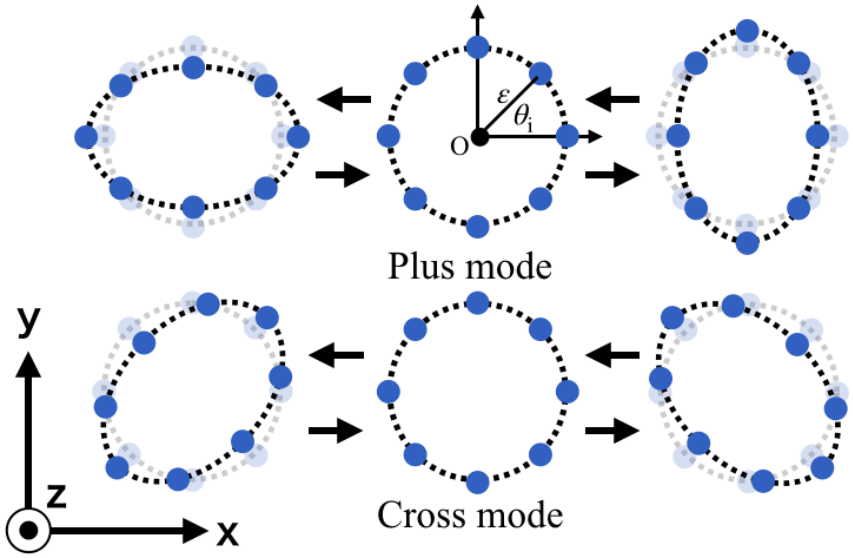

Figure 1.1: Polarization of GWs. GWs have two independent polarizations : the plus mode and the cross mode in general relativity. The polarization of GWs are the superposition of the plus mode and the cross mode.

1.1.3 Generation of gravitational waves

The aspheric symmetry motion generate the GWs. Here we describe the generation of the GWs under the assumption that the distance of the source and the observer $r_{\rm o}$ is much larger than the wavelength of the GWs $\lambda_{\rm GW}$, and $\lambda_{\rm GW}$ is much larger than the size of the source R. Then, the solution of the linearized Einstein equation (1.3) is given as

$$\bar{h}_{\mu\nu} = \frac{2G}{c^4} r_{\rm o} \ddot{I}_{\rm ij}(t - \frac{r_{\rm o}}{c}), \tag{1.11}$$

where $r_{\rm o}$ is the distance between the wave source and the observer, and $\ddot{I}_{\rm ij}$ is the mass quadrupole moment which is given as

$$\ddot{I}_{\rm ij}(t-\frac{r_{\rm o}}{c}) = \int \rho(t-\frac{r_{\rm o}}{c}, \mathbf{x}') \left(x'_{\rm i} x'_{\rm j} - \frac{1}{3}\delta_{\rm ij} x'^{\rm i} x'^{\rm j} \right). \tag{1.12}$$

As shown Eq.(1.11), the lowest order of the gravitational wave radiation is the quadrupole radiation, though it is the dipole for the electromagnetic radiation.

1.1.4 Source of GWs

Binary compact star binary

The binary star system composed of compact stars such as black holes (BHs) and neutron stars (NSs) reduce the distance between two star while generating GWs. The amplitude and the frequency during this process are written as [7]

$$h(t) = 2.1 \times 10^{-23} \left(\frac{\mathcal{M}}{1.2 M_\odot} \right)^{5/3} \left(\frac{t}{1\,[\rm sec]} \right)^{-1/4} \left(\frac{200\,[\rm MPc]}{r} \right) \tag{1.13}$$

and

$$f(t) = 135 \left(\frac{\mathcal{M}}{1.2 M_\odot} \right)^{5/8} \left(\frac{1\,[\rm sec]}{t} \right)^{-3/8} \quad \text{Hz} \tag{1.14}$$

where t is the time before the collision, r is the distance between the binary system and the observer, and $\mathcal{M} = \frac{(m_1 m_2)^{3/5}}{(m_1+m_2)^{-1/5}}$ is the chirp mass of the system, where m_1 and m_2 are the mass of each stars. Finally, when two stars close to about their radius, these two stars collapse and a new large star is made. Because the amplitude from compact binary star systems is comparable with the sensitivity of current GWD, the GWs from these systems is one of the most promised source and they have been detected by advanced LIGO and Virgo [8–13].

Especially, the GWs from the neutron star binary system is worthful to be followed up by the electromagnetic wave observations. This multi-messenger astronomy can reveal the equation of state (EoS) of the neutron star [14]. The composition of the neutron star has not been revealed though the many studies are performed using unstable nuclei, such as the hyper nuclei [15]. Using many events from the NSs, the EoS of the neutron star can be determined, and it is enable to study about the nature of neutron star on earth accurately.

Supernovae

During the core-collapse supernovae, the GWs are considered to be generated [16, 17]. The waveform of this event is considered to be the burst like, but accurate simulation is difficult because the theoretical elucidation of the process has not been determined yet. The direct observations of this GWs are willing to proceed the study of the supernovae process, though the detectable range is estimated within Andromeda Galaxy with the sensitivity of the current GWDs.

1.2 Interferometric gravitational wave detection

Several techniques have been studied for GW detections, the resonance bar antenna [18], the pulsar timing array [19] for instance. However, the laser interferometric gravitational wave detector is the only technique which has successfully detected gravitational waves so far [8–13]. In the following subsections, we introduce the basic working principle of interferometric gravitational wave detector, and the techniques to improve the detector sensitivity. The fundamental noises in a GWD are also discussed.

1.2.1 Michelson Interferometer

The basic configuration of a laser interferometric gravitational wave detector is a Michelson Interferometer (MI). Here, let us consider a simple MI shown in Fig.(1.2). The electric field of light emitted from a laser source is written as $E_{\rm i} = E_0 e^{i\Omega t}$, where E_0 and Ω the amplitude of the electric field and the angular frequency of light. This input light $E_{\rm i}$ reaches the beam splitter (BS) and is divided into the two light. These two light travel along each arm with length of $L_{\rm x}$ and $L_{\rm y}$ independently, and are reflected by the mirrors at the end of each arm. Finally, they reach BS again and inject to the photo detector (PD). During the round trip and the reflection at the end mirrors, the phase of these two light change as

$$\phi_{\rm i} = \frac{2L_{\rm i}}{c}\Omega + \pi \quad ({\rm i} = {\rm x \ or \ y})\,. \tag{1.15}$$

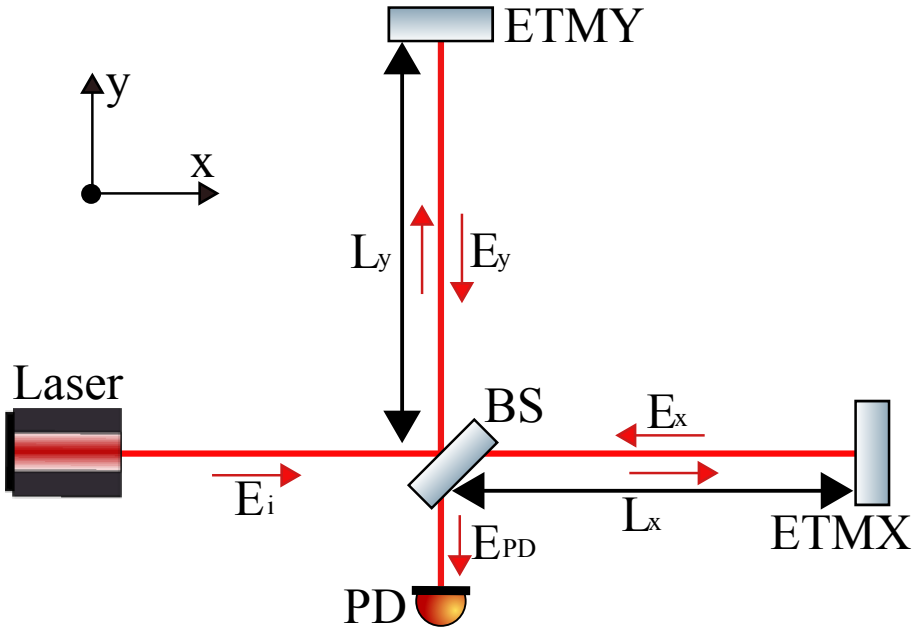

Figure 1.2: Optical configuration of a Michelson Interferometer.

The sum of the electric field injecting to the PD is described as

$$E_{\mathrm{PD}} = \frac{1}{\sqrt{2}}\left(E_{\mathrm{x}} + E_{\mathrm{y}}\right) \tag{1.16}$$

$$= \frac{1}{2}E_0 e^{i\Omega t}\left(e^{-i\phi_{\mathrm{x}}} + e^{-i(\phi_{\mathrm{y}}+\pi)}\right), \tag{1.17}$$

where $E_{\mathrm{x}} = \frac{1}{\sqrt{2}}E_0 e^{i(\Omega t-\phi_{\mathrm{x}})}$ and $E_{\mathrm{y}} = \frac{1}{\sqrt{2}}E_0 e^{i(\Omega t-\phi_{\mathrm{y}}+\pi)}$ are the electric fields just before the recombination at BS. Note that here we assumed that the power reflectivity of BS is 50%, and add phase π to the light from the y arm due to the phase shift at the BS reflection. The output of the PD P_{PD} is proportional to the power of the electric field and described as

$$P_{\mathrm{PD}} \propto |E_{\mathrm{PD}}|^2 = \frac{1}{2}|E_0|^2\left(1-\cos\left(\phi_{\mathrm{x}}-\phi_{\mathrm{y}}\right)\right). \tag{1.18}$$

Equation1.18 implies that a MI detects the phase difference $\Delta\phi \propto \phi_{\mathrm{x}} - \phi_{\mathrm{x}}$ of light that are divided into two perpendicular arms. Depending on the amount of the phase difference $\Delta\phi$, the strength of light coming to the PD changes. This signal is called the fringe, and the characteristic three states are called the bright fringe, the mid fringe and the dark fringe as shown in Fig.(1.3).

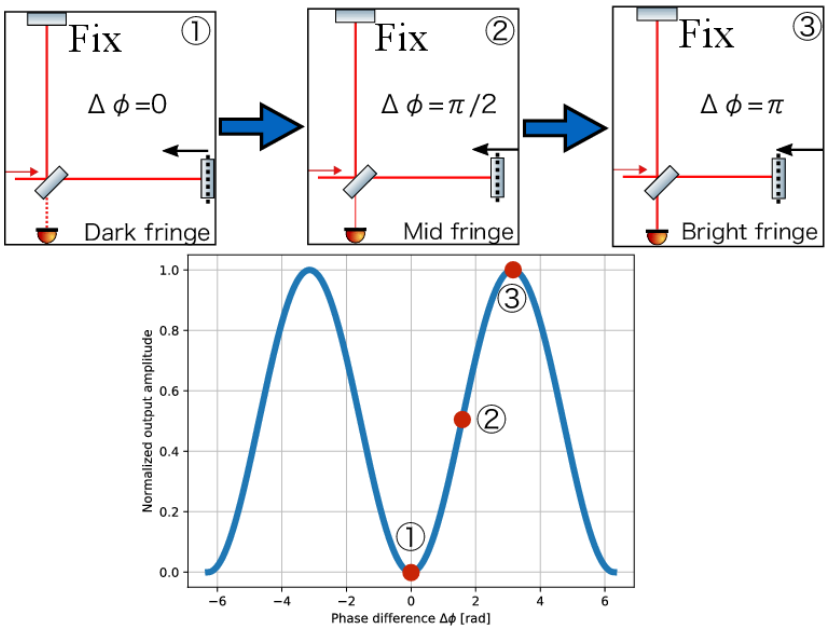

Figure 1.3: Output of a Michelson interferometer. Depending on the optical phase difference between the two arms, the output of the Michelson interferometer changes. The characteristic three states of this fringe are named as the bright fringe where the output is maximized, the dark fringe where the output is minimized, and the mid fringe where the output is the average of the bright and the dark fringe.

As discussed above, GWs change the distance between test masses in spacetime. So if it happens to the MI, the output of the MI changes because the distance of two arms are changed by the effect of GWs. Next, we calculate the transfer function from GWs input to the interferometer output P_{PD}. Considering the GWs that contain only plus mode and propagate along the z axis as shown in Fig.(1.2), the interval ds^2 becomes

$$ds^2 = -c^2dt^2 + (1 + h_+(t))dx^2 + (1 - h_+(t))dy^2 + dz^2, \tag{1.19}$$

where $h_+(t)$ describes the time dependence of GWs amplitude. By considering the light propagating along the x-axis, the minute interval along the x-axis is given as

$$dx = \pm\frac{c}{\sqrt{1 + h_+(t)}} \sim \pm\left(1 - \frac{1}{2}h_+(t)\right)cdt, \tag{1.20}$$

and the integration of Eq.(1.20) satisfies the relation

$$\int_{t-\tau_{\rm x}}^{t}\left(1-\frac{1}{2}h_{+}(t)\right)dt=\frac{2L_{\rm x}}{c}, \tag{1.21}$$

where $\tau_{\rm x}$ is the round trip time between the BS and the reflective mirror at the end of the MI. The phase shift during the round trip is calculated as

$$\phi_{\rm x}\sim\Omega\frac{2L_{\rm x}}{c}+\frac{\Omega}{2}\int_{t-2L_{\rm x}/c}^{t}h_{+}(t)dt. \tag{1.22}$$

Note that, in the integration range of Eq.(1.22), we assume that the amplitude of GWs $h_{+}(t)$ is quite small and it does not change the travel distance so much, $\tau_{\rm x}\sim 2L_{\rm x}/c$. The phase shift of the light that propagate along the y-axis is also given as

$$\phi_{\rm y}\sim\Omega\frac{2L_{\rm y}}{c}-\frac{\Omega}{2}\int_{t-2L_{\rm y}/c}^{t}h_{+}(t)dt, \tag{1.23}$$

and the difference of the phase shift $\Delta\phi$ between the light traveling along the x and y axes is

$$\begin{aligned}\Delta\phi &= \Omega\frac{2(L_{\rm x}-L_{\rm y})}{c}+\frac{\Omega}{2}\int_{t-2L_{\rm x}/c}^{t}h_{+}(t)dt+\frac{\Omega}{2}\int_{t-2L_{\rm y}/c}^{t}h_{+}(t)dt,\\ &= \Omega\frac{2(L_{\rm x}-L_{\rm y})}{c}+\Delta\phi_{\rm GW},\end{aligned} \tag{1.24}$$

where $\Delta\phi_{\rm GW}$ denotes the phase difference caused by GWs. We can chose the two lengths of the MI as $L_{\rm x}\sim L_{\rm y}\sim L$, and Eq.(1.24) becomes

$$\Delta\phi_{\rm GW}=\Omega\int_{t-2L/c}^{t}h_{+}(t)dt. \tag{1.25}$$

The Fourier transform of $h_{+}(t)$ is written as $h_{+}(t)=\int_{-\infty}^{\infty}h(\omega)e^{i\omega t}d\omega$, and Eq.(1.25) becomes

$$\begin{aligned}\Delta\phi_{\rm GW} &= \Omega\int_{t-2L/c}^{t}\int_{-\infty}^{\infty}h(\omega)e^{i\omega t}d\omega dt,\\ &= \int_{-\infty}^{\infty}\frac{2\Omega}{\omega}e^{i\omega\left(t-\frac{L}{c}\right)}\sin\left(\frac{L\omega}{c}\right)h(\omega)d\omega,\\ &= \int_{-\infty}^{\infty}H_{\rm MI}(\omega)h(\omega)d\omega,\end{aligned} \tag{1.26}$$

with

$$H_{\rm MI} = \frac{2\Omega}{\omega} e^{i\omega\left(t-\frac{L}{c}\right)} \sin\left(\frac{L\omega}{c}\right). \tag{1.27}$$

where $H_{\rm MI}$ is the transfer function of the MI, and Fig.(1.4) shows the amplitude of the transfer function for various arm length. As the function of the arm length, the amplitude of the transfer function $|H_{\rm MI}|$ is maximized when the length of the MI and the frequency of GWs satisfy the relation $\frac{L\omega}{c} = \frac{\pi}{2}$. This relation implies that there is an optimized baseline length of MI for a certain frequency of GWs. Qualitatively, it means that the amount of the phase change of light during the round trip is maximized if the phase of the GWs is reversed when the light just returns to the BS. After the optimal frequency, the response to GWs decreases, and this effect is called the cancellation. For example, the optimized base line length for the GWs of 100 Hz is $L \sim 750$ km, and it is not realistic to build such a huge MI on earth. The current GWDs are detecting GWs with the base line length of 3 or 4 km with the optical cavities to extend the effective base line length. Next subsection introduces the optical cavity that is the key feature of the laser interferometric GWD.

1.2.2 Fabry-Pérot cavity

A gravitational wave detector consists of a number of mirrors, and some of them configure optical cavities such as the arm cavities, the power recycling cavity and the signal recycling cavity. These cavities enhance the sensitivity of a detector. Here we introduce the linear optical cavity so called Fabry-Pérot cavity and explain how these cavities increase the sensitivity of a detector.

Optical parameters

The configuration of a Fabry-Pérot (FP) cavity is shown in Fig.(1.5). A FP cavity consists of two high reflective mirrors. These two mirrors reflect the input electric field many times and make standing waves inside. The amplitude reflectivity and the transmissivity of these mirrors are (r_1, t_1) and (r_2, t_2). The electric field that inject to the FP cavity is described as $E_{\rm in} = E_0 e^{i\Omega t}$. A part of input electric field transmits the input mirror and enter to the FP cavity. Then, the electric field reaches the end mirror and reflect back to the input mirror. When the electric field get to the input mirror again,

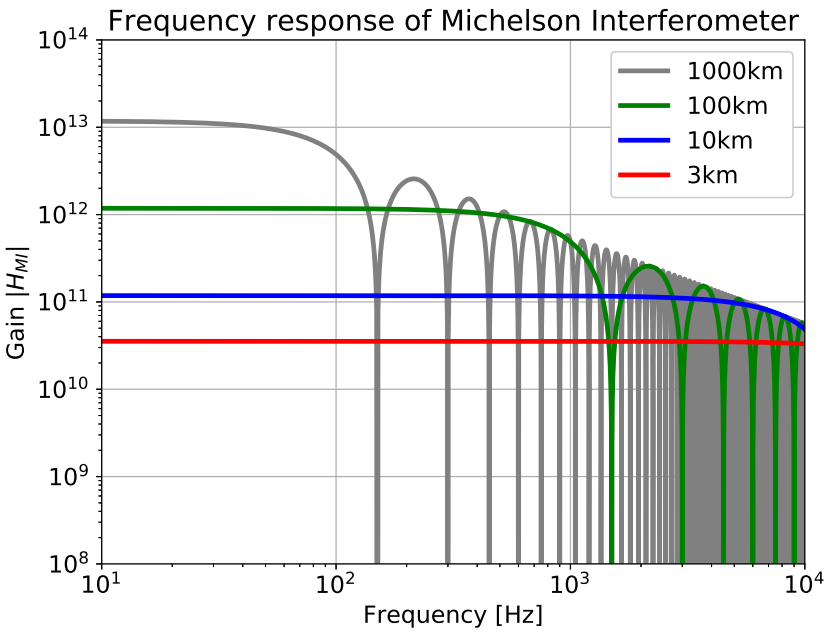

Figure 1.4: Frequency response of Michelson Interferometer with the baseline length of L = 3km, 10km, 100km and 1000km. MI with longer baseline has better sensitivity. The sensitivity decreases after the cut off frequency described as $\frac{L\omega}{c} = \frac{\pi}{2}$.

its phase changes $\phi = 2\pi\frac{2L}{\lambda}$, where L is the distance of the two mirrors. The total electric field $E_{\rm fp}$ is the sum of these circulating electric fields,

$$E_{\rm fp} = t_1 \sum_{\rm n=0}^{\infty} \left(r_1 r_2 e^{-i\Phi}\right)^n E_{\rm i} = \frac{t_1}{1 - r_1 r_2 e^{-i\Phi}} E_{\rm in}. \tag{1.28}$$

(1.29)

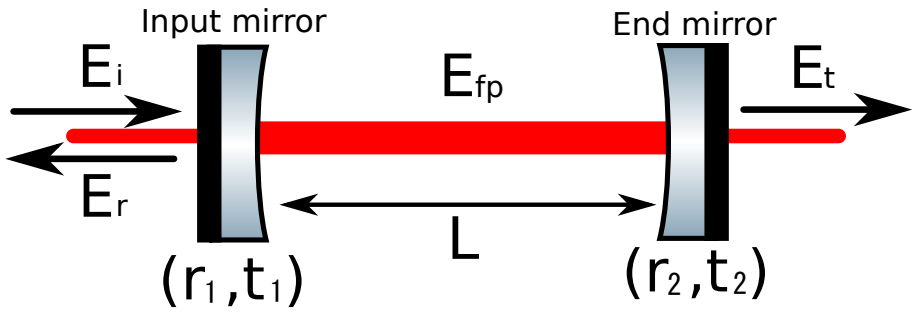

Figure 1.5: Shecmatic configuration of a Fabry-Pérot cavity.

Considering the out coming electric field from the FP cavity, the reflected and transmitted electric fields $E_{\rm r}$ and $E_{\rm t}$ are written as,

$$\begin{aligned} E_{\rm r} &= (-r_1)\,E_{\rm i} + t_1^2 r_2 e^{-i\phi}\sum_{\rm n=0}^{\infty}\left(r_1 r_2 e^{-i\phi}\right)^n E_{\rm in} \\ &= \left(-r_1 + \frac{t_1^2 r_2 e^{-i\Phi}}{1 - r_1 r_2 e^{-i\Phi}}\right) E_{\rm i} = r(\phi) E_{\rm i} \qquad (1.30) \\ E_{\rm t} &= t_1 t_2 e^{-i\frac{\phi}{2}}\sum_{\rm n=0}^{\infty}\left(r_1 r_2 e^{-i\phi}\right)^n E_{\rm i} \\ &= \frac{t_1 t_2 e^{-i\frac{\Phi}{2}}}{1 - r_1 r_2 e^{-i\Phi}} E_{\rm in} = t(\phi) E_{\rm i}, \qquad (1.31) \end{aligned}$$

where $r(\phi)$ and $t(\phi)$ are the amplitude reflectivity and transmissivity of the FP cavity. The power of these electric filed are proportional to square of the absolute electric field

$$P_{\rm fp} = \frac{t_1^2}{\left(1 - r_1 r_2\right)^2 + 4 r_1 r_2 \sin^2\frac{\Phi}{2}} P_{\rm i}, \qquad (1.32)$$

$$P_{\rm r} = \frac{\left\{\left(r_1^2 + t_1^2\right) r_2 - r_1\right\}^2 + 4 r_1 r_2 \left(r_!^2 + t_1^2\right) \sin^2\left(\frac{\Phi}{2}\right)}{\left(1 - r_1 r_2\right)^2 + 4\sin^2\left(\frac{\Phi}{2}\right)} P_{\rm i}, \qquad (1.33)$$

$$P_{\rm t} = \frac{t_1^2 t_2^2}{\left(1 - r_1 r_2\right)^2 + 4 r_1 r_2 \sin^2\frac{\Phi}{2}} P_{\rm i}, \qquad (1.34)$$

where $P_{\rm i}$ is the power of the input light. Equations (1.32) - (1.34) are the function of the phase shift ϕ. As shown in Fig.(1.6), the laser power inside the FP cavity changes periodically. Especially when the condition $\phi = 2{\rm n}\pi$ (n is an integer) is satisfied, the state is called as the resonance state. The frequency difference of adjacent resonate state is called as the free spectral

range (FSR) and written as $\nu_{\mathrm{FSR}} = c/2L$.
Equation (1.32) gives the full width at half maximum (FWHM) of the transmission peak ν_{FWHM} as

$$\frac{1}{1 + \frac{4r_1r_2}{(1-r_1r_2)^2}\sin^2\left(\frac{\nu_{\mathrm{FWHM}}}{2\nu_{\mathrm{FSR}}}\pi\right)} = \frac{1}{2}. \tag{1.35}$$

Generally, ν_{FSR} is much larger than ν_{FWHW}, hence we can assume $\frac{\nu_{\mathrm{FWHM}}}{2\nu_{\mathrm{FSR}}}\pi \ll 1$. With this approximation, Eq. (1.35) becomes,

$$\nu_{\mathrm{FWHM}} = \frac{1 - r_1r_2}{\pi\sqrt{r_1r_2}}\nu_{FSR}. \tag{1.36}$$

The ratio between the FSR ν_{FSR} and the FWHM frequency ν_{FWHM} is called the finesse $\mathcal{F}$, and it denotes the sharpness of the resonance,

$$\mathcal{F} = \frac{\nu_{FSR}}{\nu_{\mathrm{FWHM}}} = \frac{\pi\sqrt{r_1r_2}}{1 - r_1r_2}. \tag{1.37}$$

Eigenmode

To resonate the laser light in the FP cavity, there is another point to be considered, the spatial mode of the laser and the cavity are needed to be matched. Now we consider the light propagate along to the z-axis. The electric field of the laser with the spatial mode $U(\mathbf{x})$ is written as

$$E(t, \mathbf{x}) = U(\mathbf{x})E_0e^{i\omega t}. \tag{1.38}$$

Especially for the Hermite-Gaussian mode, the spatial mode $U(\mathbf{x})$ is rewritten as

$$U_{\mathrm{lm}}(\mathbf{x}) = U_{\mathrm{l}}(x, z)U_{\mathrm{m}}(y, z)\exp\left[-ikz + i(\mathrm{l} + \mathrm{m} + 1)\zeta(z)\right], \tag{1.39}$$

with

$$U_{\mathrm{l}}(x, z) = \left(\frac{2}{\pi\omega(z)}\right)^{1/4}\sqrt{\frac{1}{2^{\mathrm{l}}\mathrm{l}!}}H_{\mathrm{l}}\left(\frac{\sqrt{2}x}{\omega(z)}\right)\exp\left[-\left(\frac{x}{\omega(z)}\right)^2 - i\frac{kx^2}{2R(z)}\right], \tag{1.40}$$

where k is the wave number, ω_0 is the beam radius at its waist position, H_{l} is the Hermite polynomial,

$$\omega(z) = \omega_0\sqrt{1 + \left(\frac{z}{z_0}\right)} \tag{1.41}$$

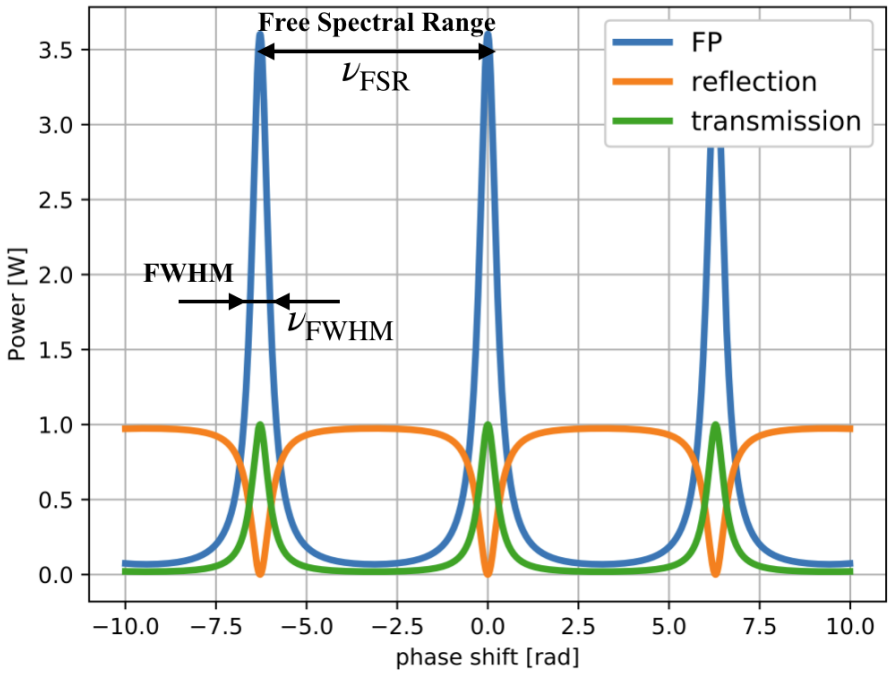

Figure 1.6: Periodic state change of a FP cavity. Depending on the optical phase change inside the FP cavity, the power inside the FP changes. When the condition $\phi = 2\mathrm{n}\pi$, where n is an integer, is satisfied, it's called resonate state. The frequency between two next resonance is called FSR, and the ratio between the FSR and FWHM is called finesse which implies the sharpness of the resonance.

is the beam radius at the position z from the waist position,

$$R(z) = z\left[1 + \left(\frac{z_0}{z}\right)^2\right] \tag{1.42}$$

is the radius of curvature of the wave front, $\zeta(z) = \angle\left(\frac{z_0}{z}\right)$ is the Gouy phase, and $z_0 = \frac{k\omega_0^2}{2}$ is the Rayleigh range. The spatial distribution and the spatial propagation of the laser is characterized only by the Rayleigh range z_0 and the position from the waist z. In order to resonate the light in the optical cavity, the spatial mode of the laser is needed not to change during the multiple reflection. This condition is equivalent to that the radius of curvature of the mirrors are same as that of the laser light at that point. Hence, it implies that the eigenmode of the optical cavity is given by the radius of curvature of the two mirrors R_{i} ($\mathrm{i} = 1, 2$) and the distance of these two mirrors L. The

Rayleigh range z_0 and the distance between the waist position and the mirror $d_{\rm i}$ $({\rm i} = 1, 2)$ is given as

$$z_0 = \frac{L\sqrt{g_1 g_2(1 - g_1 g_2)}}{g_1 + g_2 - 2g_1 g_2}, \tag{1.43}$$

$$d_{\rm i} = \frac{L g_1 g_2(1 - g_{\rm i})}{g_{\rm i}(g_1 + g_2 - 2g_1 g_2)}, \tag{1.44}$$

with

$$g_{\rm i} = 1 - \frac{L}{R_{\rm i}}, \tag{1.45}$$

where $g_{\rm i}$ is called the g-factor, and it's the important parameter to describe the eigenmode of the cavity. To satisfy the condition which is mentioned above, the spatial mode of the laser must be matched to the eigenmode of the optical cavity. Actually, the spacial mode of the injection laser is shaped to match the eigenmode using lenses and curved mirrors. Now we define the parameter which describe the spatial mode of the laser as $q \equiv z + iz_0$. This q parameter is changed by matrix as

$$\begin{pmatrix} q_2 \\ 1 \end{pmatrix} = \begin{pmatrix} A & B \\ C & D \end{pmatrix} \begin{pmatrix} q_1 \\ 1 \end{pmatrix}. \tag{1.46}$$

where q_1 and q_2 are the q parameters that before and after the change by the lenses or curved mirrors. The matrix gives the change of the q parameter, especially which is called ABCD matrix, the analysis of the spatial mode using the ABCD matrix is called the ray transfer matrix analysis. The ABCD matrix of the lens that has the focal length of f, and the mirror that has the radius of curvature of R are written as

$$\begin{pmatrix} A & B \\ C & D \end{pmatrix} = \begin{pmatrix} 1 & 0 \\ -1/f & 1 \end{pmatrix} \quad \text{(Lens)}, \tag{1.47}$$

$$= \begin{pmatrix} 1 & 0 \\ -\frac{2}{R\cos\theta} & 1 \end{pmatrix} \quad \text{(Curved mirror)}, \tag{1.48}$$

where θ is the angle of incidence. Figure (1.7) shows the image of the spatial mode shaping, the mode matching, using lenses.

1.2.3 Fabry-Pérot Michelson Interferometer

Now, let us consider a Michelson Interferometer with Fabry-Pérot cavities. As shown in Fig.(1.8), the interferometer which has FP cavities at each arm

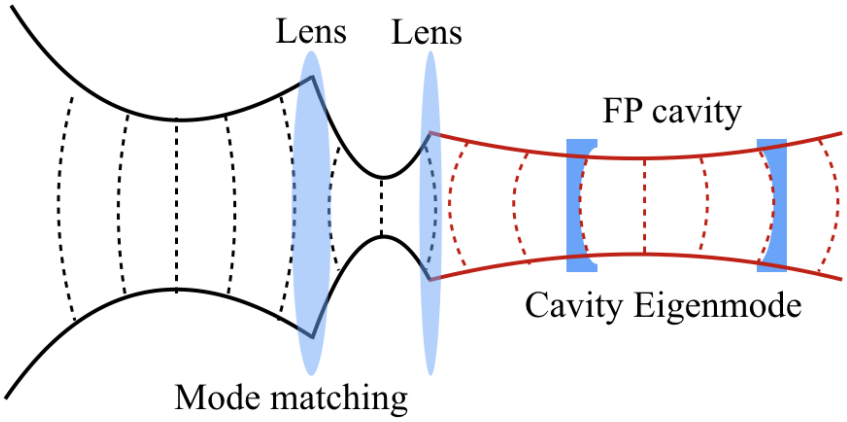

Figure 1.7: Eigenmode of the FP cavity and mode matching. The eigenmode of the FP cavity is determined when the distance and the radius of curvature of the mirrors are fixed. To resonate injection laser inside the FP cavity, the spatial mode of the laser needs to be shaped using lenses to match the eigenmode.

is called the Fabry-Pérot Michelson Interferometer (FPMI). A MI measures the phase difference of the light. In the FPMI, if the length of the MI part is always same for both arms, the phase change of light only occurs inside the FP cavities at each arm. Equation (1.30) gives the phase change $\phi_{\rm fp}$ inside the FP cavity as

$$\Phi_{\rm fp} = \angle\left(\frac{E_{\rm r}}{E_{\rm i}}\right) \tag{1.49}$$

$$= \arctan\left(-r_1 + \frac{t_1^2 r_2 e^{-i\Phi}}{1 - r_1 r_2 e^{-i\Phi}}\right), \tag{1.50}$$

especially, around the resonance point ($\Phi_0 = 2{\rm n}\pi$), Eq.(1.51) is rewritten as

$$\Phi_{\rm fp} \sim \frac{1}{1 - r_1 r_2} \frac{t_1^2 r_2}{r_1 - (r_1^2 + t_1^2) r_2} \delta, \tag{1.51}$$

where δ describes the small deviation from the resonance point. Equation (1.51) implies that the phase difference change in a FPMI is enhanced by a factor of $\frac{1}{1-r_1 r_2} \frac{t_1^2 r_2}{r_1 - (r_1^2 + t_1^2) r_2}$ comparing with a MI. Practically, the amount of the phase difference change is frequency dependent. Following the discussion

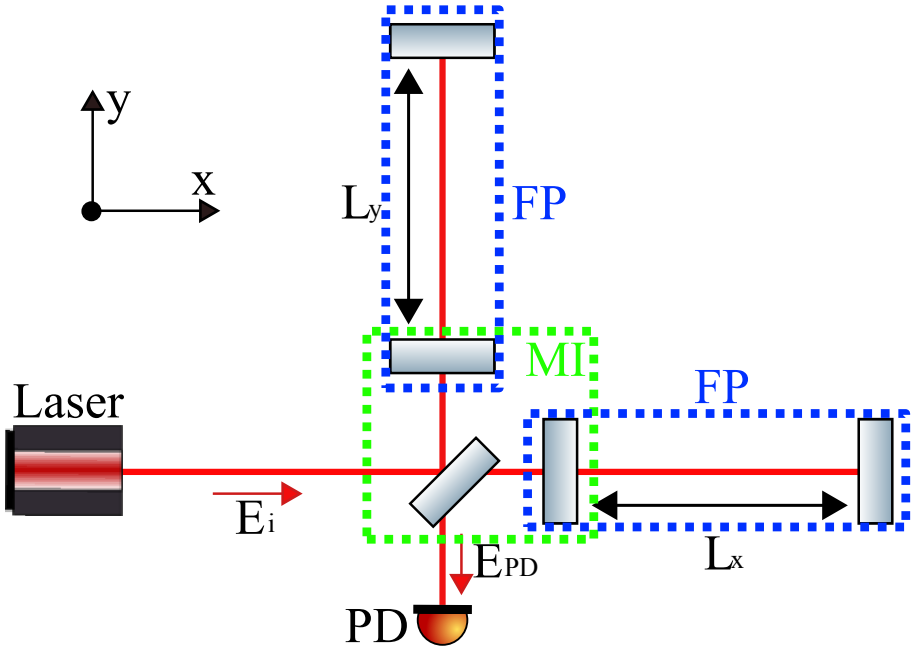

Figure 1.8: Optical configuration of a Fabry-Pérot cavity.

in subsection (1.2.1), the transfer function of a FPMI H_{FPMI} is calculated as

$$H_{\mathrm{FPMI}} = \frac{2\Omega}{\omega}\frac{1}{1-r_1r_2e^{-2i\frac{L\omega}{c}}}\frac{t_1^2r_2}{r_1-(r_1^2+t_1^2)r_2}\sin\left(\frac{L\omega}{c}\right)e^{-i\frac{L\omega}{c}} \quad (1.52)$$

$$= \frac{1}{1-r_1r_2e^{-2i\frac{L\omega}{c}}}\frac{t_1^2r_2}{r_1-(r_1^2+t_1^2)r_2}H_{\mathrm{MI}} \quad (1.53)$$

Figure (1.9) shows the transfer functions of a MI and a FPMI that have the same arm length ($L = 3$km). The figure clearly shows that the FP cavity increases the tiny phase difference change of light that is generated by the GWs, though the cancellation starts from a lower frequency. This is the reason why the current laser interferometric GWD configures the FP cavity at their arm parts.

1.2.4 Recycling techniques

To enhance a detector sensitivity, a gravitational wave detector introduces additional two cavities, the power recycling cavity and the signal recycling cavity. Here we introduce these two cavities and how they work.

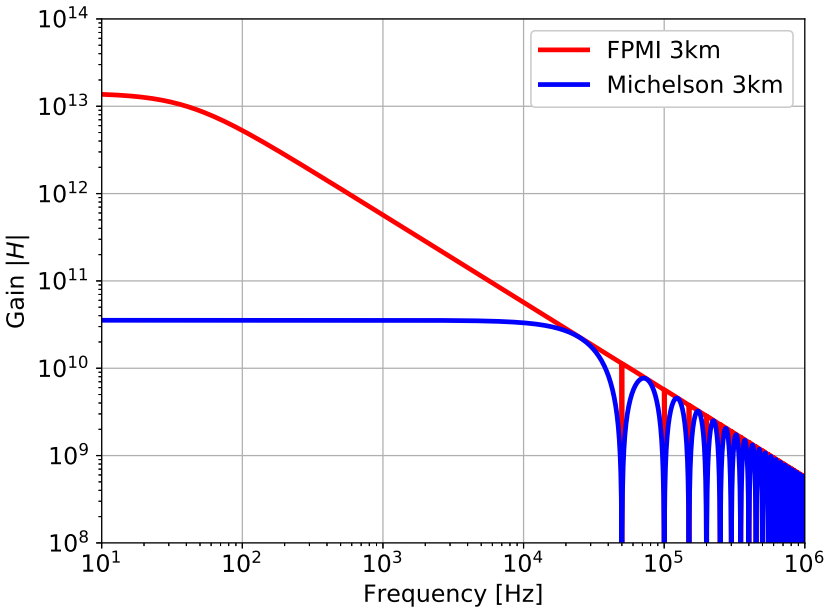

Figure 1.9: Transfer function from the GW injection to the FPMI and the MI output. The gain at the low frequency is enhanced by the FP cavity, though the cancellation starts from a lower frequency. From Eq.(1.52) the gain and the cut off frequency is parameterized by the length of the arm and the reflectivity of the mirrors.

Power Recycling

From Eq.(1.18), the output of a MI is proportional to the input laser power, and it implies that the amplitude of the GWs signal is enhanced by increasing the storage laser power inside a GWD [20]. A GWD is controlled to be dark at anti-symetric port, and following the energy conservation law, almost all of the input laser back to the input port. By reflecting these light back to the interferometer again, the storage laser power can be increased. For this purpose, a reflective mirror called the power recycling mirror (PRM) is put at the input port and make the power recycling cavity with the arm compound mirrors as shown in Fig.(1.10). The amplitude reflectivity of the compound mirror $r_{\mathrm{FP}}(\Phi)$ is given by Eq.(1.30) as

$$r_{\mathrm{FP}}(\Phi) = \left(-r_1 + \frac{t_1^2 r_2 e^{-i\Phi}}{1 - r_1 r_2 e^{-i\Phi}}\right). \tag{1.54}$$

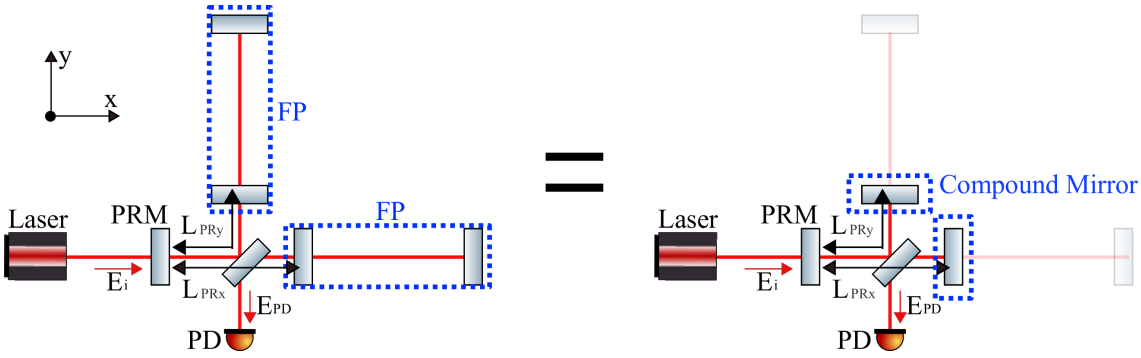

Figure 1.10: Optical configuration of a PRFPMI. The reflective mirror at the laser injection port called PRM reflects the laser from the interferometer back. By regarding the FP cavity as a compound mirror, the PRFPMI is equivalent to the power recycled MI.

Following Eq.(1.32), the laser power inside the optical cavity P_{PRC} which consists of the compound mirrors and PRM when they are on the resonant states is described as

$$P_{\mathrm{PRC}} = GP_{\mathrm{in}}, \tag{1.55}$$

$$G = \frac{t_{\mathrm{PRM}}^2}{\left(1 - r_{\mathrm{PRM}} r_{\mathrm{FP}}\right)^2}, \tag{1.56}$$

where P_{in} is the incident laser power to the PRC, and G is called the power recycling gain (PRG). Figure (1.11) shows the PRG for various r_{FP} and r_{PRM}. For the certain number of r_{FP}, the PRG is maximized when the reflectivity of PRM has the same number as that of the compound mirrors. On the other hand, the PRG increases monotonously with the increasing of r_{FP}. The optical cavity whose mirrors have the same reflectivity is called the critical coupling cavity, and typically the power recycling cavity in a GWD is designed to satisfy this condition.

Signal Recycling

Signal recycling (SR) is the technique to enhance the detector sensitivity by adding a mirror at the anti-symetric port as shown in Fig.(1.12) and modifying the shape of the response function of the detector [21]. This subsection describes how SR works in a GWD by introducing the relation between the input and the output electric field from a signal recycled Fabry-Pérot Michelson interferometer (SRFPMI).

Now we consider the FP cavity with signal recycling mirror (SRM) as shown in Fig.(1.13). This model is equivalent to the actual SRFPMI when we regard the arm cavities as the one compound mirror. The electric fields before and after the ITM, and the transmitted electric field of SRM are described as $E_{\rm a}$, $E_{\rm b}$, $E_{\rm c}$, $E_{\rm d}$ and $E_{\rm srm}$ as shown in Fig.(1.13). $L_{\rm FP}$ and $L_{\rm SR}$ are the length of the FP cavity and the signal recycling cavity (SRC). We assume that the FP cavity is controlled to satisfy the resonant condition for the frequency of the laser, $\Omega = {\rm m}\lambda$. Then, each electric field follows the simultaneous equations,

$$
\begin{aligned}
E_{\rm a} &= r_1 E_{\rm b} + t_1 (E_{\rm in} + E_{\rm d}), && (1.57)\\
E_{\rm b} &= r_2 E_{\rm a} e^{-i\frac{2L_{\rm FP}}{c}\omega}, && (1.58)\\
E_{\rm c} &= t_1 E_{\rm b} - r_1 E_{\rm d}, && (1.59)\\
E_{\rm d} &= r_{\rm s} E_{\rm c} e^{-i\frac{2L_{\rm SR}}{c}\Omega}, && (1.60)\\
E_{\rm srm} &= t_{\rm s} E_{\rm c} e^{-i\frac{L_{\rm SR}}{c}\Omega}, && (1.61)
\end{aligned}
$$

where Ω and ω are the angular frequency of the light and the GWs. Solving $E_{\rm srm}$ for $E_{\rm in}$ gives the relation between the input and output electric fields as

$$
E_{\rm srm} = \frac{r_2 t_1^2 t_2 e^{i(\psi+\phi)}}{1 + r_1 r_2 e^{2i\phi}} \left[1 - r_1 r_2 e^{i\psi} - \frac{r_2 r_{\rm s} t_1^2 e^{i(\psi+2\phi)}}{1 + r_1 r_{\rm s} e^{2i\phi}} \right]^{-1} E_{\rm in}. \qquad (1.62)
$$

The signal amplification gain of the SRFPMI $H_{\rm srm}$ is defined as

$$
H_{\rm srm} = \frac{E_{\rm srm}(r_{\rm s}, t_{\rm s})}{E_{\rm srm}(r_{\rm s} = 0, t_{\rm s} = 1)} = \frac{t_{\rm s}}{1 - r_{\rm s} e^{2i\phi} \left[-r_1 + \frac{r_2 t_1^2 e^{i\phi}}{1 - r_1 r_2 e^{i\phi}} \right]}. \qquad (1.63)
$$

When the SRC controlled to be satisfied the anti-resonant condition for the main laser frequency, $\phi = \pi + 2{\rm m}\pi$, the reflectivity of the compound mirror which is composed of the ITM and the SRM is higher than that of the ITM itself. As a result of this effect, the effective finesse of the FP cavity increases, and the GW signal at low frequency region is enhanced, the signal at high frequency region decreases because the signal cancellation frequency, or the cut off frequency, shifts to the low frequency. This configuration of the SRFPMI is called Broadband Signal Recycling (BSR). Blue line in Fig.(1.14) shows the frequency dependence of the signal amplification gain of the BSR. When the SRC satisfy the resonant condition for the main laser frequency, $\phi = \frac{\pi}{2} + 2{\rm m}\pi$, the reflectivity of the compound mirror which is composed of the ITM and the SRM is lower than that of the ITM. In this case, the finesse of

the FP cavity decreases and the sensitivity at low frequency region is lowered, but the cut off frequency shifts to the high frequency side and the sensitivity at the high frequency increases. Generally speaking, the sensitivity of ground based GWD at the low frequency region is limited by the seismic noise and the thermal noise, and the signal amplification at this region is almost useless. On the other hand, the sensitivity at high frequency region is limited by the laser quantum noise, and the signal amplification at this region is meaningful. This configuration of the SRFPMI is called Broadband Resonant Sideband Extraction (BRSE). Red line in Fig.(1.14) shows the frequency dependence of the signal amplification gain of the BRSE.

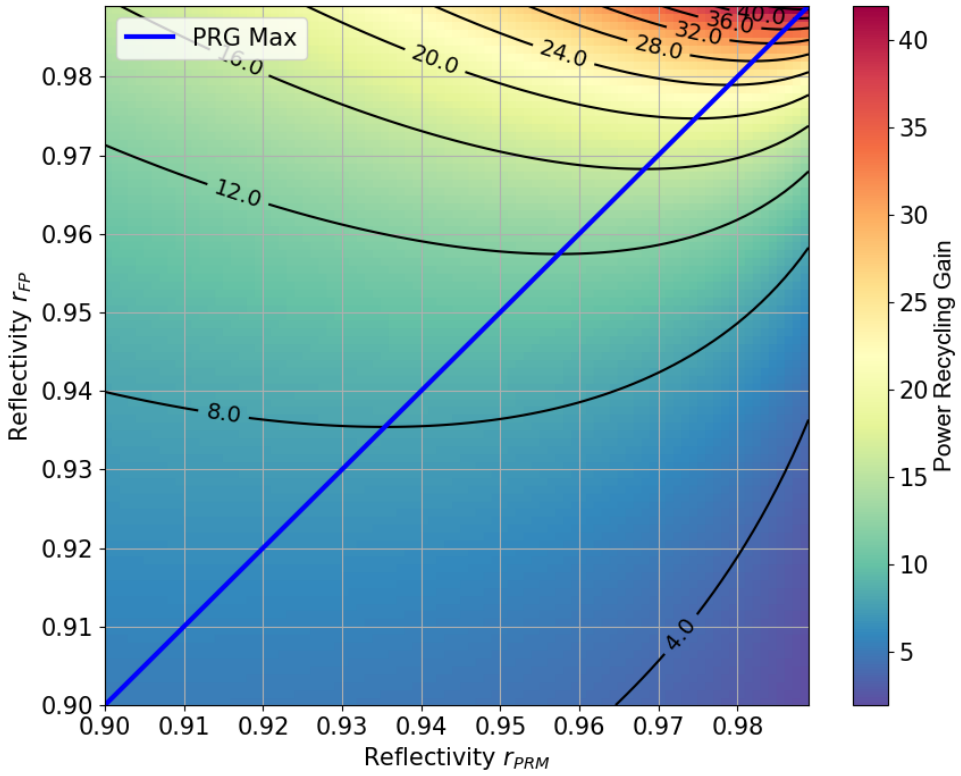

Figure 1.11: Power recycling gain for various reflectivity of the FP cavity and PRM. The power recycling gain is the ratio between the laser power before and after the PRM. For the fixed reflectivity of FP cavity, the PRG is maximized when the reflectivity of PRM is same as that of the FP cavity as shown in the figure using blue line.

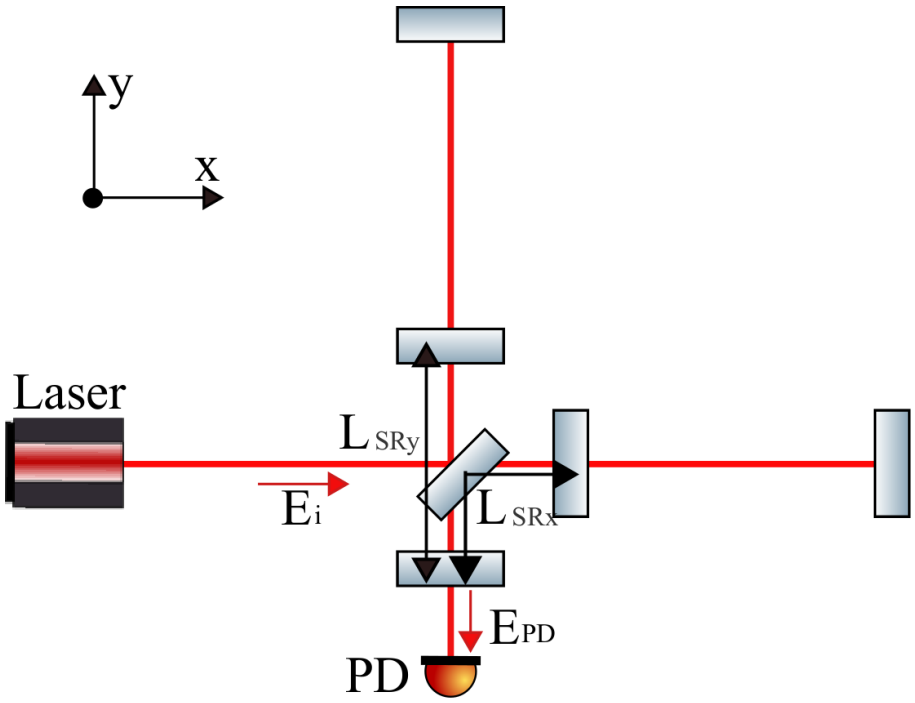

Figure 1.12: Basic optical configuration of a Signal-Recycled Fabry-Pérot interferometer. GWD put SRM at the anti-symmetric port to change the response to the GWs, and enhances the sensitivity.

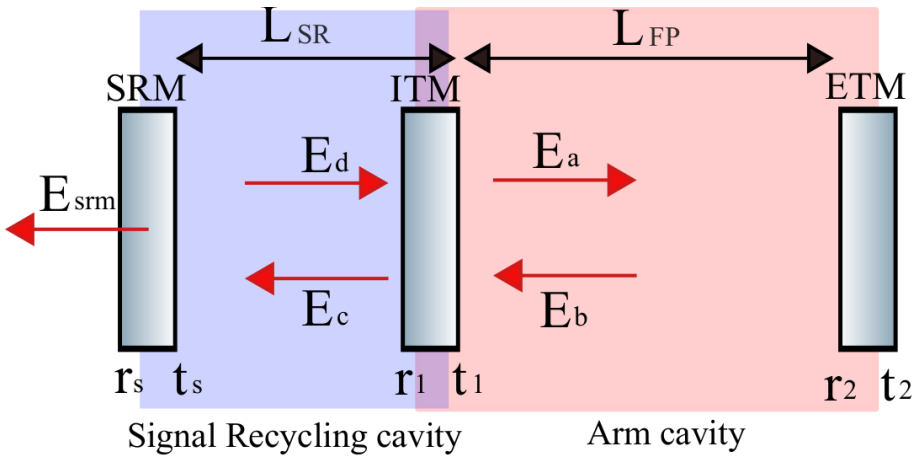

Figure 1.13: Definition of the electric fields in an SR and FP cavities. Here we define the electric fields just before and after the ITM as E_{a}, E_{b}, E_{c} and E_{d}. The transmitted electric field of SRM is written as E_{srm}. This model is equivalent to the FPMI with an SRM when we see the two arm cavities as one compound mirror.

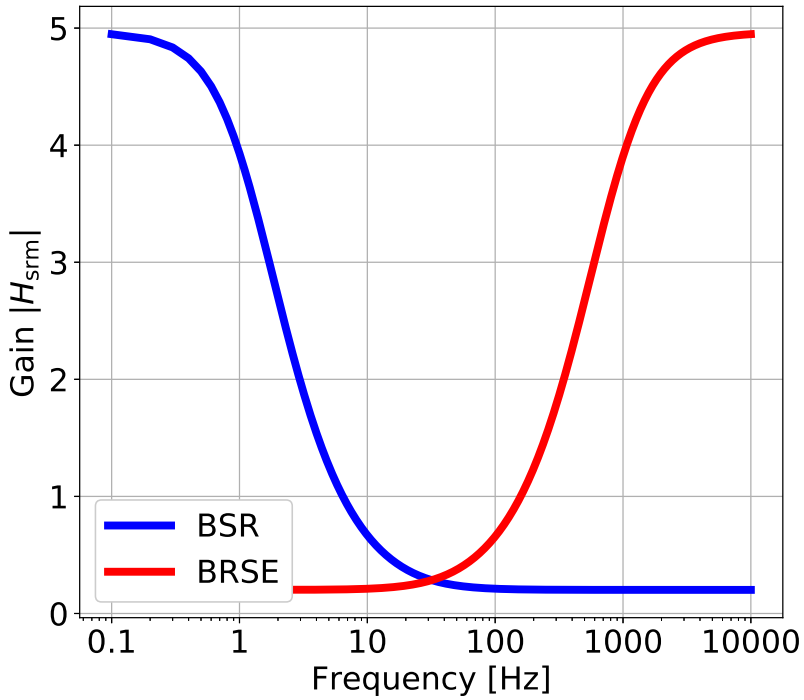

Figure 1.14: Frequency dependence of the signal amplification gain of BSR and BRSE. The signal amplification gain increases at low frequencies when the L_{sr} is set to be anti-resonate for the career light (BSE). On the other hand, it increases at high frequencies when the career light resonates at the SRC (BRSE)

1.3 Noises in a GW detector

To detect the tiny signal caused by GWs, we need to suppress any disturbances, or noises, down to the amplitude which is caused by GWs. For this purpose, it's important to give the introduction of noises in a GWD. Following subsections give the fundamental noises in a GWD, the seismic noise, the thermal noise and the quantum noise.

1.3.1 Seismic noise

Ground motion introduces large disturbance to a GWD and this disturbance mainly limits the detector sensitivity at low frequencies. The origins of this continuous large ground motion are natural phenomena like ocean and atmosphere, as well as human activities . Figure (1.15) shows the magnitude of typical seismic motion on a ground. Depending on the weather, atmospheric pressure pattern and various other factors can change the seismic motion. The distinctive peak around 0.1 Hz is called the micro seismic motion and the ocean waves beating shores are the origin of this peak. These large ground motions can introduce the noise to GWD, and this noise is called seismic noise. Not to transfer the seismic vibration to the optics that make up a GW detector, almost all of the optics in the GWDs are needed to isolate from the ground. For example, to achieve the vibration level of 10^{-18} m/$\sqrt{\text{Hz}}$ at 10 Hz, attenuation of about $10^{-8} \sim 10^{-9}$ of attenuation is required.

The basic idea of the seismic attenuation system is a pendulum [22–24]. The transfer function of the single pendulum from its suspension point to the mass is proportional to the square of the frequency (f^{-2}) above its resonant frequency defined by $\sqrt{g/L}$, where g is the gravitational acceleration and L is the length of the pendulum. However, to get attenuation of 10^{-9} with a single pendulum, the resonant frequency is needed to be 0.1 mHz and it equivalent to the length of the pendulum of 1×10^9 m, and such huge system is unrealistic. Multistage pendulum can solve this problem. The transfer function of an n-stage multistage pendulum is proportional to f^{-2n} above its resonant frequencies. In the current GWDs, the multistage pendulum is introduced, and to compensate the large vibration at its resonant frequencies, active damping controls are carefully implemented.

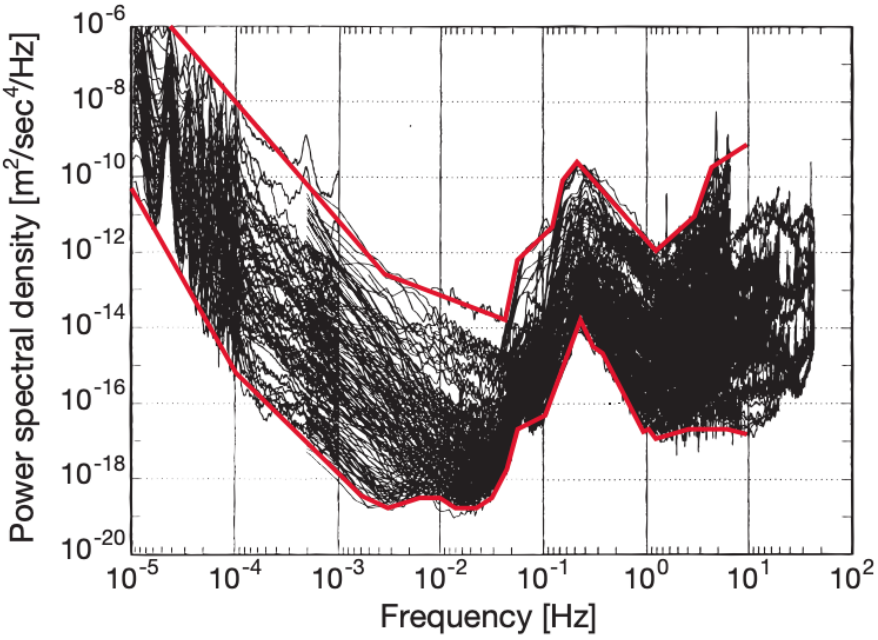

Figure 1.15: Power spectrum density of the seismic motion. Red curves show the New High/Low noise model of the seismic motion on earth. This figure is extracted from [23].

1.3.2 Thermal noise

The thermal noise is the noise formulated by the Fluctuation-dispersion theorem (FdT). According to the FdT, the intrinsic dispersion of the thermal equilibrium mirror and suspension gives the driving force which is equal to the external driving force, and the force make the fluctuation of the physical variable of the system. The thermal noise in a GWD is largely classified into two groups in response to the origin of the noise; the suspension thermal noise and the mirror thermal noise. The mirror thermal noise can be divided to the Brownian noise that is caused by the structure damping of the mirror, and the thermo-optic noise that is caused by the thermal dissipation.

Power spectrum of the thermal noise

FdT gives the power spectrum of the thermal noise S_{thermal} as [25, 26]

$$S_{\text{thermal}} = \frac{4k_{\text{B}}T}{\omega^2} \left|\text{Re}\left[Y\left(f\right)\right]\right| \tag{1.64}$$

where k_B is Boltzmann's constant, T is the temperature of the system, $\omega = 2\pi f$ is the angular frequency and $Y(f)$ is a complex admittance of the system, respectively. The mechanical admittance of the system is defined as

$$Y(f) \equiv 2\pi f i \frac{x(f)}{F(f)} \tag{1.65}$$

where $x(f)$ and $F(f)$ are the physical observable and the driving force, and the admittance of the system, Eq.(1.65), can be described using the transfer function of the system $H(f)$ as $Y(f) = i\omega H(f)$. The real part of admittance, $Re[Y(f)]$ implies the coupling of the intrinsic dispersion power to the physical observable. If we use express the real part of the admittance as

$$|\mathrm{Re}\,[Y(f)]| = \frac{2W_{\mathrm{diss}}}{F_0^2}, \tag{1.66}$$

where W_{diss} is the total power dissipated in the system and F_0 is the amplitude of the driving force. Hence, substituting Eq.(1.66) into Eq.(1.64) gives the expression of the thermal noise as

$$S_{\mathrm{thermal}} = \frac{8k_B T}{\omega^2}\frac{W_{\mathrm{diss}}}{F_0^2} \tag{1.67}$$

In the following subsections, the power spectrum density of the Brownian noise, the thermo-optic noise and the suspension thermal noise that possibly limit the detector sensitivity are introduced. Figure (1.16) expresses the relation between the FdT and the thermal noise, and the origins of the dispersions and the names of the thermal noises.

The Brownian noise

The thermal noise which is the result of the dispersion of the intrinsic friction of the mirror and the coating is called the Brownian noise [27–29]. The response $x(f)$ to the excitation is $x(f) = |x(f)|\exp(-i\phi)$, where ϕ is the mechanical loss angle, and the total power dissipated in the system W_{diss} is written as

$$W_{\mathrm{diss}} = 2\pi f U(f)\phi, \tag{1.68}$$

where $U(f)$ is the elastic energy which is stored in the mirror. All elastic energy stored in the mirror is the sum of the elastic energy of the substrate

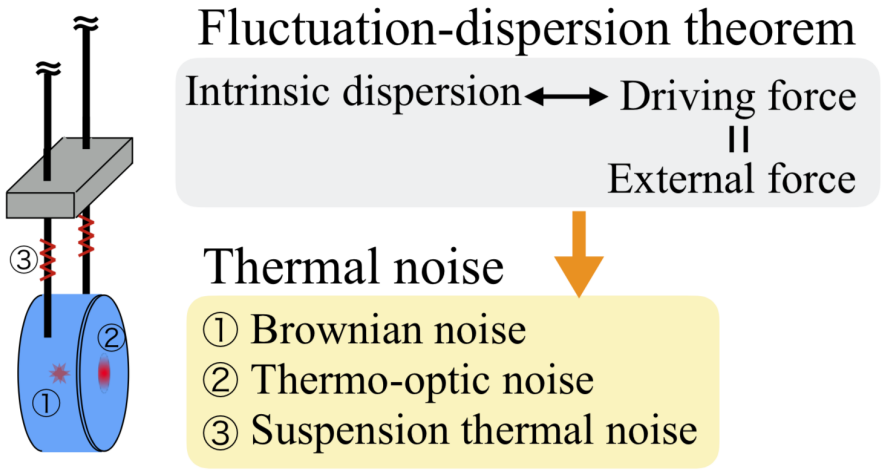

Figure 1.16: Image of the dispersion and the thermal noise. The intrinsic loss results in the thermal noise. The thermal noise is classified by the mechanism of the intrinsic loss and the position of that loss. The structure damping in the mirror and the suspension lead to the Brownian noise and the suspension thermal noise, and the thermal dispersion of the coating leads to the thermo-optic noise.

and the coating. The loss angle of the mirror is given by the sum of the weighted loss angle of the substrate and the coating as

$$\phi = \frac{1}{U}\left(U_{\rm sub}\phi_{\rm sub} + U_{\rm coat}\phi_{\rm coat}\right), \tag{1.69}$$

where $U_{\rm i}$ and $\phi_{\rm i}$ (i = sub or coat) are the elastic energy and the loss angle of the substrate and the coating. Here we assume that the thickness of the coating d is much smaller than the beam radius w, $d \ll w$, then, the elastic energy of the coating is rewritten as $U_{\rm coat} = \delta U_{\rm coat} d$, where $\delta U_{\rm coat}$ is the elastic energy density of the coating. We can also assume that the elastic energy of the substrate is much larger than that of the coating, and the elastic energy of the system is comparable with that of the substrate, $U \sim U_{\rm sub}$. Under these assumptions, Eq.(1.69) becomes

$$\phi = \phi_{\rm sub} + \frac{\delta U_{\rm coat} d}{U}\phi_{\rm coat}. \tag{1.70}$$

The elastic energy of the substrate and the elastic energy density of the coating are given as [27]

$$U = \frac{F^2\left(1-\sigma^2\right)}{2\sqrt{\pi}wY}, \tag{1.71}$$

$$\delta U_{\mathrm{coat}}/U = \frac{1}{\sqrt{\pi}w}\frac{Y'^2\left(1+\sigma\right)^2\left(1-2\sigma\right)^2+Y^2(1+\sigma')^2(1-2\sigma')}{YY'\left(1-\sigma'^2\right)\left(1-\sigma^2\right)}, \tag{1.72}$$

where Y and Y' are Young's modulus of the substrate and the coating, and σ and σ' are the Poisson ratio of the substrate and the coating. Substituting Eqs.(1.71) and (1.72) into Eq.(1.70), and substituting the result into Eq.(1.68) gives the total power dissipated in the mirror, and it gives the real part of the admittance. Substituting the calculated real part of the admittance gives the power spectrum of the mirror Brownian noise as

$$S_{\mathrm{Br}} = \frac{2k_{\mathrm{B}}T}{\pi^{3/2}f}\frac{1-\sigma^2}{wY}\left[\phi_{\mathrm{sub}}+\frac{d}{\sqrt{\pi}w}\frac{Y'^2\left(1+\sigma\right)^2\left(1-2\sigma\right)^2+Y^2(1+\sigma')^2(1-2\sigma')}{YY'\left(1-\sigma'^2\right)\left(1-\sigma^2\right)}\phi_{\mathrm{coat}}\right]. \tag{1.73}$$

According to Eq.(1.73), once we determine the material of the mirror and the coating, we can change the size of the beam and the temperature of the mirror to reduce the Brownian noise. To increase the size of the beam, larger optics is needed, and the cryogenic system is needed to decrease the temperature. In the current GWD, one of them is chosen to improve the sensitivity, i.e. LIGO and Virgo use large optics, and KAGRA use cryogenic mirror. However, in the next generation GWD, both of them have to be adapted simultaneously.

Thermo-optic noise

The thermal dissipation induces the temperature fluctuation of a mirror. This fluctuation couples with the thermal expansion and the thermo-refractive coefficient, and results in the thermo-optic noise [30, 31]. Reference [31] gives the details of the thermo-optic noise. The dissipation power of the thermo-elastic damping which causes the sensing noise in a GWD is given by

$$W_{\mathrm{diss}} = \frac{TF_0^2}{2\sqrt{2}\pi r_0^2\kappa_{\mathrm{sub}}}\sqrt{\frac{\kappa_{\mathrm{coat}}}{C_{\mathrm{coat}}\omega}}\left(\frac{\partial\Delta z}{\partial T}-\bar{\alpha}_{\mathrm{sub}}d\frac{C_{\mathrm{coat}}}{C_{\mathrm{sub}}}\right)^2, \tag{1.74}$$

and thus the power spectrum of the thermo-optic noise S_{TO} is described as

$$S_{\mathrm{TO}} = \frac{2\sqrt{2}k_{\mathrm{B}}T^2}{\pi r_0^2\kappa_{\mathrm{sub}}}\sqrt{\frac{\kappa_{\mathrm{coat}}}{C_{\mathrm{coat}}\omega}}\left(\frac{\partial\Delta z}{\partial T}-\bar{\alpha}_{\mathrm{sub}}d\frac{C_{\mathrm{coat}}}{C_{\mathrm{sub}}}\right)^2, \tag{1.75}$$

where r_0 is the beam radius and $\kappa_{\rm i}$, ρ, $C_{\rm i}$ and $\bar{\alpha}_{\rm i}$ (i = sub or coat) are the thermal conductivity, the density, the specific heat and the effective thermal expansion coefficients of the substrate and coating. The factor $\frac{\partial \Delta z}{\partial T}$ denotes the optical distance change of the coating to the temperature, and it is expressed as

$$\frac{\partial \Delta z}{\partial T} \sim \bar{\alpha}_{\rm coat} d - \bar{\beta}_{\rm coat} \lambda \tag{1.76}$$

where $\beta_{\rm coat}$ is the effective thermo-refractive coefficient of the coating.

Suspension thermal noise

The intrinsic friction inside the suspension excites the system, and causes the vibration. The thermal noise which is the result of this intrinsic dissipation of the suspension is called the suspension thermal noise. All parts of the suspension can be the origin of the suspension thermal noise, but the tiny vibration which happens at the upper parts of the suspension is negligible thanks to the transfer function of the suspension. The power spectrum of the suspension thermal noise at the lowest suspension part $S_{\rm sus}$ is described as [32, 33]

$$S_{\rm sus} = \frac{4 k_{\rm B} T_{\rm sus} \omega_{\rm sus}^2 \phi_{sus}}{m \omega^5} \tag{1.77}$$

where $T_{\rm sus}$, $\omega_{\rm sus}$ and $\phi_{\rm sus}$ are the temperature, the resonant frequency and the loss angle of the suspension.

These thermal noises possibly limit the sensitivity of the current and the next generation GWD. To improve the thermal noise, the development of the low loss system and the low temperature system is required.

1.3.3 Quantum noise

The detections of gravitational waves is achieved by continuous precise position measurement of mirrors with laser light. Hence, one of the fundamental noise of a GWD is derived from the quantum nature of light. The number of photons N which go through the certain area per unit time follows the Poisson distribution, and it described as $N = P/\hbar\omega$, where P, $\hbar$ and ω are the power of the laser, reduced Planck constant and the angular frequency of light, respectively. The root mean square of the photon number δN is given by $\delta N = \sqrt{N}$. This photon number fluctuation δN equivalents to the laser amplitude fluctuation $\delta P = \sqrt{\hbar \Omega P}$, and it results in the variation of

the laser amplitude which is reflected by a mirror or detected by a PD. The power spectrum density $S_{\delta P}$ of the laser power is $S_{\delta P} = \sqrt{2\hbar\Omega P}$.

The radiation pressure noise

The fluctuation of the reflection laser amplitude causes the radiation pressure fluctuation, and this noise is called the radiation pressure noise. The radiation pressure noise mainly limits the sensitivity at the low frequencies. Now let us consider the radiation pressure noise in the FPMI. The transfer function $H_{\rm FP}$ from the input laser power to the storage laser power inside the FP cavity and its absolute value are given as

$$H_{\rm FP} = \frac{t_1^2}{(1-r_1r_2)(1-r_1r_2e^{-i\frac{2L_{\rm cav}\omega}{c}})} \tag{1.78}$$

$$|H_{\rm FP}| = \frac{t_1^2}{(1-r_1r_2)^2}\frac{1}{\sqrt{1+\tau_{\rm FP}\omega}} \tag{1.79}$$

where $L_{\rm cav}$ is the length of the cavity, ω is the angular frequency of interest and $\tau_{\rm FP} = \frac{r_1r_2}{(1-r_1r_2)^2}\frac{2L_{\rm FP}}{c}$ is the time constant of the FP cavity. Hence, the transfer function of the FPMI, $H_{\rm FPMI}$, from the input power to the intra arm-cavity power is given as

$$H_{\rm FPMI} = \frac{1}{2}\frac{t_1^2}{(1-r_1r_2)(1-r_1r_2e^{-2\pi i\frac{2L_{\rm arm}f}{c}})} \tag{1.80}$$

and

$$|H_{\rm FPMI}| \sim \frac{\mathcal{F}}{\pi}\frac{1}{\sqrt{1+(\tau_{\rm arm}\omega)^2}} \tag{1.81}$$

where $L_{\rm arm}$ is the length of the arm FP cavity, and $\tau_{\rm arm}$ is the time constant of the arm FP cavity. To get Eq.(1.81) from Eq.(1.80), we assumed that the reflectivity of the arm mirrors is high, and used the expression of the finesse of $\mathcal{F} \sim \frac{2\pi}{t_{\rm ITM}^2}$.

The magnitude of the radiation pressure F is described as $F = 2P/c$, where P is the reflected laser power. The power spectrum density of the radiation pressure is given as

$$\delta F = 2S_{\delta P}/c. \tag{1.82}$$

The transfer function from the applied force to the displacement of the suspension is

$$H_{\rm sus} = \frac{1}{m(\omega_0^2-\omega^2)} \tag{1.83}$$

Then, the radiation pressure noise is given by the product of Eq.(1.81), Eq.(1.82) and Eq.(1.83) as

$$S_{\mathrm{RP}} = 4|H_{\mathrm{sus}}||H_{\mathrm{FPMI}}|\frac{2}{c}S_{\delta P} \tag{1.84}$$

$$\sim \frac{16\mathcal{F}}{m\omega^2 L}\sqrt{\frac{\hbar P}{\pi\lambda c}}\frac{1}{\sqrt{(1+(\tau_{\mathrm{arm}}\omega)^2)}} \qquad (\omega >> \omega_0) \tag{1.85}$$

The shot noise

The laser amplitude fluctuation which is detected by the PD directly worsen the measurement error, and this noise is called the shot noise. The shot noise mainly limits the sensitivity above 100 Hz. The ratio of the laser light incident on the PD to the energy of the photo-current is called the quantum efficiency η, and it is written as

$$\eta = \frac{I_{\mathrm{PD}}/e}{P_{\mathrm{PD}}/(\hbar\omega)}, \tag{1.86}$$

where e, $\hbar$, ω are elementary charge, reduced Planck constant and angular frequency of light, respectively. According to [34], the relation between the photo-current I_{PD} and the power spectrum density of the noise is described as $\delta I = \sqrt{2eI_{\mathrm{PD}}}$. Then, by applying Eq.(1.86), the relation between the incident laser power and that noise becomes

$$\delta P_{\mathrm{shot}} = \sqrt{\frac{2\hbar\omega P_{\mathrm{PD}}}{\eta}}. \tag{1.87}$$

Next, we transform the amplitude of the noise Eq.(1.87) to the amplitude of the GWs. The transfer function from the mirror displacement to the phase shift of the FPMI is given as

$$|\Delta\phi_{\mathrm{FPMI}}| \sim \frac{8\mathcal{F}}{\lambda}\frac{1}{\sqrt{1+(\tau_{\mathrm{arm}}\omega)^2}}\delta L. \tag{1.88}$$

Equation (1.18) gives the laser power fluctuation δP_{PD} due to the mirror displacement δL around the mid fringe as

$$\delta P_{\mathrm{PD}} = \frac{1}{2}P_0\,|\Delta\phi_{\mathrm{FPMI}}|\,. \tag{1.89}$$

Hence, the power spectrum of the shot noise is given as

$$S_{\rm shot} = \frac{\delta L}{L} = \frac{\delta P_{\rm shot}}{L}\left(\frac{\delta P_{\rm PD}}{\delta L}\right)^{-1} \tag{1.90}$$

$$= 2\frac{\delta P_{\rm shot}}{LP_0}\frac{\lambda}{16\mathcal{F}}\sqrt{1+(\tau_{\rm arm}\omega)^2} \tag{1.91}$$

$$= \frac{1}{4L\mathcal{F}}\sqrt{\frac{\pi c\hbar\lambda}{\eta P_0}}\sqrt{1+(\tau_{\rm arm}\omega)^2} \tag{1.92}$$

The standard quantum limit

The sum of the radiation pressure noise and the shot noise is calculated using Eqs.(1.84) and (1.90) as

$$S_{\rm sum} = \sqrt{S_{\rm RP}^2 + S_{\rm shot}^2}$$

$$= \frac{h_{\rm SQL}}{\sqrt{2}}\sqrt{\frac{1}{\mathcal{K}}+\mathcal{K}} \geq h_{\rm SQL} \tag{1.93}$$

with

$$h_{\rm SQL} = \sqrt{\frac{8\hbar}{m\omega^2 L}}, \tag{1.94}$$

$$\mathcal{K} = \frac{m\omega^2 L}{64\mathcal{F}^2}\frac{\pi c\lambda}{P}\left(1+(\tau_{\rm arm}f)^2\right). \tag{1.95}$$

As shown in Eq.(1.93), the sum of the radiation pressure noise and the shot noise is always larger than $h_{\rm SQL}$. This limit is called the standard quantum limit (SQL). As shown in Fig. (1.18), the most sensitive frequency of the quantum noise changes depending on the input laser power, though it is not lower than the SQL. To enhance the sensitivity beyond the SQL, the techniques based on the quantum optics have been studied and developed [35–37].

Quantum noise in BRSE

The previous subsection introduces the quantum noise in a FPMI. By adding the signal recycling mirror to these configurations, the shape of the quantum noise is modified. The quantum noise of the BRSE is given as [38]

$$S_{\rm BRSE} = \frac{8\hbar}{m\omega^2 L^2}\frac{\left((1+r_{\rm srm}^2)-2r_{\rm srm}\cos 2\beta\right)^2 t_{\rm srm}^3\mathcal{K}}{2\left(1+r_{\rm srm}e^{2i\beta}\right)^2}, \tag{1.96}$$

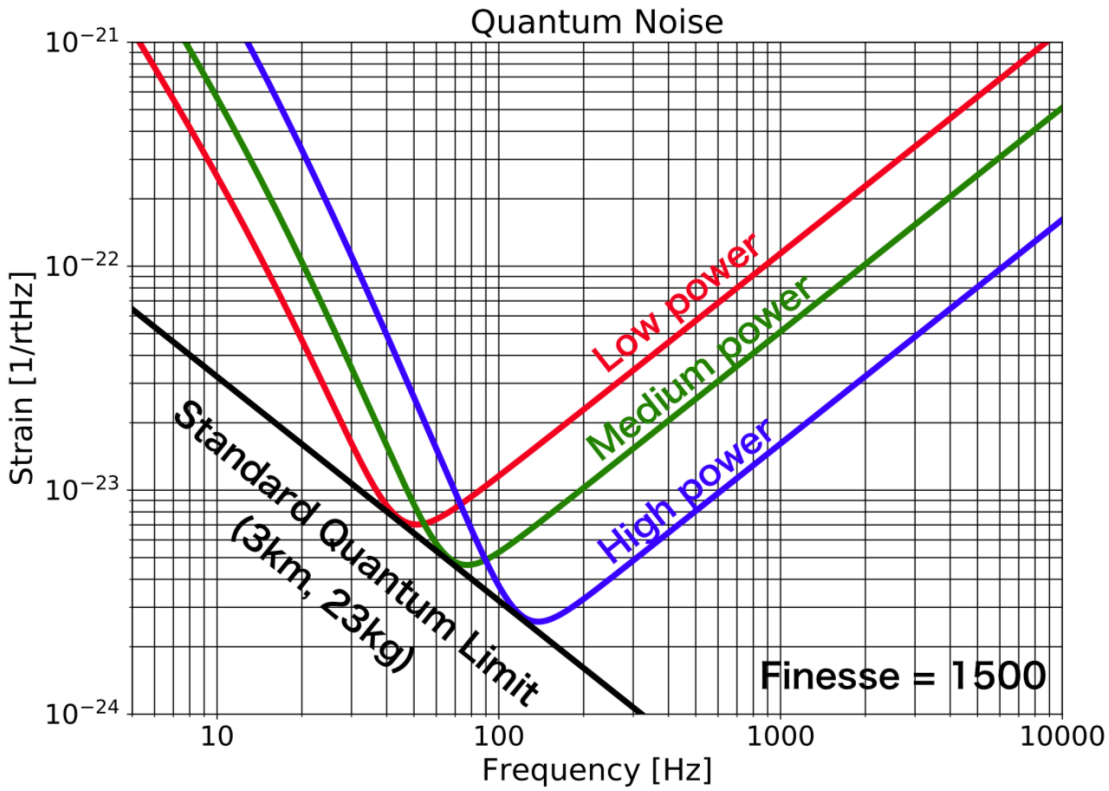

Figure 1.17: Laser power dependence of the quantum noise in FPMI. The quantum noise in the FPMI is calculated. The length of the arm is 3000m, and the finesse of the arm cavity is 1500. By changing the input laser power, the frequency and the amplitude of the lowest part of the quantum noise change, though it is not lower than the SQL.

with

$$\mathcal{K} = \frac{16\pi c P}{m\lambda L^2\omega^2(\gamma^2+\omega^2)}, \tag{1.97}$$

$$\gamma = \frac{cT_{\rm ITM}}{4L}, \tag{1.98}$$

$$\beta = \arctan\left(\frac{4L\mathcal{F}}{2\pi c}\omega\right) \tag{1.99}$$

where $r_{\rm srm}$ and $t_{\rm srm}$ is the amplitude reflectivity and transmissivity of the signal recycling mirror. Figure (1.18) shows the quantum noise in a DRFPMI with that in a FPMI. As explained in subsection (1.2.4), by adding the SRM and control to satisfy the condition, the response at high frequency region is

gained, and it broaden the sensitivity.

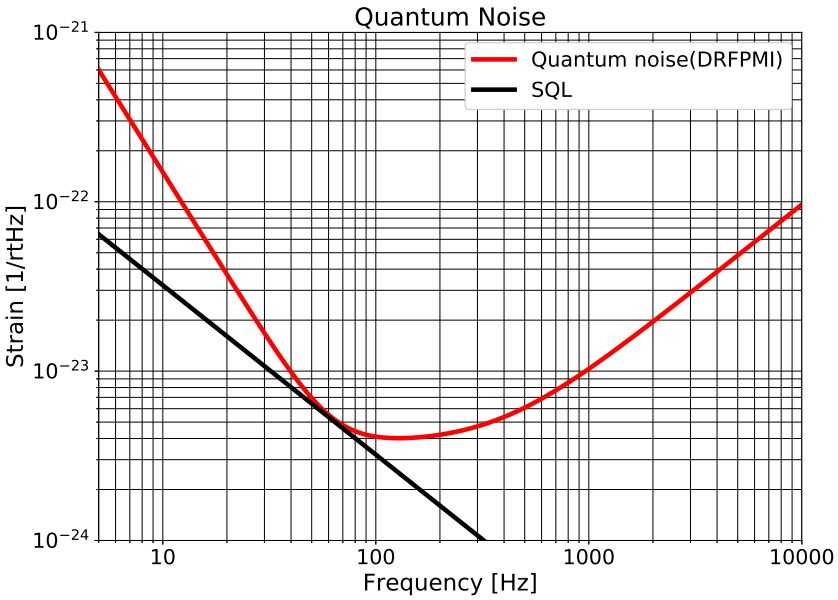

Figure 1.18: Quantum noise in the DRFPMI (BRSE). By adding the SRM and control to satisfy the condition, the response at high frequency region is gained, and it broadens the sensitivity.

1.4 Inspiral range

The fundamental noises in a GWD are introduced in last section. The inspiral range describes the distance from the detector to the source of the detectable GWs with the signal to noise ratio (SNR) of ρ_{SNR}. Here we denote the strain sensitivity of the GWD as $S(f)$, and the masses of the stars that compose the compact binary system are the same as m. The inspiral range is given as [7]

$$\mathcal{R} = \frac{0.442}{\rho_{\mathrm{SNR}}} \sqrt{\frac{6}{5}} \frac{Gm}{\pi^2/3c^2} \sqrt{\int_{f_{\mathrm{min}}}^{f_{\mathrm{max}}} \frac{f^{-7/3}}{S(f)} df} \tag{1.100}$$

with $f_{\mathrm{min}} = 10$ Hz and

$$f_{\mathrm{max}} = \frac{1}{6\sqrt{6}\pi} \frac{c^3}{2Gm}. \tag{1.101}$$

For instance, if we consider the GWD whose sensitivity is limited only by the quantum noise as shown in Fig.(1.18), the inspiral range for the 1.4 $M_{\odot}$ binary neutron star binary system, the inspiral range is about 130 Mpc.

Chapter 2
CRYOGENIC GRAVITATIONAL WAVE TELESCOPE KAGRA

The sensitivity of a gravitational wave detector is basically limited by some noises such as the seismic noise, the thermal noise and quantum noise as introduced in chapter 1. In order to maximize the detector sensitivity, the parameters of an interferometer are carefully chosen. Towards the next generation gravitational wave detector, the reduction of the thermal noise is one of the most important tasks. KAGRA, the Japanese gravitational wave detector, introduces cryogenic sapphire mirrors to improve the thermal noise and the next generation gravitational wave detectors, such as the Einstein telescope in Europe [39] and Cosmic Explolar in the U.S [40, 41], also plan to use cryogenic mirror. This chapter details the configuration of KAGRA and its estimated sensitivity.

2.1 Optical configuration

The optical configuration of KAGRA is the DRFPMI and Fig.(2.1) shows the position of the main mirrors [5]. KAGRA mainly consists of five optic systems, the input optics, the FPMI, the power recycling system, the signal recycling system and the output optics. The detector is constructed in the mountain to reduce the amplitude of the seismic motion, and all of mirrors in Fig.(2.1) are suspended using the multi-pendulum vibration isolation system. The input optics make ultra-stable laser using several optical cavities including the input mode cleaner which has the cavity length of 53 m [5]. The FPMI consists of the BS and the FP cavities that are configured by the cryogenic sapphire mirrors. The power recycling and the signal recycling techniques are aiming to improve the sensitivity by reducing the amplitude of the quantum noise. In

the detector, during the traveling of light in the FPMI, the higher-order modes of laser are generated via several processes, i.e. reflections and transmissions of imperfect mirrors, and these higher-order modes decrease the signal to noise ratio. The output optics remove disturbing higher-order modes and increase the signal to noise ratio by transmitting only the basic mode with GW signals. In the following subsections, the detail of the main interferometer parts, namely the FPMI and the recycling systems, is introduced.

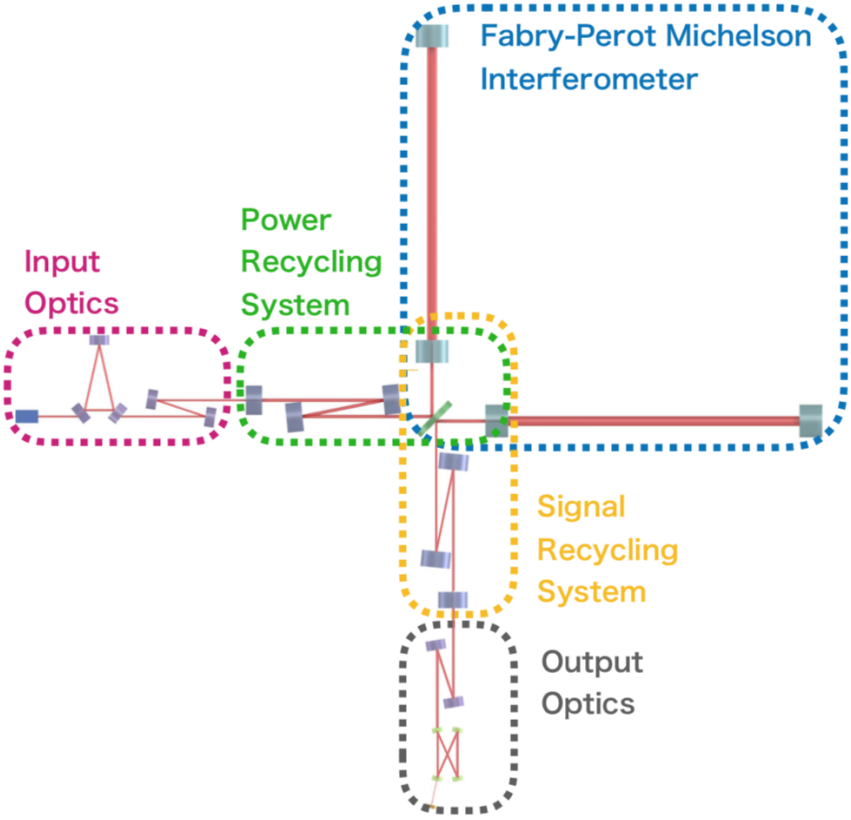

Figure 2.1: Optical configuration of KAGRA. The detector is constructed in the mountain to reduce the amplitude of the seismic motion. The main part of the detector mainly consists of five optics, the input optics, the FPMI, the power recycling system, the signal recycling system and the output optics. All of these mirrors are suspended not to disturb by the seismic motion. The length of the arm cavity is 3 km, and the arm cavity is composed of the cryogenic sapphire mirrors to reduce the thermal noise.

2.1.1 KAGRA Fabry-Pérot Michelson interferometer

The FPMI works as the antenna for the GWs. The FPMI is consists of the BS and the arm cavities. The length of the arm cavity is 3 km, and the cryogenic sapphire mirrors are used to configure the arm cavities. As introduced in Chapter 1, the mirror thermal noises, which is the sum of the Brownian noise and the thermo-optic noise, are parameterized by the parameters such as the mechanical loss angle, the beam radius at the mirror position and the temperature. To reduce the thermal noise, LIGO and Virgo adopted the fused silica mirrors that have 34 cm of diameter and 20 cm of thickness, the weight of these mirrors is about 40 kg [42, 43]. The beam radius at these mirrors is about 6cm, though the temperature of the mirrors is 300 K. On the other hand, KAGRA aims to improve the thermal noises by adopting the low temperature mirrors. The diameter, the thickness and the weight of the KAGRA sapphire mirror are 22 cm, 15 cm and 23 kg, and the temperature is kept at about 20 K during the observation [5]. Figure (2.2) shows the picture of the sapphire mirror. Adopting cryogenic mirrors for a km-scale GWD is the first attempt around the world, and it is one of the largest features of KAGRA, as well as the underground site.

The reflective and anti-reflective coating are the same as that of LIGO and Virgo. By stacking the high and the low refractive materials alternatively, and controlling the thickness of each layer so that the reflected lights satisfy the constructive interference condition. This coating is generally called the dielectric multi-layer coating [44]. Fused silica SiO_2 is used as the low refractive material, and tantalum pentoxide Ta_2O_5 is used as the high refractive index material. The number of SiO_2/Ta_2O_5 doubles on the ITM and the ETM high reflectivity surface (HR) are 11 and 20 [45], and the designed power transmittance of each mirrors are $T_{\rm ITM} = 0.004$ and $T_{\rm ETM} = 7 \times 10^{-6}$ [46]. In addition to the transmission of the ETM, the total optical loss in the arm cavity is assumed to be 93 ppm. Substituting these parameters into Eq.(1.37) gives the finesse of the KAGRA arm cavities as F $\sim$ 1530

Both of the ITM and the ETM are curved mirrors that have a radius of curvature of 1900 m. The g factor of the cavity is calculated from Eq.(1.45) as $g_{\rm ITM} = g_{\rm ETM} \sim 0.37$, the Rayleigh range and the beam radius at the waist position a re $z_0 = 775$ m and $\omega_0 = 23$ mm, and the beam radius is same at the ITM and the ETM, 35 mm. The parameters of the sapphire mirror and the arm cavity are summarized in table(2.1).

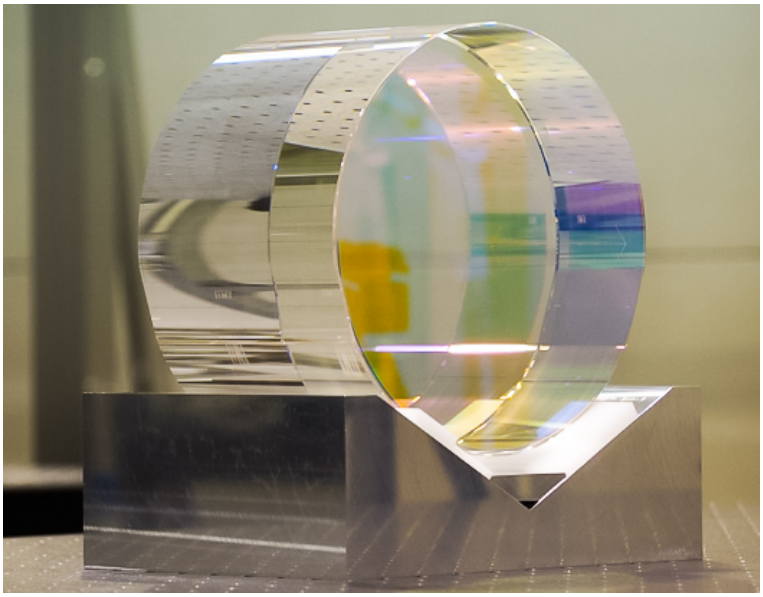

Figure 2.2: Picture of the KAGRA sapphire mirror. The diameter, the thickness and the weight of the mirror are 22 cm, 15 cm, and 23 kg. The mirror is kept at around 20 K during the observation to reduce the thermal noise. The coating of the mirror is the dielectric multilayer coating with SiO_2 and Ta_2O_5. Note that the stand is made from aluminum and designed by the author.

		Unit
Material	Sapphire (Al_2O_5)	-
Diameter	220	mm [45]
Thickness	150	mm [45]
Weight	22.8	kg [45]
Absorption of substrate	50	ppm / cm [47]
Number of doublets	11 (ITM) / 20 (ETM)	- [45]
Transmittance	0.004 (ITM)/7 $\times 10^{-6}$(ETM)	- [46]
Radius of curvature	1.9	km [46]
Cavity loss	93	ppm [46]
g-factor	35	mm
Beam radius	35	mm

Table 2.1: Properties of the KAGRA test mass.

2.1.2 Power recycling system

As discussed in chapter 1, the amplitude of the GW signal proportional to the laser power stored inside the interferometer, and by putting the PRM at the reflection port to reflect the light to the interferometer, the total laser power can be increased [48]. The power recycling system of KAGRA is composed of the PRM for the power recycling cavity, and the reflective PR2 and PR3 mirrors for the mode-matching as shown in Fig.(2.3).

Generally, the optics for the mode-matching is outside of the optical cavity. However, the mode-matching for the long cavity such as the arm cavity in a GWD needs long optical path and large optics. To reduce the size and the space of the system, the current GWDs adopt the mode-matching optics inside the cavity. The length of the power recycling cavity L_{PRC} which is composed of the PRM and the arm cavity is $L_{\mathrm{PRC}} = 66.592$, and the designed radius of curvature of the PRM, PR2, and PR3 are $f_{\mathrm{PRM}} = 458.129$ m, $f_{\mathrm{PR2}} = -3.076$ m, $f_{\mathrm{PR3}} = 24.917$ [49], respectively. Figure (2.3) shows the spacial mode of the KAGRA power recycling cavity and the arm cavity.

The power reflectivity of the KAGRA arm cavity R_{arm} is calculated to be $R_{\mathrm{arm}} \sim 0.90$ by using Eq.(1.33) with the parameters in table (2.1). Hence the power reflectivity of the PRM R_{prm} is designed to match the reflectivity of the arm cavity, $R_{\mathrm{PRM}} = 0.90$. Equation (1.56) and these parameters give the PRG of $G = 10.5$. KAGRA injects 50 - 80 W of the laser power to reach its designed sensitivity [5, 49], and consequently, 500 - 800 W of the laser is stored inside the PRC.

2.1.3 Signal recycling system

The KAGRA signal recycling gain is composed of the SRM for the SRC, and the SR2 and the SR3 for the mode-matching, as well as the power recycling system. The optical configuration of the SRC is almost the same as the PRC. The length of the SRC is $L_{\mathrm{SRC}} = 66.591$ m, and the radius of curvature of the SRM is the same as that of PRM, $f_{\mathrm{SRM}} = 458.129$ m [49]. The power transmittance of the SRM is designed to be $T_{\mathrm{SRM}} = 0.1536$. The radius of curvature of the PR2 and the PR3 are $f_{\mathrm{SR2}} = -2.9872$ m, $f_{\mathrm{SR3}} = 24.9165$ m, respectively. Hence, the spacial mode of the SRC is almost the same as the PRC.

Using the reflectivity of the arm cavity, the SRM and the length of the SRC, Eq. (1.63) gives the signal amplification gain as the Fig. (1.14). Because

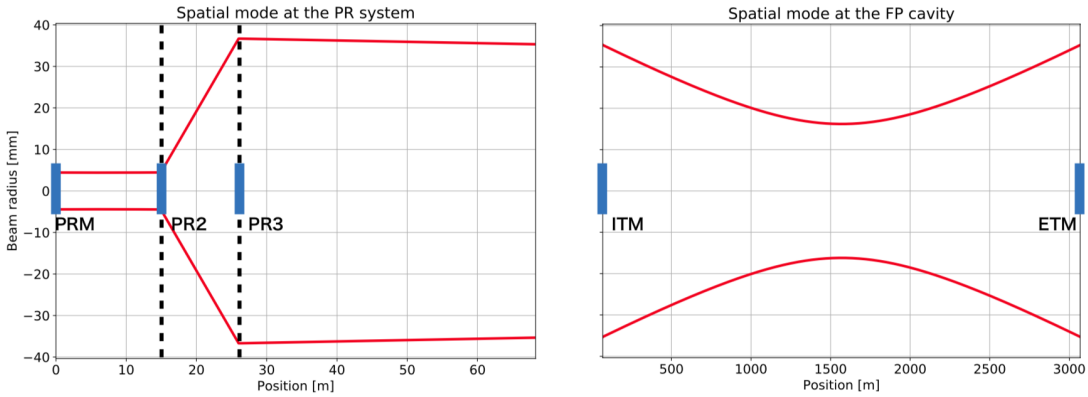

Figure 2.3: Spacial mode of the PR system and the arm cavity. Using the PR system, the spatial mode is matched to the eigen mode of the arm cavity. Left figure is the spatial mode of the laser at the PR system, and the right figure is the eigen mode of the arm cavity. The spatial mode of the SR system is almost the same as that of the PR system.

the sensitivity at the low-frequency region is mainly limited by the seismic noise and the suspension thermal noise, the SRC is set to be sensitive at the high-frequency region, though the signal recycling gain at the low-frequency region is lower.

2.2 Vibration isolation system for the test masses

In a GWD, to reduce the amplitude of transferred the seismic motion the test mass, a large suspension system is adopted for each mirror. Figure (2.4) shows the typical power spectrum density of the seismic motion at the KAGRA site. The seismic motion at KAGRA site is about 100 times smaller than Tokyo above 1 Hz due to the solid base and the underground, even so about 10^9 times attenuation is required at 10 Hz to detect GWs. For this purpose, KAGRA takes in various sizes of suspension systems depending on the requirements of each mirror [50]. Especially, the required vibration attenuation level for the sapphire test masses that work as an antenna for GWs is more strict than other suspensions [51]. To satisfy the strict requirement, the suspension for a test mass is a 13.5 m long, and it has 7 and 5 stages for the horizontal and the vertical vibration isolation. Figure (2.5-a) shows the whole suspension system for the KAGRA test masses which is called the type-A suspension,

and Fig.(2.5-c) shows the transfer function from the seismic motion to the test mass which is suspended by the type-A suspension system. The expression of the seismic noise $h_{\rm seis}$ to evaluate the KAGRA sensitivity is expressed as [5,45]

$$h_{\rm seis}^2 = 16\left(\frac{4.1\times10^{-17}}{f^{6.8}}\right)^2+\left(\frac{1.9\times10^{-16}}{f^{8}}\right)^2+\left(\frac{1.8\times10^{-18}}{f^{5.7}}\right)^2+\left(\frac{1.2\times10^{-16}}{f^{4}L}\right)^2, \tag{2.1}$$

where L is the baseline length.

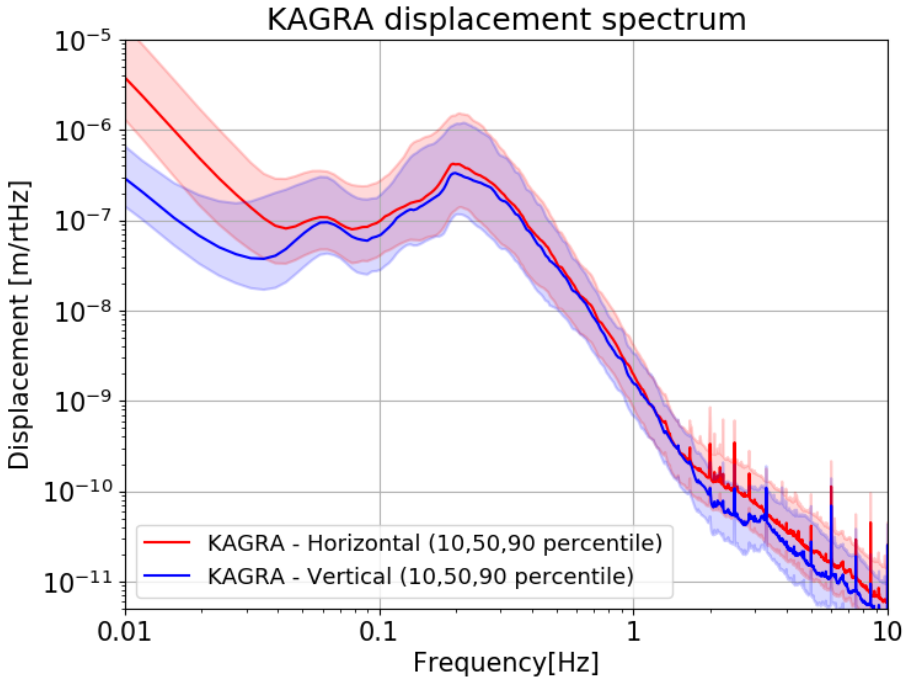

Figure 2.4: The seismic spectrum at KAGRA site. Red and blue lines show the displacement spectrum along to the horizontal and the vertical axes. The spectrums are estimated to be in the red and the blue area. The broad peak at 0.2 Hz correspond to the micro seismic that arise due to the ocean activity.

The sapphire test mass is cooled down to reduce the thermal noise, and for this purpose, the type-A suspension is composed of the two parts, the room temperature suspension part which is called the type-A tower and the cryogenic suspension part which is called cryogenic payload.
The cryogenic payload is the system to archive the good vibration isolation under the cryogenic environment as shown in Fig.(2.5-b). Type-a tower and

the cryogenic payload are connected by the rod made of maraging steel. The cryogenic payload consists of two independent pendulums, the main pendulum which contains the sapphire test mass and the recoil mass pendulum to control the masses of the main pendulum. Each stage of the main chain is named as the platform, the marionette, the intermediate-mass, and the test mass, respectively. To exhaust the heat that is generated in the test mass due to the laser absorption, the sapphire test mass and the intermediate mass are connected by the sapphire rod and sapphire blade spring. The other stages are thermally connected by the heat links that are made of pure aluminum. The thermal property of the cryogenic payload and the KAGRA cryogenic system are introduced in the next section.

2.3 Cryogenic system

KAGRA reduces the thermal noise using the cryogenic mirrors. The KAGRA cryogenic system mainly consists of the cryocoolers, the radiation shields and the cryogenic payload which suspends the cryogenic sapphire test mass. For one cryostat, there are six pulse-tube refrigerators, the dual radiation shields and the cryogenic duct shield to reduce the amount of the radiation from the room temperature regions. To adopt the cryogenic system in a GWD, the problems such as the vibration of the cryocooler and the cooling time have been studied. KAGRA has been developed the low vibration cryocoolers [52] and the heat link vibration isolation system to reduce the amplitude of vibration transferred to the test mass and studied the pure materials for the sufficient heat transfer. Furthermore, it is a unique feature of the cryogenic payload that the lowest part of the pendulum consists of sapphire to exhaust heat efficiently and to reduce the suspension thermal noise with its very low mechanical dispersion. In the following subsections, the KAGRA cryogenic system is detailed.

2.3.1 Overview of the cryostat and the radiation shields

Inside the KAGRA cryostat, there are dual radiation shields called the 8 K radiation shield and the 80K radiation shield, and there are two duct shields from the cryostat. These radiation shields reduce the amount of radiation from the room temperature region to the cryogenic payload. Figure (2.6) shows the cross-sectional view of the KAGRA cryostat. The cryostat is 4.3

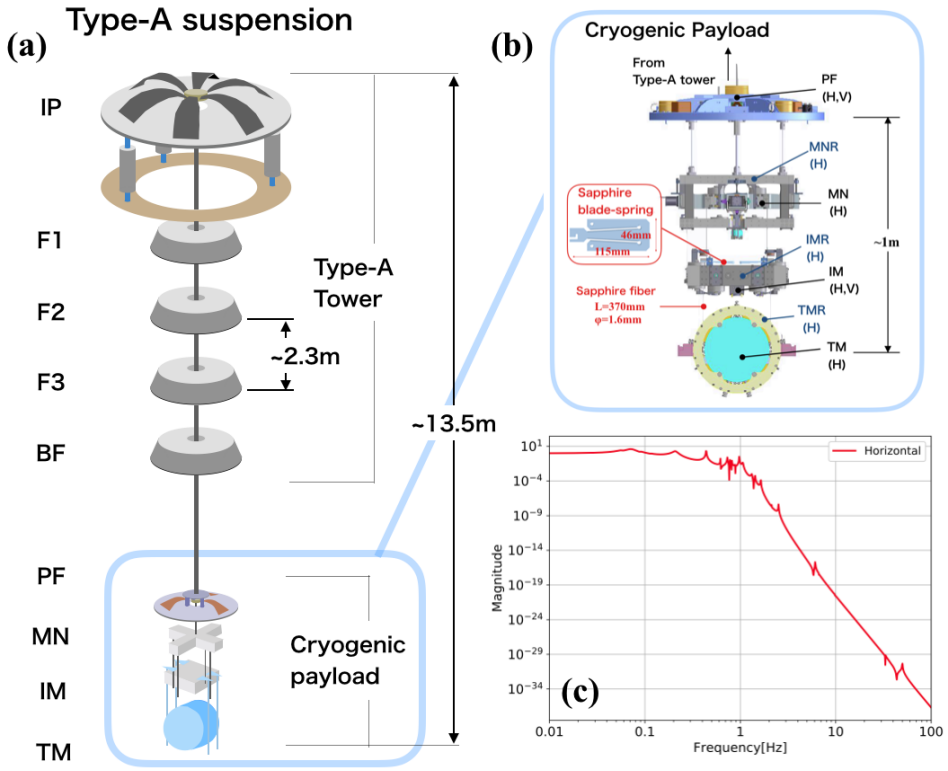

Figure 2.5: KAGRA type-A vibration isolation system. (a) The suspension is about 13.5 m tall with 7 and 5 stages for the horizontal and vertical isolation vibration isolation. The upper part is called the type-a tower and the lower part is called the cryogenic payload. bc) The cryogenic payload is inside the cryostat to cool the test mass down to 20K. The sapphire test mass and the intermediate mass (IM) is connected by the sapphire rod and the sapphire blade spring. (c)Transfer function of type-a suspension from the horizontal seismic displacement to the mirror displacement.

m high and 2.6 m in diameter. The 8K radiation shield is enclosed by the 80K radiation shield, and the 5m of the duct shields are installed along the beam axis, though these shields are not thermally connected.

The radiation shields are made of the aluminum 1000 and 5000 series, and the surface is coated with the diamond like carbon (DLC) coating [53] to increase the emissivity. The emissivity of the DLC is about $\varepsilon = 0.3 \sim 0.4$ at 300 K. Outer surfaces of the 80K, the 8K and the duct radiation shields are covered by the 50, 20, and 60 layers of the super insulator to thermally isolate from other cryogenic systems. The thickness of the walls of the 8 K and the 80 K radiation shields are 10 mm.

The duct shield is a circular cylinder with 5 m in length and 0.37 m in the diameter, and there are 5 baffles inside the duct shield to absorb the scattered light. The dimension and the position of these baffles are summarized in Fig.(2.7). The duct shield reduces the amount of radiation to about 0.1 W [54].

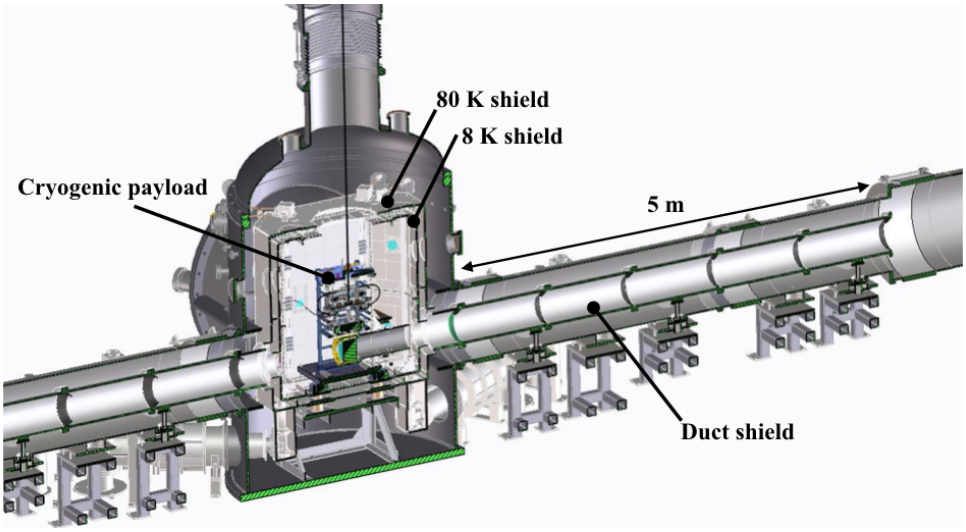

Figure 2.6: Cross-sectional view of the KAGRA cryostat. The KAGRA cryostat is mainly consists of the vacuum chamber, the cryocoolers, three types of the radiation shields, and the cryogenic payload.

2.3.2 Cryogenic payload

The cryogenic payload consists of two parallel pendulums [55]. Figure (2.5-c) shows the overall picture of the cryogenic payload. The platform (PF)

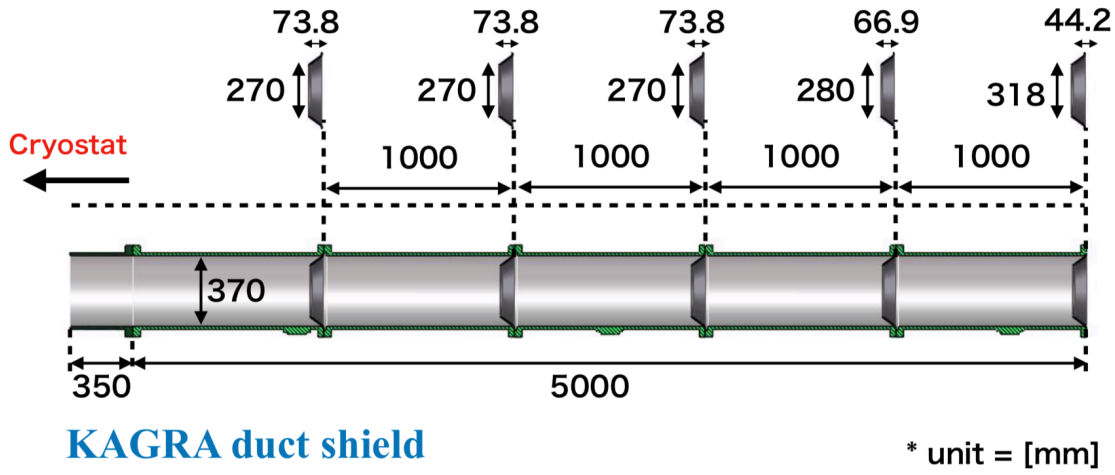

Figure 2.7: Cross-sectional view of the KAGRA duct shield. The duct shield is 5.35 m length and 0.37 in diameter. There are 5 baffles inside the duct to black the scattered light.

is common for these two pendulums. The pendulum which suspends the sapphire test mass is called the test mass chain and consists of the PF, the marionette (MN), the intermediate mass (IM), and the test mass (TM). The other pendulum called the recoil mass chain suspends the recoil masses that are used to control the masses of the test mass chain relatively. Each stage of the recoil mass chain is called the marionette recoil mass (MNR), the intermediate recoil mass (IMR), and the test mass recoil mass (TMR). All the stages are mainly made of stainless steel except for the TM which is made of the sapphire, and the weight of the cryogenic payload is about 200 kg. Table (2.2) summarizes the main three materials of each stage of the cryogenic payload and their weight. Note that these values are extracted from the 3D CAD design data.

Stage	Total mass [kg]	Material	Mass [kg]
Platform (PF)	69.6	SUS 304L	46.2
		SUS 316L	14.3
		Cu 1020	2.1
Marionette (MN)	23.4	SUS 316L	19.7
		Cu 1020	2.8
		Al 5052P	0.06
Marionette Recoil mass (MNR)	21.9	Al 5052P	12.5
		SUS 316L	8.0
Intermediate Mass (IM)	20.7	SUS 316L	19.3
		Cu 1020	0.9
		Sapphire	0.2
		Al 5052P	0.05
Intermediate Recoil mass (IMR)	21.91	SUS 316L	20.0
		Al 5052P	1.1
Test mass (TM)	23	Sapphire	23
Test mass Recoil mass (TMR)	22.9	SUS 316L	21.5
		Al 5052P	0.5

Table 2.2: Main component materials of each stage of the cryogenic payload.

To characterize the cryogenic system, it's important to know the budget of the heat input to the cryogenic system. Mainly, two paths of the heat inputs are considered to the KAGRA cryogenic payload: the radiation from the 300 K region through the duct shield and the optical absorption of the

TM. The amount of the radiation to the TM is evaluated to be 0.1 W par duct shield [56], so, as a total of two duct shield, 0.2 W of the radiation from 300 K is accounted for. The optical absorption happens on both coating and the sapphire substrate. The sapphire substrate absorbs about 35 ppm/cm of the laser with the wavelength of 1064 nm, on the other hand, the coating absorbs 0.3ppm of the laser [55]. Hence, the total amount of heat to the ITM, Q_{ITM}, and ETM, Q_{ETM}, are calculated as

$$Q_{\mathrm{ITM}} \sim \alpha_{\mathrm{coat}} P_{\mathrm{FP}} + 2\alpha_{\mathrm{sub}} T_{\mathrm{sub}} P_{\mathrm{MI}} + P_{\mathrm{rad}} = 0.67\mathrm{W} \tag{2.2}$$

$$Q_{\mathrm{ETM}} \sim \alpha_{\mathrm{coat}} P_{\mathrm{FP}} + P_{\mathrm{rad}} = 0.3\mathrm{W} \tag{2.3}$$

where $\alpha_{\mathrm{coat}} = 0.3 \times 10^{-6}$ and $\alpha_{\mathrm{sub}} = 3.5 \times 10^{-5}$ /cm are the absorption coefficients of the coating and the substrate, $P_{\mathrm{MI}} = 350$ W and $P_{\mathrm{FP}} = 350 \times 10^3$W are the storage power inside the MI and the arm FP cavity, $T_{\mathrm{sub}} = 15$cm is the thickness is the thickness of the substrate, and $P_{\mathrm{rad}} = 0.2$ W is the total amount of heat from the radiation from the radiation through the duct shield.

The cryogenic payload needs to extract these input heat to outside of the system. Each stage of the cryogenic payload except for the connection between the IM and the TM where is mechanically and thermally connected by the sapphire fibers is connected by the wire made of beryllium copper with the diameter of 0.6 mm. However, the thermal conductivity of the wire made of stainless steel is low, and it is not enough to extract these input heat. The actual cryogenic payload thermally connects each stage using heat links made of pure aluminum, and the MNR is connected to the cooling bar which is directly extended from the 2nd stage of the cryocooler through the heat link vibration isolation system. Figure (2.8) shows the thermal connection diagram of the cryogenic payload, and the thermal properties of the component materials are summarized in appendix A.

2.3.3 Cooling system

Figure (2.9-a) shows the KAGRA cryostat and its surroundings. KAGRA uses six cryo-coolers for one cryostat. Figure (2.9-b) and table (2.3) show the connection diagram between the cryostat and these cryocoolers and the details of the cryocoolers [54].

One cryocooler, model G300PHE manufactured by AIR WATER INC., is used to cool the duct shield down to about 100 K. This cryocooler is the single

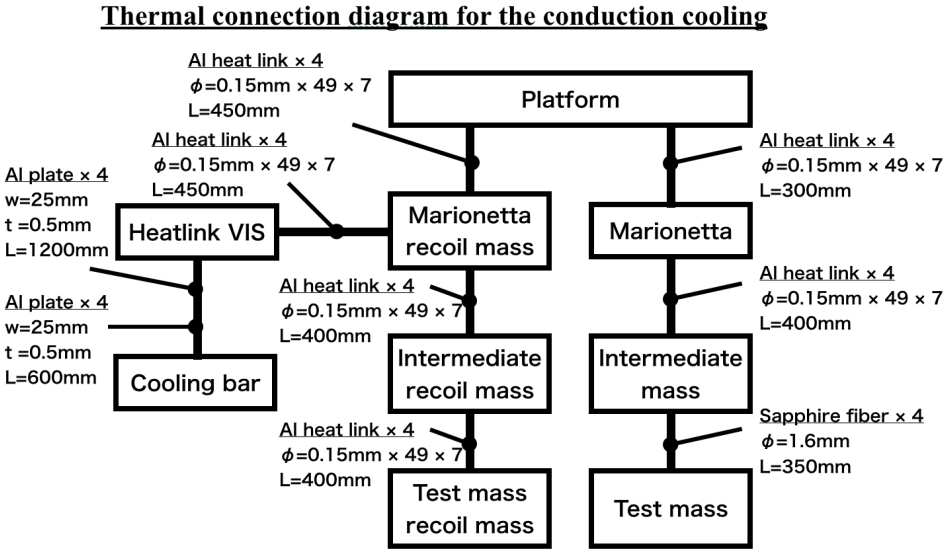

Figure 2.8: Thermal connection diagram for the conduction cooling of the KAGRA cryogenic payload. Each stage of the suspension is connected using Al heat links or the sapphire fibers.

No.	Company	Model	Type	Target1	Target2
Ref.1	Sumitomo Heavy Industries, Ltd.	RP-082B2S	Pulse Tube	80K shield	8K shield
Ref.2					
Ref.3					Cryogenic payload
Ref.4					
Ref.5	AIR WATER INC.	G300PHE		Cryogenic duct shield	—
Ref.6					

Table 2.3: KAGRA cryocoolers

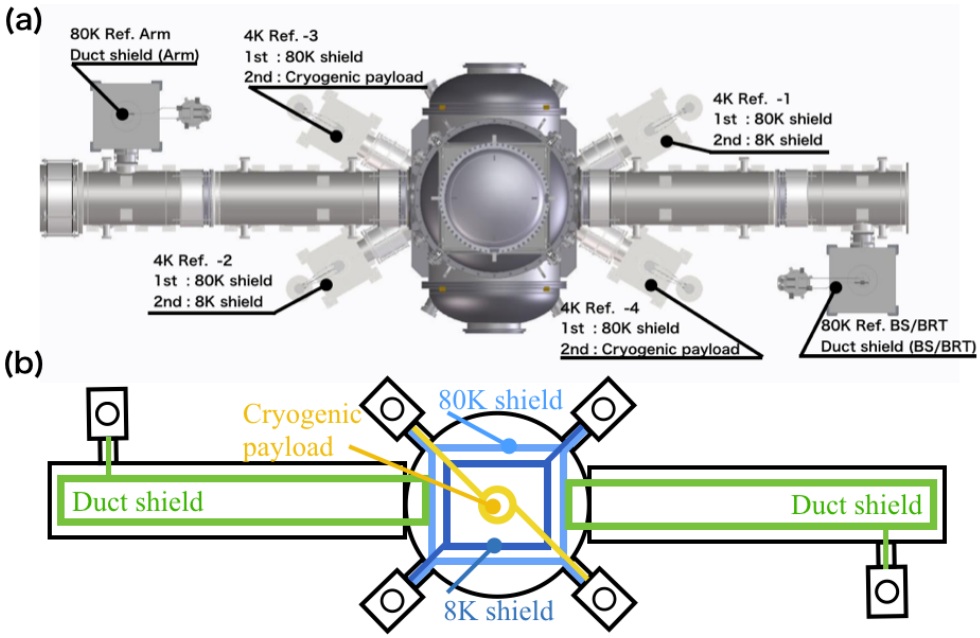

Figure 2.9: KAGRA cryostat and cryocoolers. (a) The KAGRA cryostat and the cryocoolers. Totally six cryocoolers are connected to one cryostat. (b) The connection diagram of the cryocoolers and the cryostat. Two single stage cryocoolers are connected to the duct shields. All the 80 K cold heads of four double stage cryocoolers are connected to 80 K radiation shield of the cryostat. Two of 8K cold heads are connected to the 8 K radiation shield of the cryostat, and remaining two 8 K cold heads are connected to the cryogenic payload.

stage cryocooler, and the passive vibration isolation system is implemented not to transfer the vibration caused by the operation of the cooler.

To cool the dual radiation shields of the cryostat and the cryogenic payload, four cryocoolers, model RP-082B2S manufactured by Sumitomo Heavy Industries, Ltd., are used. Figure (2.10) shows the cross-sectional view of this cryocooler. The cryocooler is the double stage pulse-tube cryocooler, and the cold heads are called the 80 K cold head and the 8 K cold head. As well as the cryocooler for the duct shield, this cryocooler contains the passive vibration isolation stages not to transfer the vibration to the cryostat. All of the 80 K cold heads of four cryocoolers are connected to the 80 K radiation shield of the cryostat, and two of four 8 K cold heads are connected to the 8 K radiation shield of the cryostat and remaining two 8 K cold heads are connected to the cryogenic payload as shown in figure (2.9-b). Tokoku et al. [52] reported the vibration attenuation and the cooling performance of these cryocoolers. The cooling power of the cryocooler is about 35 W for the 80 K head at about 67 K, while it is about 0.9 W for the 8 K head at around 8 K.

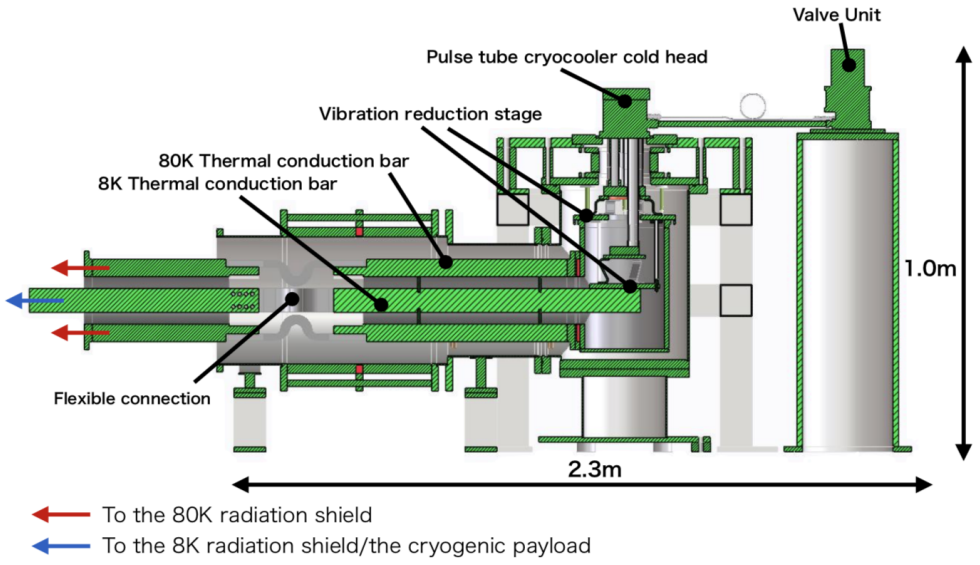

Figure 2.10: Cross-sectional view of the KAGRA cryocooler. The cryocooler is connected to the 80 K radiation shield and the 8K radiation shield or the cryogenic payload. To reduce the vibration from the cryocooler, the vibration reduction stages are inside the cryocooler.

Figure (2.11) shows the measured cooling curve of the KAGRA cryogenic

system. The heat link vibration isolation system is expected to have the large thermal resistance between the cryogenic payload and the cryocooler, and it results that the temperature of the TM didn't reach the target temperature of 20 K. To finish the cooling, it took about 27 days, and the cooling time is limited by the speed of the radiation cooling.

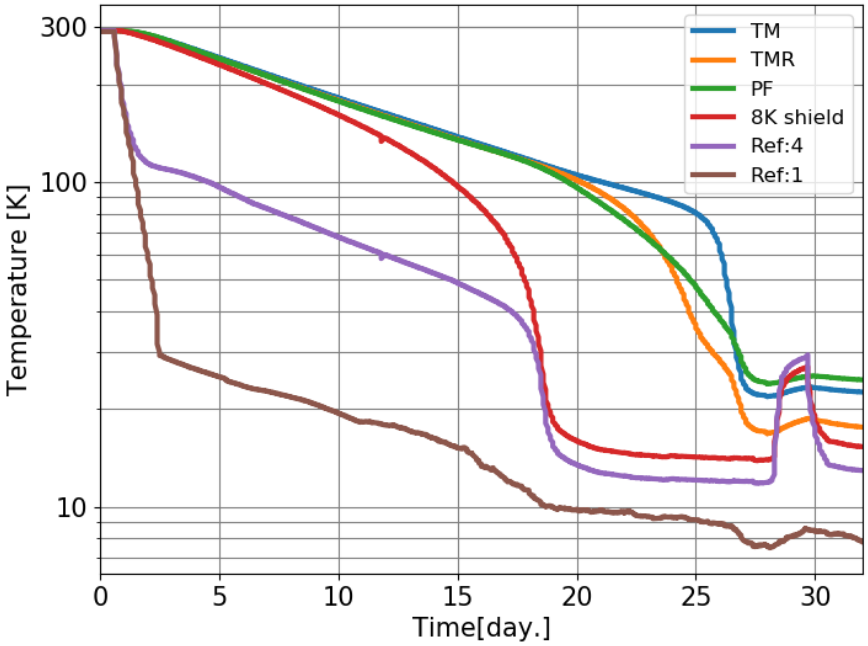

Figure 2.11: The cooling curve of KAGRA cryogenic system. The temperature of the TM didn't reach 20 K, and it is considered due to the thermal resistance in the heat link vibration isolation system. The bump at 28 days on 8 K shield and the refrigerator No.4 is due to the trouble of the cryocooler.

2.4 Vacuum system

Next, we introduce the KAGRA vacuum system. Except for the most upstream of the optical path, almost all of the large optics are inside the vacuum chamber. The total volume and surface area are 3330 m^3, and this is the largest vacuum system in Japan. Putting the optics in the vacuum chamber, the noise which is the result of the refractive index fluctuation of residual

gasses is decreased. Using the mass $m_{\rm mol}$ and the refractive index n_0 of the molecules, the power spectrum density of the noise $S_{\rm gas}$ is given as [57]

$$S_{\rm gas} = \frac{4}{L}\frac{(n_0-1)^2}{(N_0/V_0)\bar{v}\omega}\left(\frac{p}{p_0}\right)\left(\frac{T_0}{T}\right)^{3/2} \tag{2.4}$$

where $\bar{v} = \sqrt{8k_{\rm B}T/\pi m_{\rm mol}}$, ω, $N_0 = 6.02\times10^{23}$, $V_0 = 0.024\,{\rm m}^3$ and $T_0 = 273.15$ K are the mean velocity of the molecules, the beam radius, Avogadro number, the standard volume of the ideal gas and the temperature. Assuming the uniform pressure distribution for H_2O molecules, the required partial pressure of the molecules to archive the target strain sensitivity of $h = 10^{-24}\,1/\sqrt{\rm Hz}$ is calculated to be $p_{\rm H_2O} = 3.0\times10^{-6}$ Pa. KAGRA have set the target vacuum pressure of $p_{\rm target} = 2.0\times10^{-7}$ Pa with the safety factor of 10 [58].

The largest part of the vacuum system is two of the 3 km beam ducts. The duct is 0.8 m in diameter and 3000 m in length, hence the total volume of two beam duct is $3020\,{\rm m}^3$ and it occupies 90% of the whole vacuum system. The well-designed vacuum system is necessary to archive the vacuum pressure of 2.0×10^{-7} Pa with these large vacuum chambers.

KAGRA uses the stainless steel 304 L as the material of the vacuum chamber, and the inner surface of the duct and the chambers are processed by the electropolishing followed by the baking with the temperature of 200 ℃ for 20 hours. The amount of the outgases from the surface processed by the same method as KAGRA is reported in [58]. According to the report, after the 50 hours of pumping, the amount of the outgas is $q = 1.0\times10^{-8}{\rm Pa\,m^3/s/m^{-2}}$. Further, it's considered to be $q = 1.0\times10^{-9}\,{\rm Pa\,m^3/s/m^{-2}}$ after the 500 hours of pumping.

For the evacuation of the arm duct, KAGRA uses 30 units of the dry pump, the turbo pump and the ion pump at last. These units are equally spaced along the duct, and evenly spaced vacuum pumps make the periodic vacuum pressure distribution The pressure distribution between two pumps is given as [59]

$$p(x) = -\frac{qAL}{2cN^2}(\frac{x}{L/N})^2 + \frac{qAL}{2cN^2}(\frac{x}{L/N}) + p_{\rm min}, \tag{2.5}$$

with

$$p_{\rm min} = \frac{qA}{SN}, \tag{2.6}$$

where c, A, S and N are the conductance of the system in unit length, total surface area, the pumping speed of the vacuum pump and the number of the unit. Using the values of $q = 1.0 \times 10^{-9}\,\mathrm{Pa\,m^3/s/m^{-2}}$, $c = 80\,\mathrm{m^3/s/m}$, $A = 7537\,\mathrm{m^2}$, $S = 1\,\mathrm{m^3/s}$ and $N = 30$, the pressure distribution of the KAGRA beam duct is calculated to be $p_{\mathrm{min}} = 2.5 \times 10^{-7}$ Pa and $p_{\mathrm{max}} = 2.9 \times 10^{-7}$ Pa, where p_{max} is the largest vacuum pressure in the system. Note that this calculation does not contain the cryo-pumping effect that happens at the cryogenic system. From the result, the vacuum pressure of KAGRA can reach its target value, and the noise will not contaminate the sensitivity.

2.5 Sensitivity

The sensitivity of KAGRA can be calculated using the equations in Chapter 1 and the parameters that are introduced in this chapter. The seismic noise, the thermal noise, and the quantum noise that are introduced in Chapter 1 is showed in Fig.(2.12). Note that we assumed the detector configuration of BRSE. The parameters that are used to calculate the KAGRA sensitivity is summarized in the table (2.4).

Using the sensitivity in the Fig.(2.12), the inspiral range is calculated by Eq.(1.100) to be 130.5 Mpc for the 1.4 $M_\odot$ BNS, and about 1 Gpc for 20 - 30 $M_\odot$ BBH. LIGO and Virgo collaboration reported that the event rate of the BBH marge is 2 - 600 $\mathrm{Gpc^{-3}/yr^{-1}}$ [6], although it largely depending on the model. The observation efficiency, that is the ratio between the time that detector worked properly and the observation period, of the LIGO Hanford and Livingston and Virgo during the observation 2 are 61.7 %, 60.6 % and 85.08 %, respectively [60, 61]. Hence, when KAGRA achieves its design sensitivity and operates 70 % during the observation, KAGRA is expected to detect about 1 - 420 of BBH events per year. Furthermore, if we assume the above observation efficiency independent for each detector, the period when more than three detectors working properly is expected to increase from 32 % to 42 %. By increasing the number of detectors on Earth, the sky-localization become accurate, and this improvement is considered to be important to make an accurate alert to the optical telescopes for the multi messenger astronomy.

Name	Symbol	Value	Unit
Configuration of the detector		BRSE	
Arm length	$L_{\rm arm}$	3000	m
Wavelength	λ	1064	nm
Beam radius	ω_0	3.5	cm
Mirror mass	M	23	kg
Temperature of the TM	$T_{\rm TM}$	22	K
Temperature of the IM	$T_{\rm IM}$	16	K
Power transmissivity (ITM)	$T_{\rm ITM}$	0.004	-
Power transmissivity (ETM)	$T_{\rm ETM}$	7×10^{-6}	-
Amplitude reflectivity (SRM)	$r_{\rm SRM}$	0.92	-
Round trip loss (Arm cavity)	$T_{\rm loss}$	93×10^{-6}	-
Power at BS	$P_{\rm BS}$	400	W
Density (sapphire)	$\rho_{\rm sap}$	3980	kg/m^3
Specific heat	$C_{\rm sap}$	0.69	J/K/kg
Thermal expansion ratio	$\alpha_{\rm sap}$	5×10^{-6}	1/K
Thermal conductivity	$\kappa_{\rm sap}$	1.57×10^4	W/m/K
Young's modulus	$Y_{\rm sap}$	400	GPa
Poisson ratio	$\sigma_{\rm sap}$	0.25	-
Loss angle	$\phi_{\rm sap}$	1×10^{-8} [45]	rad
Refractive index (λ =1064nm)	$n_{\rm sap}$	1.7545 [62]	-
Thickness (SiO_2 coating)	d_{SiO_2}	2.75	μm
Density (SiO_2 coating)	ρ_{SiO_2}	2470 [63]	μkg/m^3
Young's modulus	Y_{SiO_2}	73.2 [63]	GPa
Poisson ratio	σ_{SiO_2}	0.164 [63]	-
Loss angle	ϕ_{SiO_2}	3×10^{-4} [5, 46]	rad
Refractive index (λ =1064nm)	n_{SiO_2}	1.442 [63]	-
Thickness (Ta_2O_5 coating)	$d_{Ta_2O_5}$	1.93	μm
Density (Ta_2O_5 coating)	$\rho_{Ta_2O_5}$	6505 [63]	μkg/m^3
Young's modulus	$Y_{Ta_2O_5}$	140 [64]	GPa
Poisson ratio	$\sigma_{Ta_2O_5}$	0.23 [64]	-
Loss angle	$\phi_{Ta_2O_5}$	5×10^{-4} [5, 46]	rad
Refractive index (λ =1064nm)	$n_{Ta_2O_5}$	2.035 [65]	-
Diameter (Sapphire fiber)	$d_{\rm f}$	1.6	mm
Length	$l_{\rm f}$	350	mm
Loss angle	$\phi_{\rm f}$	2×10^{-6}	rad

Table 2.4: Parameters to characterize the KAGRA sensitivity.

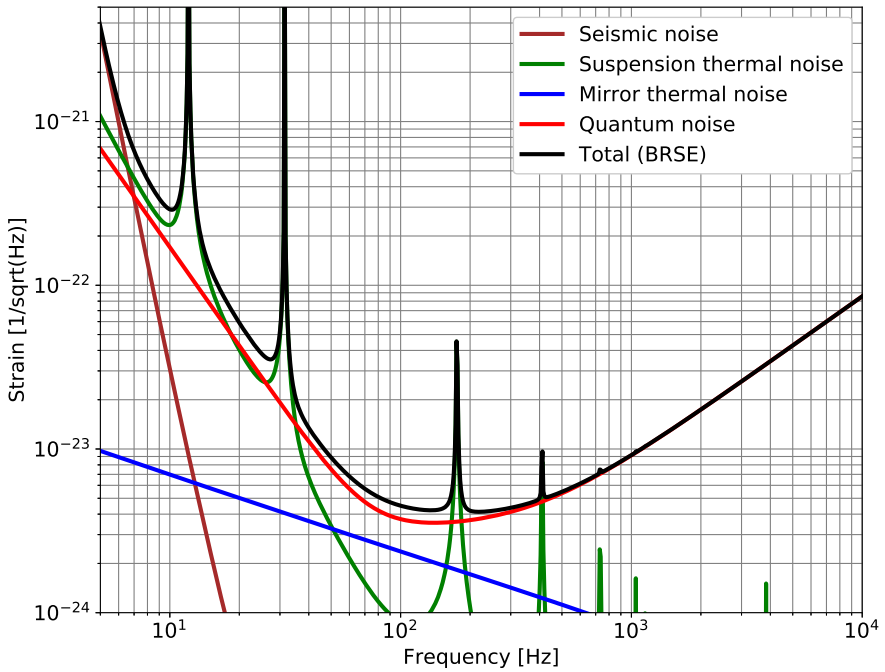

Figure 2.12: KAGRA sensitivity. Brown, green, blue, red, and black lines show the seismic noise, the suspension thermal noise, the mirror thermal noise, quantum noise, and the total of these noises, respectively. Most sensitive frequency region around 100 Hz will be limited by the quantum noise, followed by the thermal noise (by a factor of about 2).

2.6 Next generation gravitational wave telescopes

Next generation GWDs have the 10 km scale of the baseline and aim to achieve better sensitivity by a factor of 10 than current detectors. Especially, the improvement of the sensitivity at low frequency is important for the multi-messenger astronomy because the future detectors determine the sky localization using the low frequency signals [66].

Einstein Telescope (ET) is one of the future detectors which is planned to built in Europe. ET is configured of three interferometers, and they are located to make a triangle. The length of the interferometer baseline is 10 km, and one of three detectors is specialized to detect low frequency GWs and the other to high frequency GWs. To achieve the target sensitivity at low frequency, one of the interferometers adopts cryogenic mirrors with a weight of 200 kg.

Cosmic Explorer (CE) is planned to build in the U.S. CE has 40 km of the baseline and the shape of the interferometer is the same as the current detectors. CE plans to adopt 320 kg of mirrors made of silicon and cool it to 123 K to reduce the thermal noise. Because the temperature of 123 K is the region where the radiation cooling is dominant, the cooling system doesn't require the conduction cooling path which introduces the vibration to the system from outside.

Figure (2.13) shows the target sensitivity of future detectors. Adopting of the large cryogenic mirror reduces the noises to the order of $10^{-25}/\sqrt{\mathrm{Hz}}$ especially below 100 Hz. The cryogenics in GWDs will be a common technique for the future detectors.

2.7 Target of the study

As seen in Fig.(2.12), the most sensitive frequency region of KAGRA is limited by the quantum noise followed by the thermal noise. The quantum noise is expected to be reduced using the opt-quantum method such as the squeezing vacuum and the signal recycling technique beyond the standard quantum limit [67]. On the other hand, the reduction of thermal noise is thought to be tough.

As discussed in the previous section, the next generation GWDs are plan-

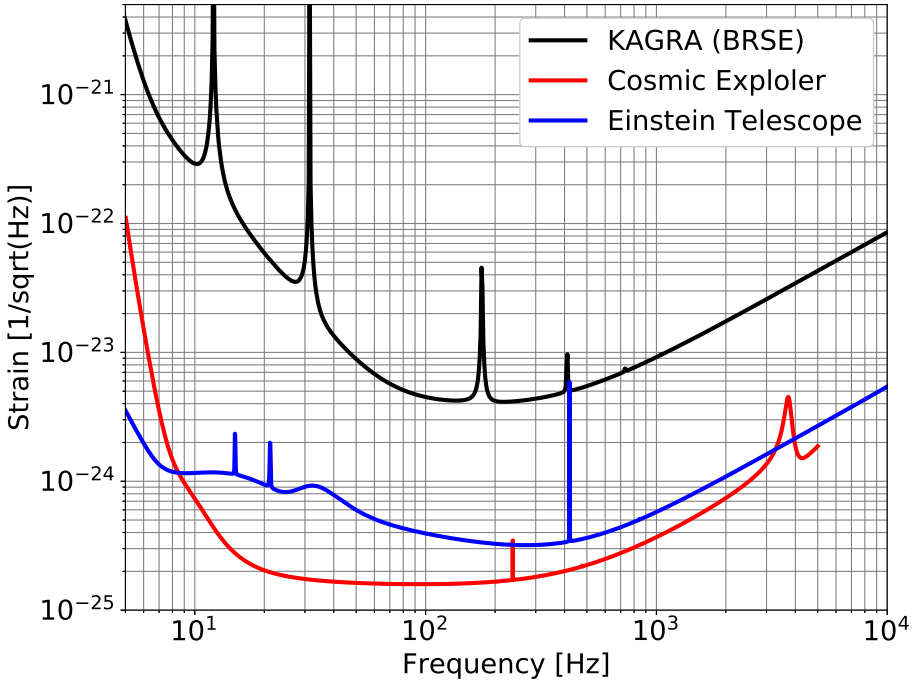

Figure 2.13: Sensitivity of the next generation GWDs. Blue and red lines represent the sensitivity of ET and CE. Adopting of the large cryogenic mirror reduces the noises to the order of $10^{-25}/\sqrt{\mathrm{Hz}}$ especially below 100Hz.

ning to introduce cryogenic mirrors to achieve their target sensitivity [39, 68]. The cryogenics in GWDs will be one of the common techniques, and it is important to gather and solve the problems related to the cryogenics in advance.

As the first detector that introduces cryogenics with the km scale of the baseline, KAGRA has studied the applicable cryogenics to GWD, the development of the cryogenic payload, the pure heat links and the DLC coating for instances. However, the interaction between the cryogenic mirrors and the vacuum residual gasses that are considered to generally happens in cryogenic GWDs have never discussed and studied except for a few experimental estimation [69, 70]. The goal of this thesis is to introduce the adsorption of the residual gasses on the cryogenic mirrors, and studies the impact of this effect on the cryogenic gravitational wave detector, and gives one of the solutions

to this problem.

These studies are important not only for KAGRA but also for GWDs which will introduce the cryogenics, The next chapter introduces the cryogenic adsorption on the cryogenic mirrors and aims to calculate the molecular layer formation speed on the KAGRA cryogenic mirror numerically.

Chapter 3
MOLECULAR LAYER FORMATION ON A CRYOGENIC MIRROR

KAGRA adopts the cryogenic test massed to reduce the thermal noise and achieve high sensitivity at around 100Hz. For now, many cryogenic related topics have been studied to make the cryogenics which is suitable in a very sensitive GWD. Though, the interaction between the vacuum residual molecules and the cryogenic system, especially the cryogenic test masses, have never studied except for very few experimental estimation

When a molecule hit to the surface of a cryogenic object, it decreases its kinetic energy, and finally, it is caught up by the surface potential. This phenomenon is generally called the cryopumping effect and this is well known as the technique to achieve the ultra-high vacuum. The KAGRA cryogenic system also works as the cryopump itself, so KAGRA doesn't use additional cryo-trap pump as LIGO and Virgo. The cryogenic test mass also catches the molecules as well the dual radiation shield, the duct shield, and cryocooler. A number of molecules on the cryogenic surface form a molecular layer. Before focusing on the effects of this molecular layer on the cryogenic test masses, first we estimate the molecular layer formation speed on the cryogenic test mass in KAGRA. As the molecular injection to the cryogenic mirror in KAGRA, we need to consider about the two case of molecular injections to the cryogenic mirror. One is the constant molecular injection from the atmosphere where the cryogenic mirror locate, inside the cryostat. The vacuum pressure of the chamber keeps constant by the balance of the degas and the evacuation, and the fact implies that the number of molecules which injecting to a specific area in the chamber is same everywhere in the chamber. The other is the molecular transport from the long vacuum duct. Especially for a cryogenic GWD, we can assume that the vacuum pressure inside the cryostat

where the cooled mirrors are located is quite low, and the molecular transportation from a long duct can be more important. However, the theoretical evaluation of the amount of the molecular transportation from the duct is not easy because the shape of the actual duct is complex and the temperature distribution is not uniform. A cryogenic GWD cooled its cryostat and a few lengths of the duct, but the almost all of the parts are operated at the room temperature. The Monte-Carlo simulation is the common way to evaluate the pressure distribution and the conductance that are the parameter to characterize the amount of the molecular transport of the actual vacuum system. This chapter introduces the previous work on the molecular layer growth rate expected in a cryogenic GWD first. Then it is re-defined based on the vacuum engineering theory, and evaluated for the KAGRA vacuum and cryogenic systems.

3.1 Previous work

Miyoki et al. [70] introduced the molecular adsorption on the cryogenic mirror in a GWD for the first time. Here we review the molecular layer formation rate expected in a GWD which is discussed in the reference [70].

The reference [70] gives the number of molecular N that inject to the cryogenic mirror as

$$N = \left(\frac{d}{4h}\right)^2 \frac{p}{\sqrt{2\pi m k_{\mathrm{B}} T}} \qquad 1/\mathrm{s/m^2}, \tag{3.1}$$

where d is the diameter of the cryogenic mirror, h is the length of the cryogenic duct which is installed between the cryostat and the room temperature duct, p is the vacuum pressure, m is the mass of the residual gas and T is the temperature. The derivation of the Eq.(3.1) is not detailed in the reference, but from its form, the equation is considered to represent the atmospheric molecular injection through the cryogenic duct. Following the calculation in the reference, the time to form a single molecular layer η is evaluated as

$$\eta = \frac{1}{N(1 \times 10^{-10})^2} \quad \mathrm{s}. \tag{3.2}$$

If we substitute $d = 0.2$ m, $h = 5$ m, $p = 10^{-6}$ Pa, $m = 3.0 \times 10^{-23}$ kg which is the mass of a H_2O molecule and $T = 300$ K, equation (3.1) is calculated to be $N \sim 2 \times 10^{12}$ 1/s/m^2 and Eq.(3.2) becomes $\eta \sim 2 \times 10^8$ s.

In this evaluations, there are some points to be improved. First of all, in this study, the molecular injection is given as the atmospheric injection from the room temperature beam duct. However, the number of molecules from the long vacuum duct is understood as molecular transportation. Without the calculation of the conductance of the system, the flux of the molecules to the cryogenic mirror cannot be evaluated.

As a second, the study didn't consider the atmospheric molecular injection from the other cryogenic parts such as the radiation shields. The molecules exist inside the cryostat even if the radiation shields are cooled down and they work as strong vacuum pumps. It important to check the molecular flux from the radiation shields is negligible.

Finally, the molecular layer growth speed is considered to be dependent on the kinds of molecules because the number of molecules on the surface and the thickness of the molecular layer is related by the density of the layer.

To evaluate the molecular layer growth rate on the cryogenic mirror in a GWD accurately, these points should be taken into account. Against these points, the following sections aim to derive the molecular layer growth speed based on the molecular kinetics and the vacuum engineering theory by considering two molecular layer formation processes; the atmospheric molecular injection and the molecular transportation from the long beam duct.

3.2 Atmospheric molecular injection

First, we consider about the atmospheric molecular injection of the chamber. We assume that the vacuum pressure of the chamber is enough low and the interaction of the molecules do not happen. The ideal gas equation of state is given as

$$PV = nRT \tag{3.3}$$

where P, V, T, n and R are the vacuum pressure, the volume of the chamber, the temperature, the number of moles and the ideal gas constant. The velocity of these molecules follows the Maxwell-Boltzmann (MB) distribution, and the x-axis component of the distribution is written as

$$f(v_{\mathrm{x}})dv_{\mathrm{x}} = \left(\frac{m}{2\pi k_{\mathrm{B}}T}\right)^{\frac{3}{2}} \exp\left(-\frac{mv_{\mathrm{x}}^2}{2k_{\mathrm{B}}T}\right) dv_{\mathrm{x}}. \tag{3.4}$$

Figure (3.1) shows the MB distribution of the H_2O molecules for various temperatures.

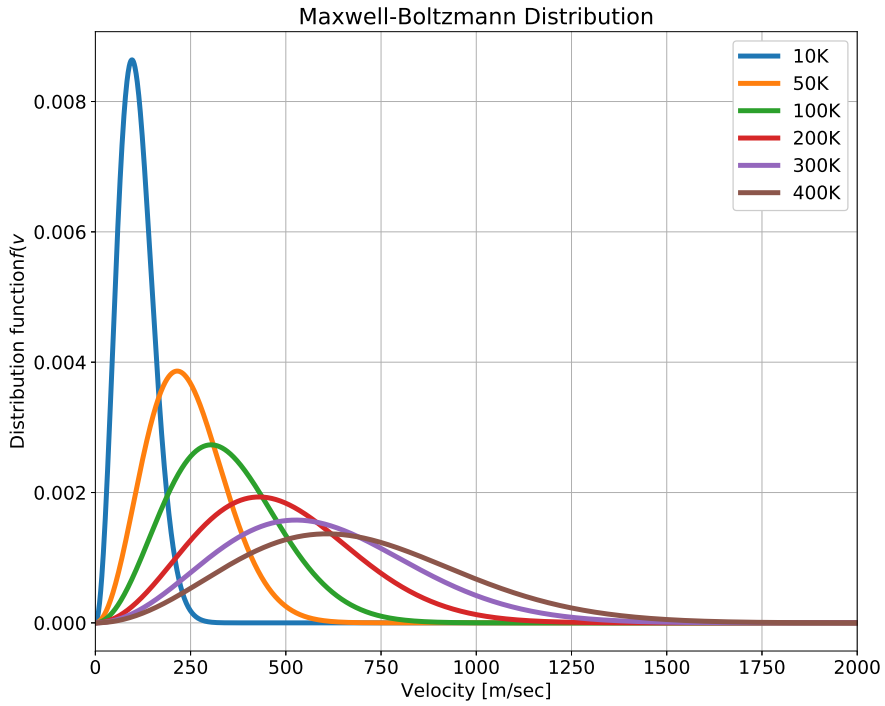

Figure 3.1: Maxwell-Boltzmann distribution of H_2O molecules. The calculation of Eq.(3.4) for H_2O molecules at various temperature. The mean velocity increases at a higher temperature, the dispersion of velocity decrease at a lower temperature.

The number of molecules N which injected to the area of δS that perpendicular to the x-axis within minute time δt is given as $N = nv_x\delta t\delta S$ [71]. Hence, its expected value $< N >$ is

$$< N > = \frac{\int_0^\infty N f(v_x) dv_x}{\delta S \delta t} \tag{3.5}$$

$$= n\sqrt{\frac{m}{2\pi k_B T}} \int_0^\infty v_x \exp\left(-\frac{mv_x^2}{2k_B T}\right) dv_x \tag{3.6}$$

$$= \frac{P}{\sqrt{2\pi m k_B T}} \qquad 1/\mathrm{sec}/\mathrm{m}^2. \tag{3.7}$$

The volumetric flow Q is given by Eq.(3.7) as

$$Q =< N > k_B T S = PS\sqrt{\frac{k_B T}{2\pi m}} \quad \mathrm{Pa\,m}^3/\mathrm{sec}. \tag{3.8}$$

where S is the area of the target which we interest.

The atmospheric molecular injection is considered to be negligible. The source of the molecules is the degas from the surfaces that compose the vacuum chamber and the cryostat and it depends on the temperature of the surface. As shown in the Fig.(2.11), the 80 K and 8 K shields are cooled to about 80 K and 15 K. Figure (3.2) shows the calculated vapor pressure of various molecules for temperature using the Antoine equation with the parameters in [72]. The vapor pressure implies the pressure that the ratio of the molecules in the gas state and the solid or liquid state is constant. Once, the temperature of the surface or the molecules decreases, the number of molecules that can escape from the surface potential statistically decrease. Because there is no solid angle from inside the 8K shield to the 80 K shield, we use the temperature of 8K shield to determine the vacuum pressure inside the cryostat. From the Fig.(3.2), the pressure of H_2O is negligible below 100 K, and the pressure of N_2 and O_2 molecules are $P_{N_2} \sim 1 \times 10^{-23}$ Pa and $P_{N_2} = 1 \times 10^{-30}$ Pa at 15 K. The volumetric flow of H_2O and N_2 molecules that are injecting to the cooled mirror with the radius of $r = 0.11$ m are calculated as $Q_{O_2} = 7.6 \times 10^{-31}$ Pa m^3/s and $Q_{N_2} = 2.05 \times 10^{-23}$ Pa m^3/s, respectively.

3.3 Molecular transport through the beam duct

Next, we consider the molecular transport from the long vacuum duct. The volumetric flow of the molecular transport between two surfaces S_1 and S_2 is written as [73]

$$Q = C\Delta P \qquad \text{Pa m}^3/\text{s}, \tag{3.9}$$

where C is the conductance of the system, and ΔP is the pressure difference between S_1 and S_2. The conductance C is rewritten as

$$C = C_0 K \qquad \text{m}^3/\text{s}, \tag{3.10}$$

with

$$C_0 = \left(\frac{D}{2}\right)^2 \sqrt{\frac{\pi k_B T}{2m}} \qquad \text{m}^3/\text{s}, \tag{3.11}$$

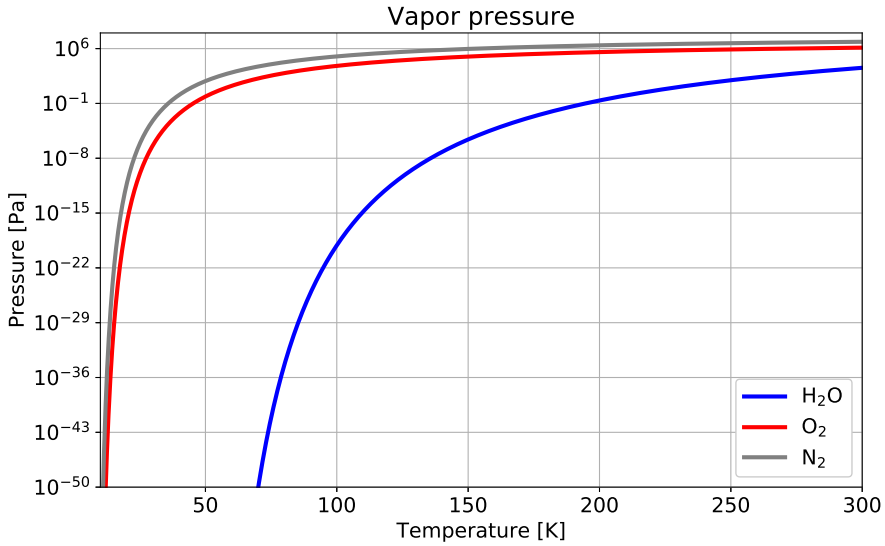

Figure 3.2: Vapor pressure of atmospheric composition molecules. The vapor pressure of H_2O, N_2 and O_2 are calculated by Antoine equation.

where C_0 is the opening conductance of the system, and K is the transmission probability of molecules pass through the vacuum system. The transmission probability of the circular duct is given by Santeler [74] as,

$$K = \frac{1}{1 + \frac{3L}{4D} + \frac{1}{\frac{4D}{L} + \frac{8}{7}}}, \tag{3.12}$$

where L and D are the length and the diameter of the duct.

Now we calculate the example of the volumetric flow of the molecular transport from the duct. For the duct with $L = 10$ m and $D = 0.8$ m, the opening conductance of H_2O, N_2 and O_2 molecules are $C_{0-H_2O} = 74.6\,\mathrm{m}^3/\mathrm{s}$, $C_{0-N_2} = 59.8\,\mathrm{m}^3/\mathrm{s}$ and $C_{0-O_2} = 56.0\,\mathrm{m}^3/\mathrm{s}$, and the transmission probability of the system is given by Eq.(3.12) to be $K \sim 0.09$. So the conductances for H_2O, N_2 and O_2 molecules are calculated to be $C_{H_2O} = 6.72\,\mathrm{m}^3/\mathrm{s}$, $C_{N_2} = 5.38\,\mathrm{m}^3/\mathrm{s}$ and $C_{O_2} = 5.03\,\mathrm{m}^3/\mathrm{s}$, respectively. Now we set the pressure difference between S_1 and S_2 as $\Delta P = 2 \times 10^{-7}$, which is considered to be the nominal pressure difference between the duct and the cryostat in KAGRA when the target vacuum pressure is achieved. Furthermore, we set one more parameter called the hitting probability H that molecules pass through the duct hit the cooled mirror to be $H = 0.01$. Then the volumetric flows of

H_2O, N_2 and O_2 molecules are calculated to be $Q_{H_2O} = 1.34 \times 10^{-8}\,\mathrm{Pa\,m^3/s}$, $Q_{N_2} = 1.08 \times 10^{-8}\,\mathrm{Pa\,m^3/s}$ and $Q_{O_2} = 1.01 \times 10^{-8}\,\mathrm{Pa\,m^3/s}$, respectively, As we calculated the volumetric flow against the two cases, in a cryogenic GWD, the atmospheric molecular injection is negligible, and the molecular transport from the beam duct is the main feed of the molecular layer growth. Hence, the pressure distribution and the conductance of the vacuum system are the important parameters to characterize the molecular layer growth in a cryogenic GWD.

As mentioned above, the transmission probability of a simple duct is given by Eq.(3.12), and it has good consistency with the simulated result for wide L/D range as discuss in later subsection. Equation (3.12), however, cannot apply for the complex vacuum system such that have baffles or adsorbent in the middle of the duct. To evaluate the transmission probability of such a complex duct, the Monte-Carlo (MC) simulation is generally applied [75].

3.3.1 Transmission probability and Monte-Carlo simulation

In the MC simulation, the transmission probability is defined as the ratio of the number of injected particles N_i and the transmitted particles N_t under the conditions as below and as shown in Fig. (3.3):

1. Particles are uniformly injected from the surface S_1 to the duct, and the injection angle distribution follows the cosine law.

2. Assuming that the vacuum pressure is enough low and the interaction between the injected particles do not happen.

3. Particles are not affected by the gravity and run straight in the vacuum chamber.

4. Reflection angle at the wall of the chamber is determined following the cosine law [76].

The condition (4) implies that a particle goes back forward with the probability of 50 %, so the number of the reflection at the wall is larger, or the L/D is larger, the transmission probability gets lower.

The number of transmission particle follows the binomial distribution, and when it gives the mean of the transmission probability $< K >$, the standard

deviation $\sigma_{<K>}$ is written as

$$\sigma^2_{<K>} = \frac{< K > (1 - < K >)}{N}, \tag{3.13}$$

where N is the number of the injected particles. The MC simulation of the transmission probability count the number of "transmission" particles, hence the number

Molflow+ is the software which developed at CERN to simulate the behavior of molecules inside the vacuum system [77]. In Molflow+, the model of the vacuum system is easily imported from 3D CAD data. The next section details Molflow+.

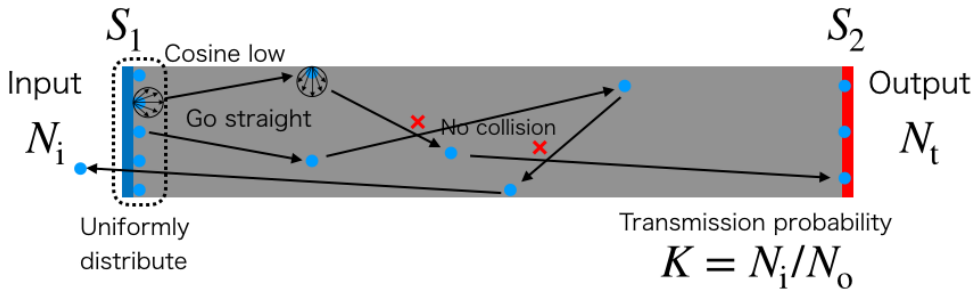

Figure 3.3: Maxwell-Boltzmann distribution of H_2O molecules. The calculation of Eq.(3.4) for H_2O molecules at various temperature. The mean velocity increases at a higher temperature, the dispersion of velocity decrease at a lower temperature.

3.4 Molflow+

Molflow+ has been developed at CERN to simulate the pressure distribution and the conductance of the vacuum system [77]. Molflow+ allows to analyze the actual vacuum system easily by importing the 3D CAD data by defining the vertexes and creating the facets to reproduce the 3D data. Users can set several parameters on facets, i.e. the degassing rate, the pumping speed or the sticking factor, the temperature and the opacity.

Table (3.1) shows the simulated transmission probability $< K >$ and its standard deviation $\sigma_{<K>}$ for several value or L/D. Figure (3.5) is the appearance of the simulation, and Fig. (3.6) is the calculated conductance

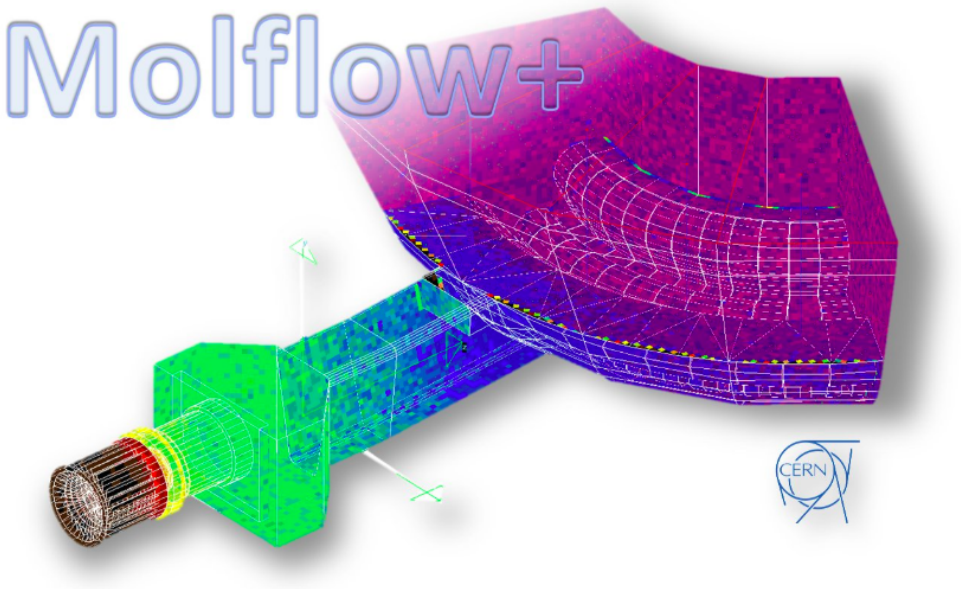

Figure 3.4: The image of the Monte-Carlo simulation with Molflow+. Molflow+ calculates the movement of molecules inside a vacuum chamber, and allow to calculate the conductance and the pressure distribution inside. The model is imported from the 3D CAD data. This image is quoted from the Molflow+ web site [77].

using the values in table (3.1) for the H_2O molecules. Red dots are the simulated values with their standard deviation. Blue line is the calculated conductance using Eq. (3.12) for the H_2O molecules, and it clearly shows that the Santeler's model for the transmission probability is consistent with the simulated result for wide L/D range.

Next subsection explains the dimension of the KAGRA vacuum system which is used for the MC simulation with Molflow+ and its results.

L/D	# of particle (N)	Transmission prob. (K)	Standard deviation (σ_K)
0.05	154515972	0.99995	5.69×10^{-7}
0.5	102137388	0.6724	4.64×10^{-5}
5	40469415	0.19081	6.18×10^{-5}
50	10430232	0.02533	4.86×10^{-5}
500	1151038	0.00254	4.69×10^{-5}
5000	249208	0.00020	2.87×10^{-5}

Table 3.1: Simulated transmission probability for various L/D.

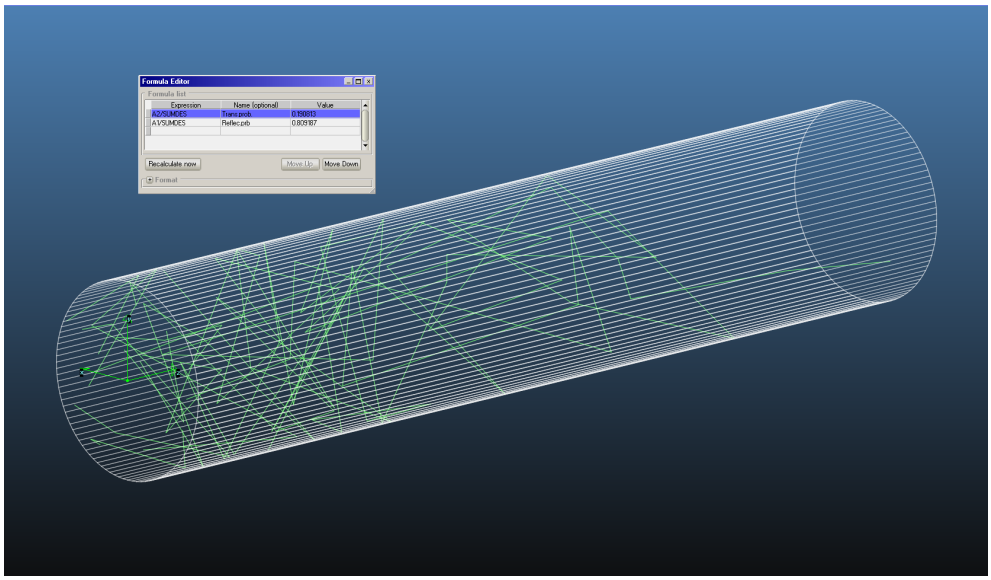

Figure 3.5: The appearance of the Molflow+ simulation. The vacuum duct is composed of white facets. The particles are injected from left large facet "S1" and absorbed by "S1" and "S2".

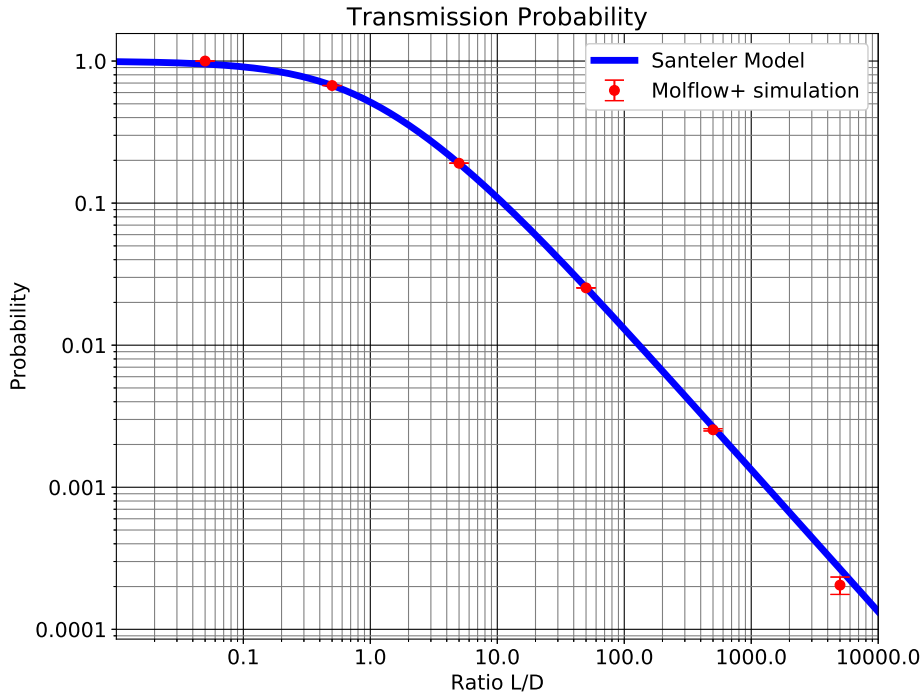

Figure 3.6: Comparison between the simulated transmission probability and Santeler model. Red dots are the simulated values, and error bars are its statistical error. Blue line shows the Santeler conductance model (Eq.(3.12)).

3.5 Simulation for the KAGRA vacuum system

In this subsection, we simulate the molecular layer formation speed (MLFS) using Molflow+. To calculate the molecular layer formation speed, the simulation of the transmission probability of the beam duct and the duct shield, and the hitting probability are needed. Following subsections detail each calculation.

3.5.1 Conductance of the beam duct

Next we calculate the conductance of the beam duct. The basic configuration of the KAGRA vacuum beam duct is as mentioned in the chapter 2. The beam duct is 3 km long, and it is configured by connecting the 12 m vacuum ducts. Here we simulate the conductance of the 12 m vacuum duct.

Because KAGRA sets the vacuum pump unit every 100 m, some of the 12 m vacuum duct has the vacuum pump. Figure (3.7) shows the 3D model of the 12 m vacuum duct with and without the vacuum pump that are used for the simulation. As results of the simulation, the transmission probability of the duct with and without the vacuum pump are

$$K_{\mathrm{w/-pump}} = 0.08740 \pm 2.0 \times 10^{-5}, \tag{3.14}$$

$$K_{\mathrm{w/o-pump}} = 0.08830 \pm 1.9 \times 10^{-5}. \tag{3.15}$$

Because the difference of the transmission probabilities is about 1 % and it will not make large difference in the calculations below, so we use averaged value $K_{\mathrm{ave}} = 0.08785 \pm 0.00045$ to calculate the conductance of the 12 m duct. The conductance of the 12 m beam duct $C_{12\mathrm{m}}$ for H_2O, N_2 and O_2 molecules are

$$C_{12\mathrm{m}} = C_0 K_{\mathrm{ave}} = \begin{cases} 10.06 \pm 0.05 & (H_2O), \\ 8.07 \pm 0.04 & (N_2), \\ 7.55 \pm 0.04 & (O_2). \end{cases} \quad \mathrm{m^3/s} \tag{3.16}$$

3.5.2 Conductance of the duct shield

At second, the conductance of the duct shield is evaluated. The conductance of the duct shield is contributed from the room temperature molecules that

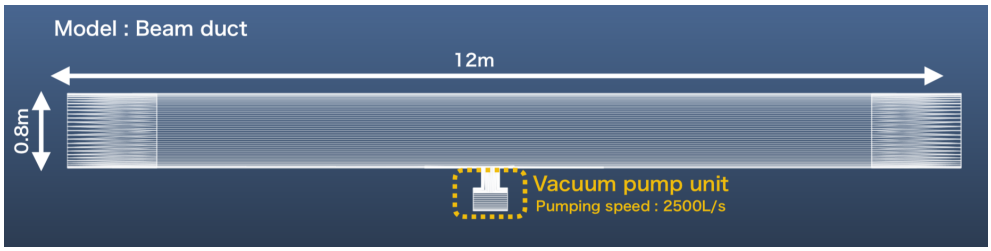

Figure 3.7: Simulation model of 12 m of the beam duct. The transmission probability of 12 m of the beam duct was simulated. Because some unit have pumping unit and the other don't have it, the transmission probability with and without the vacuum pumping unit was calculated. The pumping speed of the pump was set to 2500 L/s which is the nominal pumping speed of the pump unit in KAGRA.

transmit the duct shield without any reflection and the cryogenic molecules that transmit the duct shield by reflecting the wall of the duct. The total conductance the duct shield C_{ds} is given by the summing rule of the conductance as

$$C_{\mathrm{ds}} = C_{\mathrm{room}} + C_{\mathrm{cryo}}, \tag{3.17}$$

where C_{room} and C_{cryo} are the conductance of the room temperature and the cryogenic molecules. The ratio between the number of molecules that input to the cryogenic surface and that adhere to the surface is called the sticking coefficient P_{ab}. The sticking probability is the temperature dependence and studied in [78]. According to the report, the sticking coefficient for temperature $P_{\mathrm{ab}}(T)$ is given as

$$P_{\mathrm{ab}}(T) = \alpha \left(1 - \tanh\left(\beta \left(T - \gamma E_{\mathrm{des}}\right)\right)\right), \tag{3.18}$$

where $\alpha = 0.5$, $\beta \sim 0.11$ and $\gamma \sim 0.042$ are the parameters to reproduce the experimental results, and E_{des} is the desorption energy of the molecules that we interest. Table (3.2) summarizes the desorption energy E_{des} for H_2O, N_2 and O_2 molecules in unit Kelvin. Figure (3.8) shows the sticking coefficient for the temperature of the surface. Here we assume that the sticking coefficient of the duct shield follows the Eq.(3.18). As shown in the Fig.(3.8), the sticking coefficient of the duct shield that cooled to 100 K is 1 for H_2O molecules, and that is 0 for N_2 and O_2 molecules. Figure (3.9) shows the simulated result of the transmission probability of the duct shield for the sticking coefficient. The simulated model is the same as Fig.(2.7).

We denote the transmission probability of the duct shield for the sticking coefficient $P_{\rm ab}$ as $K_{\rm ds}(P_{\rm ab})$. Then, the conductance for the room temperature molecules that transmit the duct shield directory $C_{\rm room}$ and the conductance for the cooled molecules that transmit the duct by reflecting the wall $C_{\rm cryo}$ are rewritten as

$$C_{\rm room} = C_0(T_{\rm room})K_{\rm ds}(P_{\rm ab}=1) \tag{3.19}$$
$$C_{\rm cryo} = C_0(T_{\rm cryo})\left(K_{\rm ds}(P_{\rm ab}) - K_{\rm ds}(P_{\rm ab}=1)\right) \tag{3.20}$$

Taking these effect into account, the conductance of the duct shield $C_{\rm ds}$ are calculated as shown in Fig.(3.10). Especially for the duct shield of 100K, the conductance for H_2O, N_2 and O_2 are

$$C_{\rm ds} = \begin{cases} 0.6887 \pm 0.008 & (H_2O), \\ 0.834 \pm 0.001 & (N_2), \\ 0.849 \pm 0.001 & (O_2). \end{cases} \quad {\rm m^3/s} \tag{3.21}$$

Unit: K	H_2O	N_2	O_2
$E_{\rm des}$	6000	1250 [78]	1310 [78]

Table 3.2: Desorption energy of H_2O, N_2 and O_2 molecules

3.5.3 Hitting probability

At last, here we consider the hitting probability of molecules that reach the 80 K radiation shield. When molecules reach the 80 K radiation shield, the molecules go into the cryostat, and some of the molecules do not reach the surface of the test mass because there is the space between the radiation shield and the test mass. We define the hitting probability H as the ratio between the number of molecules that reach the 80 K radiation shield and that hit the coating surface of the test mass.

As shown in the Fig.(3.11), the distance between the edge of the duct shield and the mirror is 825 mm, and the entrance of the shield is the cylindrical tube 270 mm in diameter and 90 mm long.

When the molecules reach to the 80 K radiation shield, these molecules have the spatial and angle distribution depending on the sticking probability of the duct shield, and it's not able to input any spatial and angle distributed

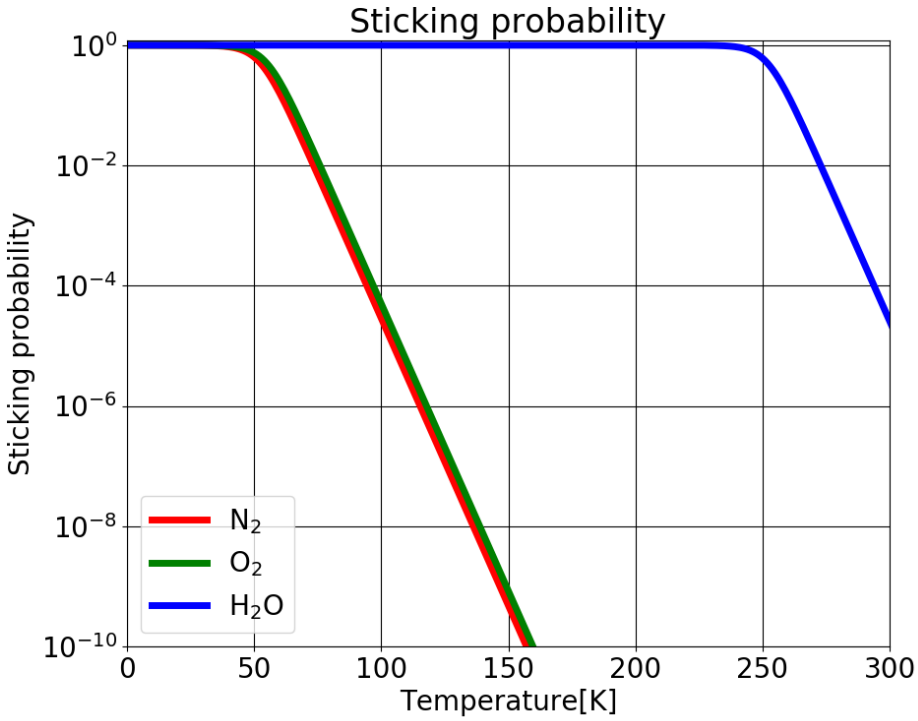

Figure 3.8: Calculated sticking probability of H_2O, N_2 and O_2 molecules for the surface temperature.

desorption from the surface in Molflow+. To solve the problem, the transmission probability of the space and the duct shield was calculated at the same time as shown in the Fig.(3.11). The total transmission probability K_{tot} is given by the multiplication of that of the duct shield K_{ds} and this space K_{spa}. Hence, the transmission probability of this part is given as

$$K_{\mathrm{spa}} = \frac{K_{\mathrm{tot}}}{K_{\mathrm{ds}}}. \tag{3.22}$$

By changing the sticking coefficient of the duct shield, the total transmission probability was simulated. Figure(3.12) shows the simulated result. For the sticking probability of 100 %, the transmission probability is $K_{\mathrm{spa-100\%}} = 0.49947 \pm 3.4 \times 10^{-5}$, and it is $K_{\mathrm{spa-0\%}} = 0.0530 \pm 0.00015$ for the sticking probability of 0 %.

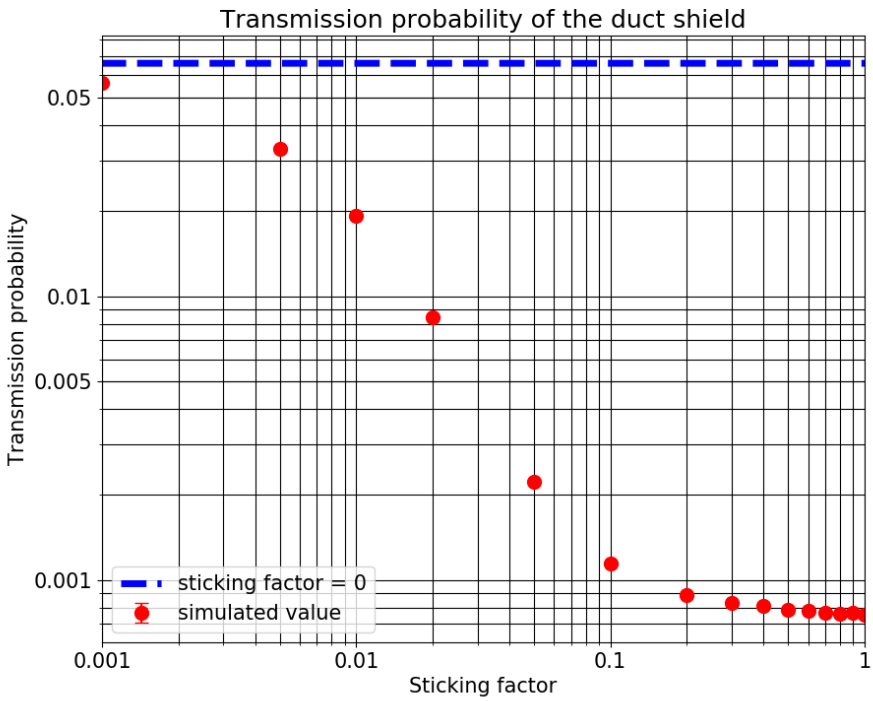

Figure 3.9: Simulated transmission probability of the duct shield for various sticking factor. Blue line shows the transmission probability when the sticking probability equals zero. The difference of the blue line and the red dot implies the number of adsorbed molecules. When the sticking probability is one, all of the transmitted molecules are not reflected by the wall.

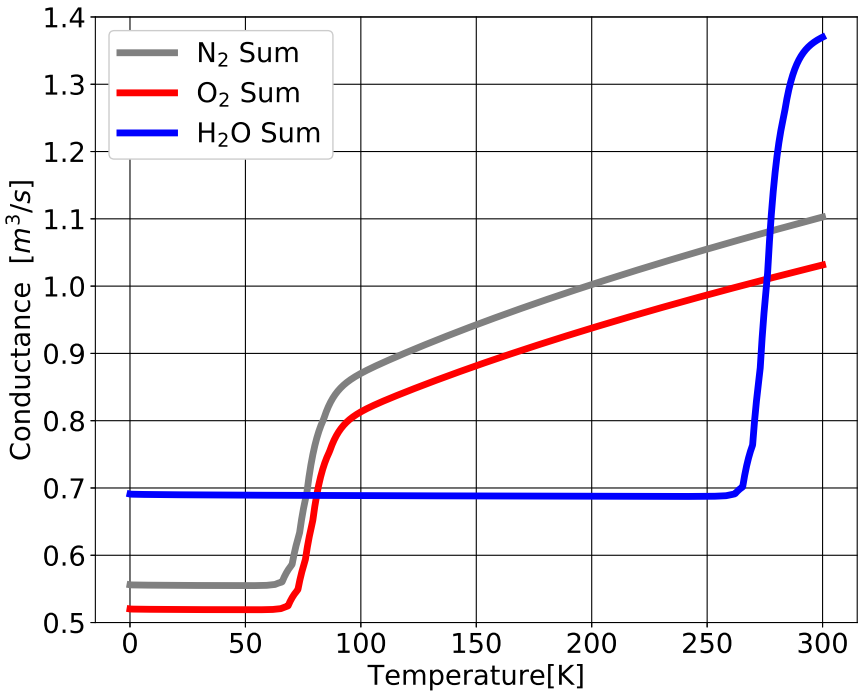

Figure 3.10: Simulated conductance of the duct shield. Gray, red and blue lines are the conductance of the duct shield for N_2, O_2 and H_2O molecules. At the cryogenic limit, these conductance are independent from the temperature of the duct shield because the conductance is affected only by the molecules that transmit the duct shield without any reflection at the cryogenic surface.

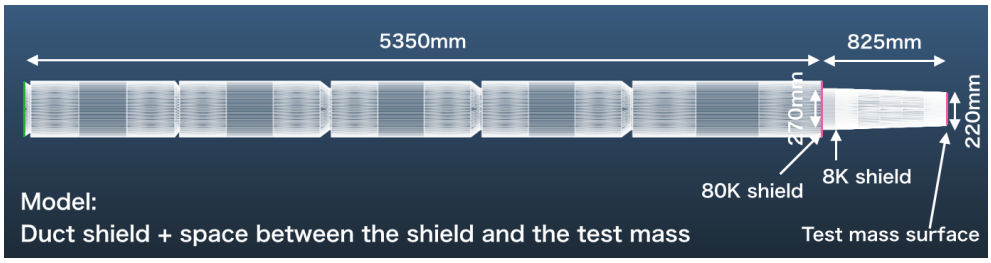

Figure 3.11: Model for the conductance simulation of the space between the duct shield and the test mass. The particles are injected from the facet shown with the green color, and the number of particles that reach to the pink lines are counted. The ratio between the number of particles that reach pink lines gives the hitting probability of the space.

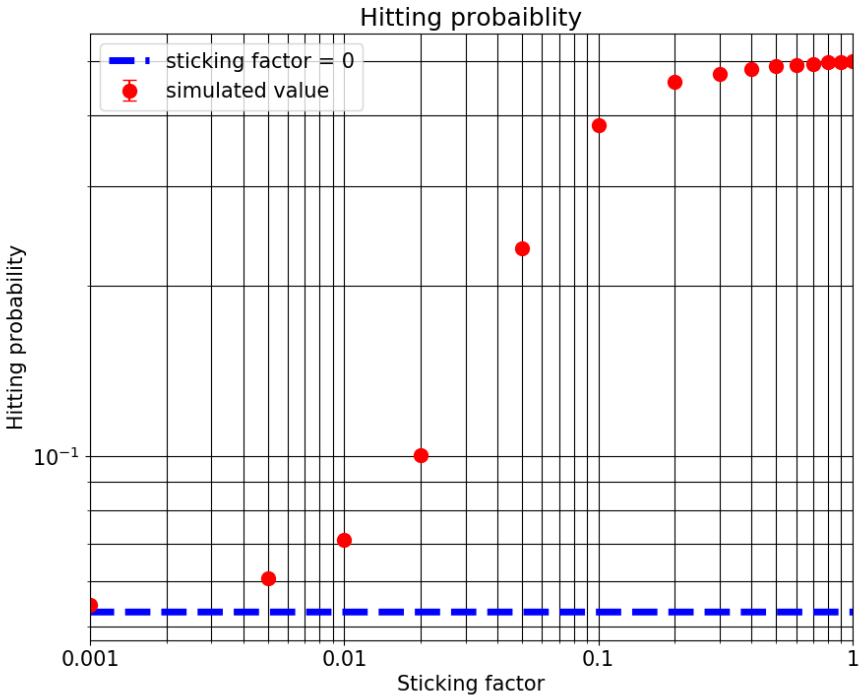

Figure 3.12: Simulated result of the hitting probability. Using the model as shown in the Fig.(3.11), the ratio between the number of the particles that reach to the 80 K radiation shield and that hit the mirror surface is calculated. When the sticking probability is around 1, the spatial and the incident angle distribution are already narrow enough to reach the mirror surface and the hitting probability is large, about 0.5. On the other hand, the spatial and angle distribution are the random, and many numbers of molecules do not reach the mirror surface though many molecules reach the 80K radiation shield, and the hitting probability is about 0.05.

3.6 Molecular flux

Using the simulated values, the molecular flux to the cryogenic mirror is calculated. Here we consider the molecular flux from the 17 m away from the cryostat. In this case, the conductance of the system C_{sys} is given by the composition of the conductance of the 12 m beam duct $C_{12\mathrm{m}}$ as

$$C_{\mathrm{sys}} = \frac{1}{\frac{1}{C_{12\mathrm{m}}} + \frac{1}{C_{\mathrm{ds}}}} = \begin{cases} 0.6446 \pm 0.0072 & (\mathrm{H_2O}), \\ 0.7559 \pm 0.0012 & (\mathrm{N_2}) \\ 0.7632 \pm 0.0012 & (\mathrm{O_2}). \end{cases} \mathrm{m^3/s}, \tag{3.23}$$

Here we assume that the partial vacuum pressure of H_2O, N_2 and O_2 at 17 m away from the cryostat are the same as $P_{17\mathrm{m}} = 1 \times 10^{-7}$ Pa. The multiplication of $P_{17\mathrm{m}}$, C_{sys} and the hitting probability K_{spa} of the space between the 80K radiation shield and the mirror surface gives the molecular flux Q_{flux} to the cryogenic mirror as

$$Q_{\mathrm{flux}} = C_{\mathrm{sys}} K_{\mathrm{spa}} P_{17\mathrm{m}} = \begin{cases} 3.22 \times 10^{-8} \pm 3.6 \times 10^{-10} & (\mathrm{H_2O}), \\ 4.01 \times 10^{-9} \pm 1.3 \times 10^{-10} & (\mathrm{N_2}) \\ 4.04 \times 10^{-8} \pm 1.3 \times 10^{-10} & (\mathrm{O_2}). \end{cases} \mathrm{Pa\,m^3/s} \tag{3.24}$$

Note that, the sticking probability of 1 is assumed for H_2O molecules, and that of 0 is assumed for N_2 and O_2 molecules.

3.7 Molecular layer formation speed

Molecular flux is the number of incident molecules to the cryogenic mirror in unit time. The factor $\frac{m}{S\rho k_{\mathrm{B}} T}$, where S is the area of the cryogenic surface, changes the molecular flux to the molecular layer formation rate [79]. Hence, the molecular layer formation speed η on the KAGRA cryogenic test mass is calculated as

$$\eta = \frac{m}{S\rho k_{\mathrm{B}} T} C_{\mathrm{sys}} P_{17\mathrm{m}} = \begin{cases} 0.562 \pm 0.0063 & (\mathrm{H_2O}), \\ 0.299 \pm 0.0097 & (\mathrm{N_2}), \\ 0.233 \pm 0.0075 & (\mathrm{O_2}). \end{cases} \mathrm{nm/day} \tag{3.25}$$

Note that the parameters in the table (3.3) were used.

The result implies that after the 1 year of the operation, the thickness of the molecular layer growth to the order of 100 nm, even if KAGRA vacuum

system get the final configuration. In the current situation, the configuration of the KAGRA vacuum system is not the finalized and the number of pumps is limited, the nominal vacuum pressure is the order of 10^{-6} Pa. In this situation, the molecular layer can be thicker than the calculation above.

Before the actual cooling of the test masses, it was needed to show the molecular layer formation on the cryogenic mirrors and characterize it experimentally. In the next chapter, the experiment that was done to characterize the molecular layer formation in KAGRA is introduced.

Molecule	H_2O	N_2	O_2	Unit
Density	940 [80]	1026 [81]	1520 [82]	kg/m^3
Mass	2.99×10^{-26}	4.65×10^{-26}	5.32×10^{-26}	kg
Temperature	300	100	100	K

Table 3.3: Parameters to calculate the speed of the molecular layer formation.

Chapter 4
CHARACTERIZATION OF THE MOLECULAR LAYER FORMATION IN KAGRA

It is important to experimentally prove the fact that molecular layer grows up on a cooled mirror in a cryogenic GWD. To measure the molecular layer growth, the small optical cavity was put inside the KAGRA cryostat, and its finesse was monitored. This section introduces the principle, setup, result and the discussion of the experimental evaluation of the molecular layer formation.

4.1 Principle of molecular layer formation measurement

4.1.1 Reflectivity of a cryogenic mirror with a molecular layer

The optical property of the coating is determined by the Fresnel coefficient. The Fresnel coefficient ρ between two materials that have the refractive index of n_1 and n_2 is given as

$$\rho = \frac{n_1 - n_2}{n_1 + n_2}. \tag{4.1}$$

Regarding the two boundaries as one composite boundary, the total Fresnel coefficient ρ_{tot} is written as

$$\rho_{\mathrm{tot}} = \frac{\rho_1 + \rho_2 \mathrm{e}^{-2\mathrm{i}\delta}}{1 + \rho_1 \rho_2 \mathrm{e}^{-2\mathrm{i}\delta}}, \tag{4.2}$$

where ρ_1 and ρ_2 are the Fresnel coefficient of two boundaries, and δ is the optical phase shift that between two boundaries. The power reflectivity of

the boundary R_0 is given by the Fresnel coefficient as $R_0 = |\rho|^2$.

From the discussion above, once the power reflectivity of the mirror R_0 which is measured in vacuum is given, the Fresnel coefficient between vacuum and the coating $\rho_{\rm vc}$ is calculated as $\rho_0 = -\sqrt{R_0}$. If the mirror put in the medium, the power reflectivity of the mirror R differs from that R_0 measured in vacuum or air as shown in Fig.(4.1).

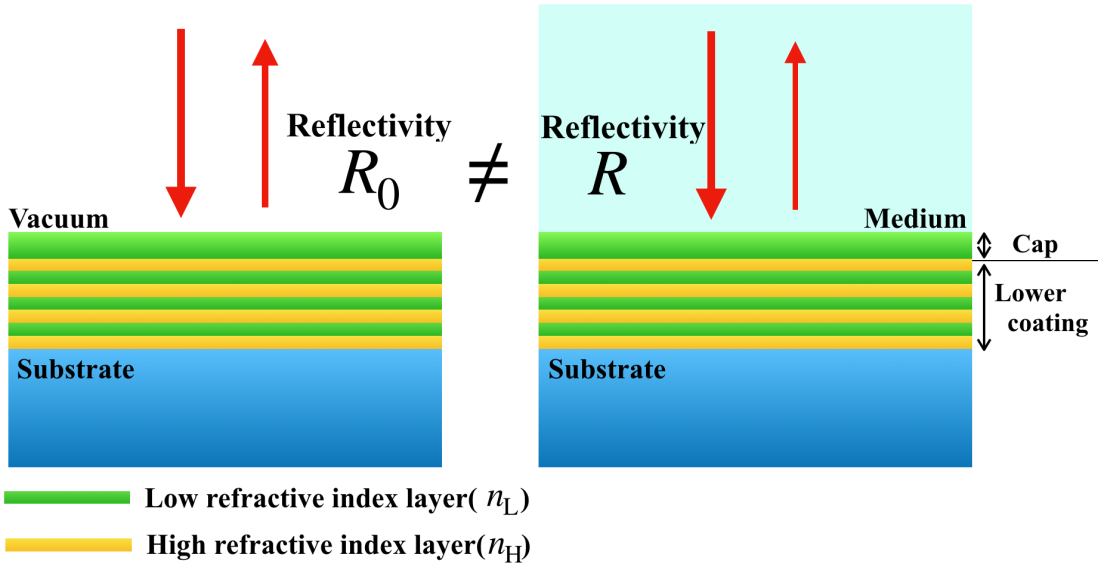

Figure 4.1: Fresnel coefficient and the power reflectivity of the coating. In the GW field, the dielectric multilayer coating is applied on the substrate to archive the high and low reflectivity. The Fresnel coefficient of the coating ρ is given by the power reflectivity of the coating R_0 as $\rho = -\sqrt{R_0}$. If the coating is covered by the medium whose refractive index is not the same as the vacuum, the power reflectivity R of the coating differs from the reflectivity R_0 which is measured without any medium on the top.

As explained in Chapter 2, the coating of the mirror in a GWD is the dielectric multilayer coating which stacks high and low refractive materials alternatively on the substrate controlling the thickness of each layer to achieve high or low reflectivity. To protect the coating, the low refractive index layer is stacked on the low refractive index layer at the top, and this part is called the cap as shown in Fig.(4.1). Hence, the Fresnel coefficient between the vacuum and the coating ρ_0 is the result of the composition of the Fresnel coefficients between the vacuum and the cap $\rho_{\rm vc}$ and that between the cap

and the lower coating layers ρ_1,

$$\rho_0 = \frac{\rho_{\rm vc} + \rho_1 {\rm e}^{-2{\rm i}\delta_{\rm cap}}}{1 + \rho_{\rm vc}\rho_1 {\rm e}^{-2{\rm i}\delta_{\rm cap}}} = \frac{\rho_{\rm vc} + \rho_1}{1 + \rho_{\rm vc}\rho_1}. \tag{4.3}$$

So the Fresnel coefficient between the cap and the lower coating layers is given as

$$\rho_1 = \frac{\rho_0 - \rho_{\rm vc}}{1 - \rho_{\rm vc}\rho_0}. \tag{4.4}$$

Now we consider the mirror with a molecular layer on the top of the coating. Composition of the Fresnel coefficient between the cap and the lower coating ρ_1 and that between a molecular layer and the cap $\rho_{\rm mol} = \frac{N_{\rm mol} - n_{\rm cap}}{N_{\rm mol} + n_{\rm cap}}$, where $N_{\rm mol}$ is the complex refractive index of the molecular layer, gives the Fresnel coefficient between the molecular layer and the coating ρ' as

$$\begin{aligned}
\rho' &= \frac{\rho_{\rm mol} + \rho_1 {\rm e}^{-2{\rm i}\delta_{\rm cap}}}{1 + \rho_{\rm mol}\rho_1 {\rm e}^{-2{\rm i}\delta_{\rm cap}}}, \\
&= \frac{\rho_{\rm mol}(1 - \rho_{\rm vc}\rho_0) + \rho_0 - \rho_{\rm vc}}{1 - \rho_{\rm vc}\rho_0 + \rho_{\rm mc}(\rho_0 - \rho_{\rm vc})}, \\
&= \frac{\rho_{\rm mol}(1 + \rho_{\rm vc}\sqrt{R_0}) - \sqrt{R_0} - \rho_{\rm vc}}{1 + \rho_{\rm vc}\sqrt{R_0} - \rho_{\rm mol}(\sqrt{R_0} + \rho_{\rm vc})}.
\end{aligned} \tag{4.5}$$

Finally, the composition of ρ' and the Fresnel coefficient between the vacuum and the molecular layer $\rho_{\rm vm} = \frac{n_0 - N_{\rm mol}}{n_0 + N_{\rm mol}}$ gives the total Fresnel coefficient of the coating ρ with the molecular layer as

$$\begin{aligned}
\rho &= \frac{\rho_{\rm vm} + \rho' {\rm e}^{-2{\rm i}\delta_{\rm mol}}}{1 + \rho_{\rm vm}\rho' {\rm e}^{-2{\rm i}\delta_{\rm mol}}}, \\
&= \frac{\rho_{\rm vm}\left(1 + \rho_{\rm vc}\sqrt{R_0} - \rho_{\rm mol}(\sqrt{R_0} + \rho_{\rm vc})\right) + \left(\rho_{\rm mol}(1 + \rho_{\rm vc}\sqrt{R_0}) - \sqrt{R_0} - \rho_{\rm vc}\right){\rm e}^{-2{\rm i}\delta_{\rm mol}}}{\left(1 + \rho_{\rm vc}\sqrt{R_0} - \rho_{\rm mol}(\sqrt{R_0} + \rho_{\rm vc})\right) + \rho_{\rm vm}\left(\rho_{\rm mol}(1 + \rho_{\rm vc}\sqrt{R_0}) - \sqrt{R_0} - \rho_{\rm vc}\right){\rm e}^{-2{\rm i}\delta_{\rm mol}}},
\end{aligned} \tag{4.6}$$

where $\delta_{\rm mol}$ is the optical phase shift inside the molecular layer. Figure(4.2) shows the power reflectivity of the mirror $R(d_{\rm mol}) = |\rho|^2$ as the function of the thickness of the molecular layer for the various original power reflectivity R_0.

As shown in Fig.(4.2), the reflectivity of the mirror periodically changes with the growth of the molecular layer. Furthermore, the amplitude of the reflectivity oscillation depends on the original reflectivity of the mirror R_0. This phenomena briefly shows the fact that the reflectivity oscillation is the result of the interference of the light reflected by the coating and the molecular

layer. Hence, considering the 1st order of the reflected light, the relative amplitude of the reflectivity oscillation to the original coating becomes 100 % when the molecular layer and the coating reflect the same amount of light.

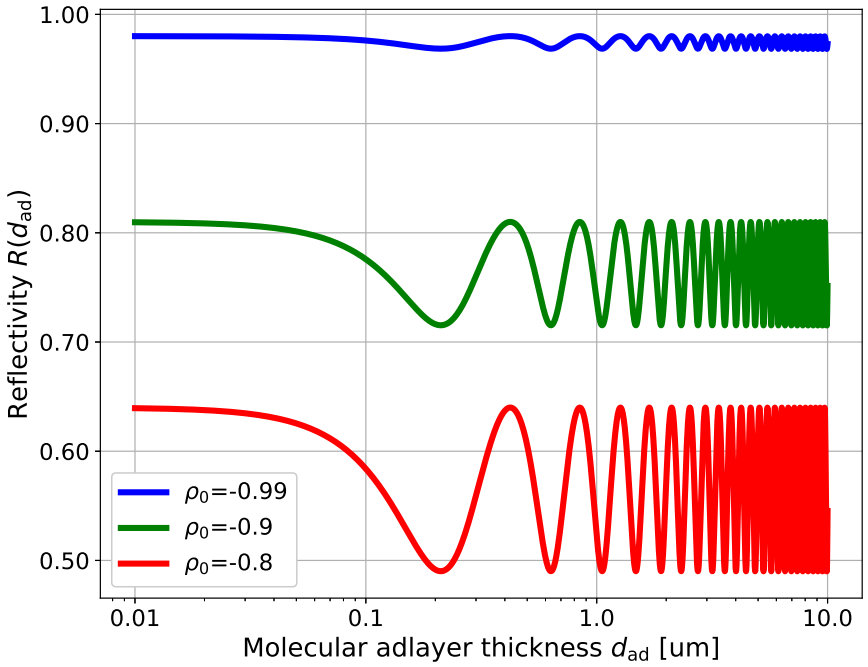

Figure 4.2: The power reflectivity of cryogenic mirror with a growing molecular layer on the top of the coating for various initial Fresnel coefficient ($\rho_0 = -0.8, 0.9$ and 0.99).

4.1.2 Optical absorption and scattering

The optical absorption and the scattering affect to the finesse of a FP cavity. Here we introduce the optical absorption and the scattering to evaluate the experimental result.

Optical absorption

When laser light passes through a molecular layer, it absorbs a part of laser. The laser power density inside a medium $I(z)$ follows the Lambert-Beer law

as

$$I(z) = I_{\mathrm{s}} \exp\left(-\alpha z\right), \tag{4.7}$$

where z implies the depth of a medium from its surface, I_{s} is the laser power density at $z = 0$ and α is the absorption coefficient which is re-written using a complex refractive index of medium N as $\alpha = 4\pi\frac{\mathrm{Im}(N)}{\lambda}$. The distribution of the Gaussian beam is described as

$$\begin{aligned} I_{\mathrm{s}}(r) &= I_0 \exp\left(-\frac{2r^2}{\omega_0^2}\right), & (4.8)\\ &= \left(\frac{2P_0}{\pi\omega_0^2}\right) \exp\left(-\frac{2r^2}{\omega_0^2}\right), & (4.9) \end{aligned}$$

where ω_0 is the radius of the Gaussian beam and P_0 is the laser power, respectively. Combining eq.(4.7) and eq.(4.8) gives the expression of the gaussian distributed laser power density inside the medium $I(r, z)$ as

$$I(r, z) = \left(\frac{2P_0}{\pi\omega_0^2}\right) \exp\left(-\frac{2r^2}{\omega_0^2} - \alpha z\right). \tag{4.10}$$

The laser power which is absorbed by the volume element $rdrd\theta dz$ of a medium $A(r, z)$ is

$$\begin{aligned} A(r, z) &= \left(I(r, z) - I(r, z + dz)\right) rdrd\theta, & (4.11)\\ &= -\frac{\partial I(r, z)}{\partial z} rdrd\theta dz, & (4.12)\\ &= \alpha \exp\left(-\frac{2r^2}{\omega_0^2} - \alpha z\right) rdrd\theta dz, & (4.13) \end{aligned}$$

and, the total laser power absorbed by a molecular layer of thickness d_{mol} is

$$A_{\mathrm{tot}} = -\int_0^{\infty} dr \int_0^{2\pi} d\theta \int_0^{d_{\mathrm{mol}}} r\frac{\partial I(r, z)}{\partial z} dz = P_0(1 - \exp(-\alpha d_{\mathrm{mol}})). \tag{4.14}$$

Under the assumption that the absorption coefficient is very low and the thickness of the molecular layer is very thin, the amount of the absorption is approximated as

$$A_{\mathrm{tot}} \sim P_0 \alpha d_{\mathrm{mol}}. \tag{4.15}$$

Scattering

The light scattering is caused by surface roughness. Here we consider the optical scattering at the surface which has the reflectivity R. The ratio between the amount of the total reflected light including the scattering light and the scattering light is called total integrated scattering (TIS), and it is defined as [83]

$$\mathrm{TIS} = \frac{P_{\mathrm{sca}}}{P_0 R + P_{\mathrm{sca}}} \sim \frac{P_{\mathrm{sca}}}{P_0 R} \tag{4.16}$$

where P_0 is the incident laser power and P_{sca} is the power of the scatted light. According to the reference [84], TIS is calculated for the laser light whose angle of incident (AoI) to the surface is $AoI = 0°$ as

$$\mathrm{TIS} = 1 - \exp\left[-\left(\frac{4\pi\sigma_{\mathrm{rel}}}{\lambda}\right)^2\right] \tag{4.17}$$

with

$$\sigma_{\mathrm{rel}}^2 = 2\pi \int_{f=0}^{1/\lambda} \mathrm{PSD}(f) f df, \tag{4.18}$$

where PSD is the surface power spectral density and f is the spatial density.

Now we assume the uniform molecular injection to a cryogenic mirror. Then the incident molecular flux to the unit area of the mirror surface follows the Poisson distribution. Hence, the standard deviation $\sigma_{<\mathrm{N}>}$ of the number of molecules in a certain area is given by $\sigma_{<\mathrm{N}>} = \sqrt{< N >}$, where N is the average of the number of molecules. The relation between the thickness t of the molecular layer and the number of molecules N is given as

$$t = N \left(\frac{M\rho}{N_{\mathrm{A}}}\right)^{1/3} \tag{4.19}$$

where ρ kg/m^3 is the density of the molecular layer, N_{A} is the Avogadro constant, and M kg/mol is the molar mass. From Eq.(4.19), the relation between the mean thickness $< t >$ of the molecular layer and its standard deviation $\sigma_{<t>}$ is written as

$$\sigma_{<t>} = \left(\frac{M\rho}{N_{\mathrm{A}}}\right)^{1/3} \sqrt{< N >} = \left(\frac{M\rho}{N_{\mathrm{A}}}\right)^{1/6} \sqrt{< t >}. \tag{4.20}$$

Using these relations, the thickness of the molecular layer at a certain area follows the normal distribution with $< t >$ and $\sigma_{<t>}$.

PSD which follows this distribution is calculated as [85]

$$\mathrm{PSD}(f) = \pi\sigma_{<t>}^2\xi^2 \exp\left(-(\pi f\xi)^2\right), \tag{4.21}$$

where ξ is the correlation length that characterizes the periodic length of the roughness along the surface. After all, the power P_{sca} of the scatter light is given as

$$P_{\mathrm{sca}} \sim P_0 R\left(1-\exp\left[-\left(\frac{4\pi\sigma_{\mathrm{rel}}}{\lambda}\right)^2\right]\right), \tag{4.22}$$

$$= P_0 R\left(1-\exp\left[-\frac{32\pi^4\sigma_{<t>}^2\xi^2}{\lambda^2}\int_{f=0}^{1/\lambda} e^{-(\pi f\xi)^2} f df\right]\right). \tag{4.23}$$

Figure (4.3) shows the ratio between the incident laser power and the power of the absorbed or the scattered light for the thickness of the molecular layer. In this figure, H_2O molecules, which have the complex refractive index of $N = 1.3-(1.0\times10^{-6})i$, are the component of the molecular layer. The calculation of the scattered light for three correlation lengths, $\xi = \sigma_{<t>}$, $\sigma_{<t>}/10$ and $\sigma_{<t>}/100$, are plotted. The amount of the scattered light is largely depending on the correlation length of ξ, and it's depending on the configuration of the system [86]. Considering the uniform molecular injection to the surface, ξ becomes short because it forms the tidy and smooth surface, and it is reasonable to neglect the optical loss due to the scattering below 1 μm of the molecular layer thickness if we assume the correlation length of $\xi = \sigma_{<t>}/10$.

4.1.3 Principle of the finesse measurement

The finesse shows the sharpness of the resonance, and it characterizes the optical cavity. Finesse $\mathcal{F}$ is the parameter which indicates the performance of an optical cavity. It is defined as Eq.(1.37) by the reflectivity of the mirrors, r_1 and r_2. The finesse of the FP cavity with a molecular layer on one of the mirrors that compose the cavity is written as

$$\mathcal{F}(d_{\mathrm{mol}}) = \frac{\pi\sqrt{r_1(d_{\mathrm{mol}})r_2}}{1-r_1(d_{\mathrm{mol}})r_2}. \tag{4.24}$$

There are several ways to measure the finesse of the optical cavity. Here, we introduce the response function of the optical cavity first. We denote the

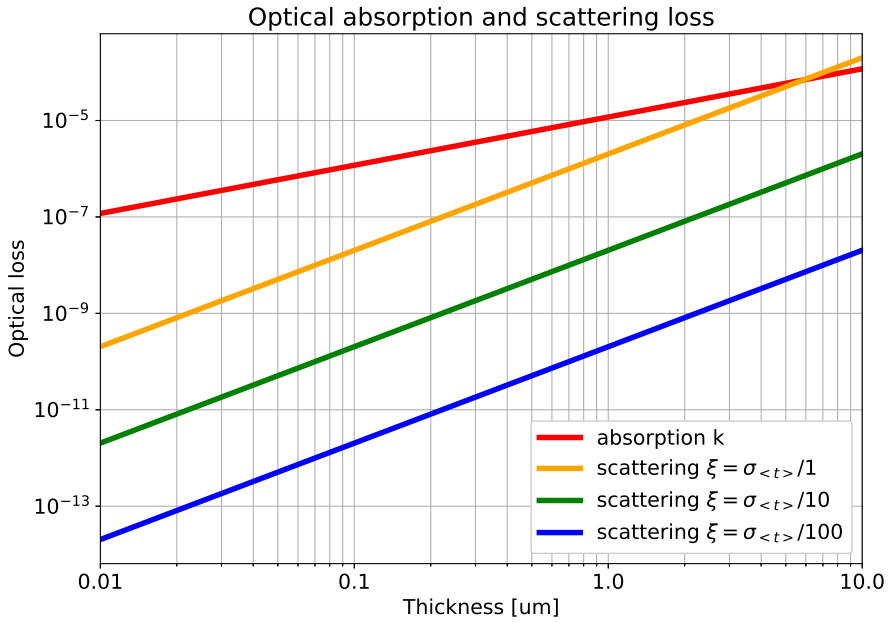

Figure 4.3: Comparison of the amount of optical absorption and scattering. The ration of the absorption and scattering to the incident laser power is calculated using the Eqs. (5.15) and (4.22). To calculate the absorption, H_2O layer is assumed (Imag(N) $= 1.0 \times 10^{-6}$). To calculate the scattering, the correlation length is assumed to be $\xi = \sigma_{<t>}$, $\sigma_{<t>}/10$ and $\sigma_{<t>}/100$. According to the result, it is reasonable to neglect the scattering when the thickness of the molecular layer is below 1μm.

input electric field as $E_{\rm i}$, then the transmitted electric field from a FP cavity $E_{\rm t}$ is written by Eq.(1.31) as

$$E_{\rm t} = \frac{t_1 t_2 e^{-i\frac{\Phi}{2}}}{1 - r_1 r_2 e^{-i\Phi}} E_{\rm in} = a\left(\Omega\right) E_{\rm in}, \tag{4.25}$$

with $a\left(\Omega\right) = \frac{t_1 t_2 e^{-i\frac{\Phi}{2}}}{1-r_1 r_2 e^{-i\Phi}}$ and $\Phi = 2L\Omega/c$, where L and Ω are the length of the cavity and the angular frequency of light.

The electric field of the intensity modulated light is described as

$$E_{\rm in} = E_0 \left[1 + \xi e^{{\rm i}\omega t} + \xi e^{-{\rm i}\omega t}\right] e^{-\Omega t}, \tag{4.26}$$

where ξ and ω are the modulation depth and the angular modulation frequency. The transmitted light of the FP cavity to the intensity modulated

light is

$$E_{\mathrm{t}} = E_0 \left[a\left(\Omega\right) + \xi a\left(\Omega+\omega\right) e^{\mathrm{i}\omega t} + \xi a\left(\Omega-\omega\right) e^{-\mathrm{i}\omega t} \right] e^{\mathrm{i}\Omega t}. \tag{4.27}$$

When the carrier light satisfies the resonant condition of the FP cavity, $\Phi = \frac{2L}{c}\Omega = 2\mathrm{m}\pi$, where m is an integer, and it is equivalent to set $\Phi = 0$ in the function $a(\Omega)$. Then, equation (4.28) is rewritten as

$$E_{\mathrm{t}} = E_0 \left[a\left(0\right) + \xi a\left(\omega\right) e^{\mathrm{i}\omega t} + \xi a\left(-\omega\right) e^{-\mathrm{i}\omega t} \right] e^{\mathrm{i}\Omega t}. \tag{4.28}$$

From now, we denote $a\left(\Omega\right)$ as a_Ω.

We focus on the components which have angular frequency of $\Omega+\omega$, then the transfer function H from the input electric field to the transmitted electric field is

$$H = \frac{E_{\mathrm{t}(\omega)}}{E_{\mathrm{in}(\omega)}} = a_\omega = \frac{t_1 t_2 e^{-\frac{L}{c}\omega}}{1 - r_1 r_2 e^{-i\frac{2L}{c}\omega}}, \tag{4.29}$$

and the gain of the transfer function is

$$|H| = \frac{a_0}{\sqrt{\left(1-r_1 r_2\right)^2 + 4 r_1 r_2 \sin^2\left(\frac{L}{c}\omega\right)}} \sim \frac{a_0}{\sqrt{1+\left(\tau_{\mathrm{fp}}\omega\right)^2}} \tag{4.30}$$

with

$$\tau_{\mathrm{fp}} = \frac{2L\mathcal{F}}{\pi c}, \tag{4.31}$$

where $\mathcal{F} = \frac{\pi\sqrt{r_1 r_2}}{1-r_1 r_2}$. Equation (4.30) shows that the FP cavity works as the 1st order low pass filter with the time constant of τ_{fp} to the intensity fluctuation.

Equation (4.30) gives the step response of the FP cavity as

$$\mathcal{L}^{-1}\left[\frac{1}{s}\frac{a_0}{1+\tau_{\mathrm{fp}}s}\right] = a_0(1-e^{-\tau_{\mathrm{fp}}t}). \tag{4.32}$$

Next, we consider the transient response of the transmitted laser power to the modulated input laser. We write the input electric field modulated like a step function as

$$E_{\mathrm{i}}(t) = \begin{cases} |E_{\mathrm{i}}|e^{i\Omega t} & t<0, \\ |E_{\mathrm{i}}-\xi|e^{i\Omega t} & 0\le t. \end{cases} \tag{4.33}$$

The transmitted light is described by Eq.(4.32) as

$$E_{\mathrm{t}}(t) = \begin{cases} a_0 E_{\mathrm{i}} e^{i\Omega t} & t<0, \\ a_0\left[E_{\mathrm{i}} - \left(1-e^{-t/\tau_{\mathrm{fp}}}\right)\xi\right] & 0\le t, \end{cases} \tag{4.34}$$

and detectable transmitted laser power at $t \geq 0$ is

$$P_{\mathrm{t}}(t) \sim \begin{cases} a_0^2 \left|E_{\mathrm{i}}\right|^2 & (\xi = 0), \\ a_0^2 \left[\left|E_{\mathrm{i}}\right| - 2E_{\mathrm{i}}\xi \left(1 - e^{-t/\tau_{\mathrm{fp}}}\right)\right] & (\xi \ll E_{\mathrm{i}}), \\ a_0^2 \left|E_{\mathrm{i}}\right|^2 e^{-2t/\tau_{\mathrm{fp}}} & (\xi \sim E_{\mathrm{i}}). \end{cases} \tag{4.35}$$

Equation (4.35) says that the time constant of the transmitted light is the function of the modulation depth ξ. When the modulation depth is enough smaller than the amplitude of the input laser electric field, the transient response of the FP cavity has the time constant τ_{fp}. On the other hand when the modulation depth is comparable with the amplitude of the input laser electric field, the measurable time constant is $\tau_{\mathrm{fp}}/2$. Figure (4.4) shows the transient response of the FP cavity for two cases, $\frac{\xi}{E_{\mathrm{i}}}$ =0.05 and 1. As discussed above, the time constant of the FP cavity changes depending on the modulation depth ξ.

Finally, we note the advantage of the finesse measurement. To measure and characterize the molecular layer formation, the measurement of the reflectivity of the cryogenic mirror is more simple. Though, the measurement of the reflectivity is much difficult to analyze if there is another cryogenic part that the laser light passes through or reflects. The molecular layer is possible formed on the other cryogenic optics and it contaminates the signal that we want to measure. Hence, in principle, we need to know the thickness of the molecular layer on all of the cryogenic optics if we try to characterize the molecular layer through the reflectivity measurement. On the other hand, the measurement of the finesse is the measurement of the time constant which is not affected by the transmissivity and reflectivity change of other cryogenic optics. In other word, the measurement of the finesse is less susceptible to the systematic error, and the components of the systematic errors are only the time constant of the laser shutter system and the photo detector. By choosing the products, it is possible to lower these systematic errors not to contaminate the measurement. This is the largest advantage of the finesse measurement.

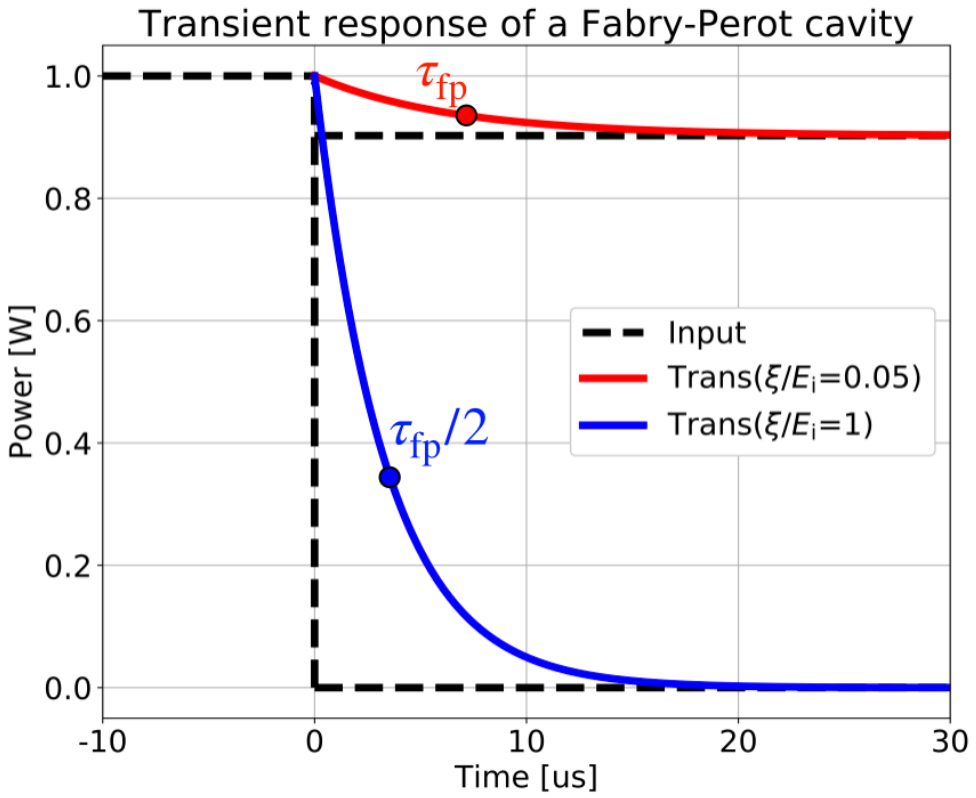

Figure 4.4: Transient response of a Fabry-Perot cavity for the modulation depth of $\frac{\xi}{E_i} = 0.05$(red curve) and 1(blue curve). Black dashed line shows the input laser power, and two points on the transient response curve correspond to the time constant of each curve. Parameters are as follows: $\mathcal{F} \sim 3000$, $L = 1$ m, and $\tau_{fp} \sim 6.7\mu$sec.

4.2 Experimental setup and equipment

4.2.1 Location

To evaluate the molecular layer formation on a cooled mirror, the KAGRA cryostat for the input test mass (IYC), and the vacuum system around the IYC were used. Figure (4.5) shows the position of the IYC in KAGRA and the appearance of the surroundings. The IYC is the cryostat for one of the KAGRA input test mass, and the cryogenic system is the same as the other cryostats as explained in Chapter 2. Because the IYC is good access so the experiment can be smoothly set up. Further, because the cryostat for another

input test mass (IXC) was occupied for the experiment with the KAGRA main laser, the IYC was used for this experiment.

The purpose of this experiment is to confirm and characterize the molecular layer formation on a cooled mirror in KAGRA using the experimental data and the simulations. For this purpose, the small FP cavity was set inside the ITMY cryostat to have a solid angle against the beam duct between the cryostat and the BS. The optics to inject the laser to the cavity and to monitor the transmitted light from the cavity were set across the duct shield as shown in Fig.(4.5). These optics are detailed in the following subsection.

Including the cryostat and the optics, all of the systems are inside the cleanroom composed of the KOACH filters as shown in Fig.(4.5). The KOACH filters are composed of the HEPA filter and the ULPA filter, and it can make the air that satisfies the ISO standard class 1. The KOACH filter introduces the vibration to the optics and disturbs the measurement, they were turned off during the measurement.

Initially, the period for the experiment was planned for about 2.5 months, 2 weeks for the construction of the setup, and 1.5 months for the measurement at cryogenic temperature. However, due to the trouble in the vacuum and the cryogenic systems, the measurement was shortened to about 1 month.

4.2.2 Optics overview

Here we introduce the overview of the optics for this experiment. Figure 4.6 shows the experimental setup of the finesse measurement of the FP cavity.

The input optics was designed to match the laser spatial mode to the cavity eigenmode, to control the FP cavity and to shut the incident laser off quickly to measure the transient response of the FP cavity. The laser profile was shaped using the lenses, and it was guided to the FP cavity inside the cryostat. To keep the FP cavity at resonant state before shutting the laser power off, the Pound-Drever-Hall (PDH) method was utilized [87], and the error signal was fed back to the laser frequency tuning PZT. To shut down the input laser power quickly and completely, an acoust optic modulator (AOM) was set and the first-order laser beam was injected to the FP cavity. The time constant (τ_{fp}) of the FP cavity was measured by monitoring the transmitted light, which includes the transient response of the FP cavity, with a high-speed photodetector. It was confirmed that the shutter speed of the AOM and the response of the photodetector were faster than the expected time

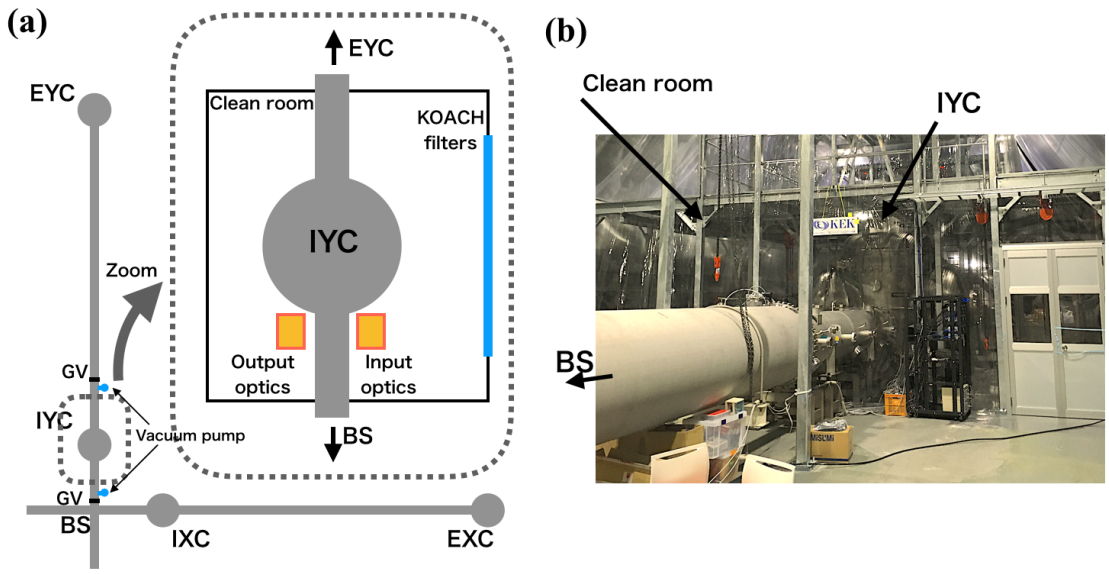

Figure 4.5: The conceptual image of the experimental location. (a)The experiment was done using the KAGRA IYC. The cryostat and surroundings are in the clean booth which is composed of the KOACH filters. The input and output optics were located at the BS side of the cryostat on the opposite side across the duct. (b)The picture of the IYC and its clean booth. The entrance of the clean booth is the opposite side. and the door in the picture was not used to enter the booth.

constant of the FP cavity. The FP cavity was installed inside the cryostat, on the 8K radiation shield. The optical axis of the FP cavity is 30° tilted against the beam axis of KAGRA. To adjust the height of the FP cavity mirrors to that of the KAGRA sapphire mirrors, the FP cavity was set on a stainless-steel table, and connected to the bottom of the inner radiation shield of the cryostat by pure aluminum heat links to maintain sufficient thermal conductivity. The output optics was set to monitor the transmitted light of the FP cavity and monitor the transient response.

Following subsections detailed the optics.

4.2.3 FP cavity

The FP cavity which was installed inside the cryostat is the sensor to measure the molecular layer formation on one of the mirrors. Figure (4.7) shows

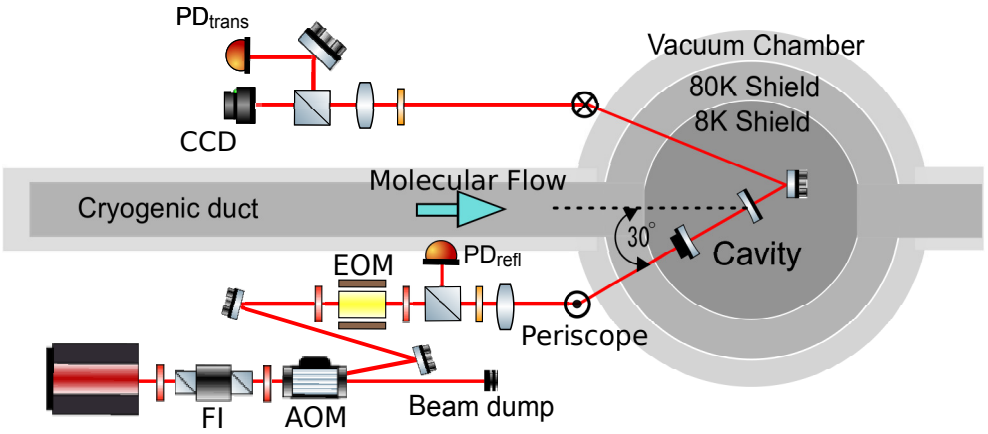

Figure 4.6: Optics overview. Input optics were constructed to control the laser frequency to maintain the resonance of the FP cavity and to shut down the injected laser beam rapidly by the AOM. The injection angle of the laser to the FP cavity is 30° tilted from the beam axis of KAGRA. FI: Faraday isolator, AOM: acoust optic modulator, EOM: electro optic modulator, PD_{refl}: photodetector to detect the reflected light from the FP cavity, PD_{trans}: photodetector to detect the transmitted light from the FP cavity.

the design of the FP cavity. Two mirrors are mechanically attached to the metal spacer to fix the length of the cavity using the caps. The spacer and the caps are made of stainless steel 304. Between the cap and the mirror, by pinching the indium foil 0.5 mm in thickness, the contact area for the thermal conduction cooling was ensured. On the other hand, the indium foil was not put between the mirror and the spacer, because it possibly causes the misalignment during the cooling due to the thermal shrink. The thermometer DL-670 manufactured by Lake Shore Cryogenic Inc. was attached on the cap of the end mirror to monitor the temperature of the mirror. The length of the spacer, which is the same as the length of the cavity, is 170mm, and the cross section is 31 mm $\times$ 45mm. Along the longitudinal axis, there is the through hole, 20mm in diameter, for the light to round trip. The feature of this spacer is the large window, 70 mm $\times$ 25 mm in cross section, for the molecules coming from the beam duct to reach one of the mirrors. The other side of the mirror doesn't have the solid angle to the beam duct and the room temperature region, and under the assumption that there is no desorption from the cryogenic surface, the molecular layer is formed only on the mirror near the window.

Table 4.1: Mechanical dimension and spec of the mirrors

Material	Fused silica	
Diameter	25.4	mm
Thickness	8.0	mm
Radius of curvature (Input/End)	Flat/1.0	m
Coating material	SiO_2/Ta_2O_5	
Power transmittance (Input/End)	20 / 16 [88]	ppm

The attached mirrors are made of fused silica, 25.4mm in diameter and 8mm in thickness. The input mirror is the flat mirror, and the end mirror is the curved mirror with 1 m of the radius of curvature. Using the Eqs.(1.41), (1.43) and (1.44) with these parameters, the waist position of the eigenmode of the cavity is at the input mirror, and the beam radii are calculated as 0.357 mm at the input mirror and 0.392 mm at the end mirror.

Table (4.1) shows the mechanical and the optical spec of the input and end mirrors.

As shown in the Fig. (4.8), the optical cavity was set on the table to match the height of the cavity to the optical axis of the KAGRA arm cavity. The table is mainly made of stainless steel, and the plates made of aluminum are attached on both side of the table to fix firmly. The table was directly put on the 8 K radiation shield and the total height of the table is 400 mm. The angle between the cavity axis and the KAGRA arm cavity axis is 30 degrees, and the center of the end mirror is about the center of the anti-reflection coating of the ITMY mirror. On the table, one of the steering mirror is also fixed to lead the transmitted light from the cavity to the output optics. The mirror is the total reflection mirror for the angle of incident of 45 degree, and it is held using the vacuum compatible mirror holder VMHG-25.4 manufactured by SIGMAKOKI Co., LTD.. All of the screws and the springs are detached in consideration of misalignment during the cooling process. To cool the table and the cavity efficiently, four of the pure aluminum plates 0.5mm in thickness were attached along the poles of the table.

4.2.4 Input optics

The laser source is the nonplanar ring oscillator laser model 126L-1064-100 manufactured by IXL Lightwave. The wavelength is $\lambda_0 = 1064$ nm, and the

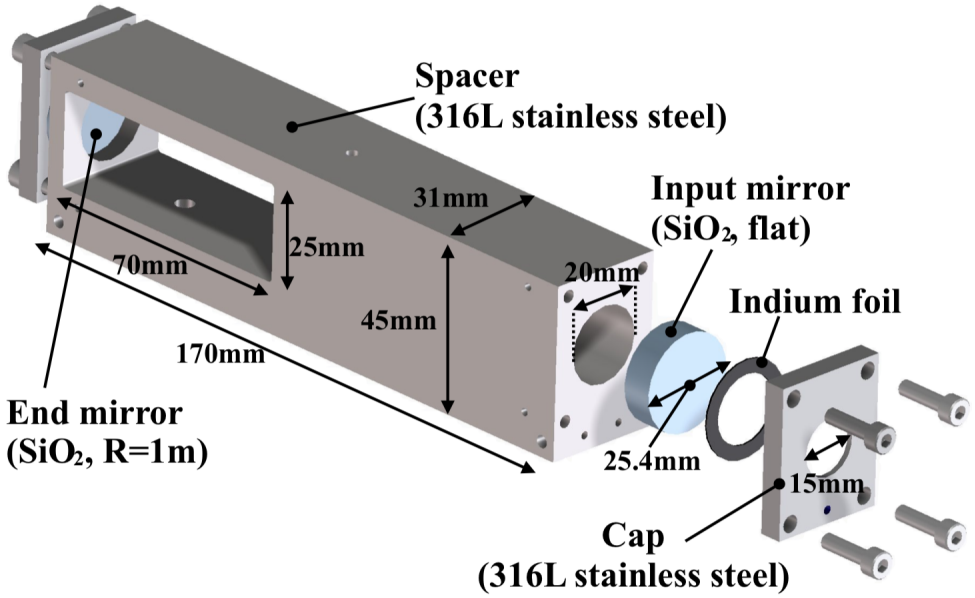

Figure 4.7: Design of the FP cavity. The spacer is made of 316L stainless steel and the cavity length is 170 mm. This spacer has a side window to expose the target cavity mirror to the room-temperature beam duct, from where molecules come. The other side of the mirror did not face the room-temperature area, and thus the molecular layer is formed only on the former mirror and the change of finesse is induced by the molecular layer on the target mirror. The temperature of the FP cavity was monitored by a thermometer that was attached near the target mirror.

output laser power is $P_0 = 100$ mW in the spec value, but the actual output was 50 mW due to the aging.

Figure (4.9) shows optical configuration of the input optics with its picture. The input optics was constructed on the optical table whose size is 800 mm $\times$ 450 mm. Using the optical table and the reflective mirrors, the length of the optical path from the exit of the laser source to the input mirror of the cavity was set to 3800 mm, 2425 mm from the exit of the laser to the periscope and 1375 mm from the periscope to the input mirror of the cavity. Hence, using 1750 mm of the optical path on the optical table, the laser is needed to shape to match the eigenmode of the cavity.

First, the profile of the laser was measured using the knife-edge type beam profiler model 135KP501 manufactured by MELLES griot. By moving and measuring the beam diameter every 25 mm, the beam profile was evaluated.

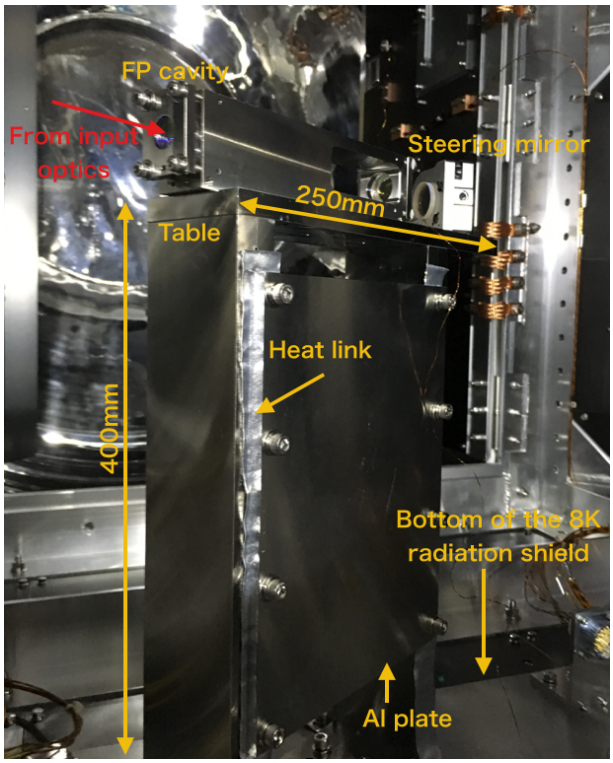

Figure 4.8: Picture of the FP cavity inside the cryostat. The FP cavity is on the table made of stainless steel. The height and the length of the table are 400mm and 250 mm, respectively.

Figure (4.10) is the result of this measurement. The distance z was counted from the exit of the laser. As a result, it was found that the laser has a radius of 143 μm at its waist position on average, and the waist position is 2.4 mm outside of the laser on average.

Using this result, the arrangement of the mode matching optics is needed to design to achieve the waist size of $\omega_0 = 0.357$ μm at the input mirror of the cavity $z = 3900$ mm. Using Jammt which is the software developed to simulate the propagation of the Gaussian beam, the set of the position z and the focal length f of the lenses were set to be $(z, f) = (170, 150), (1500, 200)$ and $(2100, 300)$ to match the mode more than 90%.

Using the result of the simulation and by tweaking the position of the lenses, the spatial mode of the laser was shaped to match the cavity eigenmode. Figure (4.11-a) shows the achieved spatial mode of the laser. The waist size was $\omega_0 = 414$ μm on average and the waist position was $z = 3906$

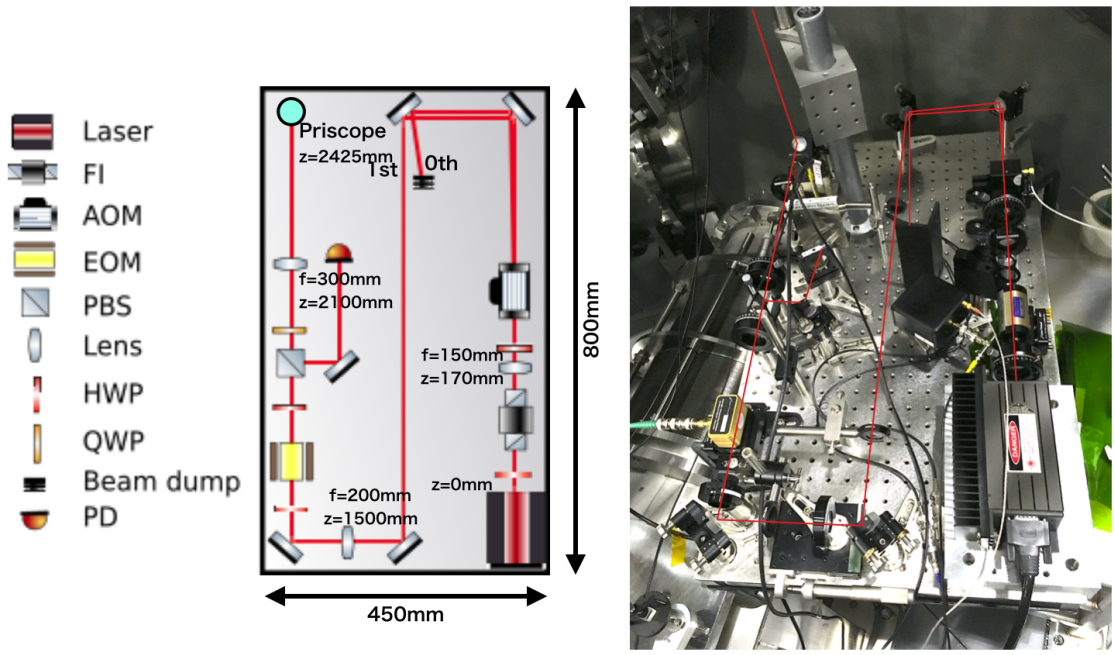

Figure 4.9: Optical path and components of the input optics. The input optics was made on the optical table whose size is 800 mm × 450 mm. AOM, EOM, lenses and PD are the main components of the input optics.

mm. To shorten the time to adjust the optics at the KAGRA site, the optics were once built in KEK, and the position of each component was marked on the optical table, and removed and transport all of the optics, and built following the mark at KAGRA site again. The shaped beam profile was measured at KAGRA site again and the waist size was $\omega_0 = 364$ μm on average and the waist position was $z = 3760$ mm as shown in Fig.(4.11-b). Because the size of the optical table was limited, only the beam radius far from the waist could be measured at the KAGRA site, and it is considered to give the gap of the evaluated beam profile between KEK and the KAGRA site. Figure (4.12) shows the comparison of the whole laser propagation measured at KEK and the KAGRA site. The optics that reconstructed at the KAGRA site reproduced the optics designed in KEK well.

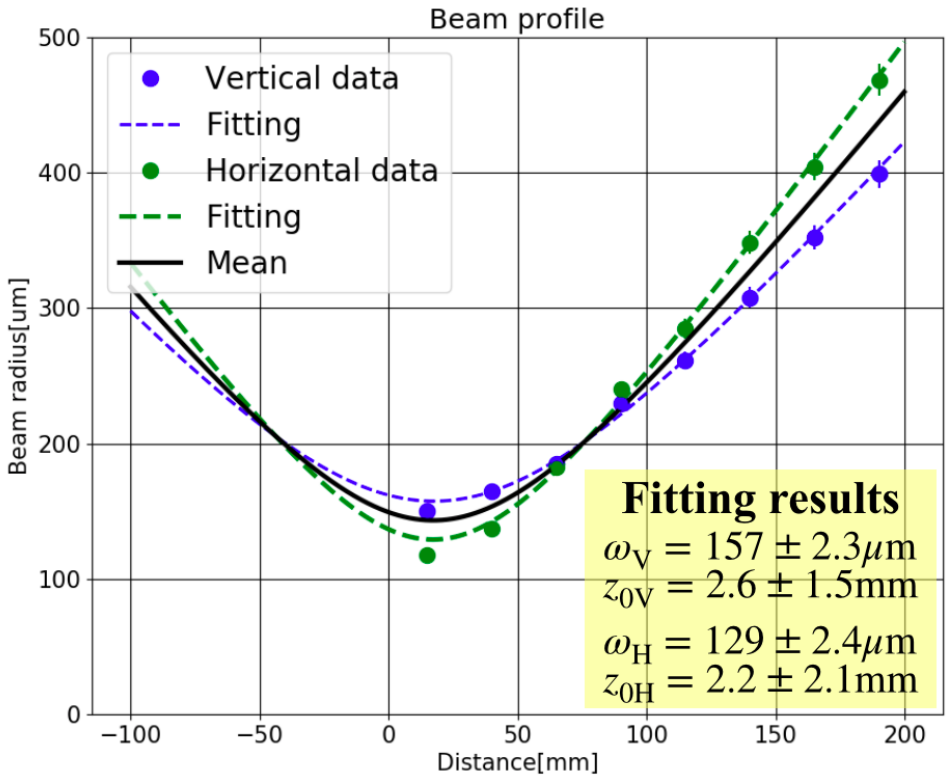

Figure 4.10: Beam profile of the laser source. The profile of the laser was evaluated by measuring the beam radius at some points. The beam radius along the vertical and the horizontal axes are measured. The origin of the distance $z = 0$ is the exit of the laser. The beam radius are $\omega_V = 157$ μm at the waist position $z_{0V} = 2.6$ mm for the vertical axis, and $\omega_H = 129$ μm at the waist position $z_{0H} = 2.2$ mm for the horizontal axis.

4.2.5 Acoust Optic Modulator and photo detector

Acoust optic modulator (AOM) is usually used to apply the intensity modulation to the input laser. An AOM is composed of a crystal and a transducer. The transducer changes the input signal to the acoustic wave inside the crystal, and the input laser is diffracted by these acoustic waves. By changing the amplitude of the input signal, the amplitude of the diffracted laser can be changed.

In this experiment, the AOM model manufactured by Brimrose Co. was used. The driving frequency is 80MHz and it is supplied from the AOM driver circuit. On the AOM driver circuit, there is the port to apply the

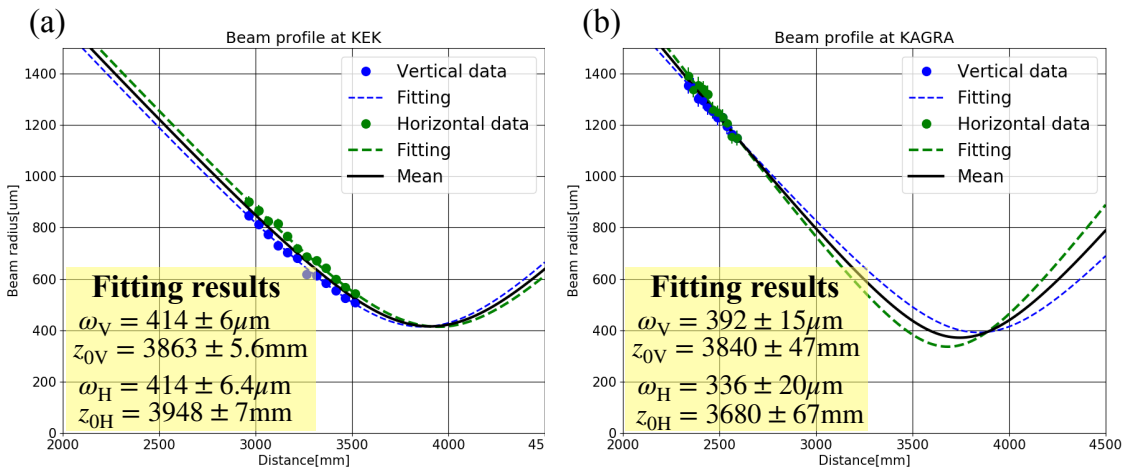

Figure 4.11: Beam profile at the FP cavity. The target beam radius is $\omega = 356$ μm at the waist position $z_0 = 3800$ mm. (a)Beam profile at the FP cavity measured in KEK. The beam radius are $\omega_V = 414$ μm at the waist position $z_{0V} = 3863$ mm for the vertical axis, and $\omega_H = 414$ μm at the waist position $z_{0H} = 3948$ mm for the horizontal axis.(b)Beam profile at the FP cavity measured at KAGRA site. The beam radius are $\omega_V = 392$ μm at the waist position $z_{0V} = 3840$ mm for the vertical axis, and $\omega_H = 336$ μm at the waist position $z_{0H} = 3680$ mm for the horizontal axis.

modulation signal to the driving signal. By applying the modulation signal to this port, the diffracted laser is modulated. When the DC offset is applied to the modulation port, the diffracted laser is continuously supplied to the downstream of the optics.

The AOM was used as the beam shutter to measure the transient response of the FP cavity. For this purpose, the diffracted laser was supplied to the downstream and the rectangle signal was applied to the modulation port of the AOM driver to shut the laser quickly. To measure the transient response of the FP, the photo detector model 1811 manufactured by New Focus Inc. was put at the output optics. The response width of the PD is 125 MHz in spec.

The total response of the AOM and the PD must be enough faster than the transient response of the FP cavity. As discussed above, the time constant of the FP cavity is expected to be $\tau_{FP} = 10$ μs. To check the total response of the AOM and the PD, the transient response of the AOM and the PD was evaluated using the setup shown in Fig.(4.13). The quarter wave plate

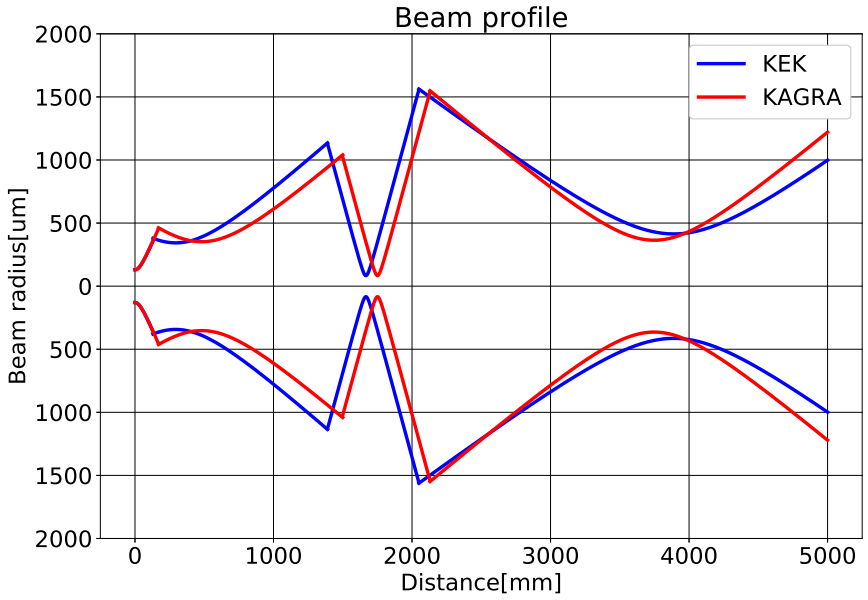

Figure 4.12: Comparison of the laser propagation measured at KEK and at the KAGRA site. Blue and red lines are the laser propagation measured at KEK and at the KAGRA site. The optics was reconstructed at KAGRA site following the marks on the optical table which were put at KEK after the tweaking of the optics.

($\lambda/4$ plate) changes the circular polarization to the linear polarization, and then, the half wave plate ($\lambda/2$) adjust the direction of the linear polarization to maximize the transmissivity of the faraday isolator (FI). The diffracted laser is directly inject to the PD and the rectangular signal is applied to the modulation port of the AOM driver. Then the transient response of the system was evaluated.

Figure (4.13) shows the measured total transient response of the AOM and the PD, and the signal was totally corrected 100 times. It looks that there are two transient response in the curve, so the curve was fitted by assuming the transient function $f(t)$

$$f(t) = a \exp\left(-\frac{t}{\tau_1}\right) + b \exp\left(-\frac{t}{\tau_2}\right) + c, \tag{4.36}$$

where a, b, c are the parameters, and τ_1 and τ_2 are the time constant of the curve. As the result of the fittings, the time constants are $\tau_1 = 0.016 \pm 8.5 \times$

10^{-5} μs and $\tau_2 = 0.027 \pm 0.0002$ μs as shown in the Fig.(4.15). Both time constants are much faster than the expected time constant of the FP cavity.

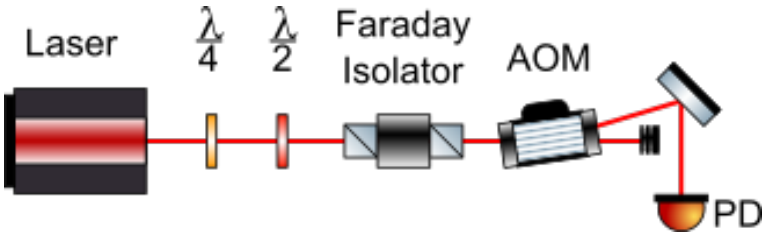

Figure 4.13: Experimental setup to measure the transient response of the AOM and the PD. The diffracted laser is directly inject to the PD and the rectangular signal is applied to the modulation port of the AOM driver. Then the transient response of the system was evaluated.

4.2.6 Vacuum and cryogenic system

As discussed above, the experiment was performed with the FP cavity which was put inside the cryostat for the ITMY. KAGRA vacuum system was separated for the experiment using the gate valves between the cryostat and the BS, and the cryostat and the arm duct as shown in Fig. (4.5), and the total length of the vacuum system is about 55 m. The dry pump model NeoDry36EU-020B manufactured by Kashiyama Industries, Ltd. and the molecular turbo pump model STP-iX3006 manufactured by Edwards were used to evacuate the system. Two units of these pumps are set at the middle of the beam duct as shown in Fig. (4.5). The vacuum pressure was monitored about 5 times per day during the pumping using the vacuum gauge which was set near the pump unit, and it was monitored 2 times per day after the enough pumping. When the vacuum pressure reached 7.9×10^{-4} Pa, the cryogenic system was turned on to cool the system down.

Figure (4.16) shows the vacuum pressure and the temperature change during the experiment. The vacuum pressure drastically changed just after each pump and the cryogenic system were turned on. When the temperature of the 80K radiation shield reached to about 250 K, the vacuum pressure stated to decrease, though the pressure didn't change when the 8K radiation shield reached to about 50 K. This implies that quite many H_2O molecules adsorbed on these surfaces and improve the vacuum pressure, though the

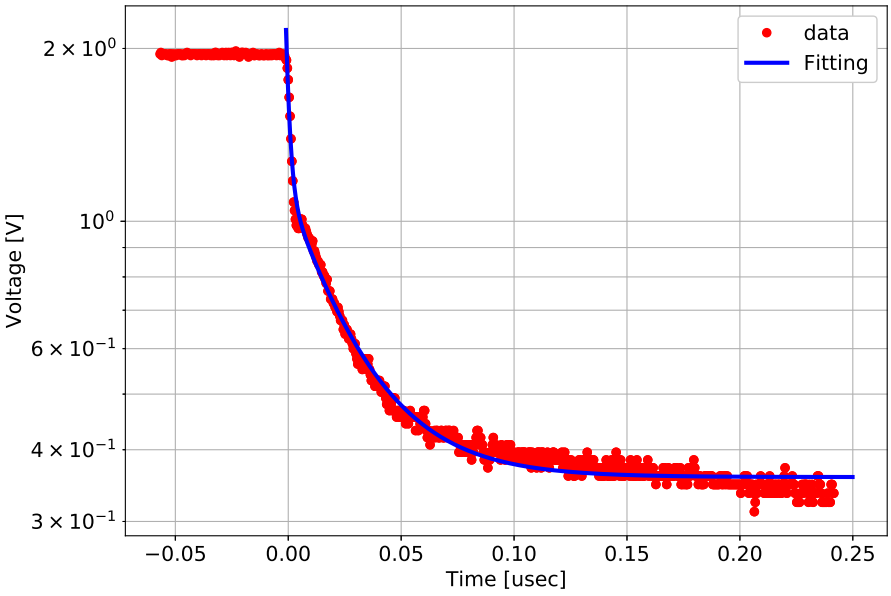

Figure 4.14: Transient response of the AOM and the PD. Red dots are the measured data and blue line shows the fitting. There are two transient response in the curve, so the function of Eq.(4.36) is assumed.

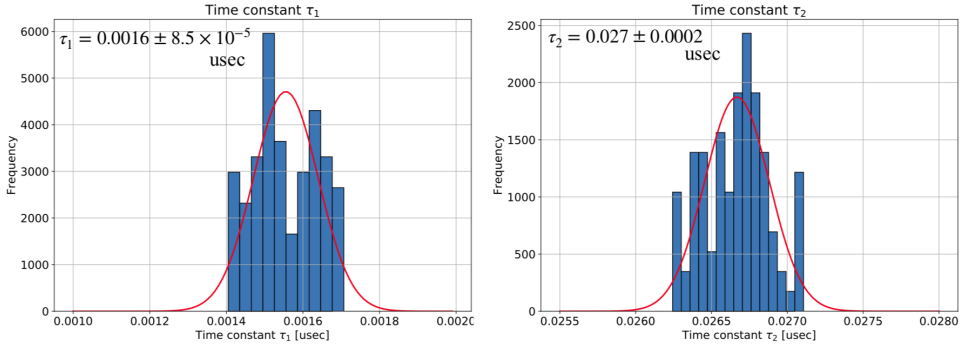

Figure 4.15: Result of the fitting of the transient response of the AOM and the PD. Red curve shows the fitting function. To fit the distribution, the gaussian distribution was assumed. The time constants of the transient response are $\tau_1 = 0.0016 \pm 8.5 \times 10^{-5}$ μs and $\tau_2 = 0.027 \pm 0.0002$ μs, respectively.

adsorption of N_2 and O_2 didn't change the pressure so much. Finally, the vacuum pressure reached to 6.0×10^{-6} at the measurement point.

After the cooling, the 80K and the 8K radiation shields were cooled to 92 and 23 K, respectively. Because of the trouble of the cooling system, the duct shield at the arm side was not cooled and it keeps at the room temperature during the experiment. The duct shield at the BS side and the FP cavity was cooled to 107 K and 47 K. The temperature of the system was relatively high because the one of the duct shield was not cooled and kept at the room temperature. This room temperature duct shield might induce large amount of the radiation to the system, and it caused the high temperature of the system.

The mass spectrometer model Qulee BGM-102 manufactured by ULVAC, Inc. was set at the duct shield at the arm side to confirm the kinds of the residual gasses. Figure (4.17) shows the typical output from the mass spectrometer. The peaks at $Q/M = 17$ and 18 indicate OH and H_2O. OH is created by the separation of H_2O at the electrode of the mass spectrometer. Hence, H_2O molecule is the main species of the residual gas inside the KAGRA vacuum chamber, and N_2 and O_2 molecule are following. The peak at $Q/M = 2$ corresponds to the H_2 molecules. though it doesn't show the partial pressure of H_2 molecules because it can generate from separation of the various molecules such as H_2O and hydrocarbon. Using the Fig.(4.17), the ratio γ of the partial pressure of H_2O, N_2 and O_2 are calculated as

$$\gamma = \begin{cases} \frac{I_{\mathrm{OH}}+I_{\mathrm{H_2O}}}{\Sigma I_{\mathrm{i}}} = 0.67 & (\mathrm{H_2O}), \\ \frac{I_{\mathrm{N_2}}}{\Sigma I_{\mathrm{i}}} = 0.17 & (\mathrm{N_2}), \\ \frac{I_{\mathrm{O_2}}}{\Sigma I_{\mathrm{i}}} = 0.05 & (\mathrm{O_2}), \end{cases} \tag{4.37}$$

where I_{i} is the output of the mass spectrometer for the molecular species of i. Note that to the H_2 was ignored to calculate the Eq.(4.37) because it is generated from many other molecules.

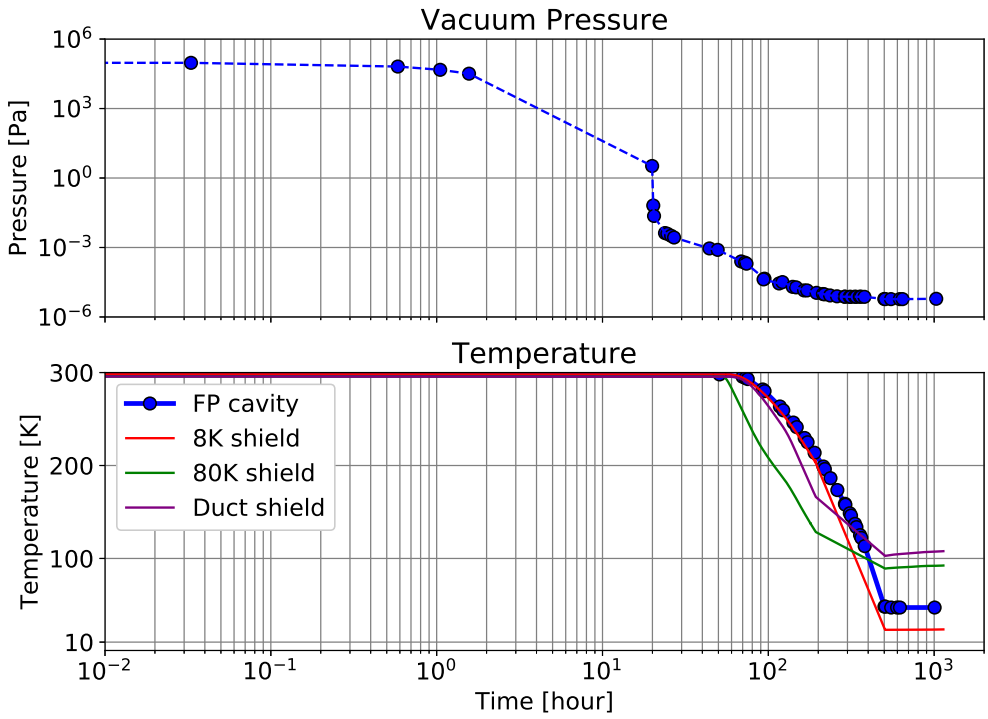

Figure 4.16: Vacuum pressure and temperature during the experiment. Upper: vacuum pressure measured at the middle of the beam duct. Lower: temperature of the radiation shields and the FP cavity. The time is measured from when the dry pump was turned on. The molecular turbo pump was turned on after 20 hours, and the cryogenic system was turned on after about 40 hours.

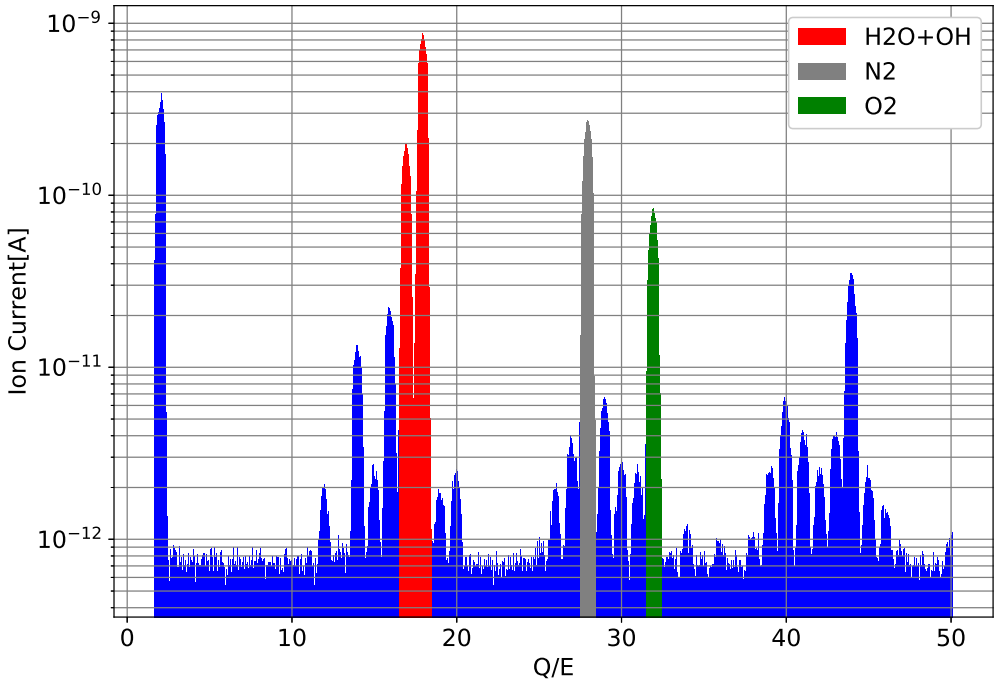

Figure 4.17: Typical component of the residual gasses inside the KAGRA vacuum chamber. Red, gray and green peaks correspond to $H_2O + OH$, N_2 and O_2 that are the main components of the residual gasses.

4.3 Analysis

4.3.1 Measurement and result

The ringdown signals of the FP cavity were corrected about 20 times per day for 35 days. The transient response of the FP cavity was triggered by the rectangular wave which was applied to the AOM to shut the injection laser to the cavity quickly, and the PD at the output optics measured the ringdown signal. Figure (4.18) shows a typical ringdown signal from the FP cavity. The blue dots and the red solid line show the measured data and the fitting curve, respectively. To fit the ringdown signal, the function

$$g(t) = a \exp\left(-\frac{t}{\tau}\right) + b, \tag{4.38}$$

is used, where a and b are the parameters, and 2τ is the time constant of the FP cavity.

Here we discuss the systematic error of the system. If the time constants of the AOM and the PD are taken into account, the fitting function $h(t)$ is written as

$$\begin{aligned} h(t) &= a \exp\left(-\frac{t}{\tau_1}\right) + b \exp\left(-\frac{t}{\tau_2}\right) + c \exp\left(-\frac{t}{\tau_3}\right) + d, & (4.39) \\ &\sim A \exp\left(-\frac{t}{\tau_1 + \tau_2 + \tau_3}\right) + B, & (4.40) \end{aligned}$$

where τ_1, τ_2 and τ_3 are the real time constant of the FP cavity, the AOM and the PD, and a, b, c, d, A, B are the constant. To estimate the maximum effect of these time constant, we choose the amplitude of these ringdowns as $a = b = c = 1$, and under the assumption, Eqs.(4.39) and (4.40) are numerically equal. Then the relation between the time constant τ in Eq.(4.38) and τ_1, τ_2 and τ_3 are given as

$$\tau_1 = \tau - \tau_2 - \tau_3. \tag{4.41}$$

Substituting $\tau = 8.2$ μs,$\tau_2 = 0.0016$ μs and $\tau_3 = 0.027$ μs into Eq.(4.41) gives the minimum value of the FP cavity as $\tau_1 = 8.17$ μs. Hence the systematic error of the system is evaluated to be -0.03 μs.

The finesse of the cavity was calculated according to the relation between the time constant and the finesse, Eq.(4.31), assuming $L = 17$ cm. Note that

we assumed that the cavity length doesn't change due to the cooling because the length of the cavity is considered not to change so much. The integrated linear thermal expansion is express as

$$\alpha = \frac{L(T) - L_{293}}{L_{293}}, \tag{4.42}$$

where $L(T)$ and L_{293} are the length of the structure at T K and 293 K. According to [89], the integrated thermal expansion of stainless steel 304 is $\alpha \sim 300 \times 10^{-5}$ at 50K, and it implies that the cavity length changes about 0.5 mm due to the cooling. So this effect changes the time constant only about 0.3 %, and it is considered not to affect to the calculation.

Figure (4.19) shows the evaluated finesse using the corrected time constant of the FP cavity. The red and the blue areas show the periods when the temperature of the FP cavity was 300 K and 47 K, respectively. The blue dots are the average of the finesse during a day and the error bars correspond to the statistical errors. To calculate the average finesse and the statistical error, 20 times of the ringdown signals were used. After the calculation, data points that are more than 10 % away from the mean value were regarded as outliers and excluded, and the average and the standard deviation were calculated again.

The order of statistic error is about ± 5 % for each point, and the systematic error is about -0.3 % for each. The averaged finesse was about 49000 when it is at the room temperature. Using the reflectivity of two mirrors, the FP cavity had the optical loss of about 100 ppm potentially.

During the cooling and the warming, it was difficult to control the FP cavity stably due to the thermal shrink of the spacer, so the ringdown couldn't be measured. The difference in finesse before and just after cooling is expected to be due to the initial huge amount of molecular adsorption or the FP cavity axis change induced by the thermal shrink of the rigid spacer.

4.3.2 Fitting and molecular layer formation speed

Here we analyze the evaluated finesse to characterize the molecular layer formation. For this analysis, the data in the blue area in Fig.(4.19) were used because the molecular layer formation happens only at the cryogenic temperature.

First, the function for the fitting is defined. As discussed above, the molecular layer is formed on only one of the mirrors that compose the FP

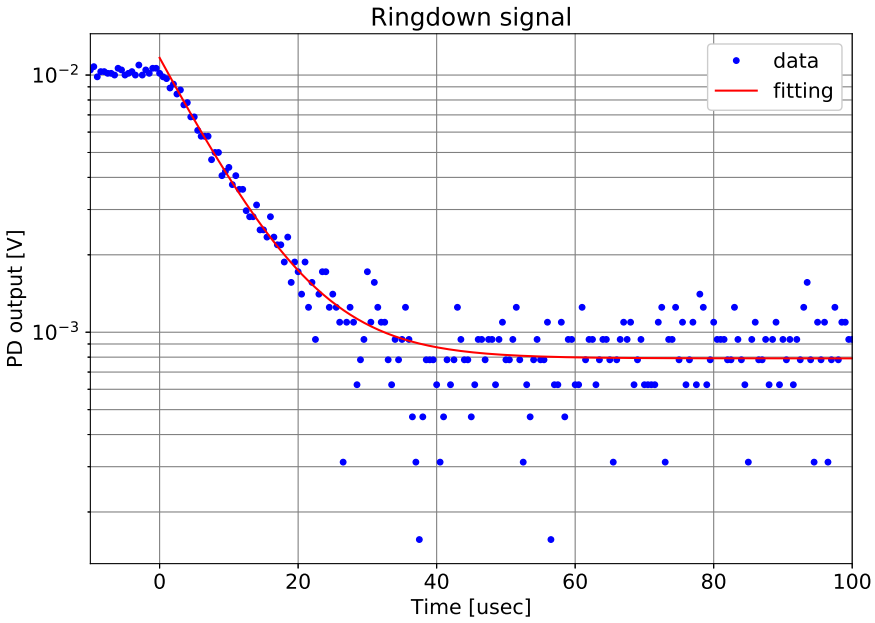

Figure 4.18: Example of the measured ringdown signal. The laser was turned off at 0 sec by the AOM, and then, the stored laser power inside the FP cavity started to decrease. The blue dots are the output voltage of the PD at the output optics, and the red curve is the fitting. In this case, the time constant was $\tau = 8.2 \pm 0.2\mu$s, and it implies that the FP cavity had a time constant of $\tau_{\rm fp} = 16.4 \pm 0.4$ μs according to the Eq.(4.35).

cavity. Hence, Eq.(4.24) is directly adopted as the fitting function with the relation between the thickness of the molecular layer and the reflectivity, Eq.(4.6). The vacuum pressure during the measurement was stable, so the speed of the molecular layer formation is assumed to be constant and the thickness $d_{\rm mol}$ of the molecular layer is rewritten as $d_{\rm mol} = v_{\rm mol}t$. Further, the optical phase shift $d\delta_{\rm mol}$ inside the molecular layer is expressed as $\delta_{\rm mol}(N_{\rm mol}, v_{\rm mol}, d\delta_{\rm mol}) = 2\pi\frac{N_{\rm mol}v_{\rm mol}}{\lambda}t + d\delta_{\rm mol}$, where $d\delta_{\rm mol}$ is the parameter to adjust the phase of the finesse change in the fitting. Then the fitting function of the finesse $\mathcal{F}$ is given as

$$\mathcal{F} = \frac{\pi\sqrt{\left(\rho_{\rm vm} + \rho' {\rm e}^{-2{\rm i}\delta_{\rm mol}}\right)\left(1 + \rho_{\rm vm}\rho' {\rm e}^{-2i\delta_{\rm mol}}\right) r_2 r_{\rm loss}}}{\rho_{\rm vm} + \rho' {\rm e}^{-2{\rm i}\delta_{\rm mol}} - \left(1 + \rho_{\rm vm}\rho' {\rm e}^{-2i\delta_{\rm mol}}\right) r_2 r_{\rm loss}}. \tag{4.43}$$

The fitting parameters are the speed of the molecular layer formation v_{mol}, the

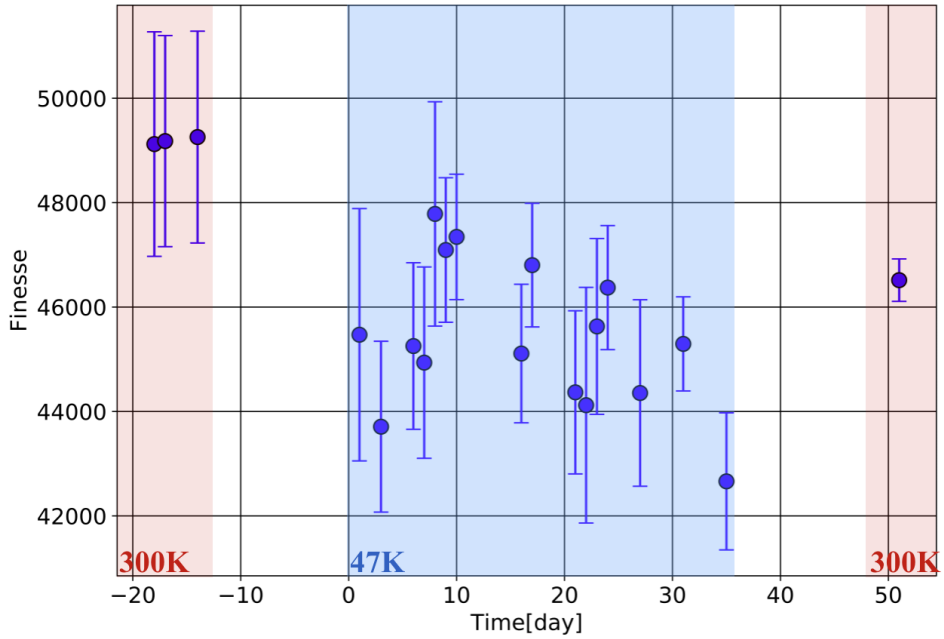

Figure 4.19: Evaluated finesse from the measured time constant of the FP cavity. The red and the blue areas show the periods when the temperature of the FP cavity was 300 K and 47 K, respectively. The blue circles are the averaged finesses and the error bars indicate the statistical error. To calculate the average finesse and statistical error, 20 times of the ringdown measurements are used.

complex refractive index of the molecular layer $N_{\mathrm{mol}} = n_{\mathrm{mol}} - ik_{\mathrm{mol}}$, the phase adjust parameter $d\delta_{\mathrm{mol}}$ and the initial optical loss inside the FP cavity A_{loss}. ρ', ρ_{vm} and δ_{mol} in Eq.(4.43) are parameterized by these fitting parameters.

Using the transmissivity of the mirrors of the FP cavity and the refractive index $n_{\mathrm{cap}} = 1.4496$ [90] of SiO_2 which constitute the coating cap. the fitting was executed and the results that are shown in Fig.(4.20) and table (4.2) are obtained. According to the fitting results, the speed of the molecular layer formation is $v_{\mathrm{mol}} = 25.5 \pm 2.8$ nm/day and the complex refractive index of the layer is $N_{\mathrm{mol}} = 1.33 \pm 0.13 - i(2.33 \pm 1.81) \times 10^{-7}$. Because the amplitude of the finesse oscillations due to the N_2 and O_2 molecular layer formation is much smaller than that of the H_2O and the period of the oscillation become long. the measured refractive index is expected to be that of H_2O molecules. Due to the large error on the measured point, the error on the complex refractive

index is large, but it's similar to that of the H_2O molecules. These facts are comparable with the measurement result with the mass spectrometer.

The chi square of the fitting is defined as

$$\chi^2 \equiv \sum \left(\frac{y_\mathrm{i} - f(x_\mathrm{i}; \mathbf{p})}{\sigma_\mathrm{i}} \right)^2, \tag{4.44}$$

where $(x_\mathrm{i}, y_\mathrm{i})$ is the measured data, σ_i is the error of y_i, $f(x_\mathrm{i}; p)$ is the fitting function and $\mathbf{p}$ shows the fitting parameters. Substituting the measured data and the fitting function Eq.(4.43) with the fitting parameters shown in the table (4.2), the chi square of the fitting is calculated as $\chi^2 = 5.94$ with the degree of freedom of 11. The probability density function of the chi square distribution is written as

$$p(x; k) = \frac{1}{2^{\frac{k}{2}} \Gamma(\frac{k}{2})} e^{-\frac{x}{2}} x^{\frac{k}{2}-1} \qquad (0 \geq x) \tag{4.45}$$

where k is the degree of freedom and $\Gamma(k)$ is the gamma function. Figure (4.21) shows the calculated probability density of the distribution for $k = 11$. Red line shows the chi square of the fitting shown in the Fig.(4.20) and black dashed line corresponds to the significance level of 10 %. The result implies that the model of the fitting is not denied statistically, though the evaluation of the errors are possibly too large. The number of data that are used to calculate each points are 20, and this small number of data causes large statistical error. By increasing the number of data, the chi square value can be more reasonable.

Note that these values are slightly different from the values reported in the reference [79]. This is because the fitting above uses the transmissivity, or the reflectivity, of the mirrors that are experimentally measured, on the other hand, the fitting in the reference [79] uses the reflectivity of mirrors that are calculated based on the quarter wavelength ($\lambda/4$) model of coating to reproduce the reflectivity of the mirrors. These two reflectivity are similar but not the same, and this difference caused the gap between two fittings. When the reference [79] was reported, the relation Eq.(4.6) between the reflectivity of the mirror which is measured in vacuum and the reflectivity change due to the molecular layer formation was not found, and the model based reflectivity analysis was used. For the comparison. both results are summarized in table (4.2).

Table 4.2: Fitting results

Name	Symbol	Value (This work)	Value ([79])	Unit
Speed of formation	v_{mol}	25.5 ± 2.8	27.1 ± 1.9	nm/day
Refractive index (Real)	n_{mol}	1.33 ± 0.13	1.26 ± 0.073	-
Refractive index (Imag.)	k_{mol}	$(2.33 \pm 1.81) \times 10^{-7}$	$(2.2 \pm 1.26) \times 10^{-7}$	-
Phase adj. parameter	$d\delta_{\mathrm{mol}}$	0.83 ± 0.37	0.81 ± 0.26	rad
Initial optical loss	T_{loss}	101.1 ± 2.3	17 ± 1.8	ppm

4.3.3 Simulation

To confirm the validity of the speed of the molecular layer formation which was extracted from the measurement result, here we calculate it for this experimental set up as discussed in Chapter 3 The conductance of the duct shield and the beam duct are the same as Chapter 3. In this subsection, the distribution of the vacuum pressure inside the vacuum chamber is reconstructed using the vacuum pressure measured during the experiment under the assumption of the uniform degas from the surface, and the molecular flux to the mirror and the speed of the molecular layer formation are calculated.

Pressure distribution

Using Molflow+, the degassing speed that gives the vacuum pressure of $P_{\mathrm{mes}} = 6.0 \times 10^{-6}$ Pa at the vacuum gauge attached near the vacuum pump is calculated by applying the uniform degassing from the room temperature surface. Figure (4.22-a) shows the model that is used for the vacuum pressure distribution analysis. The cryostat between the duct shield and the test mass was simplified as shown in the figure. First, by applying the uniform degassing from the room temperature surface, the relation between the degassing rate and the vacuum pressure at the measurement point was simulated. The absorption coefficient of the duct shield was set to unity, and the pumping speed of the vacuum pump was set to 2500 L/s which is the nominal value of the pump used for the experiment. Figure(4.22-b) shows the simulated result with the fitting. Because molecules inside the vacuum chamber don't attract each other, the relation between the degassing rate and the vacuum pressure is the linear relation in log-log scale. As the result of the fitting, it was found that the $1.9 \times 10^{-7}\mathrm{Pa\,m^3/s}$ of degassing speed provided the vacuum pressure of $P_{\mathrm{mes}} = 6.0 \times 10^{-6}$ Pa at the vacuum gauge. Then, using this degassing

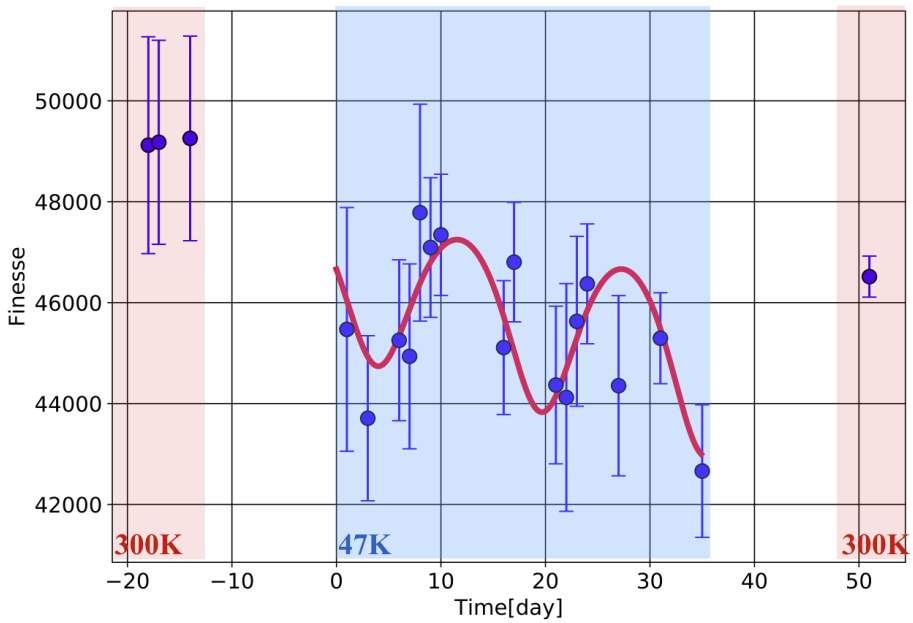

Figure 4.20: Evaluated finesse and the fitting result. Using the model of the finesse with the molecular layer Eq.(4.43), the molecular layer formation was evaluated. The red curve shows the fitting. The speed of the molecular layer formation is $v_{\rm mol} = 25.5 \pm 2.8$ nm/day and the complex refractive index of the layer is $N_{\rm mol} = 1.33 \pm 0.13 - i(2.33 \pm 1.81) \times 10^{-7}$. The result of the fitting is summarized in table (4.2).

speed, the vacuum pressure distribution along the beam duct (pink axis in the Fig.(4.22-a)) was simulated. Figure (4.22-c) shows the simulated vacuum pressure distribution, and it implies that during the experiment, the vacuum pressure at the GV is expected to be $P_{\rm GV} = 5.5 \times 10^{-6}$ Pa.

Simulated speed of molecular layer formation

The molecular flux is calculated as the multiplication of the conductance $C_{\rm sys}$ of the system and the vacuum pressure difference δP. As discussed in Chapter 3, we assume that the pressure difference is the same as the as the vacuum pressure at the GV, $\delta P = P_{\rm GV}$. First, we consider the conductance between the GV and the KAGRA ITM and calculate the molecular flux and the speed of molecular layer formation, then it's converted to that of this experiment.

The conductance of the experiment is composed of two part, 12m of the

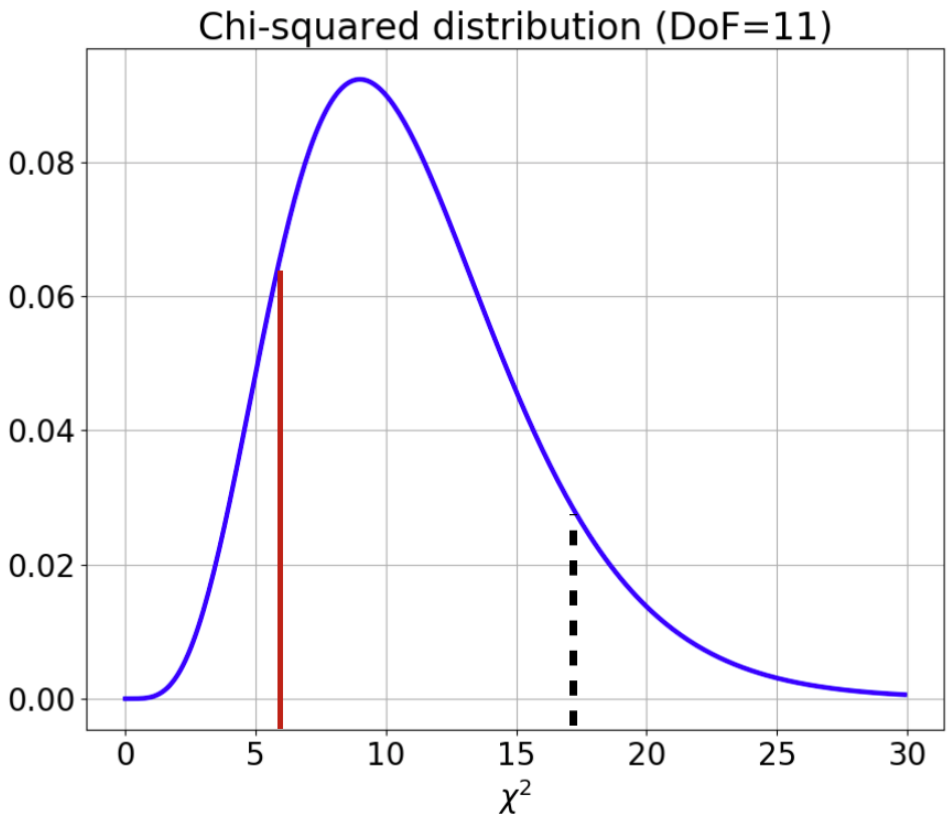

Figure 4.21: Kai square distribution (DoF = 11). Red line shows the chi square of the fitting shown in the Fig.(4.20). Black dashed line corresponds to the significance level of 10 %.

beam duct and the duct shield, and this is given by the Eq.(3.23). Because N_2 and O_2 molecules do not change the finesse drastically due to their low refractive index. Hence here we only consider about H_2O molecules. Using the Eq.(4.37), the partial pressure of H_2O, N_2 and O_2 at the GV position are given as

$$P_{H_2O} = \gamma_{H_2O} P_{GV} = 3.7 \times 10^{-6} \quad \text{Pa.} \tag{4.46}$$

Hence, the molecular flux to the KAGRA ITM is calculated by taking the hitting probability into account as

$$Q_{ITM} = K_{spa} C_{sys} \delta P = 8.05 \times 10^{-7} \qquad (H_2O). \tag{4.47}$$

Note that, the sticking probability of 1 is assumed for H_2O molecules, and that of 0 is assumed for N_2 and O_2 molecules. The speed of the molecular

layer formation for each molecule is calculated as

$$\frac{dd_{\mathrm{mol}}}{dt} = 20.2 \qquad \mathrm{nm/day}. \tag{4.48}$$

The optical axis of the FP cavity for this experiment is tilted by 30 degrees along to the optical axis of the KAGRA arm cavity. Hence, the measurable thickness of the molecular layer is different from that of the KAGRA case by the factor of $\cos 30°$, and the speed of the molecular layer formation on the mirror of the FP cavity is calculated as

$$\frac{dd_{\mathrm{mol}}}{dt} = \begin{cases} 17.5 & (\mathrm{H_2O}), \\ 2.2 & (\mathrm{N_2}) \\ 0.37 & (\mathrm{O_2}). \end{cases} \qquad \mathrm{nm/day}. \tag{4.49}$$

Comparing with the experimental result, this value is slightly small. The evaluation of the pressure distribution can contain error inside. The non-uniform degassing changes the pressure distribution, and further degassing of the MLI for the duct shield can produce much degassing. To evaluate these effect, much number of the vacuum gauge needed to install along the beam duct.

Though the experimental result and the simulated values are slightly different, both of these results imply that the molecular layer grow on the cryogenic mirror on the order of 10 nm in a day. If the condition is kept during the observation, the thickness of the molecular get the order of 1 um. In the next chapter, the impacts of the molecular layer on the GWD are introduced based on the KAGRA.

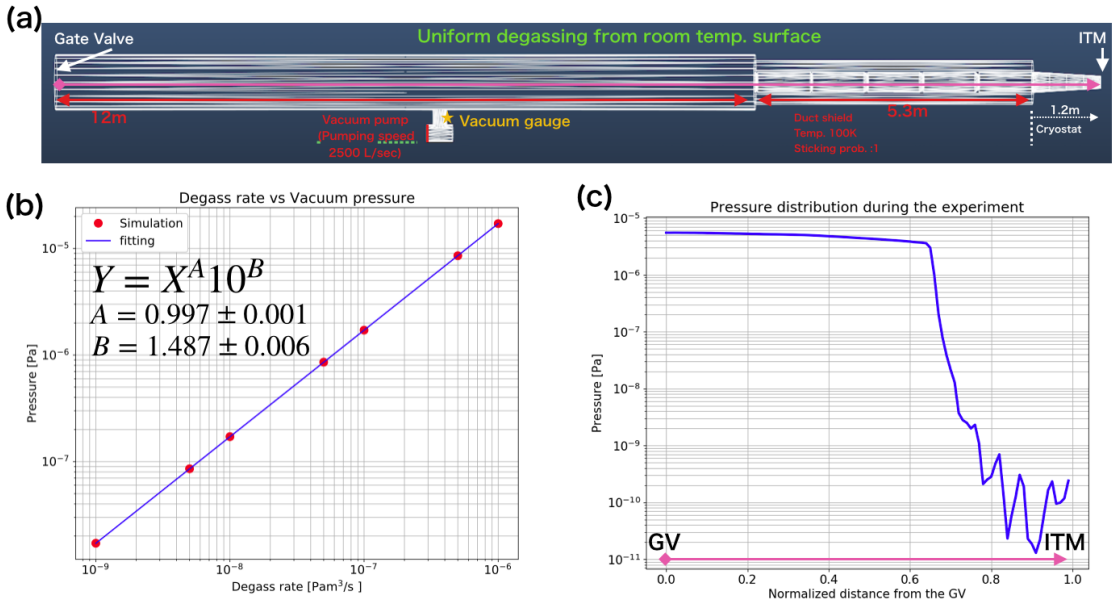

Figure 4.22: Pressure analysis with Molflow+. (a)The model used for the vacuum pressure analysis. The model is composed of three parts, beam duct, duct shield and the space between duct shield and the test mass. The sticking probability of the duct shield was set to unity, and the pumping speed of the vacuum pump was set to 2500L/s. The degassing happens from the room temperature surfaces. (b)The relation between the degassing speed and the vacuum pressure measured by the vacuum gauge attached near the vacuum pump. The simulated result was fitted, and it was found that the degassing speed of $1.9 \times 10^{-7}\,\mathrm{Pa\,m^3/s}$ gives the vacuum pressure $P_{\mathrm{mes}} = 6.0 \times 10^{-6}$ Pa that was measured during the experiment. (c)Using the degassing speed of $1.9 \times 10^{-7}\,\mathrm{Pa\,m^3/s}$, the pressure distribution inside the vacuum duct was reconstructed. The calculated vacuum pressure at the GV is $P_{\mathrm{GV}} = 5.5 \times 10^{-6}$Pa.

Chapter 5
MOLECULAR LAYER IN A CRYOGENIC GWD

In the previous chapters, the molecular layer formation on a cryogenic mirror is introduced. As already discussed in Chapter 4, the growing molecular layer changes the reflectivity of the mirror and add the optical loss such as the optical absorption and the scattering. These effects are considered to change the sensitivity of the GWD. Furthermore, the molecular layer can be a noise source itself that has not considered so far. In this chapter, the influences of the molecular layer on the cooled mirror in the cryogenic GWD are detailed.

5.1 Previous work

As introduced in Chapter 3, Miyoki et al. tried to evaluate the molecular layer formation in a GWD theoretically. They also evaluated the optical loss due to the molecular layer formation using an optical cavity as shown in Fig.(5.1-a) to estimate the impacts on a GWD. In their experiment, one of the mirrors that composed the optical cavity inside the cryostat has the solid angle to the optical window which is at the room temperature, and the molecular layer formed by the molecules from the optical window was evaluated. For the analysis of the measured result, they took only the optical scattering due to the roughness of the molecular layer in their model, and obtained the optical loss increasing rate of 0.12 ppm/day as shown in Fig.(5.1-b). Though the amount of the scattering light depends on the reflectance between the vacuum and the molecular layer as discussed in Chapter 4, they assumed the total reflection at the molecular layer surface. As a result, they assumed 6 - 14 ppm of the scattering loss due to one molecular layer formation which

corresponds to 1Åorder of the surface roughness. Based on this scattering loss efficiency, they also discussed the impacts of the molecular layer formation on a cryogenic GWD. Though it just considered the degrade of the PRG due to the scattering loss increasing, it was concluded that the performance of the GWD is kept for 130 days.

The effects of the reflectivity oscillation, the optical absorption, and the mechanical dispersion were not taken into account in the previous work.

To evaluate the impacts on a GWD including these effects, it is important to develop the model based on the thin film theory using the basic properties of the molecular layer such as the refractive index and the mechanical loss angle as partially discussed in Chapter 4. In this chapter, from the point of view of the sensitivity of a GWD, the impacts of the molecular layer formation are evaluated based on the thin film theory using the basic properties of the layer.

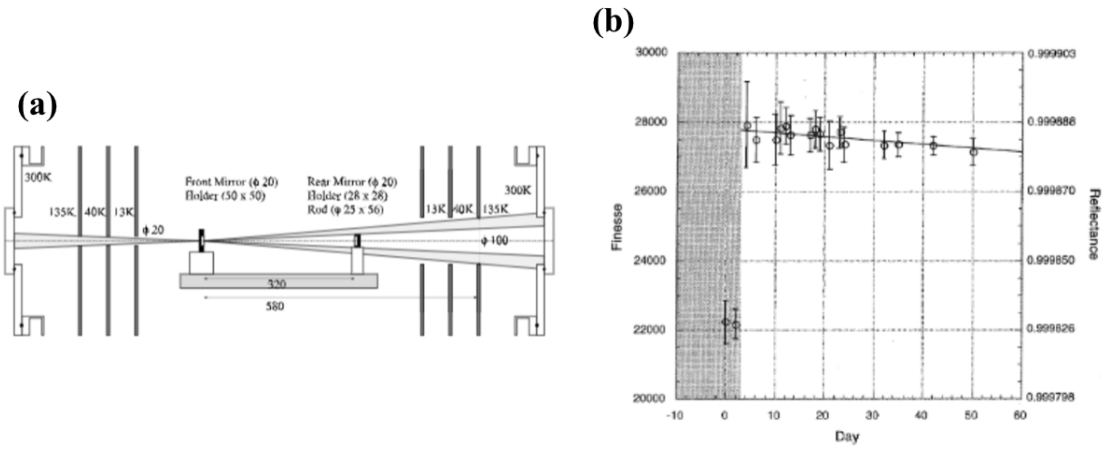

Figure 5.1: Experimental setup and result of the previous work. (a) One of the mirrors that composed the optical cavity inside the cryostat has the solid angle to the optical window which is at the room temperature, and the molecular layer formed by the molecules from the optical window was evaluated. (b) Evaluated finesse during the experiment. For the analysis of the measured result, only the optical scattering due to the roughness of the molecular layer was taken into account. The finesse continuously decreases and the optical loss increasing rate was evaluated to be 0.12 ppm/day.

5.2 Refractive index of the molecular layer

As introduced in Chapter 4, the growing molecular layer changes the reflectivity of the mirror. The amplitude of the reflectivity change depends on the original reflectivity of the mirror and the refractive index of the molecular layer. Figure (5.2) shows the amplitude of the reflectivity change δr for the refractive index, and δr is calculated using the Eq.(4.6) as

$$\delta r = \rho(\delta_{\mathrm{mol}} = 0) - \rho(\delta_{\mathrm{mol}} = \frac{\pi}{2}). \tag{5.1}$$

For the high reflective mirror, the amplitude of the reflectivity change increases with the refractive index of the molecular layer. Hence, for the KAGRA ITM and ETM that have high reflectivity, H_2O molecule is considered to give the largest amplitude of the reflectivity change for the vacuum residual gasses. Following calculation is focused on the H_2O molecules.

Generally, H_2O molecules form the low density amorphous (LDA) state [86]. Recently, V. Kofman et al. [91] reported the refractive index of the LDA for the wavelength of 210 nm - 757 nm for various growing temperatures. In point of view of the range of the wavelength, their study is not sufficient, but here we extrapolate their result to the our wavelength of 1064 nm. Because there is no characteristic structure from their wavelength to our wavelength, and it just monotonically decreases gently at other temperature and the other structures of water [92], this extrapolate would not be a bad assumption. The Lorentz-Lorentz equation gives the relation among the density ρ and the refractive index $n(\lambda)$ as [91]

$$R(\lambda) = \frac{1}{\rho}\frac{n(\lambda)^2 - 1}{n(\lambda)^2 + 2} \tag{5.2}$$

with

$$R(\lambda) = \sqrt{\frac{D_1\lambda^2}{\lambda^2 - C_1} + \frac{D_2\lambda^2}{\lambda^2 - C_2}} \tag{5.3}$$

where C_1, C_2, D_1 and D_2 are the parameters to explain the experimental result, and they are summarized in the table (5.1) with the density. C_1 and C_2 are given in [91], and D_1 and D_2 are extracted by the fitting of the data in [91] using the Eq.(5.3). Figure (5.3) shows the calculated the refractive index, and it's $n_{\mathrm{LDA}} = 1.196$ at 20 K for the wavelength of 1064 nm. Note that the refractive index at 20K is the averaged value of that of 10K and

30K. The absorption of the LDA water haven't been studied well especially for the wavelength of 1064 nm. Some of the studies imply that the imaginary part of the water for the wavelength of 1064 nm is order of 10^6, though the temperature and the state of the water is different from the LDA. To proceed to a discussion, in this section, we use two values for the imaginary part of the refractive index. One is the value extracted from the reference [93] which is the value of the Ih state of ice, $k_1 = 1.9 \times 10^{-6}$. The other is the mean value obtained from the experiment discussed in Chapter 4, $k_2 = 2 \times 10^{-7}$ So, in the following calculations, we use two of the complex refractive index, $N_1 = n_{\mathrm{LDA}} - ik_1 = 1.196 - i(1.9 \times 10^{-6})$ and $N_2 = n_{\mathrm{LDA}} - ik_2 = 1.196 - i(2 \times 10^{-6})$.

Temp. K	10	30	50	70	90	110	130	150
ρ	0.585	0.636	0.688	0.740	0.791	0.843	0.895	0.925
Symbol	$\sqrt{C_1}$		$\sqrt{C_2}$		D_1		D_2	
	71		134		0.00996		0.0319	

Table 5.1: Density and parameters to substitute into the Eqs.(5.2) and (5.3). The values of C_1 and C_2 are extracted from the reference [91], and the values of D_1 and D_2 are the fitted using the data extracted from the reference and the Eq.(5.3).

5.3 Reflectivity of the KAGRA test masses

First, the reflectivity of the KAGRA ITM and ETM with the growing molecular layer are calculated. As introduced in the table(), the designed power transmissivity of the ITM and ETM are $T_{\mathrm{ITM}} = 0.004$ and $T_{\mathrm{ETM}} = 7 \times 10^{-6}$. These reflectivities are changed following the Eq.(4.6) with the growth of the molecular layer, and Fig.(5.4) shows the calculation result. The amplitude of the reflectivity change of the ITM due to the molecular layer formation is larger than that of the ETM because the original reflectivity of the ITM is closer to the reflectivity of the molecular layer and the interference of these two lights become larger than ETM. On the other hand, the reflectivity of the ETM is very high, and it's much sensitive to the optical loss on the surface.

As the result of the reflectivity change of the test masses, the parameters of the KAGRA arm cavity are changed at the same time. The amplitude reflectivity of the resonant arm cavity r_{arm} with the thickness of the molecular

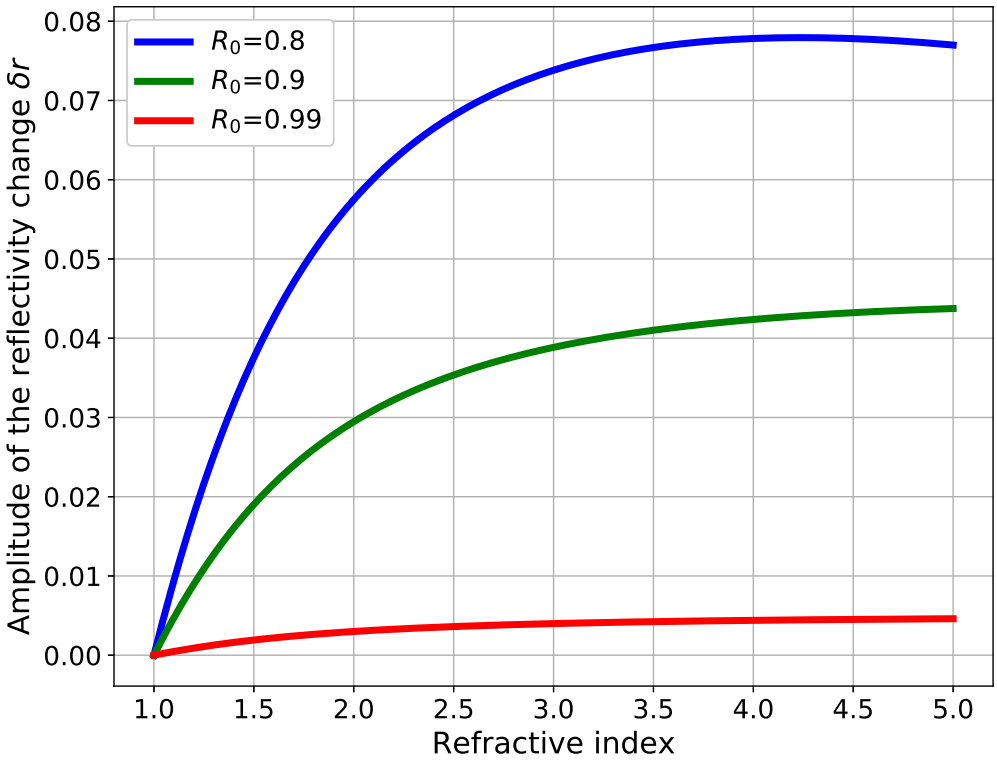

Figure 5.2: Amplitude of the reflectivity change for the refractive index of the molecular layer. The amplitude of the refractivity change depends on the refractive index and the original reflectivity of the mirror R_0. The amplitude of the change is maximized when the amount of the reflected light from the molecular layer and the coating is about the same.

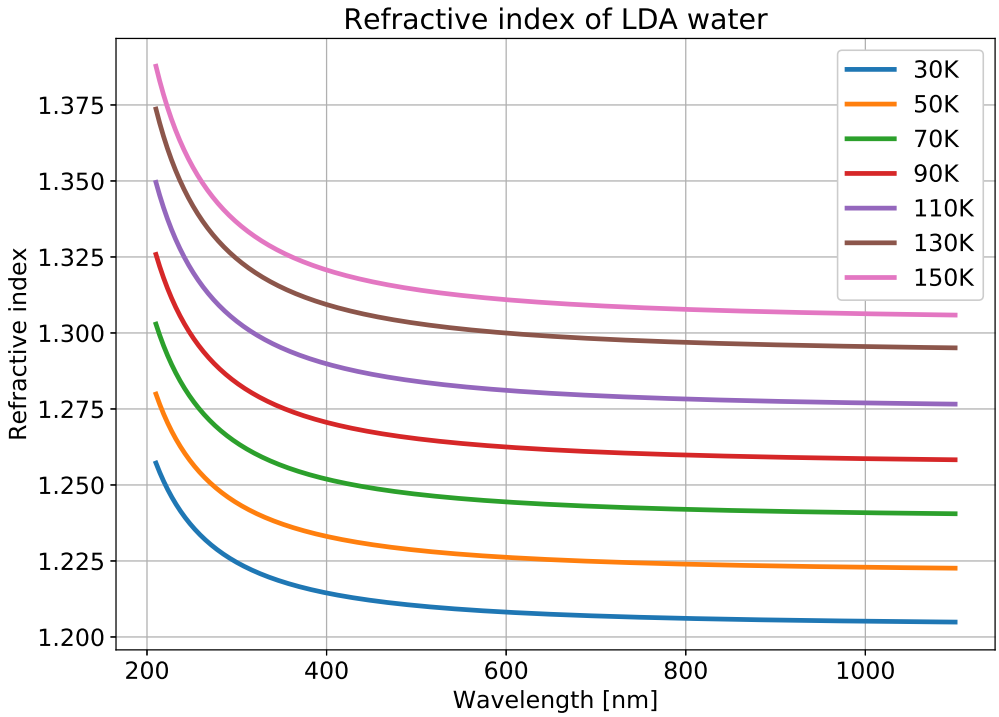

Figure 5.3: Refractive index of the LDA water. Using the Lorentz-Lorentz relation Eq.(5.2), the refractive index of the LDA water is calculated with the parameters in the table(5.3). The refractive index for the wavelength of 1064nm at 20K is calculated to be $n_{\mathrm{LDA}} = 1.196$.

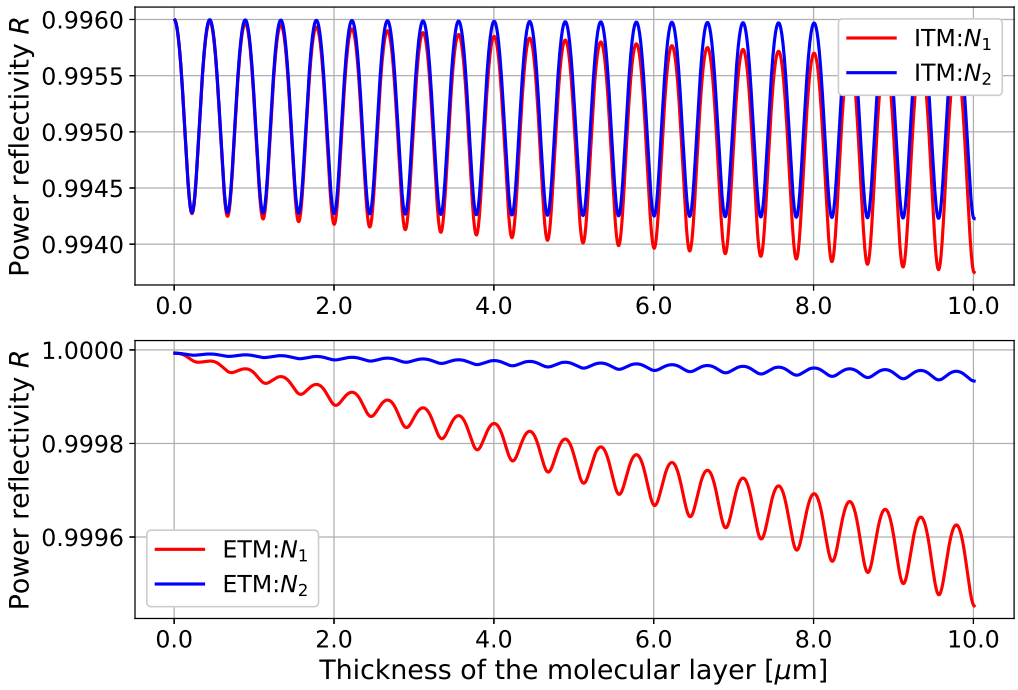

Figure 5.4: Power reflectivity of the KAGRA test masses. The reflectivity change of the KAGRA test masses are calculated. Red and blue curves show the calculation result for the refractive indices of N_1 and N_2, respectively. Because the reflectivity of ITM is smaller than that of ETM, the amplitude of the reflectivity change is larger. On the other hand, the ETM which has very high reflectivity is much sensitive to the optical loss.

layer is given by Eq.(1.30) as

$$r_{\rm arm}(d_{\rm itm}, d_{\rm etm}) = -r_{\rm itm}(d_{\rm itm}) + \frac{t^2_{\rm itm}(d_{\rm itm}) r_{\rm etm}(d_{\rm etm}) r_{\rm loss-arm}}{1 - r_{\rm itm}(d_{\rm itm}) r_{\rm etm}(d_{\rm etm}) r_{\rm loss-arm}}, \tag{5.4}$$

where d in the equation denotes the thickiness of the molecular layer on the HR coating of the test masses, and $r_{\rm loss-arm} = \sqrt{1 - T_{\rm loss}}$ is the loss equivalent reflectivity in the arm cavity, where $T_{\rm loss-arm}$ is the amount of loss inside. Figure (5.5-a) shows the calculated amplitude reflectivity of the KAGRA arm cavity with the growing molecular layer on the test masses. The reflectivity of the arm cavity is strongly correlated to the thickness of the molecular layer on the ITM than ETM. This is because the original reflectivity of the ITM is much lower than that of ETM and the amplitude of the reflectivity change is much larger than that of ETM as shown in the Fig.(5.4). Note that the change of the reflectivity of the KAGRA arm cavity is anti-phase to the change of the ITM reflectivity. This is because the KAGRA arm cavity is the over coupled cavity, the reflectivity of the ETM is higher than that of ITM, so when the reflectivity of ITM decrease, the reflectivity of the arm cavity approach to that of ETM. The finesse of the arm cavity $\mathcal{F}_{\rm arm}(d_{\rm itm}, d_{\rm etm})$ with the growing molecular layer is given as

$$\mathcal{F}_{\rm arm}(d_{\rm itm}, d_{\rm etm}) = \frac{\pi \sqrt{r_{\rm itm}(d_{\rm itm}) r_{\rm etm}(d_{\rm etm}) r_{\rm loss-arm}}}{1 - r_{\rm itm}(d_{\rm itm}) r_{\rm etm}(d_{\rm etm}) r_{\rm loss-arm}}. \tag{5.5}$$

Figure (5.5-b) shows the finesse of the arm cavities when the molecular layer grows up on the test masses. The finesse is strongly correlated with the thickness of the molecular layer on the ITM than ETM, and this is the same reason as the reflectivity change of the arm cavity.

5.4 Laser power stored in the interferometer

The reflectivity changes of the cryogenic mirrors affect to the laser power inside the interferometer. This subsection aims to derive the storage laser power in the arm cavity and the PRC depending with the molecular layer on the cryogenic test masses.

The PRG of the arm cavity with cryogenic test masses is

$$\mathrm{G}(r_{\rm x}, r_{\rm y}) = \left(\frac{t_{\rm prm}}{1 - \frac{1}{2} r_{\rm prm} \left(r_{\rm x}(d_{\rm itm-x}, d_{\rm etm-x}) + r_{\rm y}(d_{\rm itm-y}, d_{\rm etm-y}) \right)} \right)^2, \tag{5.6}$$

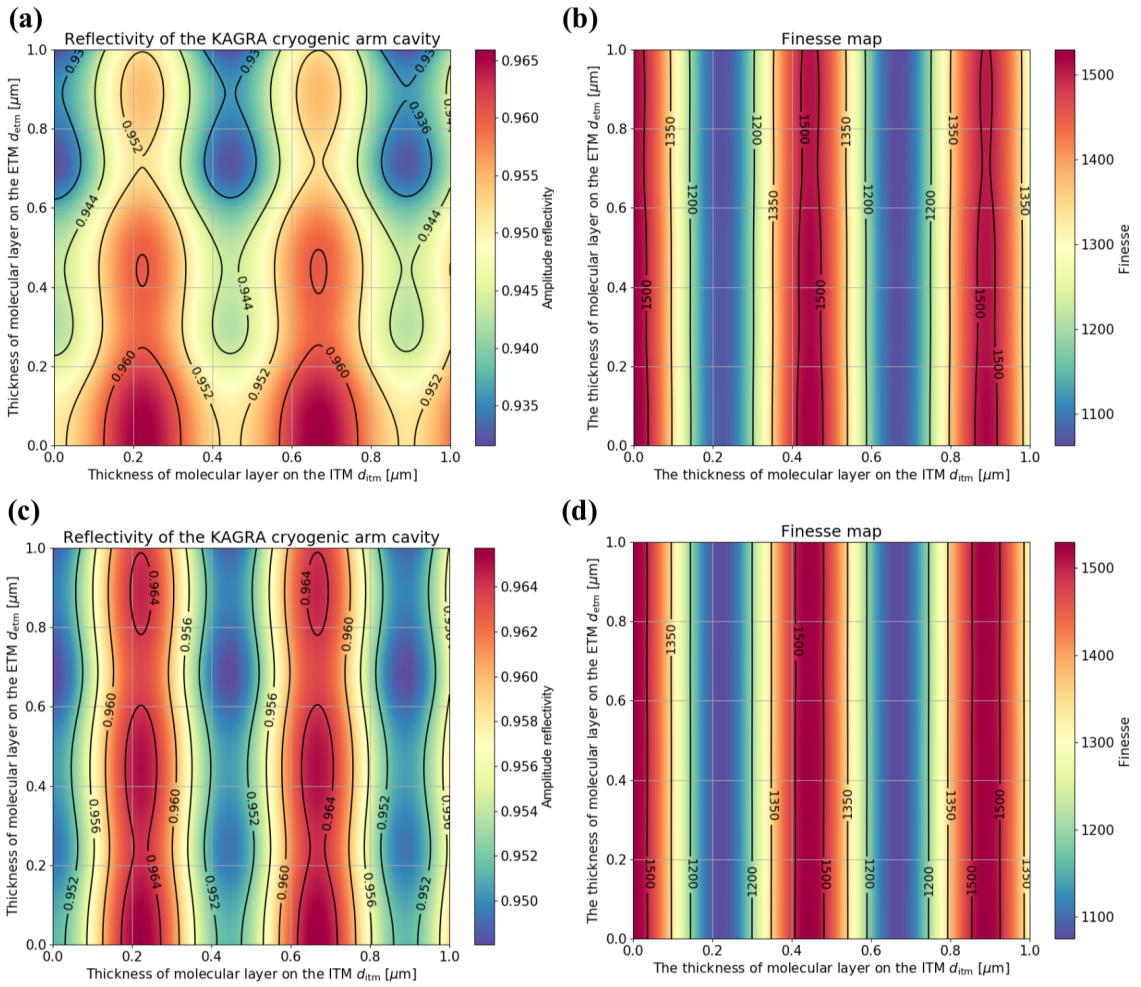

Figure 5.5: Reflectivity and finesse of the KAGRA arm cavity with the growing molecular layer. (a) and (b) : The amplitude reflectivity and the finesse of the KAGRA cryogenic arm cavity with the growing molecular layer for N_1. (c) and (d) : for N_2. The change of the reflectivity of the KAGRA arm cavity is anti-phase to the change of the ITM reflectivity. This is because the KAGRA arm cavity is the over coupled cavity, the reflectivity of the ETM is higher than that of ITM, so when the reflectivity of ITM decrease, the reflectivity of the arm cavity approach to that of ETM. Lower : The finesse of KAGRA cryogenic arm cavity with the molecular layer. The strong correlation of finesse with the thickness of the molecular layer on the ITM is the result of the lower reflectivity of ITM than ETM. The reflectivity is largely affected by the optical loss of the molecular layer, though the finesse is not so affected. These two behaviors show the magnitude of the dependence of these parameters to each mirror.

where $r_{\rm j}(d_{\rm itm-j}, d_{\rm etm-j})$ (j = x, y) is the reflectivity of the x or y arm cavity given by Eq.(5.4). If we assume that the reflectivity of two arm cavities are the same always, or the reflectivity of two ITMs and are always the same as well the ETMs, Eq.(5.8) is simplified as

$$\mathrm{G}(d_{\rm itm}, d_{\rm etm}) = \left(\frac{t_{\rm prm}}{1 - r_{\rm prm} r_{\rm arm}(d_{\rm itm}, d_{\rm etm})} \right)^2, \tag{5.7}$$

Using this expression, the laser power inside the PRC $P_{\rm PRC}$ with the molecular layer on the test masses is given by Eq.(1.55) as

$$P_{\rm PRC} = \mathrm{G}(d_{\rm itm}, d_{\rm etm}) P_{\rm in} \tag{5.8}$$

where $P_{\rm in}$ is the incident laser power to the PRC.

Equation (1.32) gives the storage laser power in the resonating arm cavity $P_{\rm arm}$ as

$$P_{\rm arm} = \frac{t_{\rm itm}(d_{\rm itm})^2}{\left(1 - r_{\rm itm}(d_{\rm itm}) r_{\rm etm}(d_{\rm etm}) r_{\rm loss-arm}\right)^2} P_{\rm in-arm} \tag{5.9}$$

$P_{\rm in-arm} = P_{\rm PRC}/2$ is the input laser power to the arm cavity. If the reflectivity of the test masses are high and we can assume them as $r_{\rm itm} \sim 1$ and $r_{\rm etm} = 1$, Eq.(5.9) is rewritten as

$$P_{\rm arm} = \frac{2}{\pi} \mathcal{F}_{\rm arm}(d_{\rm itm}, d_{\rm etm}) P_{\rm in-arm}, \tag{5.10}$$

Figure (5.6) shows the calculated result of the laser power inside the PRC and the arm cavity. When the reflectivity of the arm cavity increase, the PRG increases coherently, and the laser power inside the PRC becomes larger than the designed value at initial, and it decrease while oscillating due to the optical loss loss of the molecular layer. On the other hand, as the result of both of the PRG and the finesse change, the laser power inside the arm cavity decreases while oscillating from the initial.

5.5 Quantum noise

Starting from the reflectivity change due to the growth of the molecular layer on the cryogenic test masses, above sections introduce relation between the thickness of the molecular layer and the laser power inside the GWD. The change of the reflectivity and the laser power affect on the quantum noise

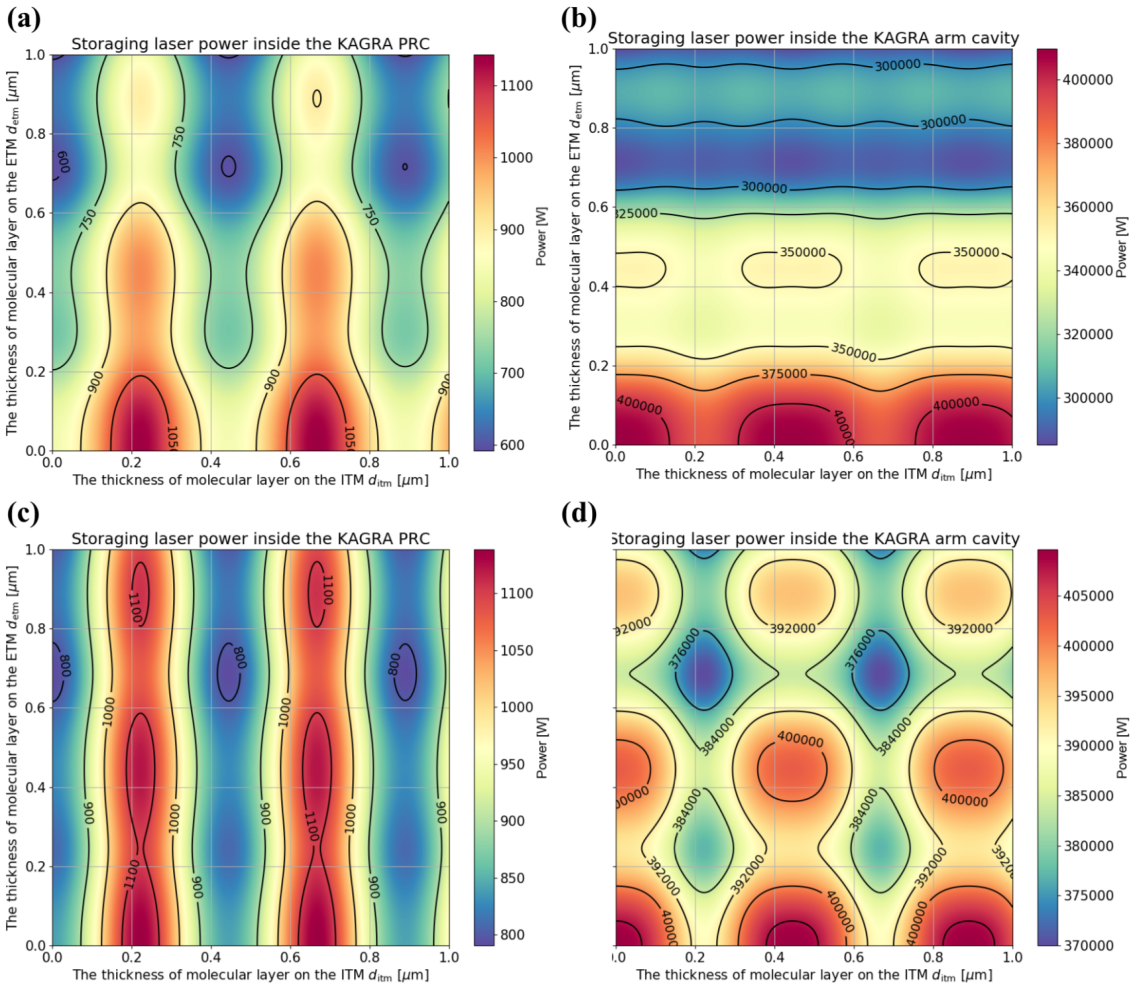

Figure 5.6: Laser power inside the PRC and the arm cavity with the molecular layer on the test masses. The thickness of the molecular layer on two ITMs are assumed to be same as well two ETMs. (a) and (b) : The laser power inside the PRC and the arm cavity for the refractive index of N_1. (c) and (d) :For the refractive index of N_2. The laser power inside the PRC is just affected by the PRG change. The laser power become larger than the designed value at initial because the PRG increase when the reflectivity of the ITM decrease. Then the laser power decreases while oscillating. The laser power inside the arm cavity is affected by both of the PRG and the finesse of the arm cavity. As a result, the power decreases while oscillating from the initial.

which is one of the fundamental noises of a GWD. This section calculates the effect of the molecular layer on the quantum noise.

As the result of the growth of the molecular layer on the test masses, some parameters such as the finesse $\mathcal{F}$ and the laser power P inside the interferometer are changed. The quantum noise of the BRSE with the molecular layer on the cryogenic mirrors is given by the Eq.(5.11) as

$$S_{\mathrm{BRSE}}(d_{\mathrm{itm}}, d_{\mathrm{etm}}) = \frac{8\hbar}{m\omega^2 L^2} \frac{\left((1+r_{\mathrm{srm}}^2) - 2r_{\mathrm{srm}}\cos\left[2\beta(d_{\mathrm{itm}}, d_{\mathrm{etm}})\right]\right)^2 t_{\mathrm{srm}}^3 \mathcal{K}(d_{\mathrm{itm}}, d_{\mathrm{etm}})}{2\left(1 + r_{\mathrm{srm}} e^{2\mathrm{i}\beta(d_{\mathrm{itm}}, d_{\mathrm{etm}})}\right)^2}, \tag{5.11}$$

with

$$\mathcal{K}(d_{\mathrm{itm}}, d_{\mathrm{etm}}) = \frac{16\pi c P(d_{\mathrm{itm}}, d_{\mathrm{etm}})}{m\lambda L^2\omega^2(\gamma(d_{\mathrm{itm}}, d_{\mathrm{etm}})^2 + \omega^2)}, \tag{5.12}$$

$$\gamma(d_{\mathrm{itm}}, d_{\mathrm{etm}}) = \frac{cT_{\mathrm{ITM}}(d_{\mathrm{itm}}, d_{\mathrm{etm}})}{4L}, \tag{5.13}$$

$$\beta(d_{\mathrm{itm}}, d_{\mathrm{etm}}) = \arctan\left(\frac{4L\mathcal{F}(d_{\mathrm{itm}}, d_{\mathrm{etm}})}{2\pi c}\omega\right). \tag{5.14}$$

Figures(5.7 and 5.8 a-c) shows the calculated quantum noise in the BRSE at 10Hz, 200Hz, and 3000Hz with the growing of the molecular layer on the test masses. In the figure, the quantum noise at each thickness of the molecular layer is normalized by the designed quantum noise, $S_{\mathrm{BRSE}}(d_{\mathrm{itm}}, d_{\mathrm{etm}})/S_{\mathrm{BRSE}}(0,0)$. Below about 50Hz. the quantum noise is the radiation pressure noise which is the vibration of the suspended mirror induced by the photon number fluctuation. Hence, the amplitude of the quantum noise around 10Hz is changed coherently with the laser power inside the arm cavity, and it decrease while oscillating. On the other hand, above 1000Hz, the quantum noise is the shot noise which is the read-out noise of the interferometer output, so the shot noise changes coherently with the power inside the PRC. So the shot noise is improved at initial, and then it decreases. Within the thickness below $5\mu m$, the quantum noise changes in the gray area shown in the Figs.(5.7-d) and (5.8-d).

5.6 Optical absorption

When laser light passes through the molecular layer, it absorbs a part of laser. Because this absorption is not taken into account in the heat load to the KAGRA cryogenic system, and is possibly changes the temperature of the

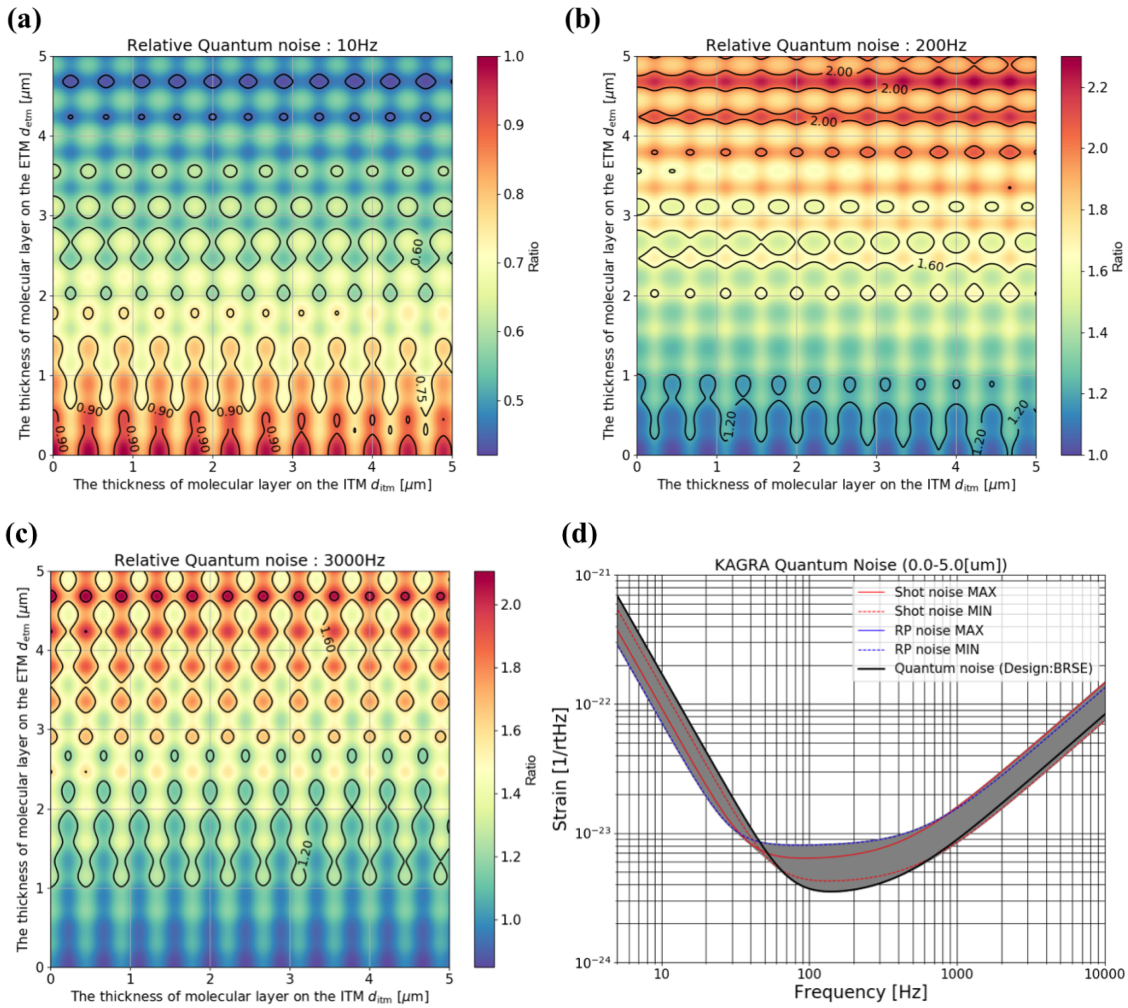

Figure 5.7: Quantum noise in the BRSE with the molecular layer on the cryogenic test masses for the refractive index of N_1. (a)The calculated relative quantum noise at 10Hz. (b)The calculated relative quantum noise at 200Hz. (c)The calculated relative quantum noise at 3000Hz. The quantum noise with the molecular layer is normalized by the designed quantum noise of KAGRA (BRSE). (d)The quantum noise changes due to the growth of the molecular layer. Within the thickness of the molecular layer of 5 μm, the quantum noise is changes in the gray area. The black curve shows the designed quantum noise of KAGRA. The red and blue solid and dashed lines are the strain sensitivity curve when the shot noise and the radiation pressure noise are maximum and minimum. When the radiation pressure noise is minimized, the strain sensitivity is the same as the designed quantum noise.

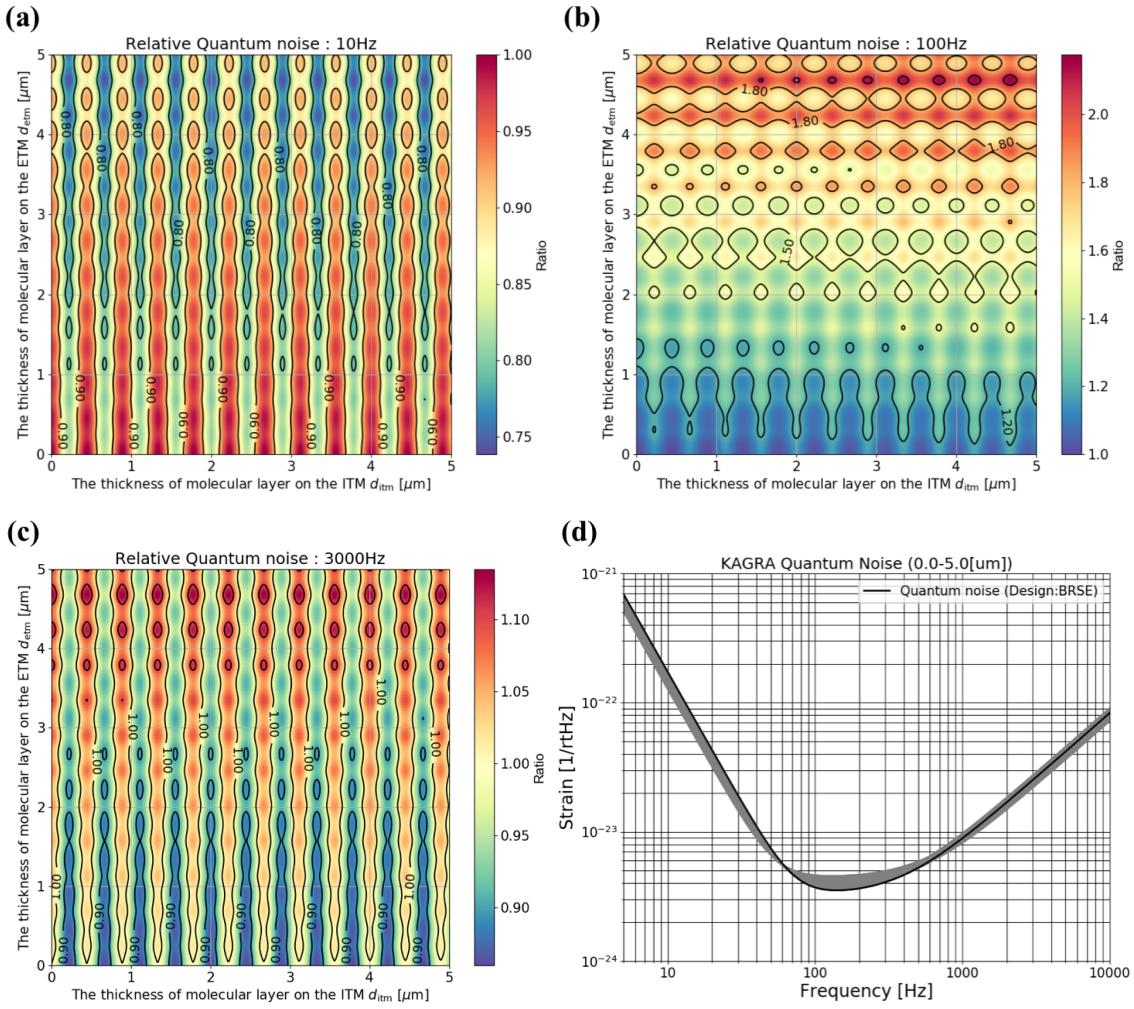

Figure 5.8: Quantum noise in the BRSE with the molecular layer on the cryogenic test masses for the refractive index of N_2. Comparing with the Fig.(5.7), the fluctuation of the quantum noise is much less.

cryogenic test mass and the cryogenic system. The temperature of the system is important to discuss the thermal noise. This section aims to introduce the relation between the temperature of the system and the thickness of the molecular layer.

5.6.1 Amount of the optical absorption

As the source of the heat load to the cryogenic system in KAGRA, the optical absorption of the coating and substrate, and the radiation through the duct shield are taken into account. Additionally, the optical absorption of the molecular layer is needed to be considered. As introduced in Chapter 4, the amplitude of the laser intensity inside a medium follows the Lambert-Beer law, the Eq.(4.7), and the total amount of the absorption A_{mol} inside the medium with the thickness d_{mol} is given by the Eq.(5.15) as

$$A_{\mathrm{tot}} = P_0(1 - \exp(-4\pi\frac{\mathrm{Im}(N_{\mathrm{mol}})}{\lambda}d_{\mathrm{mol}})), \tag{5.15}$$

where $\alpha_{\mathrm{mol}} = 4\pi\frac{\mathrm{Im}(N_{\mathrm{mol}})}{\lambda}$ is the absorption coefficient of the molecular layer.

When the laser power of P_{in} is injected to the mirror with the molecular layer, the part of the laser power P_{vm} is reflected by the molecular layer and the remaining laser power P_{mol} reaches to the coating, though the total reflectivity is given by the Eq.(4.6). The reflectance of the molecular layer if given by the Fresnel coefficient ρ_{vm} between the vacuum and the molecular layer using the Eq.(4.1) as

$$\rho_{\mathrm{vm}} = \frac{n_0 - n_{\mathrm{mol}}}{n_0 + n_{\mathrm{mol}}}, \tag{5.16}$$

and the power reflectance R_{vm} is given as

$$R_{\mathrm{vm}} = \left|\frac{n_0 - n_{\mathrm{mol}}}{n_0 + n_{\mathrm{mol}}}\right|^2. \tag{5.17}$$

Hence, the laser power reflected by the molecular layer is given as $P_{\mathrm{vm}} = R_{\mathrm{rm}}P_{\mathrm{in}}$, and the laser power that transmit the molecular layer is written as

$$P_{\mathrm{mol}} = P_{\mathrm{in}} - P_{\mathrm{vm}} = (1 - R_{\mathrm{vm}})P_{\mathrm{in}}. \tag{5.18}$$

The absorption of the molecular layer on the AR coating of the ITM and the ETM is negligible comparing with that on the HR coating. For the

molecular layer on the AR coating of the ITM, this is because the laser power inside the arm cavity is about 1000 times larger than that inside the PRC. Further, the reflectivity of the ETM is very high and few powers of the laser transmit the HR coating of the ETM and absorbed by the molecular layer on the AR coating. So here we only consider the absorption of the molecular layer on the HR coating of the test masses. Then the amount of the optical absorption inside the molecular layer on the HR coating is written as $A_{\rm HR}$ is written using the Eqs. (5.10), (5.15) and (5.18) as

$$A_{\rm HR} = \frac{(1-R_{\rm vm})}{\pi}\mathcal{F}_{\rm arm}(d_{\rm itm}, d_{\rm etm})G(d_{\rm itm}, d_{\rm etm})(1-\exp(-2\alpha_{\rm mol}d_{\rm i}))P_{\rm in}, \quad (5.19)$$

where $d_{\rm i}$ (i = ITM or ETM) denote the thickness of the molecular layer on the ITM or the ETM. Note that the index of the exponential is doubled by considering the reflection of the coating.

Figures (5.9) shows the calculated result of the total heat input to the KAGRA cryogenic test masses. In the calculation, the absorption in the substrate and the thermal radiation through the duct shield is also cosidered. Even if the thickness of the molecular layer is below 1μm, the heat input to the test masses become larger than 1.5W which is almost twice of the designed heat input. Comparing with the heat input to the ITM and ETM, the heat input to the ITM is slightly correlated with the thickness of the molecular layer on the ETM, though that of the ETM seems to be independent to that on the ITM. This is because the laser power which transmit the ITM is determined by the reflectivity of the ETM due to the PRG change. On the other hand, the absorption in the sapphire substrate of the ETM is negligible because of its very high reflectivity, it is almost independent from the reflectivity of the ITM. In the next subsection, we investigate how this additional heat load changes the temperature of the KAGRA cryogenic payload.

5.6.2 Temperature of the cryogenic system

According to the results in the previous subsection, the molecular layer introduces large heat to the cryogenic test mass. Hence, we need to investigate how this additional heat load changes the temperature of the system.

Below about 100K, the thermal conduction is the main process of the heat transfer. When two objects whose temperature are T_1 and T_2 are connected, the heat is moved from the high temperature side to the low temperature side

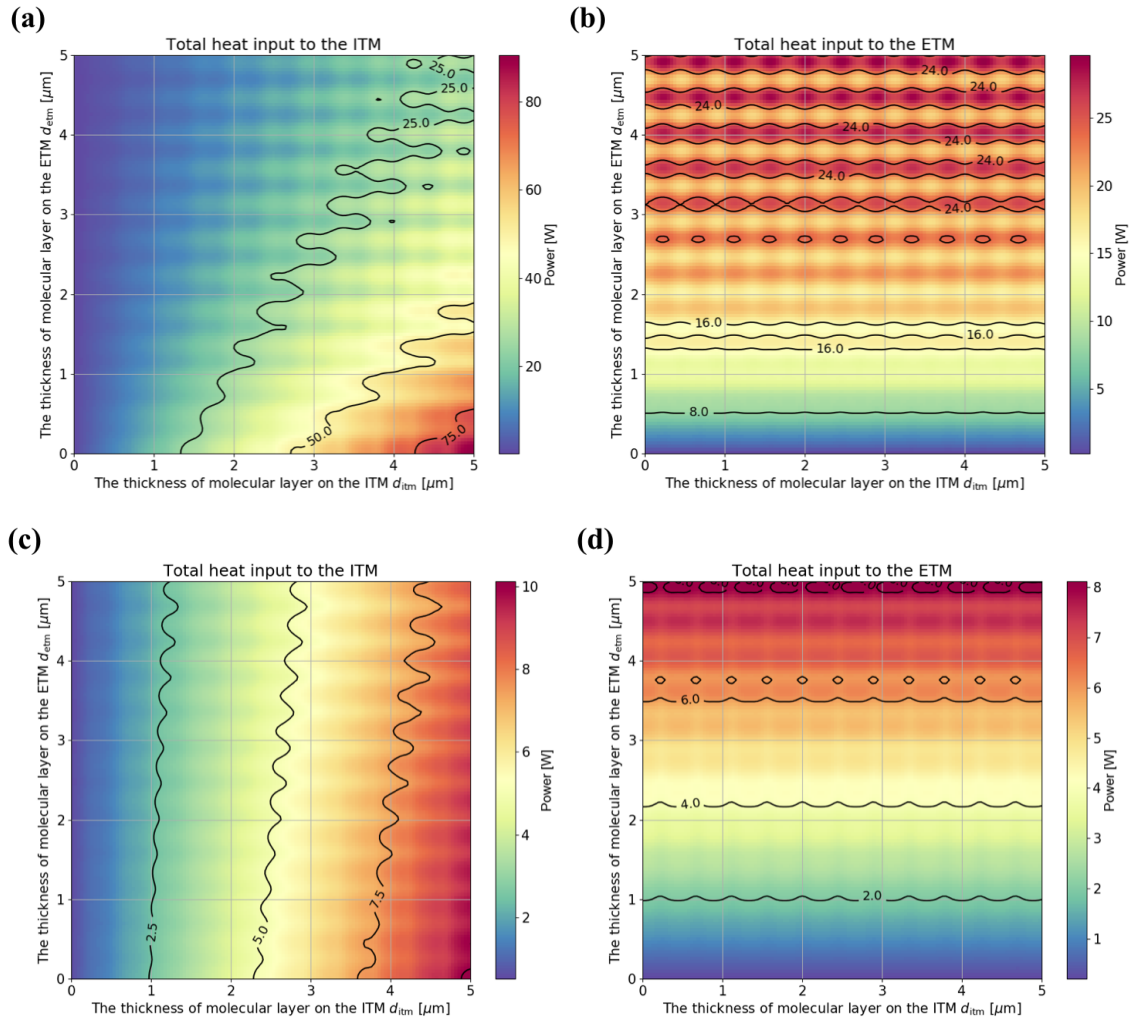

Figure 5.9: Total heat input to the ITM and the ETM. The absorption of the molecular layer has not been taken into account as the heat load to the KAGRA cryogenic system, though it can introduce large heat to the cryogenic test masses when the GWD fully controlled. (a) and (b) : Calculation for the refractive index of N_1. As the result of the strong absorption, it absorbs more than 10W even if the thickness of the molecular layer is 1μm. (c) and (d) : For the refractive index of N_2. Even if the absorption coefficient of the molecular layer is low, it absorbs more than 2W if there is 1μm of the molecular layer, though the designed heat load to the KAGRA cryogenic system is about 0.5W.

by the career such as the phonon and the conduction electron. This process is called the thermal conduction. The amount of heat $\frac{dQ_{\rm cond}}{dt}$ that is transferred by the thermal conduction process in unit time is given by the Fourier law as

$$\frac{dQ_{\rm cond}}{dt} = -\frac{\kappa(T)A}{L}\delta T \tag{5.20}$$

where κ is the thermal conductivity, A and L are the cross-sectional area and the length of the conductor and δT is the temperature difference between two points. When the amount of the heat is time independent, Eq.(5.20) directly provides the equilibrium temperature of the system.

Under the assumption of the energy conservation, the input heat to the test mass goes to the refrigerator, and the temperature of the refrigerator changes depending on the heat load. According to the references [52] and [94], the relation between the cooling power and the temperature of the KAGRA refrigerator is given as the Fig.(5.10). Hence, when we set the input heat to the test mass, it gives the temperature of the refrigerator, and the temperature of the each component is determined following the Eq.(5.20).

Fig.(5.13) shows the calculated temperature of the cryogenic system for the amount of the heat input. The thermal conductivity of the materials is in the appendix A, and the averaged temperature of the two stages are used as the temperature of the conductor. Above the heat load of 5.5 W, the temperature of the test mass beyond the 100 K.Because the total thermal resistance of the system is large because the system is large, small amount of the heat load easily changes its temperature. This temperature rise can worsen the thermal noise of the cryogenic detector, and it possibly limit the sensitivity around 100 Hz where the detector is the most sensitive. In the next chapter, the thermal noise of the cryogenic system is evaluated with this temperature increasing effect.

5.7 Brownian noise

As discussed in above sections, the molecular layer changes the reflectivity of the mirror and adds the optical loss, and it affect to the quantum noise indirectly. When we see the molecular motion of the molecular layer, it can be the noise source. Further, the temperature change affect to the thermal noise of the suspension and the mirror themselves. This section aims to calculate the thermal noise of the molecular layer and the temperature dependence of that of the suspension and the mirror.

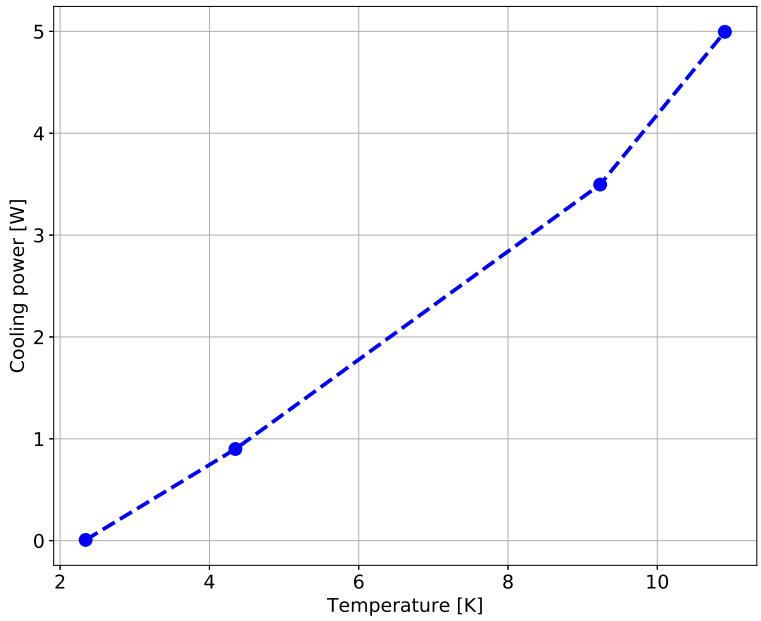

Figure 5.10: Cooling power of the 2nd stage of the KAGRA refrigerator for the cryogenic payload. The data are extracted from the references [52] and [94]. For the calculation of the temperature of the cryogenic payload below, the data were linearly interpolated.

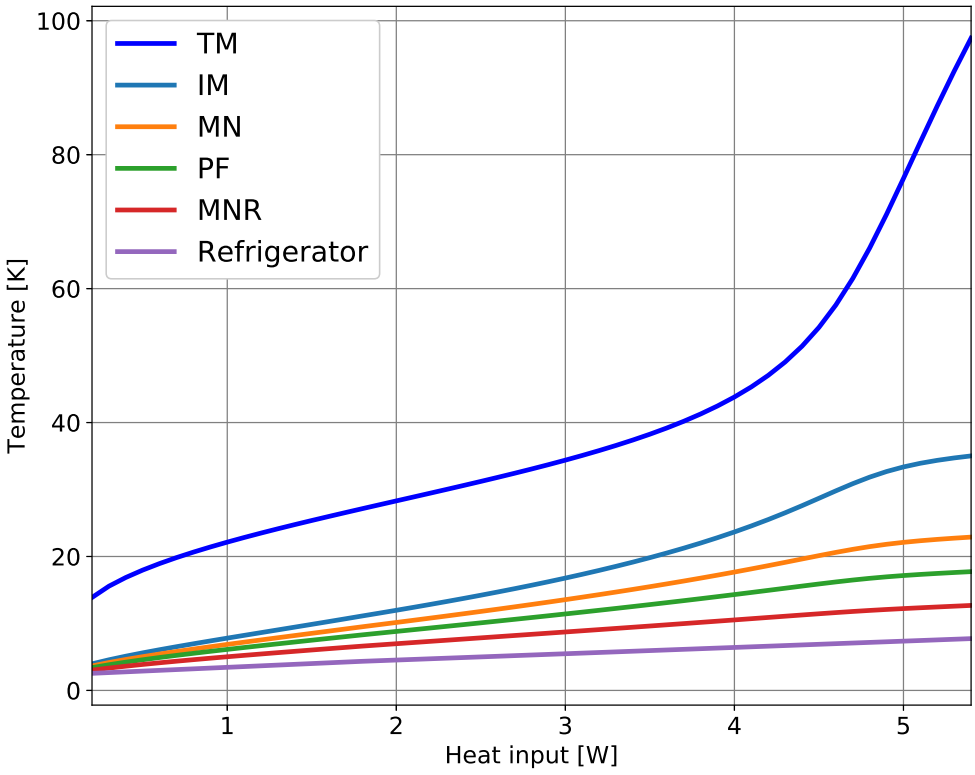

Figure 5.11: Temperature of the cryogenic payload for the input heat to the test mass. The temperature of each stage is evaluated following the Eq.(5.20). The material properties that are used in the calculation is summarized in the appendix A.

In Chapter 1, the Brownian noise is introduced using the Eq.(1.73). This equation is taken the effect of vertical and horizontal material properties into account, though it doesn't describe the effect of the interference of the reflected light from each layer. In the case of the growth of the molecular layer, the effect of the interference is considered to be much larger because the LDA state of ice doesn't have the specific axis. Ignoring the difference of the material properties for the vertical and the horizontal axes, and introducing the interference of the reflected light from each layer, the coating Brownian noise is written as

$$S_{\mathrm{Br}}(f) = \frac{2k_{\mathrm{B}}T}{\pi^2 w^2 f}\frac{1-\sigma_{\mathrm{s}}-2\sigma_{\mathrm{s}}^2}{Y_{\mathrm{s}}}\sum_j b_j d_j \phi_{M_j}, \tag{5.21}$$

with

$$b_{\mathrm{j}} = \frac{1}{1-\sigma_j}\left[\left(1-n_j\frac{\partial\theta_{\mathrm{c}}}{\partial\theta_j}\right)^2\frac{Y_{\mathrm{s}}}{Y_j} + \frac{(1-\sigma_{\mathrm{s}}-2\sigma_{\mathrm{s}}^2)^2}{(1+\sigma_j)^2(1-2\sigma_j)}\frac{Y_j}{Y_{\mathrm{s}}}\right]. \tag{5.22}$$

where j denotes the index of the layer from the top, $\phi_{M_{\mathrm{i}}}$ is the mechanical loss angle of the material M at the j-th layer. The term $\frac{\partial\theta_{\mathrm{c}}}{\partial\theta_{\mathrm{j}}}$ denotes the contribution to reflection phase from each coating layer [28], and it is calculated as

$$\frac{\partial\theta_{\mathrm{c}}}{\partial\theta_k} = \mathrm{Im}\left(\frac{1}{\bar{r}_0}\frac{\partial\bar{r}_0}{\partial\theta_k}\right) \tag{5.23}$$

with

$$\frac{\partial\bar{r}_k}{\partial\theta_j} = \begin{cases} \mathrm{e}^{i\phi_k}\frac{1-r_k^2}{(1+r_k\bar{r}_{k+1})^2}\frac{\partial\bar{r}_j}{\partial\theta_j} & k<j \\ i\bar{r}_k & k=j \\ 0 & k>j. \end{cases} \tag{5.24}$$

where $\bar{r}_{\mathrm{j}}$ is the reflectivity from the substrate to the j-th layer of the coating, and r_{j} is the reflectance of j-th layer.

If we ignore the temperature increasing due to the absorption of the molecular layer, the Eq.(5.22) at the frequency of 100Hz is calculated as Fig.(5.12-a) for the refractive index of N_1 and N_2.

J. Hessinger et al. [95] reported the mechanical loss angle of the amorphous ice film formed on the cryogenic surface. They evaluated the mechanical quality factor using a mechanical oscillator whose original mechanical loss angle is the order of 10^{-8}. The mechanical loss angle of thin ice film formed on the cryogenic oscillator is larger than that of the mechanical oscillator,

and it rapidly damps the mechanical oscillation of the oscillator. Hence, by measuring the time to damp the oscillations gives the mechanical loss angle of the amorphous ice. As a result of the measurement, they found that the amorphous ice on the 20 K surface has a mechanical loss angle of $\phi \sim 1 \times 10^{-3}$. They also reported that the mechanical loss angle of the amorphous ice changes depending on the temperature. It gets worse when the temperature increases, though it gets better after the annealing at the temperature above 100 K. To evaluate the thermal noise of the molecular layer, here we use the mechanical loss angle of $\phi \sim 1 \times 10^{-3}$ and assume that the value doesn't change depending on the temperature Table(5.2) summarize the parameters of the molecular layer that are used for the calculation.

Note that in this calculation, the thickness of the molecular layer is assumed to be the same for four test masses. Figure(5.12-b) also shows the Brownian noise with the molecular layer on the cryogenic test masses with the designed quantum noise of KAGRA.

Name	Symbol	Value	Unit
Temperature	T	20	K
Young's modulus	$Y_{\rm mol}$	3.64	GPa
Poisson ratio	$\sigma_{\rm mol}$	0.2	-
Loss angle	$\phi_{\rm mol}$	1×10^{-3} [95]	rad

Table 5.2: Parameters of the molecular layer for the calculation of the Brownian noise.

Under the assumption that the temperature of the molecular layer is the same as that of the test mass, the temperature of the test mass and the molecular layer is given as the combination of the Figs.(5.9) and (5.13). Within the thickness of the molecular layer below 2.5 μm, the Brownian noise is evaluated as the Fig.(5.13). The amount of the total absorption beyond the 5.5W when the molecular layer is thicker than 2.5 μm. This fact implies that the temperature of the test mass is higher than 100K. Comparing with the Fig.(5.12), the Brownian noise of the ITM coating increases, though that of ETM is not changed so much. This is because absorption inside the substrate. The PRG rise increases the input heat inside the sapphire test mass, and the temperature of the test mass gets higher than the ETM.

From the point of view of the temperature, we can conclude that even if the thickness of the molecular layer is within 2.5 μm and that does not absorb

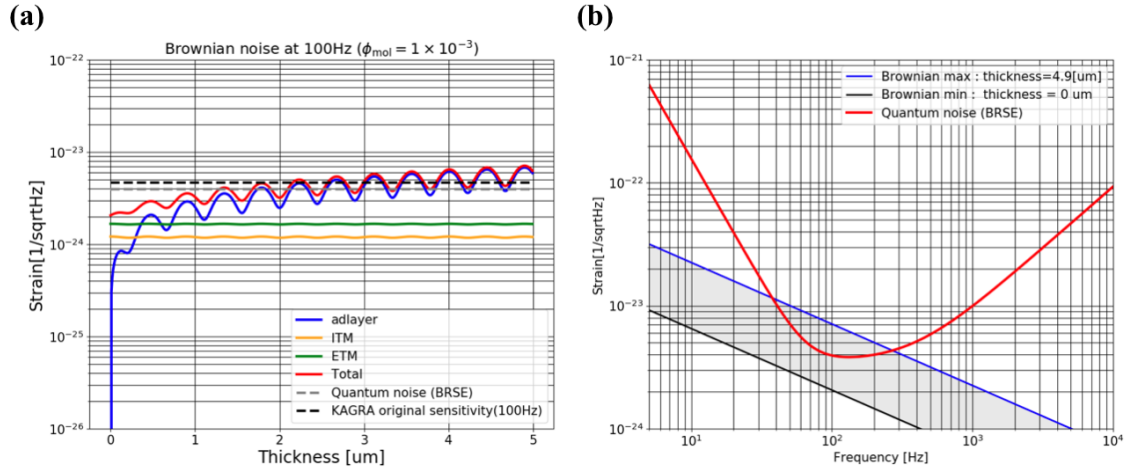

Figure 5.12: Brownian noise of the molecular layer. (a)Comparison of the Brownian noise of the molecular layer with that of the coating on the ITM and ETM. Blue, yellow and green lines are the Brownian noise of the molecular layer and the coating on the ITM and the ETM. Red curve is the total of these Brownian noise and black dashed line is the designed sensitivity of KAGRA at 100Hz. The Brownian noise of the molecular layer can be the dominant Brownian noise, and it possibly contaminate the most sensitive frequency soon. (b)The Brownian noise with the molecular layer changes within the gray area while oscillating, within the molecular thickness of 5μm. Note that these calculations don't include the temperature increasing due to the optical absorption discussed in the previous subsection.

the main laser so much as well the H_2O molecules at room temperature, the temperature of the test mass becomes higher than 100 K which is the temperature five times larger than the target temperature of the KAGRA cryogenic sapphire test mass.

In the next subsection, inspiral range for the BNS is evaluated by considering the modification of the quantum noise, Brownian noise and the suspension thermal noise, though the effect of the parameters that have the temperature dependence are ignored.

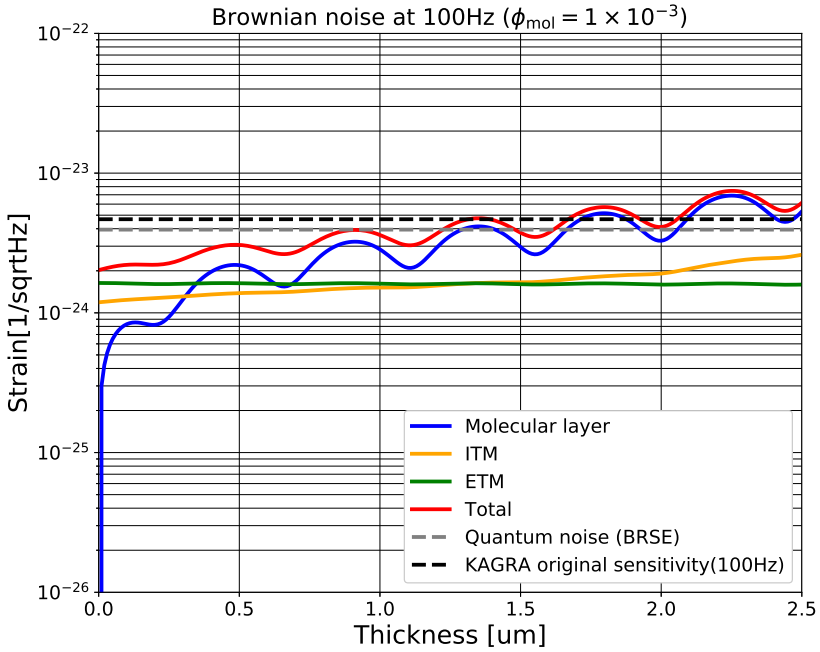

Figure 5.13: Brownian noise of the molecular layer with the temperature effect due to the optical absorption. The amount of the total absorption beyond the 5.5W when the molecular thickness of 2.5 μm. Comparing with the FIg.(5.12), the Brownian noise of the ITM coating increases, though that of ETM is not changed so much. This is because absorption inside the substrate. The PRG rise increases the input heat inside the sapphire test mass, and the temperature of the test mass gets higher than the ETM.

5.8 Inspiral range

As the total of the quantum noise, the Brownian noise and the suspension thermal noise modification due to the molecular layer formation, the sensitivity of the molecular layer fluctuate inside the gray area as shown in the Fig.(5.14-a). In this calculation, the temperature dependence of the parameters such as the mechanical loss angle and the resonant frequencies are not included. If we assume that the molecular layer formed on the test masses coherently, then within the thickness of 2.5 μm, the sensitivity moves inside the gray area. Using the sensitivity, the inspiral range is calculated for 1.4 $M_{\odot}$ binary neutron star binary system as shown in Fig.(5.14-b). Without the

molecular layer, it is 137 Mpc, and it continuously decreases while oscillating. The inspiral range without the molecular layer is little better than the KAGRA original one. This is because the temperature of the test mass and the intermediate mass used in this calculation is based on the temperature evaluation shown the Fig.(5.13), and it is slightly colder than the designed temperature. At worst, the inspiral range decrease to 75 Mpc, and it implies that the detection rate of the BNS is decreased by 84 %.

The parameters that have the temperature dependence would worse the sensitivity more, and the measurements of the temperature dependence of the parameters are quite important to characterize the cryogenic GWD well. In spite of the huge impacts on the GWD, there is no system in KAGRA to deal with the molecular layer formation, though the duct shield delays that slightly. As one of the system to deal with the molecular layer formation, the CO_2 based thermal desorption system has been tested in the laboratory. Next chapter introduces the thermal desorption and the developed system.

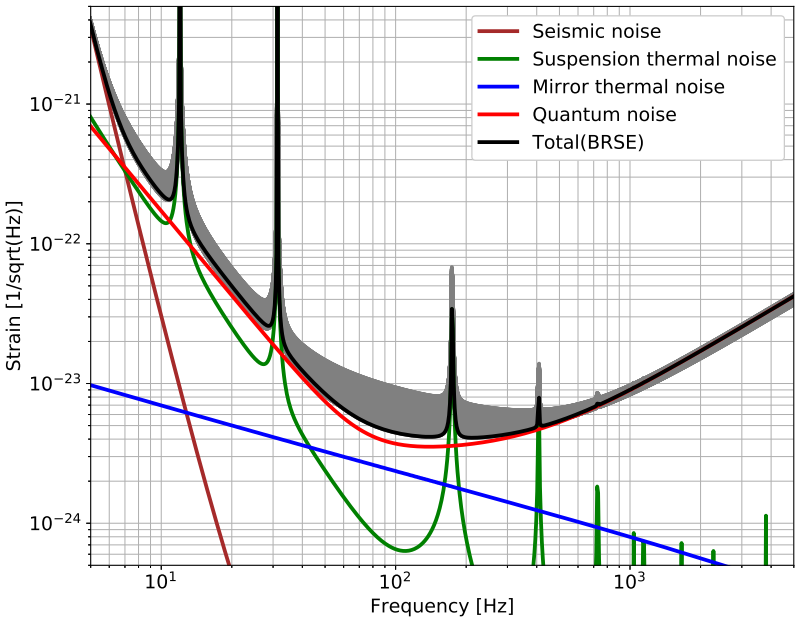

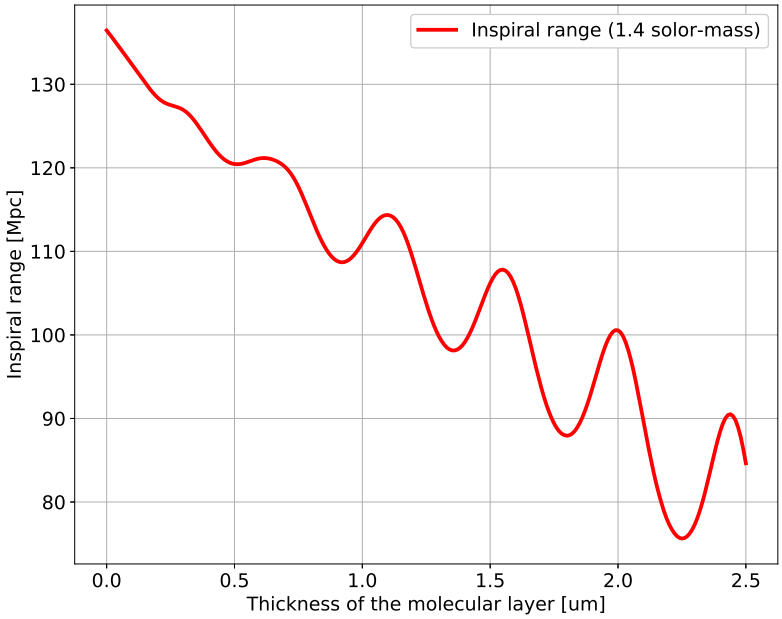

Figure 5.14: KAGRA sensitivity with the molecular layer. (upper) As a result of the molecular layer formation, the quantum noise, the Brownian noise and suspension thermal noise are modified. Within the thickness of 2.5 μm, the sensitivity moves inside the gray area. Note that the effect of the temperature increase is not taken into account, though the equivalent quantity of the optical loss is considered. (lower)Using the sensitivity, the inspiral range is calculated for 1.4 $M_{\odot}$ binary neutron star binary system. Without the molecular layer, it is 137 Mpc, and it continuously decreases while oscillating.

Chapter 6
LASER INDUCED THERMAL DESORPTION SYSTEM

As discussed in the previous chapters, the molecular layer is formed on the cryogenic mirrors in the GWD, and it affect to the sensitivity of the detector so much. Even if the molecular formation speed becomes very slow enough to observe GWs in the future with the improvement of the vacuum technology, the troubles of the cryogenic and the vacuum system easily introduce thick molecular layers on the cryogenic mirrors. For example, the formation of a thick molecular layer was reported during the initial cooling in KAGRA, and it remarkably decreased the finesse [96]. If the test mass is cooled down about the same time with the other cryogenic system, the initial cryopump which adsorbs a quite huge number of molecules on the surface happens not only the surface of the radiation shields but also that of the test mass. Further, when the cryogenic system accidentally stopped and warmed up, these adsorbed molecules were released, and some of them reached the test mass which was kept at a cryogenic temperature a long time due to the time constant of the cryogenic system, and finally formed very thick molecular layers. Figure (6.1) shows the pictures of the test mass with the incident of the green laser when it is at room temperature, at cryogenic temperature and after the trouble of the cryogenic system [97]. When it is at room temperature, the green beam is not so obvious, but the beam shape was seen when it cooled down due to the molecular layer formation, and the amount of the scattered light becomes larger after the trouble of the cryogenic system.

During these problems, the finesse of the KAGRA arm cavity was measured several times. The finesse was about its designed value, $\mathcal{F} \sim 1500$ when the mirrors are the room temperature. After the cooling down and the thick molecular layer happened on the cryogenic mirror, the finesse decreased to

about $\mathcal{F} \sim 200$ at worst [98]. The optical loss due to the scattering of the thick molecular layer is considered to reduce the optical performance of the KAGRA arm cavity.

To remove these molecules, the test mass is warmed up by stopping the refrigerators. Usually, to remove H_2O, the temperature of the test mass is needed to increase to about 200K, and it takes order of one month to return to the cryogenic temperature. During this process, the detector cannot observe the GWs due to the large thermal noise and the thermal drift, and it worsens the rate of the multi-detector operation.

This problem can happen not only in KAGRA but also in the next generation cryogenic GWD such as ET and CE. To deal with the problem of keeping the operation time, the development of the active temperature actuation system is needed. For this purpose, the laser induced thermal desorption system was tested on the laboratory. In this section, the theory of the thermal desorption is introduced first, and the developed desorption system is described. Finally, this experiment is scaled to the KAGRA case for the installation near the future.

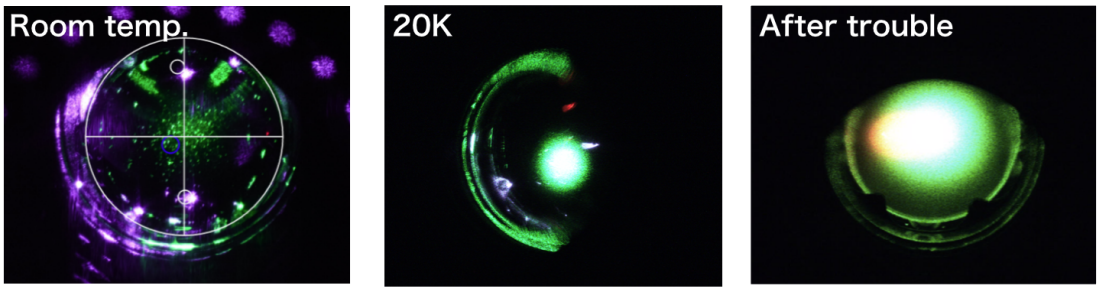

Figure 6.1: Pictures of the KAGRA test mass with the green laser injection. The shape of the green laser is not obvious when it is at the room temperature. But, when it cooled down without enough pumping before, the thick molecular layer formed and the green laser scatted. After the trouble of the refrigerator, it become worth and the mirror surface looked like the ground glass. The pictures were copied from KAGRA log book [97].

6.1 Laser induced thermal desorption

The thermal desorption is one of the techniques to remove the molecular layer from the cryogenic surface [99]. Using a heater on the cryogenic surface, the temperature of the surface can increase enough to sublime the molecules. However, in the GWD, a heater will introduce the vibration to the test mass through the cable, and it would contaminate the sensitivity. To avoid that, development of the non-contact heat applying system, namely the laser induced desorption system, is required.

Applying the long wavelength of laser and exiting the molecular vibrations, the temperature of the system is increased enough to escape from the surface potential. Especially, the process that desorb adsorbed molecules by increasing the temperature of the system is called the thermal desorption, and it is characterized by the depth of the surface potential, the number of molecules in the unit area, the reaction order and the speed of the temperature increasing.

In GWDs, the CO_2 laser have been used for the correction of the radius of curvature of the mirror. When the mirror substrate absorbs the laser, the center of the mirror gets higher temperature comparing the edge of the mirror, and this temperature unbalance effectively causes the lens. This phenomenon is generally called thermal lens effect, and it worsens the mode matching of the laser to the cavity [100]. To solve the thermal lensing effect, the CO_2 laser is applied on the edge of the test mass to cancel the thermal lensing effect [101]. But in the cryogenic GWD, it was concluded that the amplitude of the thermal lensing is enough small and it doesn't affect the detector [102]. So the development of the CO_2 laser system has not proceeded in KAGRA. To remove the molecular layer while keeping the Cooperativeness with other GWDs, the development of the CO_2 laser induced thermal desorption system for cryogenic GWDs is meaningful. Next section introduces the thermal desorption.

6.2 Theory of thermal desorption

When the molecules hit the cryogenic surface, it is caught up by the surface potential whose potential depth is E_{abs}. The energy E_{des} to remove the molecules from the potential equals to the potential depth E_{des}, $E_{\mathrm{des}} = E_{\mathrm{abs}}$,

if the dissociation of the molecules doesn't happen. The number of molecules $\frac{dN_S}{dt}$ that are desorbed from the potential in unit time follows the Arrhenius behavior as [103]

$$\frac{dN_S}{dt} = A(N_S)^m e^{-\frac{E_{des}}{k_B T}} \tag{6.1}$$

where N_S is the number of molecules on the surface in unit area, A is the pre-exponential factor, m is the reaction order and T is the temperature of the surface. Using the temperature change coefficient $\beta = \frac{dT}{dt}$, the Eq.(6.1) is rewritten as

$$\frac{dN_S}{dT} = A\frac{(N_S)^m}{\beta} e^{-\frac{E_{des}}{k_B T}}. \tag{6.2}$$

Eq.(6.2) described the thermal desorption. Especially when the temperature coefficient is controlled to be the constant $\beta = \text{const.}$, the thermal desorption is called the temperature programmed desorption (TPD) [104]. For the H_2O, the Eq.(6.2) is plotted as shown in the Fig.(6.2) using the parameters in the table(6.1). In the TPD, the number of molecules desorbed from the surface increases exponentially first, and when the number of molecules on the surface becomes low, the desorption stops rapidly. This is the unique desorption signal when the reaction order $m = 0$, and the starting temperature of the desorption is depending on the temperature coefficient and the desorption energy, and when these parameters are the same, only the height of the peak changes depending on the pre-exponential factor A.

Molecules	N_2	O_2	H_2O	Unit
Desorption energy E_{des}	0.5 [105]	0.072 [105]	0.090 [105]	eV
Reaction order m	0			—
Pre-exponential factor A	10^{30} [106]			$1/cm^2s^1$

Table 6.1: Parameters for the thermal desorption of N_2,O_2, and H_2O.

6.3 Experiment

In this section, the TPD experiment and the heating experiment using the CO_2 are introduced.

In the TPD experiment, the water vapor is applied to the sample in the cryostat, and the temperature of the sample is increased using the heater attached on the sample. By increasing the temperature of the sample linearly,

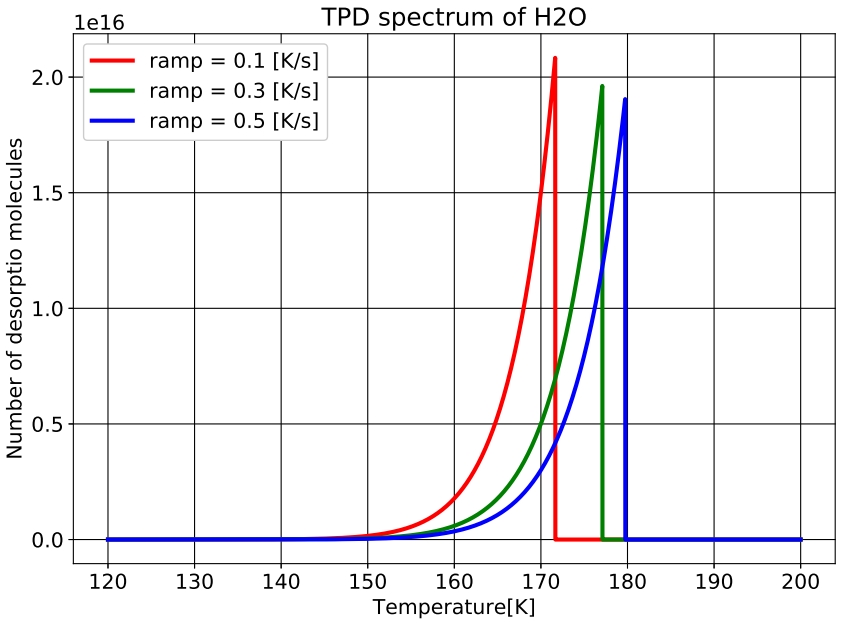

Figure 6.2: TPD curve of the H_2O desorption. The number of desorbed molecules exponentially increased for the reaction number of $m = 0$. When the number of molecules on the surface becomes few, the desorption stop rapidly. The starting point of the desorption is depending on the temperature coefficient β.

the TPD spectrum is measured by the mass spectrometer. The purpose of this experiment is to confirm the thermal desorption because, in the next experiment, it's possibly difficult to measure the TPD spectrum due to the experimental setup. Hence, the experiment was separated to the two: the TPD experiment and the heating experiment.

In the heating experiment, the small sapphire sample was set inside the cryostat and cooled down to around 20 K, and the CO_2 laser was applied to heat it up. This sapphire sample is made with the actual KAGRA test mass, the coating on the sample is the same as that of the ETM. The incident laser power is increased from 0.3 W to 7.2 W step by step, and the achievable temperature was monitored for each laser power. Simultaneously with the heating, the molecular desorption was measured using the vacuum gauge and the mass spectrometer, and it was confirmed that the temperature of the sample was increased enough to desorb the molecules. Finally, the absorbed

laser power was calibrated using the heater attached near the sample. Using the calibrated power, the laser power required to heat the cryogenic test mass in KAGRA is calculated in the next section.

6.3.1 TPD experiment

In the TPD experiment, water vapor was applied on the sample made of fused silica, it was heated by the hater attached on the sample, and the TPD spectrum was measured by the mass spectrometer. Figure (6.3) shows the conceptual figure of the cryogenic-vacuum system. The system is mainly composed of the vacuum pumps, the refrigerator, the vacuum gauge and the mass spectrometer, the molecular injection system and the sapphire sample.

The vacuum pumps, RV8 and STP-301 manufactured by EDWARDS and SEIKO SEIKI, are connected to the cryostat through about 0.8 m of the flexible tube.

The refrigerator and the compressor are PT415-RM and CP1000 manufactured by CRYOMECH. Inside the cryostat, there is the single radiation shield made of copper and the optical table made of aluminum. The refrigerator is connected to connected to the optical table through the heat links made of pure aluminum. Because the radiation shield has holes to input the laser inside the cryostat, large amount of the thermal radiation is injected through the holes and it results in the high temperature of the cryogenic parts.

The molecular injection system is composed of the two tanks; one to put the source of the molecules, and the other is to keep the gassed source inside. In this experiment, because H_2O is considered to be the molecules that requires the most high temperature to remove from the cryogenic surface in KAGRA, the pure water was set inside the tank for the source. The sample made of fused silica was attached on the holder made of aluminum using the indium foil. The sample is 25.4 mm in diameter and 8mm in thickness. The holder is supported by the bar made of glass epoxy, and the length of the bar is 45.5 mm. Glass epoxy thermally isolates the sample from the cryogenic system to heat the sample uniformly. To cool the sample to below 100 K to adhere the water vapor, the sample is connected to the table via the heat switch. Thermometer model DL670 manufactured by Lake Shore Cryotronics, Inc. is attached on the holder, and the temperature of the sample is measured by this thermometer.

The mass spectrometer model BGM-102 manufactured by ULVAC, Inc.

is attached near the sample to measure the TPD spectrum of H_2O molecules.

To increase the temperature of the sample linearly, the thermometer on the sample was connected to the temperature controller model 331 Temperature Controller manufactured by Lake Shore Cryotronics Inc., and it was increased to at 200 K via PID control. The temperature coefficient was set to $\beta = 4$ K/s.

Before the measurement, water vapor was applied to the sample. Figure(6.4-a) shows the temperature of the sample with the fitting line when it heated. Because the temperature rise was set to linear, the data was fitted by the linear function. As the result, the temperature coefficient was evaluated to be $\beta = 0.08204 \pm 0.000014\,\mathrm{K/s}$ at this measurement.

Figure(6.4-b) shows the partial pressure of H_2O molecules for the temperature with the fitting curve. Note that the vertical axis is converted to the natural logarithm of the product of the thermal coefficient β and the measured partial pressure, and the horizontal axis is the reciprocal of the temperature.

The desorption was started from 150 K, and the data was fitted using the Eq.(6.2). As the result, the desorption energy was evaluated to be $E_{\mathrm{des}} = 52.1 \pm 0.1\,\mathrm{kJ/mol}$.

By changing the temperature of the sample, the formed molecular layer is removed. In the next subsection, the heating experiment with the CO_2 laser is introduced.

6.3.2 Experimental setup

In this subsection, the experimental setup is introduced. The experimental system is mainly composed of two small setups, the optical system for the CO_2 laser and the cryogenic-vacuum system which includes the sapphire sample.

Optical system

Figure(6.5) shows schematic view and the picture of the optical system for the CO_2 laser. The optics is composed of the CO_2 laser, the steering mirrors, the flipping mirror and the power meter. The CO_2 pulse laser model ULCR-100 manufactured by Universal laser systems, Inc. was used. The repetition frequency of the laser is set to be 10 kHz, and the pulse width is changed to adjust the laser power, though the pulse height is always constant. When the

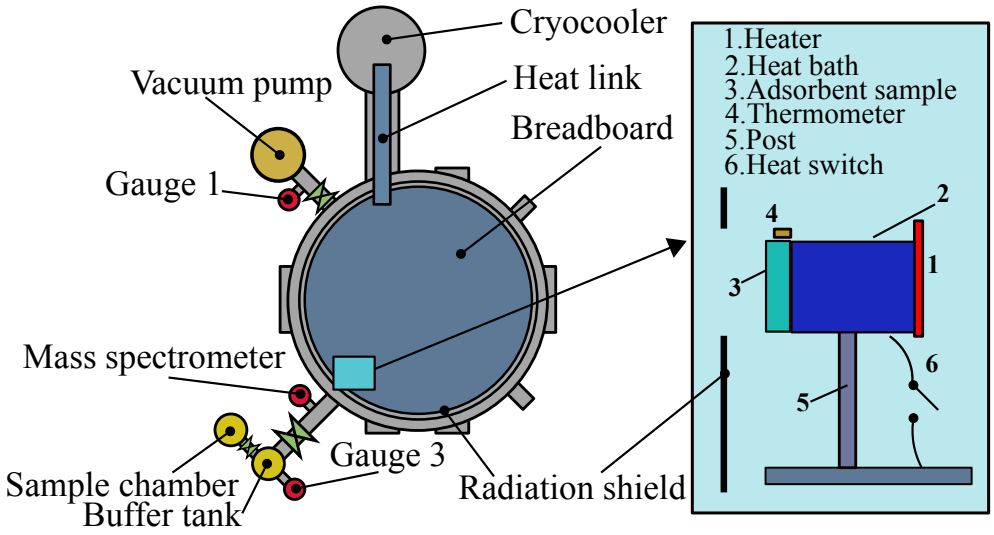

Figure 6.3: Schematic image and picture of the cryogenic-vacuum system. The system is mainly composed of the vacuum pumps, the refrigerator, the vacuum gauge and the mass spectrometer, the molecular injection system and the sample.

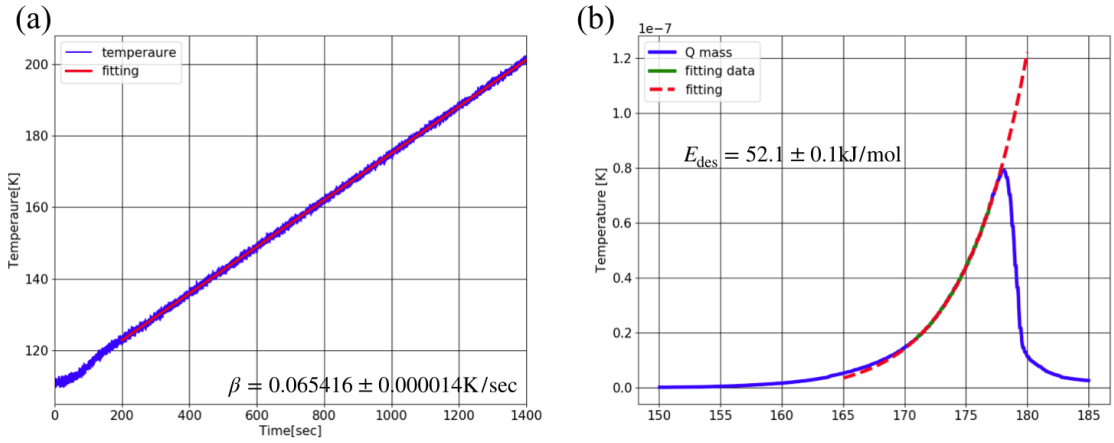

Figure 6.4: Analysis of the TPD spectrum. The temperature of the sample was changed linearly using the temperature controller. (a)The temperature of the sample during the measurement. The temperature coefficient was evaluated to be $\beta = 0.06541261 \pm 0.000014\,\mathrm{K/s}$. (b)Measured TPD spectrum with the fitting. Note that the vertical axis is converted to the natural logarithm of the product of the thermal coefficient β and the measured partial pressure, and the horizontal axis is the reciprocal of the temperature. As a result of the fitting, the desorption energy of the water molecules is evaluated to be $E_{\mathrm{des}} = 52.1 \pm 0.1\,\mathrm{kJ/mol}$.

pulse width is set to the maximum, the laser power is larger than 100W. As the steering mirror, the gold coated copper mirror manufactured by Thorlabs, Inc. were used, and the reflectivity of the mirror is about 99% for the angle of incident of 0° - 45°. The flipping mirror leads the laser to the power meter to estimate the incident laser power to the cryostat. The power meter is model LM-100 manufactured by Coherent, Inc, and when the laser injected, the laser was aligned to hit the center of the sensor.

Finally, the laser is injected to the cryostat through the periscope. As the viewport, the substrate made of zinc selenide (ZnSe) with the anti-reflection coating is attached. The length of the laser path from the laser exit to the viewport is 1000mm, and that from the viewport to the sapphire sample is 450mm.

Before the experiment, the relation γ between the laser power just after the laser emission P_{in} and the just before the sapphire sample P_{sample} was evaluated in the air. First the laser was picked up using the flipping mirror and the laser power was measured, then the laser power was also measured at the position of the sapphire sample. The averaged ratio of these two laser power is evaluated to be

$$\gamma = \frac{P_{\mathrm{sample}}}{P_{\mathrm{in}}} = 0.91 \pm 0.01. \tag{6.3}$$

This ratio gives the effective transmittance of the optical path, and it indicates that the 0.91 ± 0.1 % of the emitted laser power is reached to the sapphire sample.

Cryogenic-Vacuum system

The cryogenic vacuum system is almost same as that of the TPD experiment except for the position of the sample, the mass spectrometer and the molecular injection system. Figure (6.6) shows the conceptual figure of the cryogenic-vacuum system.

The sapphire sample was made with the KAGRA sapphire test mass, and its coating is the same as that of the ETM. This sapphire sample is attached on the holder made of aluminum using the indium foil. The sample is 25.4 mm in diameter and 8 mm in thickness. The holder is supported by the bar made of stainless steel, and the length of the bar is 45.5 mm. To introduce the CO_2 laser to the sapphire sample and cool it down well, the sample was set at the center of the table.

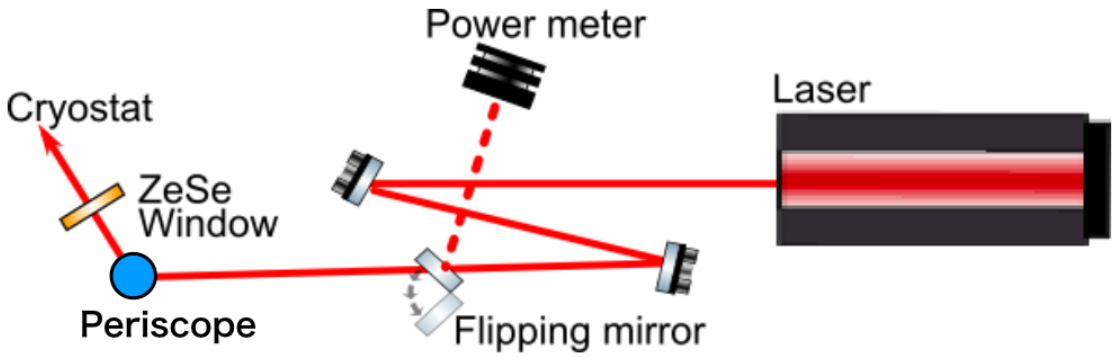

Figure 6.5: Schematic image of the optics. The CO2 laser is lead to the cryostat using the steering mirror and the periscope. By pick the laser up using the flipping mirror, the incident laser power can be measured.

As shown in the Fig.(6.6), the sample is not aligned to the molecular injection system and the mass spectrometer. This setup makes it difficult to measure the desorbed molecules while the heating process. The measurement was tried by increasing the amount of the incident molecules, though the obvious spectrum of H_2O molecules was not observed. It is considered that almost all of the desorbed H_2O molecules are absorbed by the radiation shield and other cryogenic part before they reach to the mass spectrometer. Hence, only the absorption coefficient of the sapphire sample for the the CO_2 laser is evaluated in this experiment.

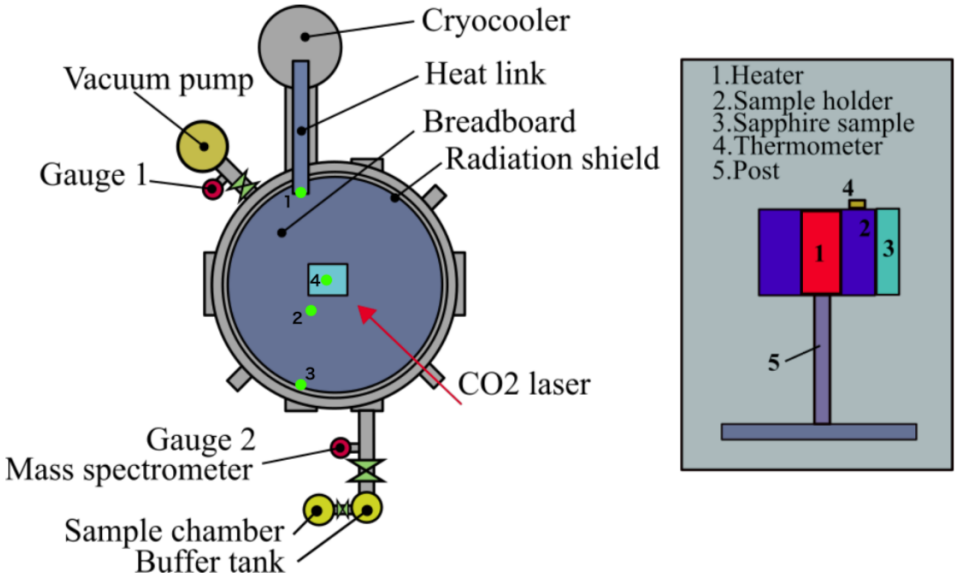

Figure 6.6: Schematic image and picture of the cryogenic-vacuum system. The system is mainly composed of the vacuum pumps, the refrigerator, the vacuum gauge and the mass spectrometer, the molecular injection system and the sapphire sample. Green dots with the number shows the position of the thermometers in the cryostat.

6.3.3 Measurement of transverse mode

The transverse mode of the CO_2 was evaluated by the knife edge method. Figure(6.7) shows the schematic appearance of the measurement. The laser power was measured while chopping the beam using the knife. Figure(6.8-a) shows the measured power for the position of the knife along the beam

radius. If we assume that the beam is the gaussian beam, the transverse power distribution $P(x, y)$ in the cross sectional plane is described as

$$P(x,y) = \frac{2P_0}{\pi\omega^2} \exp\left(-\frac{2((x-x_0)^2+(y-y_0)^2)}{\omega^2}\right) \tag{6.4}$$

with

$$\omega = \omega_0 \sqrt{1+\left(\frac{z}{z_0}\right)^2}, \tag{6.5}$$

where (x_0, y_0), P_0, ω_0, z are the position of the beam center, the radius position, the laser power, and the beam radius at the waist position, and the position along to the beam propagating axis. When this beam is chopped using the knife, the laser power after the knife decreases and it is measured as

$$P = \frac{P_0}{2}\left(1 - \mathrm{erf}\left(\frac{\sqrt{2}(x-x_0)}{\omega}\right)\right), \tag{6.6}$$

where

$$\mathrm{erf}(x) = \frac{2}{\sqrt{\pi}} \int_0^x \exp\left(-t^2\right) dt. \tag{6.7}$$

By fitting the measured laser power using the Eq.(6.6), the beam waist $\omega(z)$ can be evaluated. Finally the series the measured beam waist at various position z along the beam axis give the transverse propagation of the laser. Figure (6.8) shows the measured laser power for the chopping amount of r_{chop}, and red line shows the fitting function. Further, Fig.(6.8-b) is the evaluated beam radius at the position z from the laser, and it was fitted using the Eq.(6.5). As the result, the waist position and the waist size of the laser are $z_0 = -176 \pm 62$ mm and $\omega_0 = 1.356 \pm 0.081$ mm, and at the sapphire sample where the distance from the laser is $z = 1450$ mm, the laser waist is evaluated to be $\omega = 4.27^{+0.32}_{-0.38}$ mm. So the peak intensity I_{max} at the sapphire sample is calculated to be $I_{\mathrm{max}} = 17.5^{+3.6}_{-2.3}$ W/cm^2 when the laser power of 5 W are injected.

6.3.4 Laser heating

After the enough cooling, the temperature of the sapphire sample was 21 K. Against to the cooled sapphire sample, the laser was injected by changing the laser power from about 0.8 W to 6.7 W step by step.

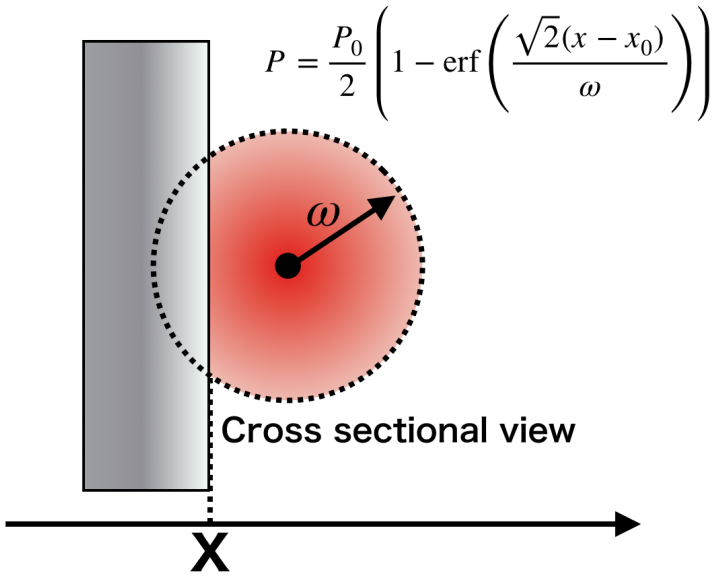

Figure 6.7: Schematic image of the knife edge method to measure the beam radius at position z.

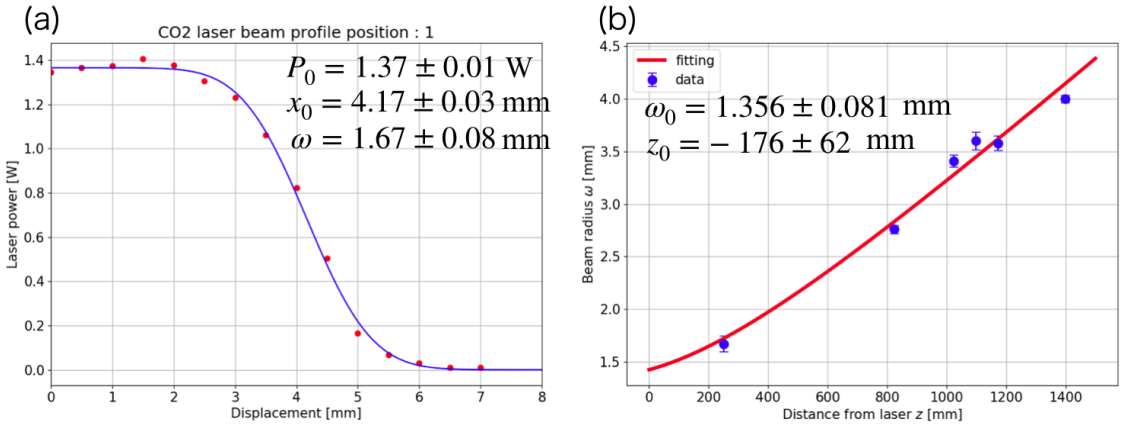

Figure 6.8: Laser power measured for the position of the knife along the cross-sectional axis. Red dots is the laser power measured when the knife is at the position x, and red line is the fitting function.

The incident laser power was evaluated by picking the laser up using the flipping mirror for 10 minutes before and after the injection, and the incident laser power is given as the averaged value of these 20 minutes of the power measurement. Figure (6.9) shows the temperature change when the laser was injected, and the evaluated laser power is described in the legend of the figure. The temperature of the sapphire sample starts to increase rapidly when the CO_2 laser started to input. The incident laser power was evaluated by the laser power measured before and after the injection for 10 minutes using the flipping mirror. The optical loss during the propagation, Eq.(6.3), is taken into account. When the incident laser was stopped, the temperature of the sample started to decrease rapidly.

Using the temperature during the heating process and the desorption energy of the water molecules, the desorption spectrum is calculated as the Fig.(6.10). The desorption started from about 170 K and we can conclude that the heating was enough to remove the water molecules from the sapphire sample. In the next subsection, we discuss about the required laser power to heat the cryogenic test mass up to remove the molecules.

6.4 Scale to the KAGRA

Above the temperature of 100 K, the thermal radiation is the main process to transfer the heat.

The energy that is released in unit time from unit area due to the thermal radiation is given by the Stefan-Boltzmann law as

$$E_{\mathrm{tot}} = \varepsilon \sigma T^4, \tag{6.8}$$

where $\sigma = 5.67 \times 10^{-8}\,\mathrm{W/m^2/K^4}$ is the Stefan-Boltzmann constant, T is the temperature of the object or the surface and ε is the emissivity. When we consider the heat transfer via the thermal radiation between two surfaces whose area are S_1 and S_2 ($S_1 << S_2$), the amount of the heat $\frac{dQ_{\mathrm{rad}}}{dt}$ moved from the S_1 surface to the S_2 surface in unit time is written as

$$\frac{dQ_{\mathrm{rad}}}{dt} = \varepsilon_1 S_1 \sigma (T_1^4 - T_2^4) \tag{6.9}$$

where T_1 and T_2 are the temperature of the surfaces. As a total of the conduction and the radiation heat transfer, the amount of the heat to warm the KAGRA cryogenic test mass is determined.

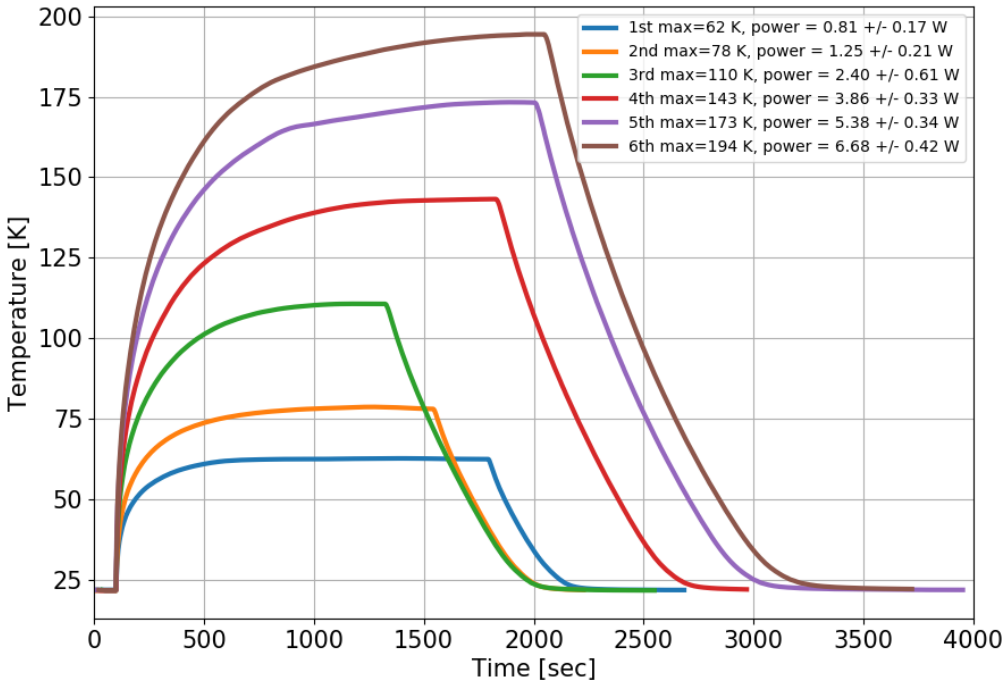

Figure 6.9: Temperature of the sapphire sample with CO_2 laser injection. The temperature of the sapphire sample start to increase rapidly when the CO_2 laser started to input. The incident laser power was evaluated by the laser power measured before and after the injection for 10 minute using the flipping mirror. The optical loss during the propagation, Eq.(6.3), is taken into account. It starts to decrease rapidly when the incident laser was stopped.

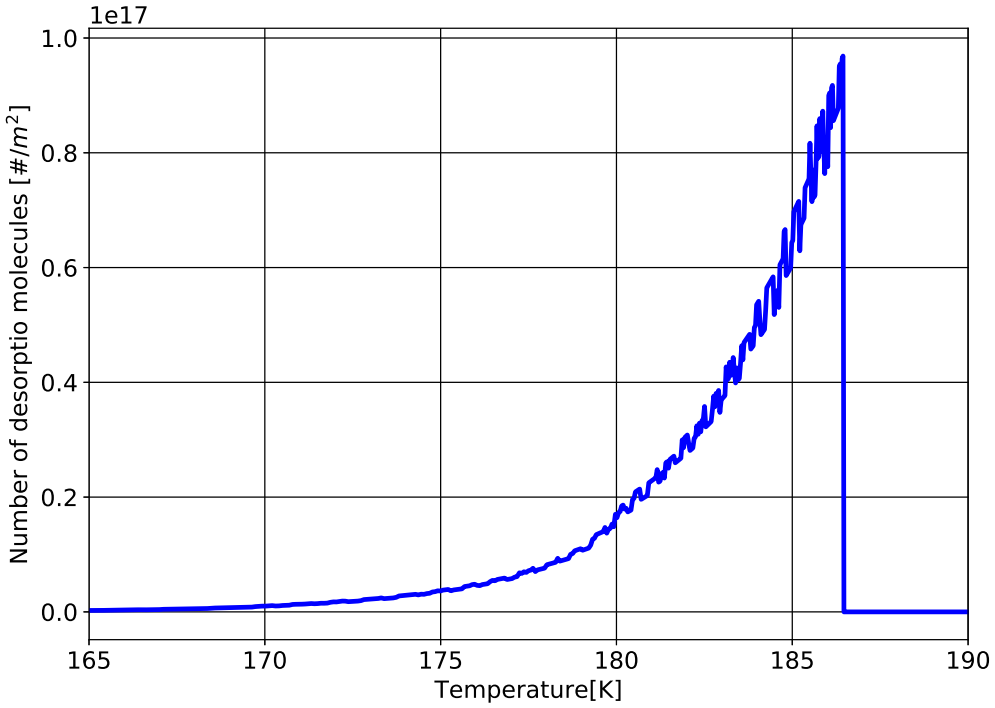

Figure 6.10: Simulated thermal desorption of H_2O molecules during the heating process with CO_2 laser. Substituting the temperature coefficient β calculated from the temperature during the heating process shown in the FIg.(6.9) and the desorption energy $E_{\mathrm{des}} = 52.1 \pm 0.1\,\mathrm{kJ/mol}$ into the Eq.(6.2) gives the thermal desorption spectrum.

Figure (6.11) shows the calculated results of the relation between the amount of heat input to the cryogenic mirror and the temperature. For the calculation, the surface area of the test mass against the 8 K radiation shield is $S_1 = 0.076\,\mathrm{m}^2$, and the emissivity ε_1 of the sapphire test mass are assumed. As a result of the calculation, it implies that the heat input of $P_{\mathrm{CO}_2} = 13.5$ W can increase the temperature of the cryogenic mirror to 200 K. Figure (6.12-a) shows the temperature of the cryogenic test mass after the heat input of $P_{\mathrm{CO}_2} = 13.5$ W is applied. The temperature of the mirror gets 180 K after 30 hours and 200 K after 110 hours.

Substituting the heating process shown in Fig.(6.12-a) into Eq.(6.2) gives the thermal desorption of H_2O molecules from the KAGRA cryogenic mirror as Fig.(6.12-b). The desorption of the molecules starts from 150 K and ends at 170 K. Hence, by applying $P_{\mathrm{CO}_2} = 13.5$ W of CO_2 laser, the temperature of the cryogenic mirror increases to 180 K which is enough to desorb all of adsorbed H_2O molecules after 30 hours.

After the heating of the test mass to the 200 K, the temperature of the test mass decrease to the nominal temperature after about 30 hours as shown in Fig. (6.13). For the calculation, as the initial temperature of the cryogenic system, the temperature of 45 K for IM, and 30 K for the other parts was applied. The temperature of the refrigerator was kept at 7 K which is the nominal temperature when the total heat load is 5.5 W.

As the total of the heating and the cooling, it takes about 60 hours to remove the molecular layer perfectly and return to the nominal temperature. Without the system, it is considered that it takes 1.5 months for the same process. It is concluded that the desorption system using a CO_2 laser can remove the molecular layer perfectly and shorten the observation dead time to recover from the problem of the molecular layer from 1.5 months to 60 hours.

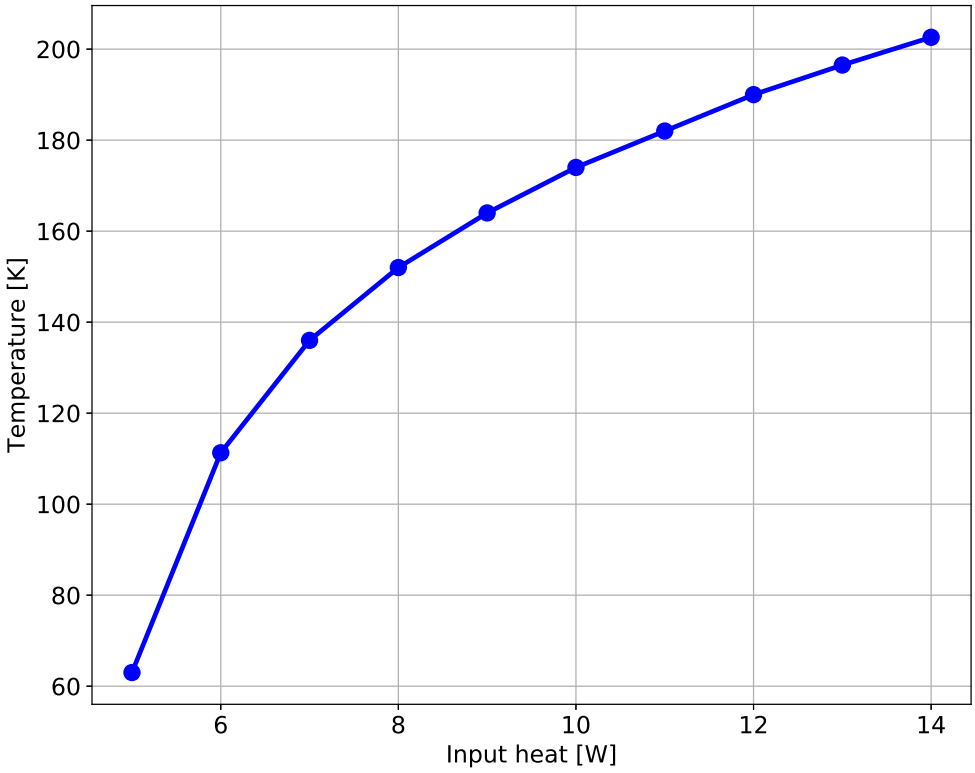

Figure 6.11: Relation between the amount of heat input and the temperature. To increase the temperature of the test mass up to 200 K, the laser power of 13.5 W is required.

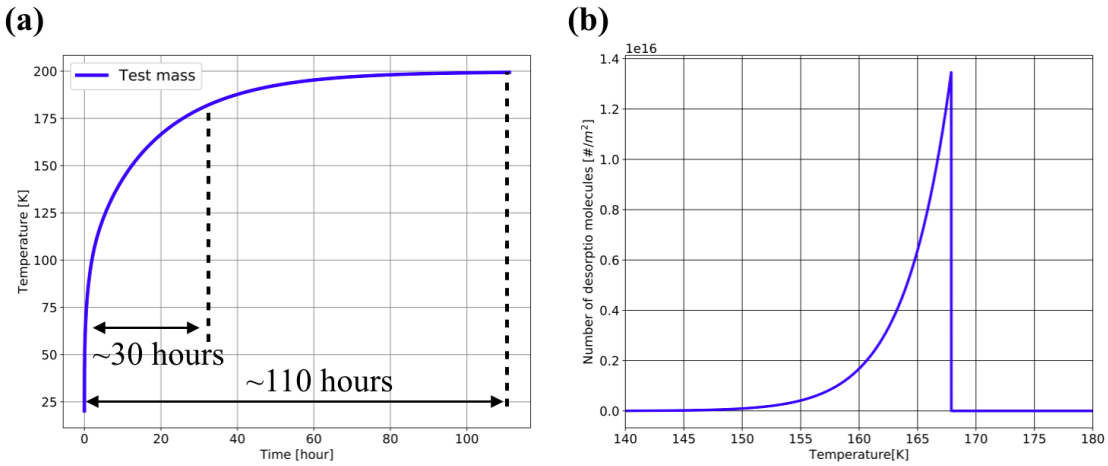

Figure 6.12: Temperature of the KAGRA cryogenic mirror during the heating process and desorption of the molecular layer. (a) By applying $P_{CO_2} = 13.5$ W of CO_2 laser, the temperature of the cryogenic mirror increases to 180 K after 30 hours. (b) H_2O molecules start to desorb from the cryogenic surface at 150 K, and it ends at about 170K.

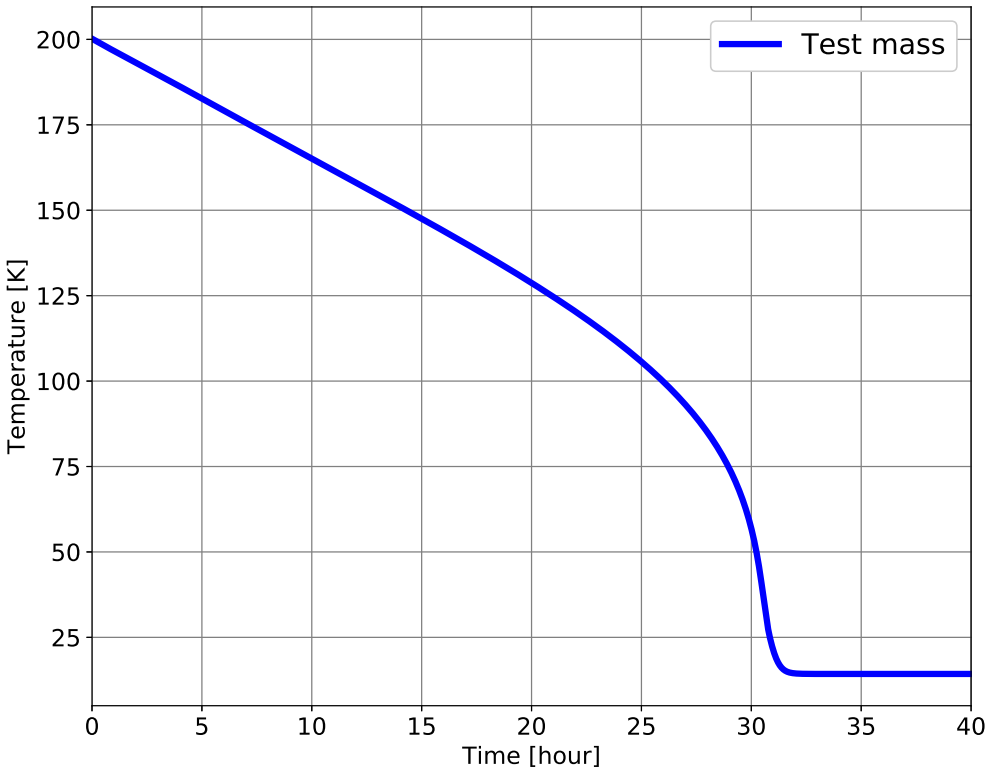

Figure 6.13: Cooling time after the heating to remove the molecular layer. After the heating, it takes about 30 hours to cool down to the nominal temperature. For the calculation, as the initial temperature of the cryogenic system, the temperature of 45 K for IM, and 30 K for the other parts was applied. The temperature of the refrigerator was kept at 7 K which is the nominal temperature when the heat load is 5.5 W.

Chapter 7
DISCUSSION

7.1 Design of cryogenic and vacuum system

As an application of the discussion in Chapter 3, it's possible to design the vacuum and cryogenic system that have small conductance. To decrease the conductance of the KAGRA duct shield, the duct shield is needed to be longer and colder. The current target temperature of the duct shield is around 100 K, but it does not adsorb N_2 and O_2 molecules efficiently as shown in the Fig.(3.8). The temperature of 50 K reduce the conductance of the duct shield from $C_{\rm ds} \sim 0.85$ to $C_{\rm ds} \sim 0.55$ for these molecules, and it implies that the molecular layer formation speed of N_2 and O_2 is reduced by 35 %. Longer duct shield is also effective to reduce the conductance for all kinds of molecules. The conductance of the combined duct is reduced by the factor of N, where N is the number of the duct shield. Hence, if we prepare the 10 times longer duct shield, the molecular layer formation rate slow about 10 times. Based on the same consideration in Chapter 3, it is possible to determine the design of the duct shield for next generation GWDs.

7.2 Accurate measurement of molecular layer formation

In Chapter 4, the measurement of the molecular layer formation was discussed. However, the error of the measured data was large and it leaves room for the discussion in Chapter 5. For more accurate measurement and characterization of the molecular layer formation in KAGRA, it is beneficial to discuss the optimization of the experimental system.

Further, the other type of measurement possibly improves the accuracy

of the experiment. Here we also introduce the spectroscopic measurement briefly.

7.2.1 Optimization of the experimental system

It is considered to be possible to measure and characterize the molecular layer formation with an optical cavity accurately by optimizing the cavity for the reflectivity oscillation that is caused by the real part of the refractive index, or for the optical loss that is caused by the imaginary part of the refractive index.

First, we consider the measurement of the real part of the refractive index. Finesse $\mathcal{F}$ of the optical cavity with a growing molecular layer is written as Eq.(4.24). Neglecting the optical loss inside the molecular layer, the reflectivity of the mirror $r_1(d_{\mathrm{mol}})$ is maximized when the thickness of the molecular layer d_{mol} satisfies the condition $d_{\mathrm{mol}} = \lambda \mathrm{m}/4n_{\mathrm{mol}}$ with $\mathrm{m} = 0, 2, 4...$, and that is minimized when $\mathrm{m} = 1, 3, 5....$ Hence, the relative amplitude of the finesse change $\delta\mathcal{F}$ is given as

$$\delta\mathcal{F} = \frac{\mathcal{F}_{\mathrm{max}} - \mathcal{F}_{\mathrm{min}}}{\mathcal{F}}, \tag{7.1}$$

where $\mathcal{F}_{\mathrm{max}}$ and $\mathcal{F}_{\mathrm{min}}$ are the maximized and the minimized finesse of the cavity.

Figure (7.1-a) shows the amplitude of the finesse changes due to the molecular layer formation. For the same reflectivity of the reference mirror, the relative amplitude of the finesse change is larger when the original reflectivity of the target mirror is lower. This is because the amplitude of the reflectivity change is maximized when the original reflectivity of the target mirror is the same as that of the molecular layer. Hence, by setting the reflectivity of the reference mirror higher and the target mirror lower, the amplitude of the finesse change gets large.

From the experimental result, the accuracy of the finesse measurement is typically about $\pm 5\%$. By setting the amplitude of the finesse change larger than the measurement accuracy, the signal of the finesse change can be obviously measured. Also, the time constant of the cavity is needed to be enough larger than that of the measurement system.

Next, we consider the measurement of the optical loss due to the absorption inside the molecular layer. Generally, the mirror with higher reflectivity degrades more due to the optical loss. If we assume the optical loss equivalent

to the optical absorption of the molecular layer with 5 μm and the imaginary part of the refractive index as $k = 1 \times 10^{-7}$, the Finesse change is calculated as shown in Fig.(7.1-b). Hence, the optical cavity with higher optical finesse measures the imaginary part of the refractive index accurately. Combining the above considerations, the molecular layer formation, and its property is measured accurately by using two optical cavities that are optimized to measure the real and imaginary part of the refractive indices.

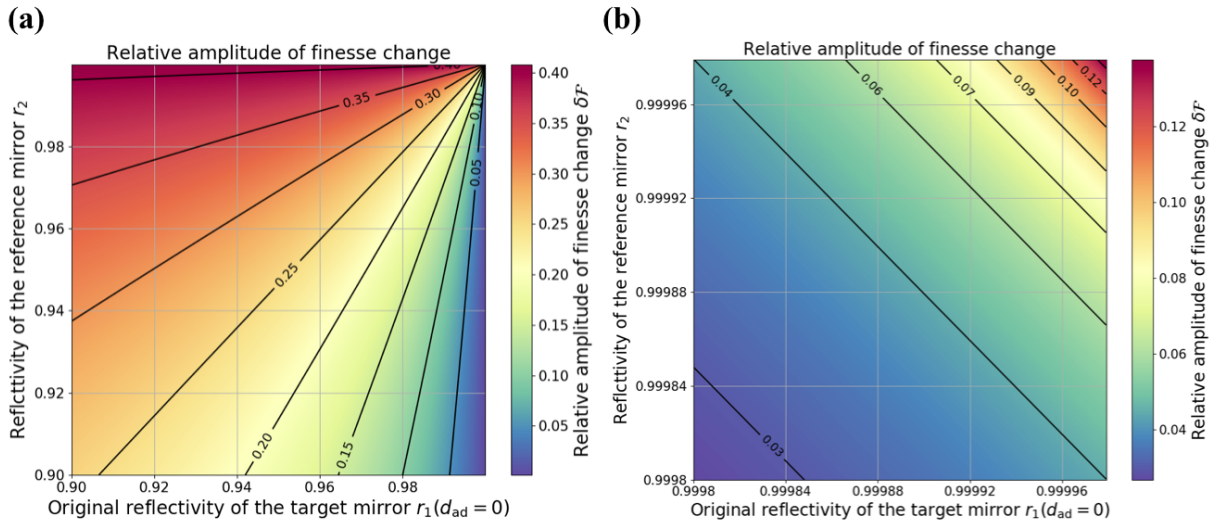

Figure 7.1: Finesse change due to the molecular layer formation. (a) The amplitude of the finesse change due to the reflectivity oscillation. The relative amplitude of the finesse change is larger when the original reflectivity of the target mirror is lower. The reflectivity of the other mirror is needed to be large enough to keep the finesse of the cavity high. (b) The amount of finesse change due to the optical loss of the molecular layer. The optical cavity with higher finesse is more sensitive to the optical loss inside. For these calculations, the refractive index of the molecular layer of $N = 1.3 - 1 \times 10^{-7}i$ and the initial optical loss of 30 ppm are assumed.

7.2.2 Molecular layer formation monitor in a GWD

Here we consider the monitoring system of the molecular layer formation during the observation of GWs. At least, four of the monitoring system is needed to measure the molecular layer on four of the HR surface of the cryogenic mir-

rors, The spectroscopic measurement using white light is suitable for GWDs because it doesn't introduce any vibration to the mirror.

There are three kinds of molecules, H_2O, N_2 and N_2, in a GWD at least. The monitoring of multi kinds of molecular layer formation with one wavelength is quite difficult. The spectroscopic measurement with a white light gives the absorption spectrum characteristic of each molecule accurately [107]. The change of the absorption spectrum gives the thickness of each molecular layer, and the information makes it possible to characterize the GWD with molecular layers in real-time.

Due to the configuration of the cryogenic GWD, the input port of the white light is quite limited. Though, it is considered that the coexistence with the calibration system using the radiation pressure solves the problem.

7.3 Unbalanced arm cavities

In Chapter 5, we assumed that the molecular layer grows on four cryogenic mirrors at the same time with same speed. But, generally speaking, the thickness of the molecular layer on the cryogenic mirrors are different each other because the vacuum pressure around the mirror and the timing to turn on the cryogenic system is different. To fully calculate the effects, huge amount of calculation resource is required. Here we assume the molecular layer growth only on the cryogenic ITMs and discuss how it affect to the interferometer.

When the reflectivity of two ITMs change separately, the shot noise is considered to be worth due to the contrast defect. Originally, the amount of the reflected light from two arm cavities are assumed to be the same, and the shot noise is evaluated under that assumption. Though, when the reflectivity of two ITMs are different, the amplitude of the interference gets low, a part of the light leaks to the AS port and the shot noise is worsen.

To estimate the effect of the contrast defect, here we consider two arm cavities. One is the room temperature cavity and the molecular layer is not formed, and the other is the cryogenic cavity with the molecular layers. Here we describe the amplitude reflectivity of the room temperature and the cryogenic cavity as r_{room} and $r_{\mathrm{cryo}}(d_{\mathrm{itm}}, d_{\mathrm{etm}})$. Using the parameter of KAGRA cryogenic mirror, the reflectivity of the room temperature cavity is calculated to be $r_{\mathrm{room}} = 0.95$, and the reflectivity of the cryogenic cavity is calculated as shown in Fig.(5.5-a) for thickness of the molecular layer on the ITM and the ETM.

Regarding the FPMI as a compound mirror, the amplitude transmissivity t_{FPMI} of the FPMI is defined by the ratio between the amplitude of the input laser electric field and the amplitude of electric field at AS port. When the interferometer is controlled to be dark fringe at AS port, the amplitude of the electric field at AS port is calculated as the difference of the amplitude of that reflected by two arms as

$$t_{\mathrm{FPMI}} = \frac{1}{2}\left(r_{\mathrm{room}} - r_{\mathrm{cryo}}\right), \tag{7.2}$$

In the case of DRFPMI, the power transmissivity T_{DRFPMI} is written as

$$T_{\mathrm{PRFPMI}} = G\left|t_{\mathrm{FPMI}}\right|^2 T_{\mathrm{SRM}} \frac{1}{\left(1+\sqrt{R_{\mathrm{FPMI}} R_{\mathrm{SRM}}}\right)} \tag{7.3}$$

where G is the power recycling gain, T_{SRM} is the power transmissivity of the SRM, R_{SRM} is the power reflectivity of the SRM and R_{FPMI} is the power reflectivity of the SRM . Figure (7.2) is the calculated result of amount of light which leaks to the AS port due to the contrast defect. Below the thickness of the molecular layer of 2.5 μm, maximum leak power to the AS port is calculated to be 2.1 mW.

The PD in KAGRA can detect 40 mW or 150 mW of laser power at maximum depends on its transimpedance gain. Here we assume that the injection to the KAGRA PD is $P_{\mathrm{normal}} = 20$ mW at normal operation.

By adding the leak laser power due to the contrast defect, the power to the PD P_{PD} is described as $P_{\mathrm{PD}} = P_{\mathrm{normal}} + P_{\mathrm{leak}}$. Hence, the laser power to the PD increases from 20 mW to 22.1 mW. The result implies that the laser power to the PD increases about 10 %. Because the shot noise is proportional to the square root of the laser power to the PD, the shot noise is worsen about 1 % for all frequency range due to the contrast defect.

7.4 Observation dead time

As a result of Chapter 6, the observation dead time due to a thermal cycle to desorb the molecular layer is shortened to 60 hours by the CO_2 laser thermal desorption system. The ratio of the observation dead time occupied by one thermal cycle during the one-year observation is calculated to be 0.8 %, and it is 8% even if the system turned on once a month. Because the target value of the KAGRA observation dead time is 10 %, the total observation dead time is expected to be 18%.

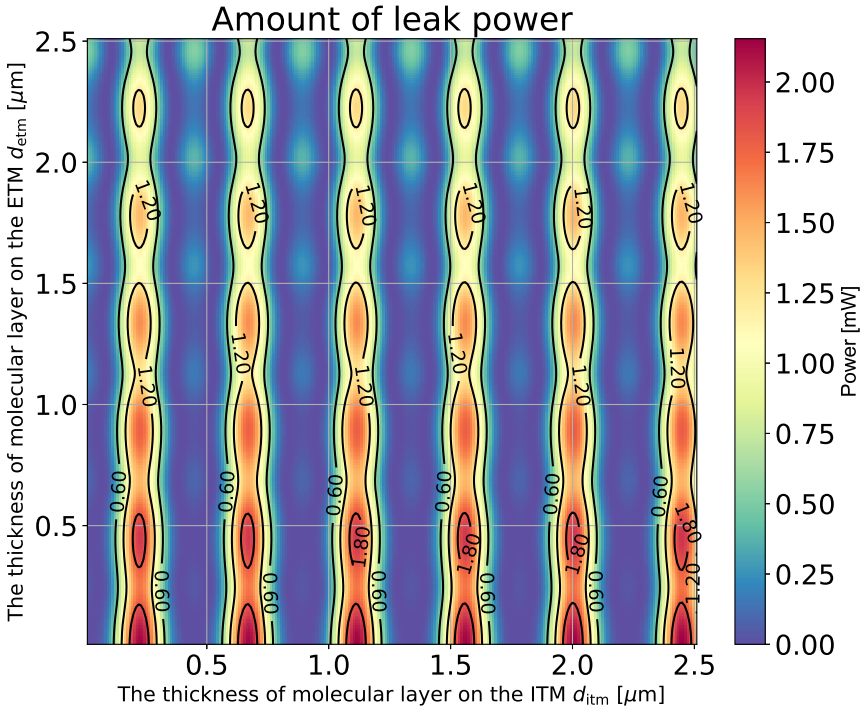

Figure 7.2: Amount of the laser power to the AS port due to the contrast defect.

This value does not achieve KAGRA target observation dead time, but it is still comparable with that of LIGO and Virgo [60,61]. Further, the adaptation of the vacuum and the cryogenic system design discussed in the previous section slows the growth of the molecular layer and reduce the number of the heating process. Hence, we can conclude that the molecular desorption system with a CO_2 laser is one of the systems that solve the problem of the molecular layer formation in cryogenic GWDs practically.

Chapter 8
CONCLUSION

8.1 Future prospects

8.1.1 Accurate measurement in KAGRA

In Chapter 4, we tried to measure the molecular layer formation experimentally in KAGRA. The results were well consistent with the numerical evaluation, though the error of the material properties are too large to consider the impacts on the telescopes. Hence, under the assumption that the main components of the molecular layer is the water molecules, the values extracted from the references were used. Generally speaking, the material properties of the molecular layer is unique to the system. This is because that density of the porous and the structure of the surface is depending on the molecular incident frequency and the spatial distribution of the source. Hence, to understand the impacts of the molecular layer on KAGRA, the accurate measurement is necessary in each detector.

The accurate measurement of such material properties using the ultra-stable arm cavity gives the important information to the ET and the Voyager. Further, the measurement of the material properties using the GWD is a unique measurement, perhaps, it open the new window to the other field such as the synchrotron radiation facility.

8.1.2 Installation of the laser based desorption system

The laser-based thermal desorption system is tested in this thesis. To install this system to KAGRA, the integration with other systems such as the vacuum and the cryogenic system is necessary. For example, the substrate which transmit the CO_2 laser is also transparent for the wavelength of the

thermal radiation. So it's not suitable to attach the substrate on the cryostat to inject the CO_2 laser. The small vacuum chamber which is set about 25 m away from the cryostat is one of the solution. By constructing the optics for the CO_2 laser, it is injected to the cryogenic test mass.

For now, the development of the CO_2 laser system for the cryogenic GWD has not been progressed. But it is also necessary to understand the detail of the cryogenic system, the thermal response of the cryogenic system to the input heat for instance.

8.1.3 Change disadvantage to advantage

Though this thesis, the molecular layer is regarded as the disadvantage of the cryogenic GWD. Here we discuss the idea of the reflectivity actuator as the application of the molecular layer formation in a cryogenic GWD and its desorption system.

The thermal desorption system is one of the actuator to change the thickness of the molecular layer with the speed of heat. On the other hand, the UV laser changes the thickness of the molecular layer more quickly. Using these auxiliary optics, the molecular layer works as the actuator to change the reflectivity of the mirror. In a GWD, the reflectivity of two ITM, and two ETM, are needed to match accurately to cancel the common noise in two arms. But it is not easy, and LIGO and Virgo made many mirrors and installed that match the requirement. If we can use the molecular layer and the desorption system as the reflectivity actuator, it reduce the time to find the mirrors that require the strict requirements, and it makes it possible to achieve designed sensitivity smoothly.

The development of the system to control the thickness of the molecular layer solve the problem. Though this is one of the examples, the change of the unique feature of the cryogenic GWD to the advantage gives the significance of the cryogenic GWD.

8.2 Conclusion

The accurate measurement of the GW is important to reveal the physics in neutron stars, the evolution of black holes and the Hubble constant. KAGRA is the first GWD which introduces the cryogenic test masses in its km scale arm, aiming to measure GWs accurately by reducing the thermal noise which

generally limits the most sensitive frequency region. Not only KAGRA but also the future GWDs such as Einstein telescope and Voyager plan to use the cryogenic mirrors to improve the sensitivity. The development of the GWD adaptable cryogenic system is one of the mission of KAGRA.

The phenomenon that the adhesion of the molecules on the cryogenic surface is well known as the cryopump. In KAGRA, it is considered that the molecules that come though the long beam duct hit and accumulate on the cryogenic mirror. This molecular layer formation has never considered except for some experimental evaluation.

In this thesis, the molecular layer formation is evaluated theoretically and numerically based on the vacuum engineering theory. As a result, if KAGRA achieve its target vacuum pressure of 1×10^{-7} Pa, the speed of the water molecular layer formation is calculated to be 0.5 μm/day. Though the current situation is far from the design, and the vacuum pressure is order of 1×10^{-6} Pa. The molecular layer speed under the current situation is evaluated experimentally and numerically, and it was found that the water molecular layer grows about 20 nm/day

Then the impacts of the molecular layer in the GWD is detailed. As a result of the reflectivity change, the quantum noise is modified, and the thermal noise of the molecular layer is added. Further, due to the optical absorption of the molecular layer, the temperature of the system is increased. These effect reduces the inspiral range for the BNS system from 137 Mpc to 75 Mpc at worst within the thickness of 2.5 μm, and the result implies that the detection rate decreases by 84%. It is also suggested that the parameters that have temperature dependence worsen the sensitivity more, and the studies on the temperature dependence of the parameters are important to characterize the cryogenic GWD well.

At last, to solve the problem, the laser-based thermal desorption system was tested in the laboratory. As a result, using the 13.5 W of the CO_2 laser, the KAGRA cryogenic test mass is warmed up to 180 K which is the enough temperature to remove H_2O molecules from the surface after about 30 hours. Auxiliary experiment also shows that this temperature is enough to remove H_2O molecules. Further, after the heating using the CO_2 to 200 K, the temperature of the test mass decreases to the nominal temperature after about 30 hours. As a total of the heating and the cooling process, the observation dead time to recover from the problem of the molecular layer is considered to be 60 hours.

This thesis discussed the formation, effects, and countermeasures of molecular layers in the GWD, first in the world. We hope that this dissertation helps the design and the construction of all of future cryogenic gravitational wave telescopes.

Chapter A
THERMAL PROPERTY

A.1 Thermal conductivity

Thermal conductivity is the value that shows the amount of the heat flow due to the conduction. The experimentally measured thermal conductivity $\kappa(T)$ of aluminum, stainless steel and sapphire are fitted using the function

$$\begin{aligned} \log_{10}\kappa(T) = a &+ b\left(\log_{10}T\right) + c\left(\log_{10}T\right)^2 + d\left(\log_{10}T\right)^3 + e\left(\log_{10}T\right)^4 \\ &+ f\left(\log_{10}T\right)^5 + g\left(\log_{10}T\right)^6 + h\left(\log_{10}T\right)^7 + i\left(\log_{10}T\right)^8 \end{aligned} \tag{A.1}$$

where a, b, c, d, e, f, g, h and i are the fitting parameters. The value of each parameters for the aluminum, stainless steel and sapphire fiber are summarized in the table(A.1), and the calculated thermal conductivity is shown in the Fig.(A.1).

A.2 Specific heat

Specific heat of the material determines how much heat is needed to increase the temperature of the material. The experimentally measured specific heat $C(T)$ of aluminum, stainless steel and sapphire are fitted using the function

$$\begin{aligned} \log_{10}C(T) = a &+ b\left(\log_{10}T\right) + c\left(\log_{10}T\right)^2 + d\left(\log_{10}T\right)^3 + e\left(\log_{10}T\right)^4 \\ &+ f\left(\log_{10}T\right)^5 + g\left(\log_{10}T\right)^6 + h\left(\log_{10}T\right)^7 + i\left(\log_{10}T\right)^8 \end{aligned} \tag{A.2}$$

where a, b, c, d, e, f, g, h and i are the fitting parameters. The value of each parameters for the aluminum, stainless steel and sapphire are summarized in the table(A.2), and the calculated linear expansion is shown in the Fig.(A.2).

	a	b	c	d
Aluminum 5083	-0.90933	5.751	-11.112	13.612
SUS316	-1.4087	1.3982	0.2543	-0.6260
Sapphire (fiber)	0.51198	-15.53082	101.14378	-230.25518
e	f	g	h	i
-9.3977	3.6873	-0.77295	0.067336	0
0.2334	0.4256	-0.4658	0.1650	-0.0199
272.02718	-178.81381	65.27225	-12.29679	0.9250

Table A.1: Fitting parameters for the specific heat.

	a	b	c	d
Aluminum 5083	46.6467	-314.292	866.662	-1298.3
SUS316 (T<50K)	12.2486	-80.6422	218.743	-308.854
(50<T<300K)	-1879.464	3643.198	76.70125	-6176.028
Sapphire	24.0167	-153.903	363.051	-455.547
e	f	g	h	i
1162.27	-637.795	210.351	-38.3094	2.96344
239.5296	-89.9982	3.15315	8.44996	-1.91368
7437.6247	-4305.7217	1382.4627	-237.22704	17.05262
339.736	-154.631	42.1373	-6.32213	0.402076

Table A.2: Fitting parameters for the linear expansion.

A.3 Linear Expansion

The linear expansion α is defined as

$$\alpha = \frac{L(T) - L_{293}}{L_{293}}, \tag{A.3}$$

where $L(T)$ and L_{293} are the length at T K and 293 K.

The experimentally measured linear expansion of aluminum, stainless steel and sapphire are fitted using the function

$$\alpha(T) = a + bT + cT^2 + dT^3 + eT^4 \tag{A.4}$$

where a, b, c, d and e are the fitting parameters. The value of each parameters for the aluminum, stainless steel and sapphire are summarized in the table(A.3), and the calculated specific heat is shown in the Fig.(A.3).

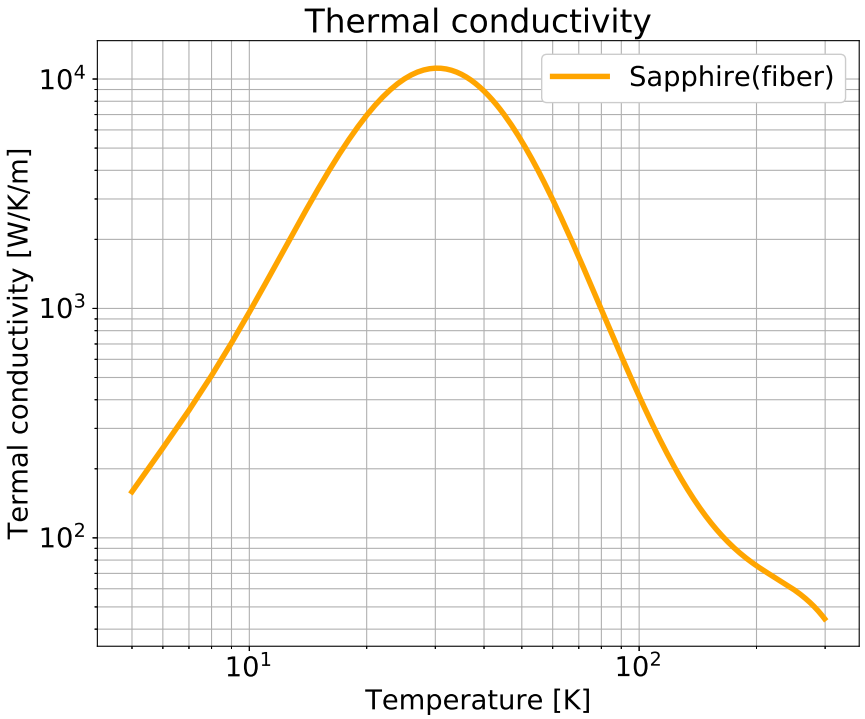

Figure A.1: Specific heat

	a	b	c	d	e
Aluminum 5083	-4.13×10^{2}	-3.04×10^{-1}	8.77×10^{-3}	-9.98×10^{-6}	0
SUS304L	-2.96×10^{2}	-3.98×10^{-1}	9.27×10^{-3}	-2.03×10^{-5}	1.71×10^{-8}
Sapphire	-7.89×10^{1}	-2.23×10^{-2}	1.02×10^{-4}	5.56×10^{-6}	-8.54×10^{-9}

Table A.3: Fitting parameters for the linear expansion.

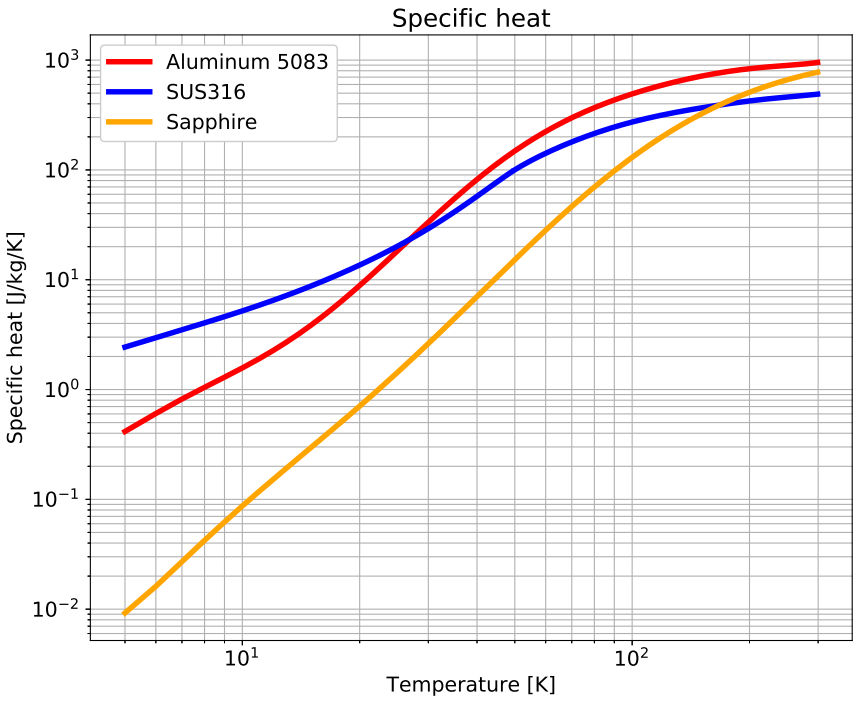

Figure A.2: Specific heat

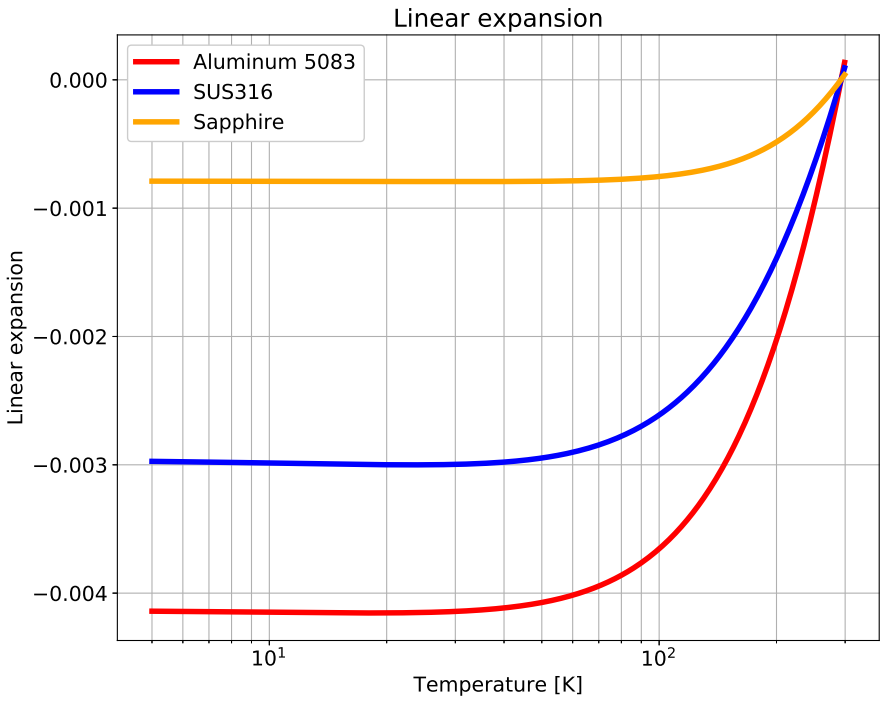

Figure A.3: Linear Expansion.

Chapter B
DIELECTRIC MULTILAYER COATING

B.1 $\lambda/4$ model

The dielectric multilayer coating is usually used in the GW research field. The reflectivity of the coating is controlled by stacking the high and low refractive index materials alternatively on the substrate. It works as the high reflective coating when all of the reflected light from each layer constructive interfere.

Generally speaking, the information about the details of the coating, the thickness and the refractive index of each layer, for instance, is internal secret, and researchers cannot know about them. To carry out the study on the coating, the $\lambda/4$ model is used. In the $\lambda/4$ model, the optical thickness of each layer is considered to be the quoter of the wavelength we use. Then, the reflected light from each layer constructive interfere with each other, and the reflectivity of the coating is changed by the number of the doublet.

B.2 Characteristic matrix

Once we determine the details of the coating, the reflectivity of the coating is calculated by considering the composition of the fresnel coefficient of boundaries. Here, the characteristic matrix which is developed to compute the fresnel coefficient systematically is introduced.

The characteristic matrix of a layer which has the complex refractive index N_i and the mechanical thickness of d_i is defined as

$$M_i = \begin{bmatrix} \cos\delta_\mathrm{i} & i\sin\delta_\mathrm{i}/N_\mathrm{i} \\ iN_\mathrm{i}\sin\delta_\mathrm{i} & \cos\delta_\mathrm{i} \end{bmatrix}, \tag{B.1}$$

where $\delta_{\mathrm{i}} = 2\pi N_{\mathrm{i}} d_{\mathrm{i}}/\lambda$ is an optical phase shift inside the layer. Then, the total characteristic matrix M_{tot} of n layer coating is calculated as

$$\begin{aligned} M_{\mathrm{tot}} &= M_1 \cdot M_2 \cdots M_{\mathrm{n}-1} \cdot M_{\mathrm{n}} \\ &= \prod_{\mathrm{k}=1}^{\mathrm{n}} M_{\mathrm{k}} = \begin{bmatrix} m_{11} & im_{12} \\ im_{21} & m_{22} \end{bmatrix}. \end{aligned} \tag{B.2}$$

where m_{ij} are the elements of the matrix. For the total characteristic matrix, two coefficients B and C are calculated as

$$\begin{bmatrix} B \\ C \end{bmatrix} = \begin{bmatrix} m_{11} & im_{12} \\ im_{21} & m_{22} \end{bmatrix} \begin{bmatrix} 1 \\ n_{\mathrm{sub}} \end{bmatrix}, \tag{B.3}$$

where n_{sub} is the refractive index of the substrate material. Equation(B.3) gives the Fresnel coefficient of the coating as

$$\rho = \frac{n_0 B - C}{n_0 B + C}. \tag{B.4}$$

The Fresnel coefficient directly leads to the power reflectance of light as $R = |\rho|^2$.

For example, the reflectivity of the dielectric multilayer coating which is composed of SiO_2 and Ta_2O_5 for the number of the doublet is calculated as shown in Fig.(B.1), and it implies that the reflectivity of the coating get high when the number of the doublet is increased. This calculation method is suitable for the computation of the reflective index and enables to calculate simply compared with the decent calculation of the compound fresnel coefficient.

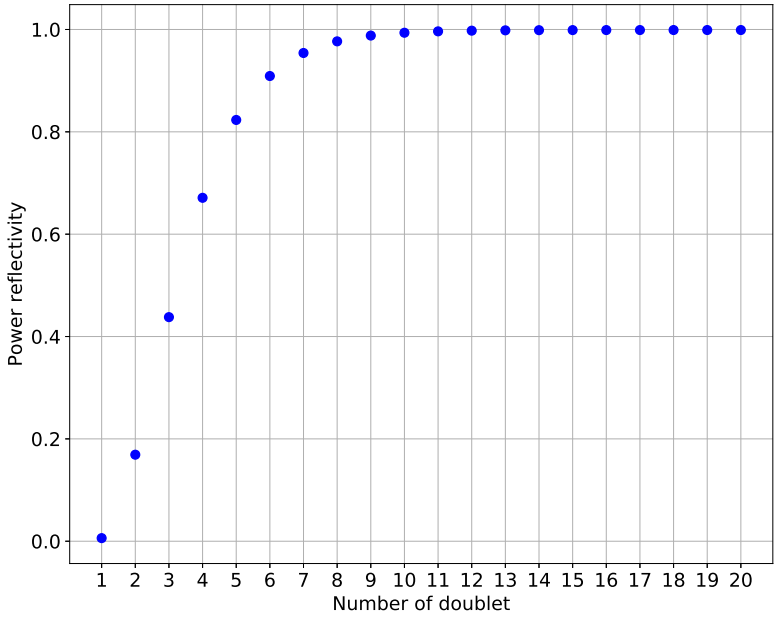

Figure B.1: Reflectivity of the dielectric multilayer coating. The reflectivity of the dielectric multilayer coating get higher when the number of the doublet is increased.

BIBLIOGRAPHY

[1] A.Eintein, *Integration der Feldgleichungen der.* Sitzungsber.K.Preuss.Akad.Wiss., pages 688–696, (1916).

[2] A.Einstein, *Über Gravitationswellen.* Sitzungsber.K.Preuss.Akad.Wiss., page 154, (1918).

[3] B. P. Abbott *et al.* , *LIGO: The laser interferometer gravitational-wave observatory.* Reports on Progress in Physics, **72**(7), (2009).

[4] F. Acernese *et al.* , *Virgo status.* Classical and Quantum Gravity, **25**(18), (2008).

[5] K. Somiya, *Detector configuration of KAGRA the Japanese cryogenic gravitational-wave detector.* Classical and Quantum Gravity, **29**:124007, (2012).

[6] B. P. Abbott *et al.* , *the Rate of Binary Black Hole Mergers Inferred From Advanced Ligo Observations Surrounding Gw150914.* The Astrophysical Journal, **833**(1):L1, (2016).

[7] M. Magiiore. *Gravitational Waves: Volume 1: Theory and Experiments.* Oxford University Press, (2007).

[8] B. P. Abbott, *Observation of Gravitational Waves from a Binary Black Hole Merger.* Physical Review Letters, **061102**(February):1–16, (2016).

[9] B. P. Abbott *et al.* , *GW151226: Observation of Gravitational Waves from a 22-Solar-Mass Binary Black Hole Coalescence.* Physical Review Letters, **116**(24):1–14, (2016).

[10] B. P. Abbott *et al.* , *GW170104: Observation of a 50-Solar-Mass Binary Black Hole Coalescence at Redshift 0.2.* Physical Review Letters, **118**(22):1–17, (2017).

[11] B. P. Abbott *et al.* , *GW170608: Observation of a 19 Solar-mass Binary Black Hole Coalescence.* The Astrophysical Journal, **851**(2):L35, (2017).

[12] B. P. Abbott *et al.* , *GW170814: A Three-Detector Observation of Gravitational Waves from a Binary Black Hole Coalescence.* Physical Review Letters, **119**(14):1–16, (2017).

[13] B. P. Abbott, *GW170817 : Observation of Gravitational Waves from a Binary Neutron Star Inspiral.* **161101**(October):30–33, (2017).

[14] L. Baiotti, *Gravitational waves from neutron star mergers and their relation to the nuclear equation of state.* Progress in Particle and Nuclear Physics, **109**:1–100, (2019).

[15] T. T. Sun, C. J. Xia, S. S. Zhang, and M. S. Smith, *Massive neutron stars and Λ-hypernuclei in relativistic mean field models.* Chinese Physics C, **42**(2):1–8, (2018).

[16] E. Muller, M. Rampp, R. Buras, H. Janka, and D. H. Shoemaker, *Toward Gravitational Wave Signals from Realistic Core- Collapse Supernova Models.* The Astrophysical Journal, **603**(1):221–230, (2004).

[17] V. Morozova, D. Radice, A. Burrows, and D. Vartanyan, *The Gravitational Wave Signal from Core-collapse Supernovae.* The Astrophysical Journal, **861**(1):10, (2018).

[18] G. Pizzella, *Resonant detectors for gravitational waves and their bandwidth.* Gravitational Waves, **48**:91–102, (2001).

[19] R. S. Foster and D. C. Backer, *CONSTRUCTING A PULSAR TIMING ARRAY.* The Astrophysical Journal, **361**:300–308, (1990).

[20] M. Ando, *Power recycling for an interferometric gravitational wave detector.* PhD Thesis,The University of Tokyo, (December), (1998).

[21] J. Mizuno *et al.* , *Resonant sideband extraction: a new configuration for interferometric gravitational wave detectors.* Physics Letters A, **175**(5):273–276, (1993).

[22] T. Sekiguchi, *A Study of Low Frequency Vibration Isolation System for Large Scale Gravitational Wave Detectors 27 12*. PhD Thesis, The University of Tokyo, (2015).

[23] K. Okutomi, *Development of 13.5-meter-tall Vibration Isolation System for the Main Mirrors in KAGRA*. PhD Thesis, The Graduate University for Advanced Studies, SOKENDAI, (2019).

[24] Y. Akiyama *et al.* , *Vibration isolation system with a compact damping system for power recycling mirrors of KAGRA*. Classical and Quantum Gravity, **36**(9), (2019).

[25] H. Callen and T. Elton, *Irreversibility and Generalized Noise*. Physical Review, **87**(3):471–472, (1952).

[26] Y. Levin, *Internal thermal noise in the LIGO test masses: A direct approach*. Physical Review D, **57**(2):659–663, (1998).

[27] G. M. Harry *et al.* , *Thermal noise in interferometric gravitational wave detectors due to dielectric optical coatings*. Classical and Quantum Gravity, **19**(5):897–917, (2002).

[28] W. Yam, S. Gras, and M. Evans, *Multimaterial coatings with reduced thermal noise*. Physical Review D - Particles, Fields, Gravitation and Cosmology, **91**(4):1–6, (2015).

[29] K. Yamamoto, S. Otsuka, M. Ando, K. Kawabe, and K. Tsubono, *Study of the thermal noise caused by inhomogeneously distributed loss*. Classical and Quantum Gravity, **19**(7):1689–1696, (2002).

[30] Y. Levin, *Fluctuation-dissipation theorem for thermo-refractive noise*. Physics Letters, Section A: General, Atomic and Solid State Physics, **372**(12):1941–1944, (2008).

[31] M. Evans *et al.* , *Thermo-optic noise in coated mirrors for high-precision optical measurements*. Physical Review D - Particles, Fields, Gravitation and Cosmology, **78**(10):1–10, (2008).

[32] G. González, *Suspensions thermal noise in the LIGO gravitational wave detector*. Classical and Quantum Gravity, **17**(21):4409–4435, (2000).

[33] G. D. Hammond *et al.* , *Reducing the suspension thermal noise of advanced gravitational wave detectors.* Classical and Quantum Gravity, **29**(12), (2012).

[34] N. Takashi, M. Norikatsu, and O. Masatake. *Detection of Gravitaitonal Waves.* (1998).

[35] K. Somiya *et al.* , *Development of a frequency-detuned interferometer as a prototype experiment for next-generation gravitational-wave detectors.* Applied Optics, **44**(16):3179–3191, (2005).

[36] E. Oelker *et al.* , *Audio-Band Frequency-Dependent Squeezing for Gravitational-Wave Detectors.* Physical Review Letters, **116**(4):1–6, (2016).

[37] M. Tse *et al.* , *Quantum-Enhanced Advanced LIGO Detectors in the Era of Gravitational-Wave Astronomy.* Physical Review Letters, **123**(23):231107, (2019).

[38] A. Buonanno and Y. Chen, *Quantum noise in second generation, signal-recycled laser interferometric gravitational-wave detectors.* Physical Review D - Particles, Fields, Gravitation and Cosmology, **64**(4):21, (2001).

[39] M. Punturo *et al.* , *The Einstein Telescope: A third-generation gravitational wave observatory.* Classical and Quantum Gravity, **27**(19), (2010).

[40] B. P. Abbott *et al.* , *Exploring the sensitivity of next generation gravitational wave detectors.* Classical and Quantum Gravity, **34**(4), (2017).

[41] D. Reitze *et al.* , *Cosmic Explorer: The U.S. Contribution to Gravitational-Wave Astronomy beyond LIGO.* (2019).

[42] D. V. Martynov *et al.* , *Sensitivity of the Advanced LIGO detectors at the beginning of gravitational wave astronomy.* Physical Review D, **93**(11):1–20, (2016).

[43] F. Acernese *et al.* , *Advanced Virgo: A second-generation interferometric gravitational wave detector.* Classical and Quantum Gravity, **32**(2), (2015).

[44] J. Agresti *et al.* , *Optimized multilayer dielectric mirror coatings for gravitational wave interferometers.* Advances in Thin-Film Coatings for Optical Applications III, **6286**(August 2006):628608, (2006).

[45] K. Komori, Y. Michimura, and K. Somiya, *Parameters for the latest estimated sensitivity of KAGRA.* KAGRA Technical Note, **JGW-T17070**:1–5, (2017).

[46] E. Hirose *et al.* , *Sapphire mirror for the KAGRA gravitational wave detector.* Physical Review D - Particles, Fields, Gravitation and Cosmology, **89**(6):1–7, (2014).

[47] E. Hirose, *Update from MIR subgroup.* KAGRA Technical Note, **JGW-G17064**, (2017).

[48] M. Ando, K. Arai, K. Kawabe, and K. Tsubono, *Demonstration of power recycling on a Fabry-Perot-type prototype gravitational wave detector.* Physics Letters, Section A: General, Atomic and Solid State Physics, **248**(2-4):145–150, (1998).

[49] Y. Aso *et al.* , *Interferometer design of the KAGRA gravitational wave detector.* Physical Review D, **88**(4):1–15, (2013).

[50] Y. Michimura *et al.* , *Mirror actuation design for the interferometer control of the KAGRA gravitational wave telescope.* Classical and Quantum Gravity, **34**(22), (2017).

[51] Y. Enomoto, *Requirement on Displacement Noise of Each MIF Mirror (bKAGRA sensitivity v201708).* KAGRA Technical Note, **JGW-T18092**:10, (2018).

[52] C. Tokoku *et al.* , *Cryogenic System for the Interferometric Cryogenic GravitationalWave Telescope, KAGRA - Design, Fabrication, and Performance Test -.* AIP Conference Proceedings, **1573**:1254–1261, (2014).

[53] Y. Sakakibara *et al.* , *A study of cooling time reduction of interferometric cryogenic gravitational wave detectors using a high-emissivity coating A Study of Cooling Time Reduction of Interferometric Cryogenic Gravitational Wave Detectors Using a High-Emissivity Coating.* Advances in Cryogenic Engineering AIP Conf. Proc, **1176**(February), (2015).

[54] Y. Sakakibara, *A Study of Cryogenic Techniques for Gravitaitonal Wave Detection*. Ph. D. Thesis, (2016).

[55] D. Chen, *Study of a cryogenic suspension system for the gravitational wave telescope KAGRA*. PhD Thesis, The University of Tokyo, (2014).

[56] Y. Sakakibara, N. Kimura, T. Akutsu, T. Suzuki, and K. Kuroda, *Performance test of pipe-shaped radiation shields for cryogenic interferometric gravitational wave detectors*. Classical and Quantum Gravity, **32**(15), (2015).

[57] R. Takahashi *et al.* , *Direct measurement of residual gas effect on the sensitivity in TAMA300*. Journal of Vacuum Science & Technology A: Vacuum, Surfaces, and Films, **20**(4):1237–1241, (2002).

[58] Y. Saito and R. Takahashi, *Production Process of the Interferometer Beam Tubes in LCGT Project*. **54**(12):621–626, (2011).

[59] Y. Saito, *Vacuum design for bLCGT/iLCGT*. KAGRA Technical Note, **JGW-T1100372-v1**, (2011).

[60] LIGO Scientific Collaboration & Virgo Collaboration. Gravitational-Wave Observatory Status Observing Run 1 Summary.

[61] LIGO Scientific Collaboration & Virgo Collaboration. Gravitational-Wave Observatory Status Observing Run 2 Summary.

[62] I. H. Malitson, *Refraction and Dispersion of Synthetic Sapphire*. Journal of the Optical Society of America, **52**(12):1377, (1962).

[63] M. Granata *et al.* , *Mechanical loss in state-of-the-art amorphous optical coatings*. Physical Review D, **93**(1):1–16, (2016).

[64] M. M. Fejer *et al.* , *Thermoelastic dissipation in inhomogeneous media: Loss measurements and displacement noise in coated test masses for interferometric gravitational wave detectors*. Physical Review D - Particles, Fields, Gravitation and Cosmology, **70**(8):1–19, (2004).

[65] R. Flaminio *et al.* , *A study of coating mechanical and optical losses in view of reducing mirror thermal noise in gravitational wave detectors*. Classical and Quantum Gravity, **27**(8), (2010).

[66] M. L. Chan, C. Messenger, I. S. Heng, and M. Hendry, *Binary neutron star mergers and third generation detectors: Localization and early warning*. Physical Review D, **97**(12):27–31, (2018).

[67] J. Aasi *et al.* , *Enhanced sensitivity of the LIGO gravitational wave detector by using squeezed states of light*. Nature Photonics, **7**(8):613–619, (2013).

[68] The LIGO Scientific Collaboration, *Instrument Science White Paper*. LIGO Technical Note, (225), (2015).

[69] S. Miyoki, T. Uchiyama, T. Tomaru, and D. Tatsumi, *Cryogenic contamination of an ultra-low loss mirror for cryogenic laser interferometric gravitational wave detector*. Cryogenics, **40**:61–66, (2000).

[70] S. Miyoki *et al.* , *Cryogenic contamination speed for cryogenic laser interferometric gravitational wave detector*. Cryogenics, **41**(5-6):415–420, (2001).

[71] N. Matuda, *Basic concepts to kinetic theory of gases*. Journal of the Vacuum Society of Japan, **56**(6):199–203, (2013).

[72] Dortmund-Data-Bank. Saturated Vapor Pressure.

[73] J. Yuyama and Y. Suetsugu, *Evacuation and vacuum pumps*. Journal of the Vacuum Society of Japan, **56**(6):210–219, (2013).

[74] D. J. Santeler, *New concepts in molecular gas flow*. Journal of Vacuum Science & Technology A: Vacuum, Surfaces, and Films, **4**(3):338–343, (1986).

[75] M. MATSUMOTO and S. SUKENOBU, *Calculation of Transmission Probability of Gas Molecule through Vacuum Pipe by Monte-Carlo Method*. Journal of the Vacuum Society of Japan, **58**(8):299–305, (2015).

[76] K. Fukutani, *Surfaces in vacuum technology*. Journal of the Vacuum Society of Japan, **56**(6):204–209, (2013).

[77] CERN and ESRF. Molflow+.

[78] J. He, K. Acharyya, and G. Vidali, *Sticking of Molecules on Nonporous Amorphous Water Ice*. The Astrophysical Journal, **823**(1):56, (2016).

[79] K. Hasegawa *et al.* , *Molecular adsorbed layer formation on cooled mirrors and its impacts on cryogenic gravitational wave telescopes*. Physical Review D, **99**(2):22003, (2019).

[80] N. Giovambattista, H. E. Stanley, and F. Sciortino, *Phase diagram of amorphous solid water: Low-density, high-density, and very-high-density amorphous ices*. Physical Review E - Statistical, Nonlinear, and Soft Matter Physics, **72**(3):1–12, (2005).

[81] D. R. Lide. *CRC Handbook of Chemistry and Physics: A Ready-reference Book of Chemical and Physical Data*. CRC PRESS, (1995).

[82] H. M. Roder, *The molar volume (density) of solid oxygen in equilibrium with vapor*. Journal of Physical and Chemical Reference Data, **7**(3):949–958, (1978).

[83] J. M. Elson, J. P. Rahn, and J. M. Bennett, *Relationship of the total integrated scattering from multilayer-coated optics to angle of incidence , polarization , correlation length , and roughness cross-correlation properties*. Applied optics, **22**(20):3207–3219, (1983).

[84] J. E. Harvey, *Total integrated scatter from surfaces with arbitrary roughness, correlation widths, and incident angles*. Optical Engineering, **51**(1):013402, (2012).

[85] C. A. Mack, *Analytic form for the power spectral density in one, two, and three dimensions*. Journal of Micro/Nanolithography, MEMS, and MOEMS, **10**(4):040501, (2011).

[86] J. M. Labello, *Water Ice Films in Cryogenic Vacuum Chambers*. PhD Thesis, University of Tennessee, (2011).

[87] M. Nickerson, *A review of Pound-Drever-Hall laser frequency locking*. Jila, page 11, (2013).

[88] K. Hasegawa. *Methodological development for optical loss estimation due to dust particles on low-loss mirrors of KAGRA gravitational wave telescope*. Master thesis, The University of Tokyo, (2017).

[89] MATERIAL MEASUREMENT LABORATORY, NIST. Material Properties: 304 Stainless (UNS S30400), https://trc.nist.gov/cryogenics/materials/304Stainless/304Stainless_rev.htm

[90] I. H. Malitson, *Interspecimen Comparison of the Refractive Index of Fused Silica*. Journal of the Optical Society of America, **55**(10):1205, (1965).

[91] V. Kofman, J. He, I. Loes ten Kate, and H. Linnartz, *The Refractive Index of Amorphous and Crystalline Water Ice in the UVvis*. The Astrophysical Journal, **875**(2):131, (2019).

[92] D. T. Limmer and D. Chandler, *Theory of amorphous ices*. Proceedings of the National Academy of Sciences of the United States of America, **111**(26):9413–9418, (2014).

[93] S. G. Warren and R. E. Brandt, *Optical constants of ice from the ultraviolet to the microwave: A revised compilation*. Journal of Geophysical Research Atmospheres, **113**(14):1–10, (2008).

[94] T. Yamada, *Heat Extraction Capacity*. KAGRA Technical Note, **JGW-G19105**, (2019).

[95] J. Hessinger, B. E. White, and R. O. Pohl, *Elastic properties of amorphous and crystalline ice films*. Planetary and Space Science, **44**(9):937–944, (1996).

[96] M. Nakano and Y. Michimura, *Comment to Xarm finesse dropped.*. KAGRA Logbook, 10033, http://klog.icrr.u-tokyo.ac.jp/osl/?r=10033,(2019)

[97] Y. Enomoto, *Fogged ITMY*. KAGRA Logbook, 9377, http://klog.icrr.u-tokyo.ac.jp/osl/?r=9377, (2019)

[98] Y. Michimura, *Comment to Xarm finesse dropped*. KAGRA Logbook, 9827, http://klog.icrr.u-tokyo.ac.jp/osl/?r=9827, (2019)

[99] P. A. Redhead, *Thermal desorption of gases*. Vacuum, **12**(4):203–211, (1962).

[100] C. A. Klein, *Materials for high-power laser optics: the thermal lensing issue*. Inorganic Optical Materials: A Critical Review, **10286**(August 1996):102860D, (1996).

[101] J. Degallaix, C. Zhao, L. Ju, and D. Blair, *Simulation of bulk-absorption thermal lensing in transmissive optics of gravitational waves detectors*. Applied Physics B: Lasers and Optics, **77**(4):409–414, (2003).

[102] T. Tomaru, T. Suzuki, and S. Miyoki, *Thermal lensing in cryogenic sapphire substrates*. Classical and Quantum Gravity, **19**:2045, (2002).

[103] P. J. Barrie, *Analysis of temperature programmed desorption (TPD) data for the characterisation of catalysts containing a distribution of adsorption sites*. Physical Chemistry Chemical Physics, **10**(12):1688–1696, (2008).

[104] D. L. Rakić V. *Temperature-Programmed Desorption (TPD) Methods. In: Auroux A. (eds) Calorimetry and Thermal Methods in Catalysis*. Springer, Berlin, Heidelberg, (2013).

[105] H. Shakeel, H. Wei, and J. M. Pomeroy, *Measurements of Enthalpy of Sublimation of Ne , N2 , O2 , Ar , CO2 , Kr , Xe , and H2O using a Double Paddle Oscillator*.

[106] H. J. Fraser, M. P. Collings, M. R. McCoustra, and D. A. Williams, *Thermal desorption of water ice in the interstellar medium*. Monthly Notices of the Royal Astronomical Society, **327**(4):1165–1172, (2001).

[107] C. S. Roesler, *Theoretical and experimental approaches to improve the accuracy of particulate absorption coefficients derived from the quantitative filter technique*. Limnology and Oceanography, **43**(7):1649–1660, (1998).